Development of the Detector Control System and Instrumentation for the Silicon Tracking System in the Compressed Baryonic Matter Experiment

Dissertation
zur Erlangung des Doktorgrades
der Naturwissenschaftens

vorgelegt beim Fachbereich Physik
der Johann Wolfgang Goethe-Universität
in Frankfurt am Main

von
Marcel Bajdel
aus Katowice, Polen

Frankfurt am Main 2023
D30

vom Fachbereich Physik der
Johann Wolfgang Goethe-Universität als Dissertation angenommen.

Dekan:	Prof. Dr. Roger Erb
Gutachter:	Prof. Dr. Joachim Stroth Prof. Dr. Hans Rudolf Schmidt

Datum der Disputation:

Δεν υπάρχει τίποτα μόνιμο, εκτός από την αλλαγή.

There is nothing permanent, except change.

Ἡράκλειτος

to my family

Table of Contents

Table of Contents

Table of Contents

Abstract

The Compressed Baryonic Matter (CBM) is one of the core experiments at the future Facility for Anti-proton and Ion Research (FAIR), Darmstadt, Germany. Its goal is to investigate nuclear matter characteristics at high net-baryon densities and moderate temperatures. The Silicon Tracking System (STS) is a central detector system of CBM. It is placed inside a 1 Tm magnet and operated at a temperature of about −10 °C to keep radiation-induced bulk current in the 300 µm double-sided microstrip silicon sensors low. The design of the STS aims to minimize the material budget in the detector acceptance ($2.5° < \theta < 25°$). In order to do so, the readout electronics is placed outside the active area, and the analog signals are transported via ultra-thin micro-cables. The STS comprises eight tracking stations with 876 modules. Each module is assembled on a carbon fiber ladder, which is subsequently mounted in the C-shaped aluminum frame.

The scope of the thesis focused on developing a modular control system framework that can be implemented for different sizes of experimental setups. The developed framework was used for setups that required a remote operation, like the irradiation of the powering modules for the front-end electronics (FEE), but also in laboratory-based setups where the automation and archiving were needed (thermal cycling of the STS electronics).

The low voltage powering modules will be placed in the vicinity of the experiment, therefore they will experience a total dose of up to 40 mGy over the 10 years of STS lifetime. To estimate the effects of the radiation on the low-voltage module performance, a dedicated irradiation campaign took place. It aimed at estimating the rate of radiation-induced soft errors, that lead to the switch off of the FEE.

Regular power cycles of multiple front-end boards (FEBs) pose a risk to the experiment operation. Firstly, such behavior could negatively influence the physics performance but also have deteriorating effects on the hardware. It was further assessed what are the limitations of the FEBs with respect to the thermal cycling and the mechanical stress. The results served as an indication of possible failure modes of the FEB at the end of STS lifetime. Failure modes after repeated cycles and potential reasons were determined (e.g., Coefficient of Thermal Expansion (CTE) difference between the materials).

Due to the conditions inside the STS efficient temperature and humidity monitoring and control are required to avoid icing or water condensation on the electronics or silicon sensors. The most important properties of a suitable sensor candidate are resilience

to the magnetic field, ionizing radiation tolerance, and fairly small size.

A general strategy for ambient parameters monitoring inside the STS was developed, and potential sensor candidates were chosen. To characterize the chosen relative humidity sensors the developed control framework was introduced. A sampling system with a ceramic sensor and Fiber Optic Sensors (FOS) were identified as reliable solutions for the distributed sensing system. Additionally, the industrial capacitive sensors will be used as a reference during the commissioning.

Two different designs of FOS were tested: a hygrometer and 5 sensors multiplexed in an array. The FOS hygrometer turned out to be a more reliable solution. One of the possible reasons for a worse performance is a relatively low distance between the subsequent sensors (15 cm) and a thicker coating. The results obtained from the time response study pointed out that the thinner coating of about 15 µm should be a good compromise between the humidity sensitivity and the time response.

The implementation of the containerized-based control system framework for the mSTS is described in detail. The deployed EPICS-based framework proved to be a reliable solution and ensured the safety of the detector for almost 1.5 years. Moreover, the data related to the performance of the detector modules were analyzed and significant progress in the quality of modules was noted. Obtained data was also used to estimate the total fluence, which was based on the leakage current changes.

The developed framework provided a unique opportunity to automate and control different experimental setups which provided crucial data for the STS. Furthermore, the work underlines the importance of such a system and outlines the next steps toward the realization of a reliable Detector Control System for STS.

Kurzfassung

Das Compressed Baryonic Matter (CBM) Experiment ist eines der vie geplanten Experiment an der zukünftigen Facility for Anti-proton and Ion Research (FAIR) in Darmstadt, Deutschland. Sein Ziel ist es, die Eigenschaften von Kernmaterie bei hohen Baryonenkonzentrationen und moderaten Temperaturen zu untersuchen. Das Silicon Tracking System (STS) ist das zentrale Detektorsystem des CBM. Es ist in einem 1 Tm Magneten untergebracht und wird bei einer Betriebstemperatur von etwa −10 °C arbeiten, um den strahlungsinduzierten Leckstrom in den 300 µm doppelseitigen Silizium-Mikrostreifensensoren niedrig zu halten. Das Design des STS zielt darauf ab, das Materialbudget in der Detektorakzeptanz ($2.5° < \theta < 25°$) zu minimieren. Dazu wird die Ausleseelektronik außerhalb des aktiven Bereichs platziert, und die analogen Signale werden über ultradünne Mikrokabel ausgelesen. Das STS besteht aus acht Tracking-Stationen mit insgesamt 876 Modulen. Jedes Modul ist auf einer Stützstruktur aus Kohlefaser montiert, die anschließend in den C-förmigen Aluminiumrahmen eingebaut wird.

Der Schwerpunkt der Arbeit lag auf der Entwicklung eines modularen Steuerungs- und Kontrollsystems, das für verschiedene Größen von Versuchsaufbauten eingesetzt werden kann. Das entwickelte, modulare Kontrollsystem wurde für Versuchsaufbauten verwendet, die eine Fernsteuerung erfordern, wie die Bestrahlung der Stromversorgungsmodule für die FEE, aber auch in laborgestützten Versuchsaufbauten, bei denen die Automatisierung und Archivierung erforderlich ist (thermische Zyklen der STS-Elektronik).

Die Niederspannungsstromversorgungsmodule werden in der Nähe des Experiments platziert. Während der 10-jährigen Lebensdauer des STS werden Sie einer Gesamtdosis von bis zu 40 mGy pro Monat ausgesetzt sein. Um die Auswirkungen der Strahlung auf die Leistung der Niederspannungsmodule abzuschätzen, wurde eine spezielle Bestrahlungskampagne durchgeführt. Das Ziel war, die Rate der strahleninduzierten weichen Fehler abzuschätzen, die zum Abschalten der Frontend-Elektronik (FEE) führen.

Zyklische Spannungsversorgungsunterbrechungen mehrerer Front-End-Platinen (FEBs) stellen ein Risiko für den Betrieb des Experiments dar. Zum einen könnte sich ein solches Verhalten negativ auf die physikalischen Messerergebnisse auswirken, zum anderen aber auch zu einer Beschädigung der Hardware führen. Ferner wurde untersucht, wo die Grenzen des FEBs in Bezug auf thermische Zyklen und mechanische

Belastung liegen. Die Ergebnisse dienten als Hinweis auf mögliche Fehlertypen des FEB im Laufe der Lebensdauer des STS. Die Fehlertypen nach wiederholten Zyklen und die möglichen Ursachen wurden ermittelt (z. B. Wärmeausdehnungskoeffizient Unterschiede zwischen den Materialien).

Aufgrund der Bedingungen im Inneren des STS ist eine effiziente Temperatur- und Feuchtigkeitsüberwachung und -steuerung erforderlich, um Vereisung oder Wasserkondensation an der Elektronik oder den Siliziumsensoren zu vermeiden. Die wichtigsten Eigenschaften eines geeigneten Sensorkandidaten sind Unempfindlichkeit gegenüber dem Magnetfeld, Toleranz gegenüber ionisierender Strahlung und eine relativ geringe Größe.

Es wurde eine allgemeine Strategie für die Überwachung von Umgebungsparametern im Inneren des STS entwickelt, und es wurden potenzielle Sensorkandidaten ausgewählt. Zur Charakterisierung der ausgewählten Sensoren für die relative Luftfeuchtigkeit wurde das entwickelte Kontrollsystem eingeführt. Ein Probenahmesystem mit einem Keramiksensor und faseroptische Sensoren (FOS) wurden als zuverlässige Lösungen für das verteilte Messsystem identifiziert. Zusätzlich werden die industriellen kapazitiven Sensoren als Referenz während der Inbetriebnahme verwendet.

Es wurden zwei verschiedene Ausführungen von FOS getestet: ein Hygrometer und 5 Sensoren, die in einem Array gemultiplext sind. Das FOS-Hygrometer erwies sich als die zuverlässigere Lösung. Einer der möglichen Gründe für die schlechtere Leistung ist ein relativ geringer Abstand zwischen den nachfolgenden Sensoren (15 cm) und eine dickere Beschichtung. Die Ergebnisse der Untersuchung des Zeitverhaltens zeigten, dass die dünnere Beschichtung von etwa 15 µm einen guten Kompromiss zwischen der Feuchtigkeitsempfindlichkeit und dem Zeitverhalten darstellen sollte.

Die Implementierung der auf Containern basierenden Kontrollsoftware für das mSTS basiert auf international anerkannten und auch industriell eingesetztem System EPICS. Das eingesetzte System erwies sich als zuverlässige Lösung und gewährleistete die Sicherheit des Detektors für fast 1,5 Jahre. Darüber hinaus wurden die Daten zur Leistung der Detektormodule analysiert, und es wurden erhebliche Fortschritte bei der Qualität der Module erzielt. Die gewonnenen Daten wurden auch zur Schätzung der Gesamtfluenz verwendet, die auf den Veränderungen des Leckstroms beruhte.

Das entwickelte System bietet die Möglichkeit, verschiedene Versuchsaufbauten zu automatisieren und zu steuern, die wichtige Daten für das STS lieferten. Darüber hinaus unterstreicht die Arbeit die Bedeutung eines solchen Systems und skizziert die nächsten Schritte zur Realisierung eines zuverlässigen Detektor-Kontrollsystems für STS.

Chapter

1 Introduction to physics background

Throughout history, mankind has always been fascinated by the physics laws governing the universe. The concept known as atomism was one of the first attempts to understand the nature of matter. The concept of atoms formulated by Leucippus of Abdera (5th century before the common era) and further pursued by Democritus initiated the search for the building blocks of nature [1]. According to this theory, everything consists of "atoms" (in ancient Greek ἄτομος which means uncuttable) that are physically indivisible, and the rest of space is just void.

It is astounding to consider that at the turn of the twentieth century (roughly, 2500 years after atomism was formulated), the structure of the atom remained unknown. The electron had just been discovered, and its behavior and characteristics were still poorly understood. Knowledge about particle physics was scarce. Particles like nuclei, protons, and neutrons were pporly understood or not discovered [2]. Further discoveries of radioactivity (in the year 1896) and radioactive elements (in the year 1898) by H. Becquerel and M. Skłodowska-Curie marked the gateway to 20th-century physics.

High energy physics aims to explore the smallest and largest scales of the universe, seeking out new discoveries from the tiniest particles to the largest objects in space. The number of important discoveries that have been made in the twentieth century is truly remarkable. Eventually, in 1970 these findings led to the formulation of a mathematical model called the Standard Model [2]. It describes the strong, weak, and electromagnetic fundamental interactions[1] between the particles.

This work aims to take the reader on a journey from the theoretical objectives of physics, to the often complex process of development and construction of particle detectors for a high-energy physics experiment.

[1] The interactions that are considered not to be reducible to more basic ones.

1.1 Standard Model and the strong interaction

The standard model is one of the most successful physics theories to date. It has explained numerous results from experiments worldwide. The most notable predictions of the Standard Model are the Higgs boson, W and Z bosons, the gluon, and the top and charm quark.

The standard model contains 17 particles (summarized in Figure 1.1) that are the smallest building blocks and are categorized into two groups: bosons and fermions. These groups are distinguished by their spin properties: fermions (characterized by half-integer spin) obey Fermi–Dirac statistics and bosons (integer spin) obey Bose–Einstein statistics.

Fermions are divided into two classes: quarks, which interact with the strong nuclear force, and leptons, which do not interact with it. Up and down quarks are located at the heart of atoms, inside the protons and neutrons. The other four quarks are only observed in particle accelerator collisions.

The electron is the most recognized of the leptons. Other charged leptons, known as muons and taus, are only discovered in particle accelerators and cosmic rays from space. Furthermore, each of the mentioned leptons has its corresponding neutrino, which has no electrical charge and a very small mass.

In addition to the particles, the Standard Model includes three forces that govern the behavior of matter. These forces are electromagnetism, strong and weak nuclear forces. The force-transmitting particles are the photon (electromagnetism), the gluon (strong nuclear force), the W & Z bosons (the weak force), and the Higgs boson.

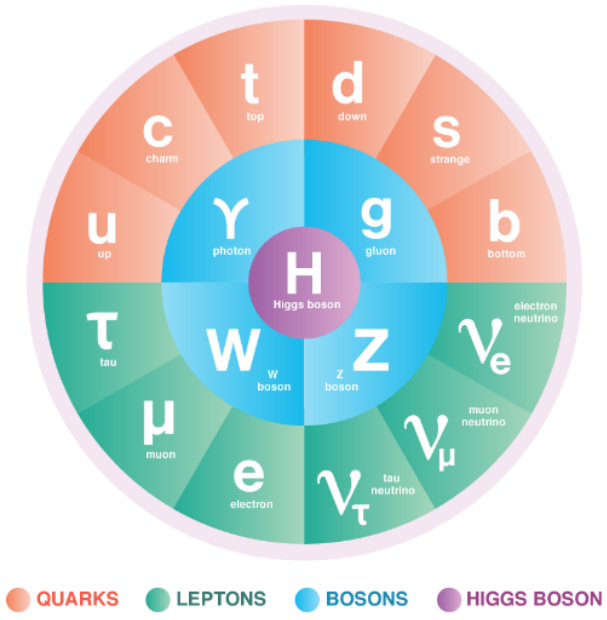

Figure 1.1: Fermions and bosons of the Standard Model [3].

The Strong Force theoretical foundation, Quantum Chromodynamics (QCD), is a well-established theory describing the interaction between quarks through the exchange of gluons.

Yet, key phenomena in strong interactions, like the confinement of quarks and gluons into hadrons[2] and the creation of mass, have remained unclear.

In extreme environments such as high-temperature T, or the high baryon density ρ, the confined baryonic matter forms a new state of matter called the quark-gluon plasma (QGP) [4]. Hot deconfined matter dominated the early cosmos just a few microseconds after the Big Bang, but compact stars may also contain cold and baryon[3]-rich quark matter in their interiors.

A well-established non-perturbative approach to solving quantum chromodynamics theory is known as Lattice QCD. LQCD can also be used to address issues like the confinement mechanism and chiral symmetry breaking, the role of topology, and the equilibrium properties of QCD at finite temperature [5].

1.2 Studies of nuclear matter and its forms

The strong interacting matter phase diagram represents various phases, such as liquid, gas, or plasma. It also describes the borders between these states and types of transitions (see Figure 1.2). The diagram illustrates the experimental results and theoretical predictions for the properties of strongly interacting matter.

The direct insight into the QGP is impossible, as it rapidly changes to the hadronic gas in a heavy-ion reaction. The experimental search for QGP in heavy-ion collisions was related to several model predictions of possible QGP signatures:

- Suppressed production of charmonium states (bound states of a charmed quark and a charmed antiquark), in particular, J/ψ mesons [6]
- Enhanced production of strange and multi-strange hadrons from the QGP [7]
- Characteristic radiation of photons and dilepton pairs from the QGP
- Elliptic flow [8]
- Inelastic fluctuations [8]

The results of the QGP search program at The Super Proton Synchrotron SPS on central collisions of medium and heavy nuclei were found to be adequate with the QGP predictions [9].

The crossover transition region was experimentally investigated at the Large Hadron Collider (LHC) and Relativistic Heavy Ioc Colllider (RHIC). This region is characterized by a low baryon chemical potential and high temperatures (around $150\,\mathrm{MeV}$), at

[2] Hadrons are composed of quarks, and therefore they experience the strong nuclear force.

[3] Baryons are composed of three quarks, and they make up most of the visible matter in the universe.

which the number of baryons to antibaryons is equal. Lattice QCD calculations show that the transition at $\mu_B = 0$ is a crossover transition [10]. The nuclear matter is expected to hadronize at the temperature of 155–160 MeV [11], [12].

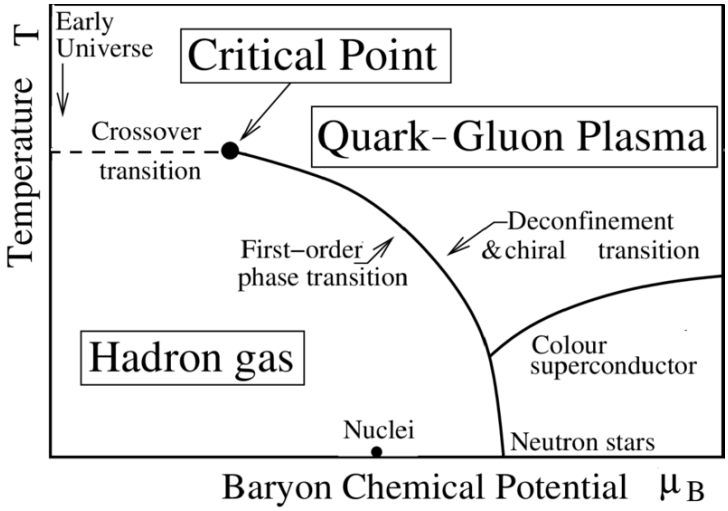

Figure 1.2: The phase diagram illustrating the regimes of confined and deconfined states of nuclear matter. The critical point separates the region of a crossover (explored by RHIC and LHC) from that of a first-order phase transition to be studied by the CBM experiment [13].

Figure 1.2 also depicts structures at higher baryon-chemical potentials, such as a chiral and a deconfinement first-order phase transition merging at a critical point. To date, none of these structures or phases have been discovered. As previously stated, first-principles theories, such as perturbative QCD, continue to struggle to generate solid predictions for matter characteristics at higher baryon-chemical potentials [14]–[16].

1.3 Probing dense nuclear matter with heavy-ion collisions

Heavy-ion collisions at beam energies between 2 AGeV and 11 AGeV have an enormous potential to explore many aspects of the phase diagram. Figure 1.3 represents the time evolution of Au+Au collision system at 10 AGeV beam energy. Similar densities as those produced in heavy-ion collisions are expected to prevail during the supernovae core collapse and in the core of neutron stars. Furthermore, the calculations of different transport models and hydrodynamics show that the density of the fireball will reach more than $8\rho_0$ during the Au+Au collisions at 10 AGeV [17].

Figure 1.4 depicts the presumed evolution of the heavy-ions collision. Depending on the temperature and net-baryon density of the system, there are two outcomes described in Figure 1.4. It illustrates the various forms of QCD matter intervening during

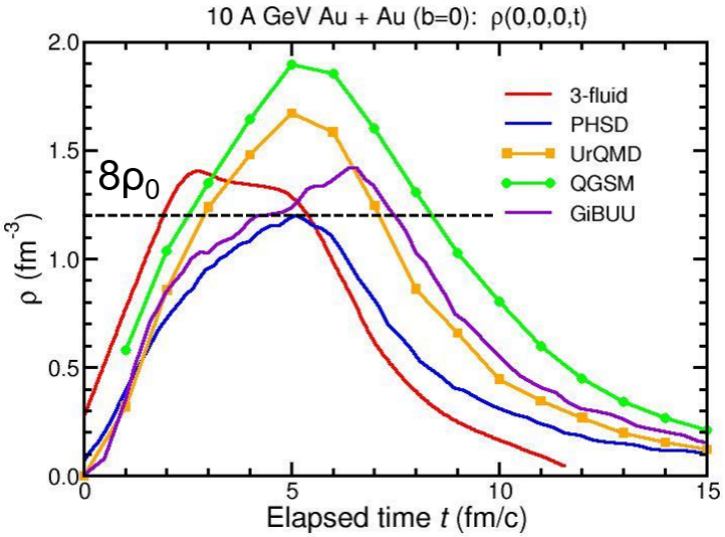

Figure 1.3: The time evolution of the central net-baryon density $\rho(t)$ calculated using different transport models and 3-fluid hydrodynamics of a head-on Au+Au collision at 10 AGeV energy [17].

the subsequent phases of the hadronic and heavy-ion collisions.

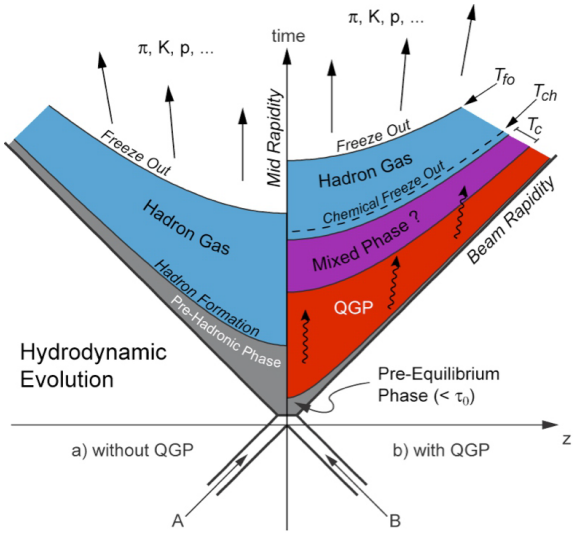

Figure 1.4: Schematic representation of the various stages of a heavy-ion collision as a function of time t and the longitudinal coordinate z (the collision axis). The critical temperature is represented by T_c, whilst the freeze-out and chemical freeze-out temperatures are indicated by T_{fo} and T_{ch}, respectively [18].

After the collision (right side of the graph in Figure 1.4), the system enters a pre-equilibrium phase, followed by a deconfined QGP medium and a probable mixed phase (which should exhibit first-order phase transition signals).

Experiments around the world have been exploring the facets of the phase diagram through systems characterized by a wide range of temperatures and densities. Figure 1.5 shows the interaction rates of existing and planned heavy-ion experiments. In the upcoming facilities, the main focus is put on the highest possible luminosity. Groundbreaking heavy-ion experiments at AGS in Brookhaven and at low CERN-SPS beam energies have investigated the QCD phase diagram at high baryo-chemical potentials. Because of the detector technologies available at the time, these observations were limited to abundantly generated hadrons and di-electrons with severely constrained statistics.

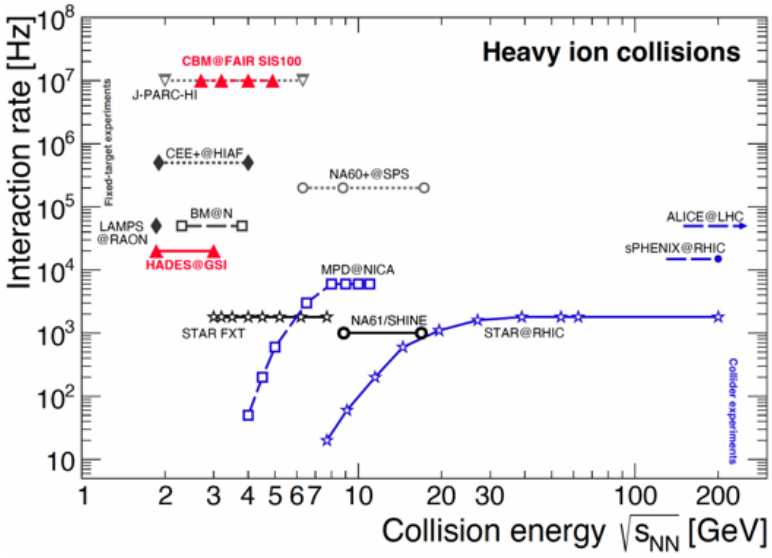

Figure 1.5: Interaction rates achieved by existing and planned heavy-ion experiments as a function of the center-of-mass energy. "STAR FXT" denotes the fixed-target operation of STAR. Blue symbols show collider experiments, whereas black and gray symbols show fixed-target experiments [19].

The NA61/SHINE experiment at CERN-SPS has been searching for the first-order phase transition by investigating collisions of hadrons with light and heavy-ion beams (pions, protons, beryllium, argon, and xenon ions) with a variety of nuclear targets [17], [20]. The collision energies varied from 13 AGeV to 158 AGeV depending on the size of the colliding system [21].

The Solenoidal Tracker at RHIC has performed a beam energy scan $\sqrt{s_{NN}} = 7.7\,\text{GeV}$–$200\,\text{GeV}$, where $\sqrt{s_{NN}}$ is the center of mass energy of the nucleus-nucleus (NN) system. The studied systems included gold, uranium, aluminum, deuteron, helium, and zirconium ions and protons ($\sqrt{s_{NN}} = 200\,\text{GeV}$) [8]. The Beam Energy Scan (BES) phase I

program findings shed light on first-order phase transition in the QCD phase diagram and the turn-off of the quark-gluon plasma distinctive fingerprints at low collision energy. BES phase II program (BES II) covers the $\sqrt{s_{NN}}$ from 7.7 AGeV to 19.6 AGeV in the collider mode and from 3 AGeV to 7.7 AGeV in the fixed-target mode [22], [23]. The studies conducted at STAR and A Large Ion Collider Experiment (ALICE) at LHC aimed at studies related to the QGP and revealed that the partonic degrees of freedom prevail at the early phase of the fireball evolution [17].

The Nuclotron at the Joint Institute for Nuclear Research (JINR) in Dubna is preparing the fixed-target experiment BM@N to explore heavy-ion collisions at gold beam energy up to roughly 4 AGeV. Furthermore, the Nuclotron-based Ion Collider fAcility NICA with the Multi-Purpose Detector (MPD) is being built at JINR. The NICA collider is intended to operate at collision energies ranging from $\sqrt{s_{NN}} = 8$ AGeV to 11 AGeV, with reaction rates up to 6 kHz for minimal bias Au+Au collisions [19].

The High-Acceptance DiElectron Spectrometer (HADES) detector at SIS18 detects hadrons and electron pairs in heavy-ion collision systems at reaction rates of up to 20 kHz and beam energy of 1-2 AGeV [19].

Unfortunately, due to luminosity or detector limits, the investigations with the previously mentioned experiments were unable to measure rare observables with extremely low production cross-sections and must instead focus on abundantly generated particles. As the CBM experiment will measure with event rate up to 10 MHz, it is well-positioned to explore many facets of the QCD matter. CBM is a fixed target experiment that aims to measure rare particles as probes of dense matter with very good precision at beam energies up to 11 AGeV or $\sqrt{s_{NN}} = 4.9$ GeV (up to 14 AGeV for light nuclei and 29 AGeV for protons) and interaction intensities up to 10 MHz [24].

The CBM experiment will be able to explore the equation of state at densities (2–6 times saturation density) close to those existing in cores of massive neutron stars, supernovas, and neutron star mergers (4-5 ρ_0) [25]. The majority of the experimental observables which are sensitive to the properties of dense nuclear matter, like the flow of (anti-) particles, higher moments of event-by-event multiplicity distributions of conserved quantities, multi-strange (anti-) hyperons, di-leptons, and particles containing charm quarks are prone to the statistics. Therefore, the key feature of successful experiments is high rate capability, which ensures high precision [19].

The CBM experiment aims to investigate:

1. The equation of state of baryonic matter at neutron star densities.
    - Differential collective behavior of protons, pions, and deuterons - the collective hadrons motion provides information on the dense stage of the heavy-ion collision. It is driven by the pressure gradient created at the beginning of the fireball evolution [26].
    - Hyperons and their interactions - are preferentially produced in the dense phase of the fireball via sequential collisions [17].

2. Modifications of hadron properties in the dense baryonic matter and the onset of chiral symmetry restoration. These phenomena affect the invariant-mass spectra of di-leptons, which will be measured both in the electron and the muon channel.

3. Phase transitions from hadronic matter to quarkonic or partonic matter.
   - The excitation function of multi-strange hyperons, which are driven into equilibrium at the phase boundary [17].
   - The excitation function of the invariant mass spectra of lepton pairs which reflect the fireball temperature, and, hence, may reveal a caloric curve and a first-order phase transition [17].
   - The excitation function of higher-order event-by-event fluctuations of conserved quantities such as strangeness, charge, and baryon number, which are expected to occur in the vicinity of the critical point [17].

4. Hypernuclei (double Λ, strange di-baryons, etc.) and the measurement of their lifetime, which will provide information on the hyperon-nucleon and hyperon-hyperon interaction [17].

5. Charm production mechanisms [17].

A detailed description and explanation of the CBM physics program can be found in the CBM Physics Book [17] and in [19].

1.4 Overview of the FAIR facility

The Facility of Antiproton and Ion Research in Europe (FAIR) [27] is a future international research facility for accelerator-based research.

It will provide unique research opportunities in hadron and nuclear physics, atomic physics, nuclear astrophysics, materials research, plasma physics, and radiation biophysics, including developing novel medical treatments and applications for space science [28].

FAIR (see Figure 1.6) will extend GSI with Schwerionensynchrotron 100 (SIS100) accelerator, storage rings, and dedicated experiments from different fields, namely Atomic Physics, Plasma physics and Applications (APPA), antiProton ANnihilation at DArmstadt (PANDA), Nuclear Structure, Astrophysics, and Reactions (NUSTAR), and Compressed Baryonic Matter (CBM). The latest status of SIS100 and its plans were recently described by Spiller [29].

The SIS100, which will provide high-intensity beams of protons up to energy of 29 GeV with intensities up to 2.5×10^{13} protons/cycle and nuclei up to 15 AGeV for $Z/A = 0.5$. Gold or uranium beams with kinetic energies up to 11 AGeV will be available. Typical intensities for the heavy ions also depend on charge state and vary from 2.7 GeV/u for U^{28+} ions with 5×10^{11} ions/cycle to 10 GeV/u for U^{92+} ions with

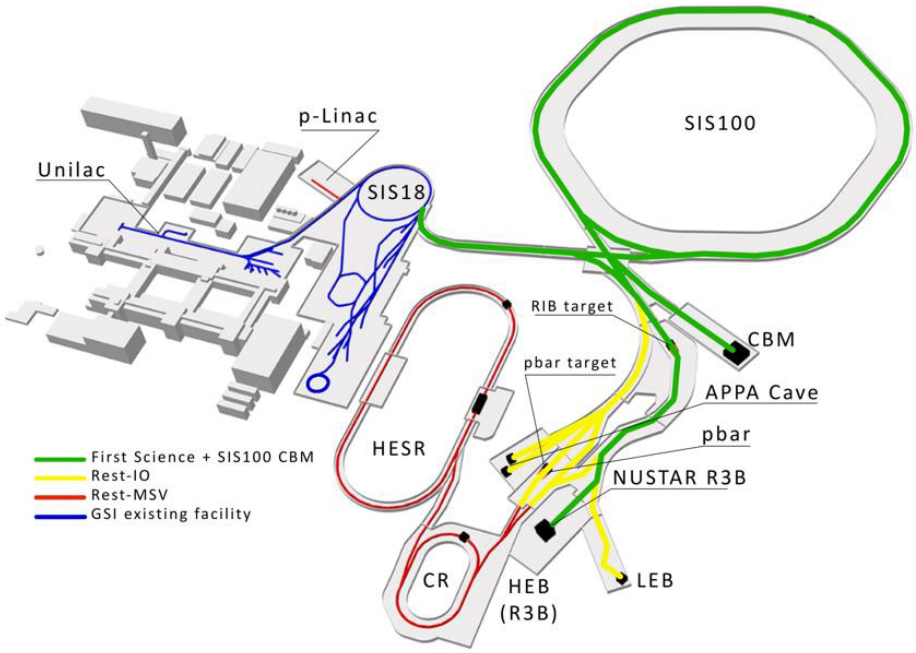

Figure 1.6: Overview of the GSI/FAIR research facility [27]. The existing beam lines of the GSI facility are denoted with blue lines. The planned facility and the corresponding experiments are located to the right.

4×10^{10} ions/cycle. High-intensity secondary beams will be produced by a large acceptance Superconducting Fragment Separator, which investigates very efficiently rare isotopes created in reactions with the primary beams.

Moreover, a secondary antiproton beam will be produced by bombarding a metal target with 27.5 GeV protons. The collection of the pbar will be achieved with the [4]magnetic horn. The separation of the antiprotons from primary protons and other secondary particles will be provided by the succeeding pbar separator, which will transfer antiprotons to the collector ring (CR) [30].

1.5 Compressed Baryonic Matter experiment, subdetectors and their tasks

The Compressed Baryonic Matter (CBM) experiment is currently being constructed at FAIR. Figure 1.7 depicts the CAD drawing of the CBM experiment. The beam enters the experimental cave from the left side and traverses the High Acceptance Di-Electron Spectrometer (HADES) experiment to finally reach the target of the CBM experiment.

[4]Magnetic horn is a high-current, pulsed focusing device used for the antiproton beam.

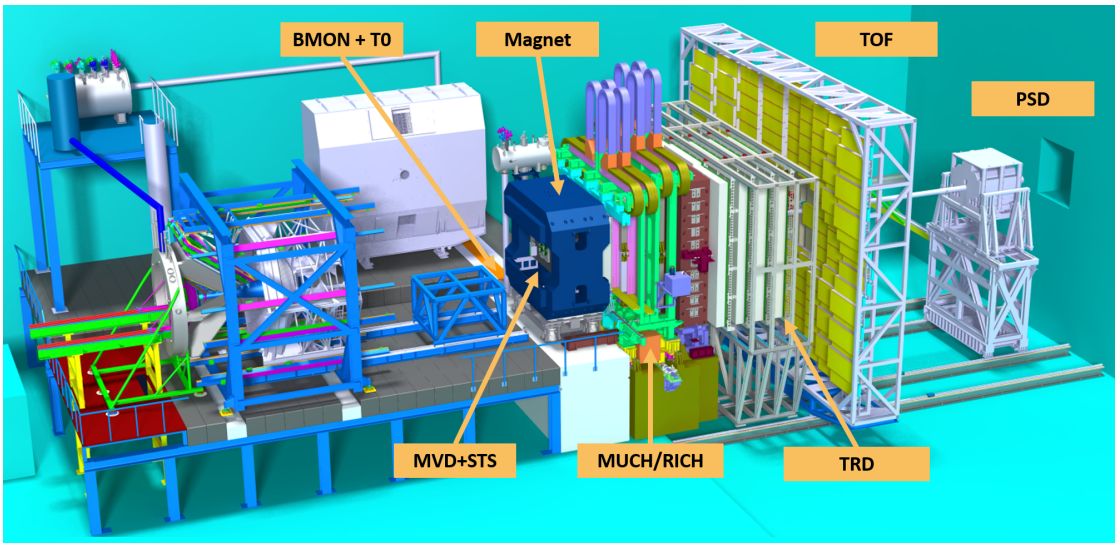

Figure 1.7: HADES experiment on the left side and the CBM experiment on the right side.

The main features of the experiment are described below:

- Tracking acceptance: $2.5° < \theta_{lab} < 25°$
- Peak event intensities up to 10 MHz for Au+Au systems
- Fast and radiation hard detectors
- Free-streaming triggerless Data Acquisition (DAQ)
- 4D tracking (spatial and time)
- Online event reconstruction and selection
- Data rates from the readout electronics of up to 2 TB/s

In order to get valuable insight into the physics observables proper detector systems need to be developed. The detector concept is based on identifying the stable charged particles that are often decay products of resonances and unstable particles. Charged particles can be bent in a magnetic field of known strength to investigate their momentum. Together with information from Time-of-flight (TOF) the mass of particles can be distinguished. Di-leptons are considered special due to their nature. They may contain undisturbed information from the early, dense phase of the fireball evolution. On the other hand, it is necessary to separate them from the abundant pions. In order to perform the complete analysis, the following detector systems are foreseen for the CBM experiment:

Beam monitor, or T0 (BMON) and its conceptual design, was summarized during the 40th CBM Collaboration Meeting [31]. Two separate stations in front of the target are made out of high-purity poly-crystalline CVD diamond material. This detector is foreseen to monitor beam quality (position, time structure) and determine the start time of the reaction.

Micro Vertex Detector (MVD) consists of four planar stations with Monolithic Active Pixel Sensor (MAPS) chips. A station layout and distance from the target can be tailored to the needs of a specific run, for example, to optimize vertexing or tracking. The vertexing detector geometry aims at a precision of secondary vertices determination of about $50 - 100\,\mu m$ along the beam axis. The main aim is decay vertex identification of the very short-lived particles such as charmed mesons, which decay within a few hundred µm behind the target, as well as background rejection in di-electron spectroscopy [32].

Silicon Tracking System (STS) which is responsible for tracking charged particles inside the magnetic field. The STS is located inside a superconducting dipole magnet [33]. The charged particles traversing the active volume of STS are bent due to the applied magnetic field. The trajectories of charged particles inside the magnetic field will be determined by MVD and STS across a 1 m length downstream of the target [34].

Muon Chamber System (MUCH) is the fourth subsystem of the CBM experiment. It is dedicated to muon detection (for example rare particles decaying into muons like J/ψ) and track reconstruction. This concept is based on the layered design of the hadron absorbers (5 layers), separated with tracking detector planes which are based on Gas Electron Multiplication (GEM) and Resistive Plate Chambers (RPC) detectors [35].

Ring Imaging Cherenkov Detector (RICH) is responsible for electron identification via Cherenkov radiation [36]. The detector consists of 1.7 m a long CO_2 gas radiator with pion threshold for Cherenkov radiation of 4.65 GeV/c, two arrays of mirrors, and photon detector planes. It allows separating electrons from pions up to 8 GeV/c. The models predict that a pion suppression on the level of 500 will be accomplished thanks to the high granularity (about 55000 channels) and high number of photons per ring [36].

Transition Radiation Detector (TRD) suppresses pions and supports track reconstruction with 9-10 detector layers grouped into 3 stations. It is placed between 4 m to 9 m downstream of the target, and the total active area reaches $600\,m^2$. Because the RICH electron identification capabilities are limited to the lower momentum range ($p < 5$ GeV/c), the TRD will be employed as a supplementary device to supplement and expand the electron identification into higher momenta. The TRD configuration designed for the SIS100 CBM setup will therefore be capable of identifying electrons beyond a momentum threshold of $p > 1$ GeV/c with a 90% efficiency while reducing the hadronic background by a factor of $10 - 20$. The working principle of the detector

is based on the phenomenon that the ultra-relativistic particles traversing through a medium with alternating dielectric constant produce transition radiation. It is composed of two parts, the readout chamber, and the radiator. The photons are generated by the electrons passing through the radiator, while the heavier pions do not produce any radiation. For detection of the produced radiation, multi-wire proportional chambers will be used with a $85\%\,\mathrm{Xe}/15\%\,\mathrm{CO_2}$ gas mixture) [37].

Time-of-Flight Detector (TOF) is designed to identify hadrons (pions, kaons, and protons). As the name indicates, the detector measures the time-of-flight of the reaction products with Multi-Gap Resistive-Plate Chambers (MRPC). The MRPCs have an excellent time resolution of 60 ps. It might be located between 6 m and 10 m (depending on the physics objectives) and will cover an area of about $120\,\mathrm{m}^2$ [38].

Projectile Spectator Detector (PSD) is the last subsystem of the CBM experiment, and it determines the collision centrality and event plane. The detector is meant to measure the nucleons from a projectile nucleus in heavy-ion collisions. The proposed 44 module design of the PSD covers a large transverse area around the beam spot position, such that most of the projectile spectator fragments deposit their energy in the PSD. The detector concept is a compensating hadron calorimeter consisting of lead-scintillator sandwich modules [39].

The CBM detector system can be used in two operation modes: the first one is optimized for electron identification (electron configuration) and the second is designed for muon identification (muon configuration). In the first one, all the subsystems apart from MUCH will be involved. In the muon configuration, the RICH detector is replaced by MUCH.

For the high-rate CBM experiment, the triggerless data read-out and acquisition system plays a crucial role. The time-stamped signals will be read out without event correlation and transferred to a high-performance computing farm, the GSI GreenIT Cube. The online event reconstruction and selection will be performed by high-speed algorithms. In the first step, the tracks of the charged particles are reconstructed from the space and time information from the various detector signals. This process is based on the Cellular Automaton (CA) track finder [40]. Subsequently, the particles are identified, taking into account secondary decay vertices and information from RICH or MUCH, TRD, and TOF. Finally, the particles are grouped into events, which will be selected for storage if they contain important observables. In parallel, the event and its plane are characterized using information from the PSD.

Another important online system is called Experiment Control System (ECS). It is a software structure that aims to provide automatization, monitoring, and control of hardware and the detector subsystems. A detailed description of ECS and the detector-specific control system (DCS) will be given in Chapter 3.

1.6 Thesis overview and its rationale

The thesis consists of seven chapters. The second chapter introduces the role of silicon trackers in large scientific experiments and discusses the design details of STS, including the physics performance and experimental challenges. Those elements define the requirements for the Detector Control System (DCS). The third chapter serves as an introduction to the control and monitoring of a large experiment, with an extended focus on the detector-related slow control system and the developed control framework. The following three chapters are focused on the results and their consequences for the experiment:

- Chapter 4 covers the first implementations of the mentioned control framework. The first application is related to the slow control interface for the Front-End Electronics (FEE) readout. The second and third examples are related to the irradiation studies of the powering modules for the Low Voltage (LV) powering of STS electronics and thermal cycling of Front-end boards (FEBs). The performed studies and results of these activities are discussed in detail.

- Chapter 5 describes the efforts to design and test a distributed sensing system for STS with a focus on humidity sensing. Three considered technologies feature capacitive sensors, fiber optic sensors, and remote sensing with the use of a sampling system. The chapter focuses on the design choices and characterization of the fiber Bragg grating-based sensors.

- Chapter 6 focuses on controlling a small-scale prototype version of STS in the mCBM experiment. The first sections describe in detail the hardware and software solutions implemented in the detector. Subsequently, the results from the full-blown DCS are presented and discussed, including the radiation effects on the silicon sensors and general considerations about the power dissipation of different elements of STS powering scheme. Moreover, considerations about the DCS are given.

The last part of the thesis summarizes the results and sheds light on the next steps toward the realization of STS and its controls. The most important findings and results from the performed studies are also discussed.

Chapter

2 The Silicon Tracking System and its role in the CBM experiment

All semiconductor-based detector systems include very similar functions. The signals from the detector channels have to be amplified and processed for storage and analysis. The sensor, analog-digital converter, and all the necessary support structures, and data are often referred to as a detector module. Apart from these structures, there are also services and design constraints that need to be taken into account while designing a detector. One of the first decisions is the detector material, which depends on many factors like the availability, energy needed for electron-hole production, technological feasibility, or integration with the electronics. Silicon (Si), germanium (Ge), gallium arsenide (GaAs), and Diamond are the most common semiconductor detector materials used [41], [42].

This chapter aims to present an introduction to silicon-based detector systems and general working principles. Subsequently, the design of the STS is discussed with a focus on the hardware. Finally, the requirements for the detector control system are considered.

2.1 Fundamentals of silicon detectors

Semiconductor diodes operated with reverse bias voltage can be considered ionization chambers, which feature a pair of electrodes and applied external voltage. The particles passing through the volume of a sensor lose their energy by producing electron and hole pairs. The charge is retrieved by one or more electrodes. The analog signals are converted into digital ones, processed, and analyzed.

To achieve precise measurement of particle position the electrodes can be segmented into strips. To address this problem, the electrodes can be segmented into strips. Figure 2.1 shows an example of implementing segmented electrodes to determine the particle position. To achieve the two-dimensional information, the second electrode strips

have usually an inclination of a few degrees. Hence, the contribution of fake ghost hits is minimized.

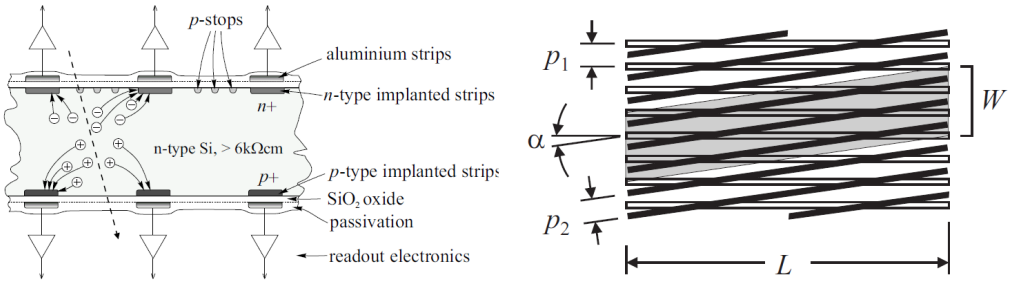

Figure 2.1: The segmented electrode enables defining the particle position (left) [43]. The right scheme depicts the strips oriented at a small angle α, which aims to reduce fake hits [44].

The operation principle of semiconductor-based devices is related to the fact that the charged particles traversing the volume of the detector may ionize it (creating electron hole pairs). On the other hand, photons must first interact with an electron through the photo or Compton effect, or with the Si nucleus.

The sensitive volume of a silicon sensor produces an average charge given by

$$Q_s = \frac{E}{E_i} e, \tag{2.1}$$

where E is the absorbed energy, E_i is the energy required to form a charge pair. The energy needs to be greater than the band gap of the semiconductor so that the electron can move to the conduction band. The silicon has a band gap of $1.12\,\text{eV}$. Nevertheless, the average ionization energy is about $3.6\,\text{eV}$. This effect is related to the fact that only about 30% of the particle energy is converted into an electrical signal, and the rest goes into phonon excitation (lattice vibrations). A typical charge deposition by a minimum ionizing particle in a $300\,\mu\text{m}$ thick wafer is around 25000 electron-hole pairs.

Considering a simple example if a sensor had about $\sim 10^9$ thermally produced free charge carriers[1], but a passing charged particle would generate only $\sim 2\times10^4$ electrons-hole pairs. Such a signal would be lost in the remaining free-charge carriers. There are two ways to address this problem, either by cooling the sensor to very low temperatures or depleting the silicon volume of free-charge carriers. The depletion process of a pn-junction requires applying an external voltage so that the sensor is fully depleted [44]. This external voltage V disturbs the equilibrium of spontaneous generation and recombination of electrons/holes. It increases the potential barrier of the pn-junction and the depletion width.

[1] Electrons or holes introduced to the conduction (valence) band by doping.

The full depletion voltage is one of the most important parameters for silicon sensors, as it defines the operating range

$$V_{FD} = \frac{D^2}{2\epsilon\mu\rho}, \tag{2.2}$$

where D is the sensor thickness, ϵ is the dielectric constant, μ is the mobility and ρ the resistivity.

When the sensor is operated in the over-depleted mode, the electric field is established

$$E_{max/min} = \frac{V_{bias} \pm V_{FD}}{D}, \tag{2.3}$$

where V_{FD} is the effective full depletion voltage and V_{bias} is the additional voltage. The thermally generated electron-hole pairs are swept out of the depletion region. This effect results in a reverse current called leakage current which is strongly influenced by mid-gap levels occupied by impurities. The current increases with the applied voltage V until the detector reaches full depletion. An electric breakdown is found at greater bias voltages, where the current begins to increase exponentially. The breakdown can be understood by either "avalanche breakdown" (charge multiplication in collisions with the lattice) or "Zener breakdown" (based on the quantum mechanical "tunnel effect") [42].

If the detector is fully depleted, the generated electrons and holes drift in the electric field according to their velocities v_p and v_n in the direction of respective electrodes. The current induced by a single charge carrier can be described by Ramo's theorem

$$I = q_0 \frac{v_{n,p}}{D}, \tag{2.4}$$

where the drift velocity $v_{n,p}$ depends on the mobility of the holes and electrons and the electric field strength, and D is the thickness.

2.2 Radiation damage to the silicon sensors

To understand the properties of the silicon sensor after irradiation, it is necessary to consider the damage caused to the lattice by the particles and the process called annealing. Radiation damage can be divided into two main groups: displacement damage and ionization damage. The first mentioned phenomenon is related to the incident particles displacing the silicon atoms from their position in the lattice. The ionization damage occurs in the insulating layers of the sensor (usually forming SiO_2 – Si interface states) [45]. Displaced atoms form defects, which introduce new levels in the band gap, therefore changing the properties of the semiconductor. It results in the increase of the dark current, change of depletion voltage, and decrease of Charge Collection Efficiency (CCE). In practice, the damage depends on the particle interacting with the sensors and its energy. Figure 2.2 describes the behavior of displacement damage for different particles and their energies.

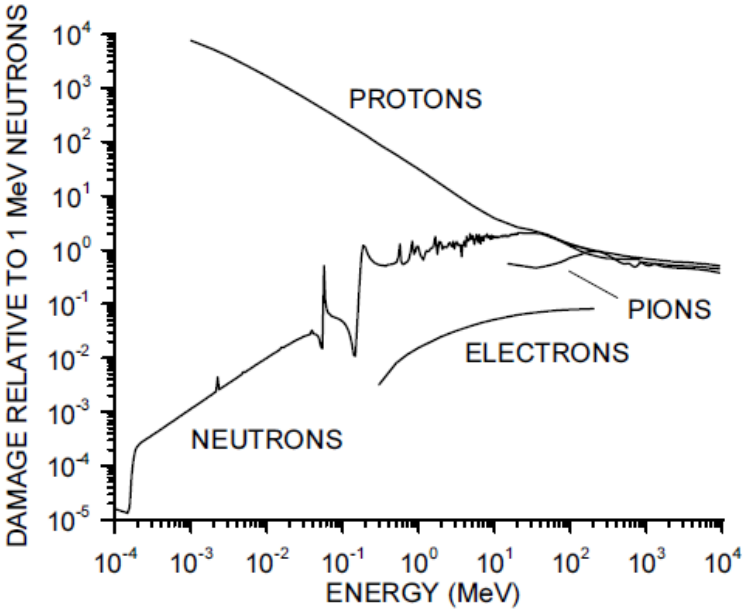

Figure 2.2: Displacement damage vs. kinetic energy for neutrons, protons, pions, and electrons, plotted relative to 1 MeV neutrons [44].

Annealing can be described as the combination of various effects, such as the movement of particles or defects through the lattice structure, the rearrangement, or break-up of defects, and the interaction between defects as they propagate. Silicon sensors annealing is a process used to reduce the leakage current of silicon sensors. This process involves heating the sensors to a very high temperature for an extended period of time, allowing the bonds between the atoms in the silicon lattice to become more stable and reduce the amount of current flowing through the device. The annealing process also helps to reduce the amount of noise generated by the sensor, as well as improve its temperature stability.

Leakage current

Production of additional mid-gap levels is the major contributor to the increase of leakage current during the radiation. It was found in a number of experiments that the sensor leakage current is related to the fluence as follows

$$I_d = I_0 + \alpha \phi A d, \tag{2.5}$$

where I_0 is the leakage current before the irradiation, α is a damage coefficient dependent on particle type and temperature, ϕ is the particle fluence, d is the detector thickness, and A is the area. Figure 2.3 provides a more detailed overview of bulk-

damage-induced leakage current in different types of silicon detectors. Moreover, leakage current changes also with the temperature

$$I(T) \propto T^2 e^{\frac{-E}{2kT}}, \tag{2.6}$$

where T is the temperature, k is the Boltzmann constant and E is the band gap energy. If the temperature of the silicon sensors is known, then it is possible to normalize the leakage current to a predefined value (e.g., 20 °C). It allows comparing the leakage current of sensors before and after irradiation, even though the ambient conditions were different.

It allows us to scale down leakage current to 20 °C using the equation 2.7.

$$\frac{I_R(T_2)}{I_R(T_1)} = (\frac{T_2}{T_1})^2 e^{\frac{-E_g}{2kT}(\frac{T_1-T_2}{T_1 T_2})}, \tag{2.7}$$

where E_g is the band gap, k is the Boltzmann constant, I is the current and T is the temperature.

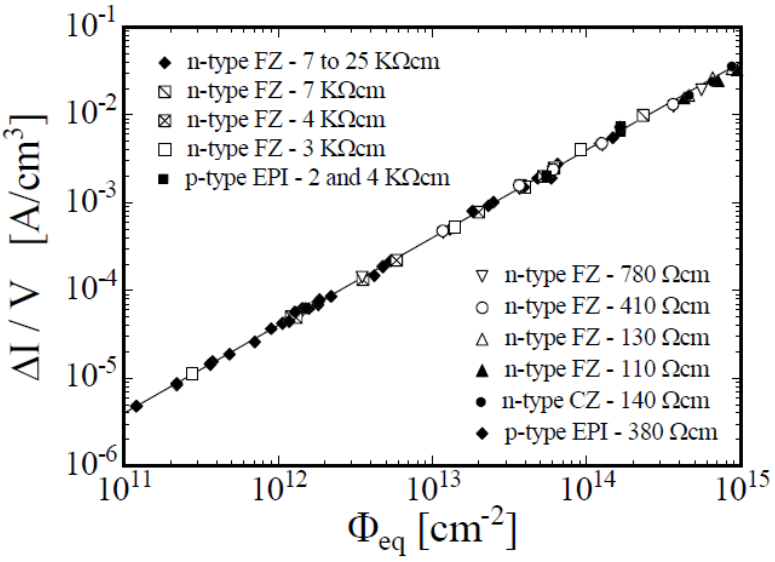

Figure 2.3: Damage induced bulk current as a function of particle fluence for different detector types [45].

Depletion Voltage

Radiation-induced defects in detectors can alter their effective doping, leading to changes in the space charge within the material. Initially, n-type silicon detectors doped with phosphorus or arsenic act as donors. However, irradiation reduces the effective n-doping until the remaining donor states match the number of acceptor states,

resulting in intrinsic behavior. With further irradiation, the newly formed defects act as acceptors, causing space charge inversion and p-doping. The accumulation of acceptor-like defects leads to a linear increase in negative space charge. It's important to note that the specific behavior varies depending on the detector material and radiation exposure [42], [46].

Signal-to-noise ratio and Charge Collection Efficiency

Signal-to-noise ratio and CCE are two very important factors characterizing the detector. The noise level can be controlled by operating the detector at low temperatures or by limiting the exposition to electromagnetic interference. On the other hand, the CCE of non-irradiated sensors is assumed to be 100%. The CCE after the irradiation could be defined as the ratio

$$\eta = 100\% \times \frac{Q_{irr}}{Q}, \tag{2.8}$$

where Q_{irr} is the charge collected by the irradiated sensor, and Q is the charge collected by non-irradiated sensor. The CCE depends on the depletion voltage and its changes with the radiation, as the full collection of the charge could only be achieved at the maximum electric field. Therefore, the fluence and/or depletion voltage remain crucial for the operation of the detector.

2.3 Design of the Silicon Tracking System

The physics observables together with the foreseen accelerator energy and beam intensity mentioned in the previous chapter define the requirements for the detector system. The STS is designed to provide track reconstruction and momentum determination of the charged particles. Those particles are produced in collisions of an ion beam with energies from 2 AGeV to 14 AGeV (protons 29 GeV) with a target. For example, a central Au+Au collision results in up to 700 tracks. The STS extends more than 1 m downstream of the target and will be installed in a volume of 3 m^3.

In order to achieve physics goals, STS has to address the following:

- aperture - the aperture of the whole experiment is set to cover polar angles from 2° up to 25° [34].
- spatial resolution - a single-hit resolution of about 20 µm in X direction and 120 µm in Y [34].
- single-hit efficiency - the detector layer should provide almost 100% detection efficiency. The signal-to-noise[2] ratio needs to be above 10. Having that, the track reconstruction efficiency should exceed 95% for particle momenta larger than 1 GeV/c [34].

[2]Ratio of the most probable signal amplitude for a minimum ionizing particle divided by the mean root square of the single strip noise.

- momentum resolution - it is mainly influenced by the material budget of the system. The STS is designed with the aim of minimizing multiple scattering. It is achieved by placing the electronics, mechanical infrastructure, and cooling outside the active area. For the STS the momentum resolution better than 2% is required, which will be achieved by placing the STS in a 1 Tm dipole magnet [34].
- radiation hardness - the silicon sensors and the electronics need to withstand the total dose of 10^{14} neutrons/cm² (1 MeVn$_{eq}$). It was confirmed that after receiving twice the mentioned dose the CCE decreases by up to 20%. The total dose of 12 kGy is expected only for the 5 – 10% sensors in the innermost region of the detector after 10 years of operation, 2 months per year of 10 AGeV Au+Au collisions at 10 MHz interaction rate [34].
- hit rates and readout - the hit rates of charged particles for the inner-most silicon sensors (10 MHz/cm² define the requirements for the readout system (signal shaping time, number of readout channels, etc.) [34].

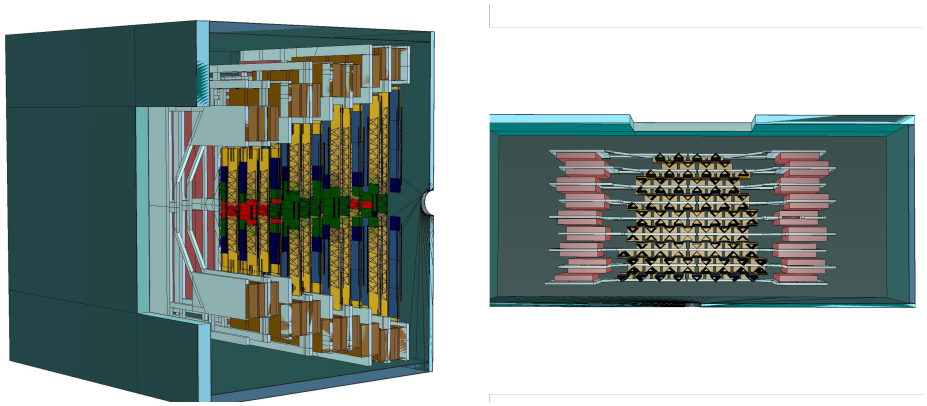

Figure 2.4: A simplified geometry of the Silicon Tracking System. The 8 tracking stations cover the polar angle from 2° up to 25°.

A simplified CAD drawing of the STS is presented in Figure 2.4. The detector consists of 876 detectors modules. A module is composed of a double-sided silicon microstrip sensor, ultralight microcables (of up to 50 cm length), and Front End Boards (FEB) populated with Application-specific integrated circuits (ASICs) glued to T-shaped aluminum structures (so-called fins). The modules are mounted on carbon fiber support structures that populate C-frames [47]. Two C-frames form a tracking station of STS. Figure 2.5 depicts a simplified assembly workflow of STS. The modules are produced in 166 variants, which differ in sensor size, micro-cable length, and the orientation of the Front End Electronics (FEE).

The stations are placed inside a thermally insulated box that resides in a dipole magnet gap. During STS operation, the temperature inside the enclosure will be gradually decreased with the increasing radiation damage to the silicon sensors, to minimize

thermal runaway [44]. The largest amount of heat is dissipated by the low-voltage powering of the electronics and not the sensors themselves. Hence, effective cooling is needed to address this problem. The temperature of about −10 °C will ensure a safe performance (away from the thermal runaway[3] temperatures) of the semiconductor sensors and minimize the contribution of the shot noise [44]. The low ambient temperature also sets hard limits on the frost point inside the STS enclosure. As the coolant temperatures might reach down to −40 °C, the frost point needs to be below −45 °C at all times.

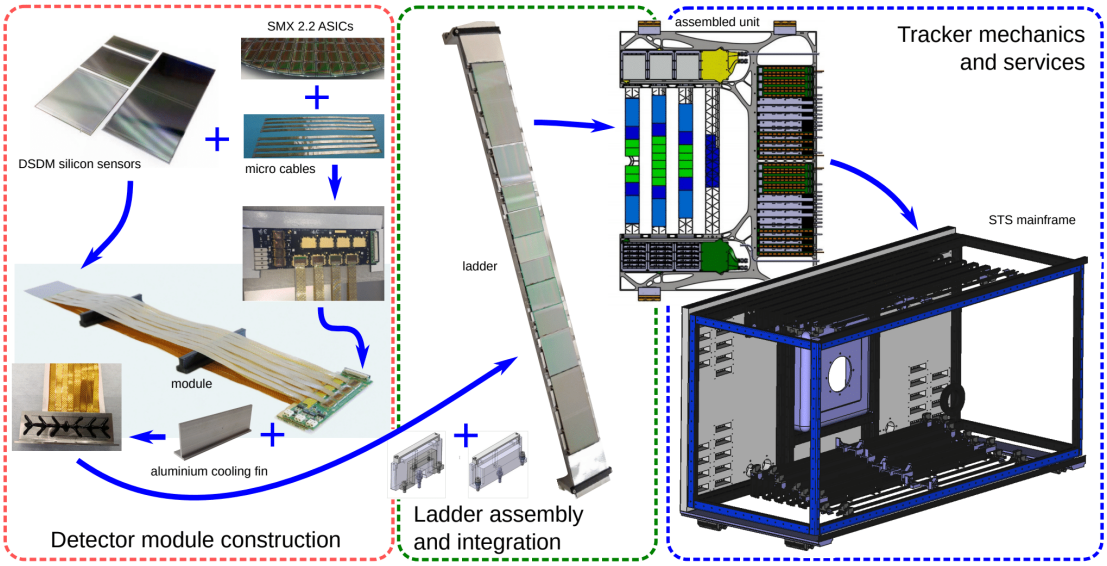

Figure 2.5: A simplified assembly workflow of the STS; silicon sensors are connected to the ASICs on the FEBs via microcables, then the modules are assembled onto carbon fiber ladders which form a C-frame [48].

2.3.1 Double-sided microstrip silicon sensors

The use of microstrip silicon sensors has been demonstrated in many well-known experiments like those operated at CERN (ALICE and CMS) and Brookhaven National Laboratory (STAR). The STS sensors are produced on 320 µm thick n-type wafers by Hamamatsu Photonics K.K. The p^+ strips are located on one of the sides (called p-side) forming a pn-junction. The strips at the n-side are isolated using a p-spray technology [34]. Each of the sensors features 1024 strips with 58 µm pitch. The signal from the sensors is transported to the front-end electronics via ultra-light microcables. These cables are electrically shielded to protect the analog signals from any interference.

[3] Thermal runaway occurs when the power dissipation of a device increases rapidly with temperature, and it is impossible to evacuate the excess heat.

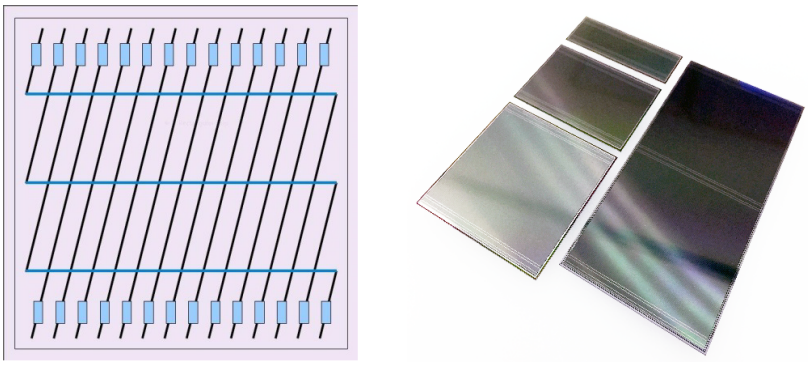

Figure 2.6: Left: An example of a sensor segmented into strips inclined by a small angle. The shortest strips are interconnected with each other. Right: Silicon sensors to be used for the STS. The width of the sensor is 6.2 cm and there are 4 strip lengths: 2.2 cm, 4.2 cm, 6.2 cm, 12.4 cm [34].

The aluminum strips on the p-side of the sensors are inclined by 7.5° with respect to the n-side. That implies that there is a set of shorter strips on the p-side. These strips are interconnected with each other using a second metallization layer on the sensors. An example of this solution is presented in Figure 2.6. Moreover, to protect the electronics from the dark current, the sensor is AC coupled with the readout.

2.3.2 Functional module

The silicon sensor, the microcables together with the two FEBs form a functional module of the STS. The assembly is realized stepwise, where each step requires extensive testing of the components. Therefore, a laborious workflow was developed to address the complexity of the module assembly [49].

A module ASICs are powered using low-voltage supply lines. A high voltage supply for the silicon sensor biasing is realized using two separated coaxial lines for positive and negative voltage. The low-voltage powering is provided by dedicated power boards (POB), which reside outside the detector acceptance. The POBs are populated with DC-DC converters [50] which provide the powering for FEE. There are two flavors of the DC-DC converters used: 3 V and 2.5 V. As the voltage conversion efficiency is not 100%, the heat produced in this process has to be evacuated. Hence, the POBs are in thermal contact with the cooling plates.

Upon completion of calibration and testing, the module together with the cooling fin is installed onto a carbon-fiber support structure (ladder). Up to ten modules form one ladder. Subsequently, the ladders are mounted on a C-frame, which accommodates a cooling structure.

2.4 The readout chain of the STS

The STS readout chain is designed to control, readout, and preprocess analog signals acquired from the silicon sensors. The CBM experiment is going to run with a free-streaming Data Acquisition (DAQ) system. Moreover, it has to handle a high data throughput and store it. It consists of the FEE, data transport, online event reconstruction, and online event selection [51].

The first layer of the STS readout chain is a Front-End Board (FEB) which is populated with eight Application-Specific Integrated Circuits (ASICs) [52]. Each STS-XYTER ASIC is responsible for the readout of 128 channels. The chips feature the analog front-end (AFE), generation of hits using an Analog Digital Converter (ADC), and timestamp information.

The next element is the readout board (ROB). It aggregates data from multiple FEBs and sends it via optical links out of the detector enclosure to the Common Readout Interface (CRI) board. Subsequently, the data is transported to a computing farm for online processing, the First Event Level Selector (FLES).

In total, the STS features roughly 14000 STS-XYTERs, 600 ROBs. It requires not only extensive testing capabilities but also the possibility to handle a high data throughput. Given a typical average raw event size of roughly 50 kB for minimum-bias Au+Au collisions, a peak collision rate of 10 MHz results in an instantaneous raw data rate of about 500 GB/s (for all the detector systems). Figure 2.7 depicts the complete readout chain of the STS at the CBM experiment.

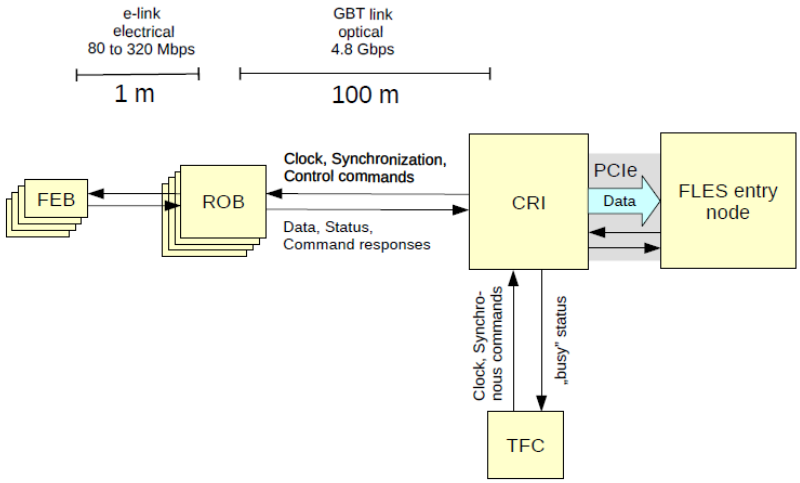

Figure 2.7: The basic building parts for one FLES entry node are shown schematically. An entry node can hold multiple CRIs. A CRI serves up to 8 or 12 ROBs, whereas a ROB can serve up to FEBs. The Timing and Fast Control (TFC) is a core system that is shared by all CRIs.

There are two other readout chains that have been exercised for different detector development activities. The first option uses on Data Processing Board (DPB), a precursor to the CRI-based readout. The second option is based on the GBTxEMU-based tester, which emulates the ROB.

2.4.1 Front-end electronics and the readout ASIC

A readout of a detector module is based on the two FEBs (see Figure 2.8) which have 8 STS-XYTERs each. These chips discriminate and digitize the analog signals coming through the microcables from the silicon strips. As described in the section 2.3, the FEBs are located in the perimeter of the detector stations and will receive up to 100 krad/year [34].

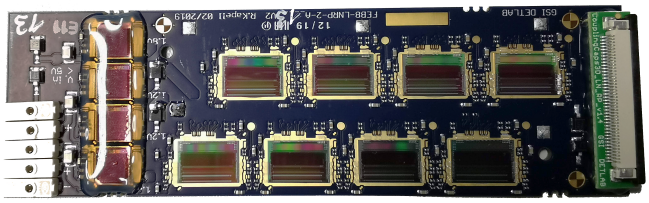

Figure 2.8: Prototype design of a FEB for reading out 1024 channels from a silicon sensor. There are 8 readout ASICs and four low dropout voltage regulators on the left. These active parts are covered by a protective glue called glob top.

The data load for the sensors will vary depending on their position in the detector. Each readout link of the FEB has a bandwidth of about 320 Mb/s, therefore for the innermost sensors the FEB has 5 readout links instead of 2 or 1.

The dimensions of the FEB are tightly constrained due to the limited space inside the STS. Hence, the dimensions of the FEB are approximately 3 cm by 10 cm. The chips need also to be powered, which is achieved by the onboard linear voltage regulators (LDO regulators). Each ASIC has an analog (VDDM) and digital power domain that are powered by 1.2 V and 1.8 V LDOs. The analog part is powered by 1.2 V and 1.8 V LDOs, whereas the digital part is supplied from 1.8 V LDO.

FEBs are glued to aluminum fins, in order to achieve good thermal coupling. Subsequently, the fins are fixed to the base plate of the FEB box (see Figure 2.9) before mounting them on a ladder. The FEB boxes reside on cooling plates. The carbon composite, which is the interface between the fin and base plate, has an ultrahigh thermal conductivity. Therefore, the excess heat is efficiently removed by the coolant (NOVEC 649) which circulates through the cooling plate providing temperatures down to −40 °C.

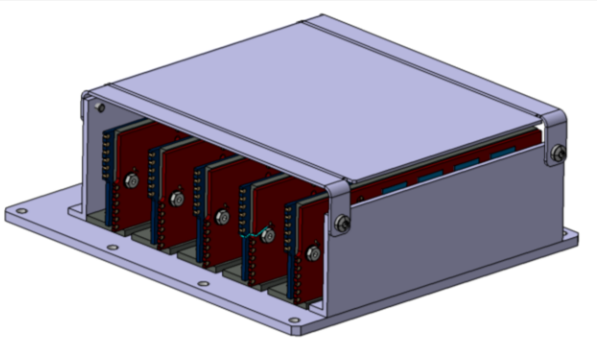

Figure 2.9: A simplified CAD drawing of the FEB box. The box contains 5 cooling shelfs screwed to the base of the cooling plate.

The characterization of the STS-XYTER ASICs is an extensive procedure that investigates the chip. Information about proper amplitude and time calibrations is necessary to interpret the data correctly. It represents an essential step before using the chip in the readout of the silicon sensors. The characterization procedures are designed to check many parameters that influence the FEB performance.

2.4.1.1 Design of the STS-XYTER

The STS-XYTER (see Figure 2.10) is an integrated circuit designed for the readout of STS and MUCH. It consists of 128 analog channels. One of the elements of the chip is a so-called low noise Charge Sensitive Amplifier (CSA), which converts the collected charge into a voltage signal with an amplitude proportional to the charge. Subsequently, the signals pass through the Polarity Selection Circuit (PSC) which allows measuring both polarities of the detector signal with the same ASIC. It makes the use of the ASIC for double-sided silicon sensors feasible. Signal processing is distinguished into two paths: fast and slow. The first one is responsible for the determination of the timestamp and the second one has been adjusted for low noise discrimination and energy measurement with a 5-bit flash ADC. When operating the ASIC in self-triggered mode, hit information is saved and latched by the arrival of each signal using the information from the 5-bit continuous-time ADC and the slow path.

The digital back-end allows accessing registers and reading out the data. It also provides measures to monitor the performance of the chip via i.e., upset counters, link error monitor, and diagnostic circuitry (temperature, VDDM potential, CSA bias value). The serial communication with the chip is based on a custom-developed Hit and Control Transfer Synchronous Protocol (STS-HCTSP) protocol [54]. A detailed description of the STS-XYTER can be found in [55].

STS-XYTER also features an internal monitoring circuit - a diagnostic circuit. It enables the measurement of several potentials inside the chip. By monitoring the analog powering domain (VDDM), temperature, it is possible to have a general understanding

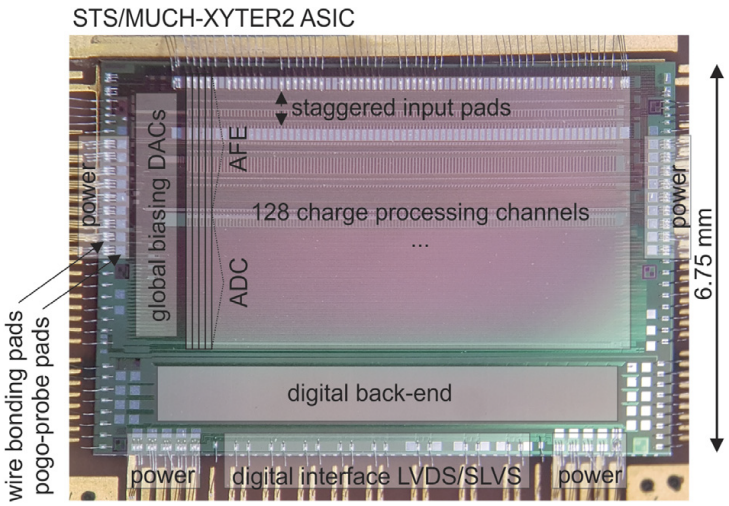

Figure 2.10: The final version of the STS-XYTER chip with the major parts marked [53].

of the chip state without running extensive tests. The diagnostic circuit of the ASICs and the obtained results will be discussed in detail in Chapter 4.

2.4.1.2 Noise considerations for the detector module

Noise levels are among the most important parameters for the STS. The contribution of noise becomes even more crucial in triggerless systems like the CBM experiment. The noise hit is produced once it exceeds the set thresholds of the discriminator. It is digitized and constitutes the data together with the real hits. Too high noise levels may not only worsen the obtained data but also affect the performance of the DAQ chain [34].

The noise level is relatively high due to the fast path higher bandwidth. The slow path, on the other hand, has been adjusted for minimal noise, allowing the hit to be validated only in case a slow shaper signal passes the ADC first comparator threshold [55]. The noise level may be influenced by a number of factors including load capacitance (different silicon sensors sizes and microcable lengths), peaking time, temperature, glob-top type, powering, and external contributions.

In order to estimate the overall noise performance it's necessary to include the silicon sensor, cables, and readout chip. There are three main contributions to the noise levels [56]:

- Parallel current noise (detector leakage current, leakage current flowing through transistors in the Electrostatic Discharge protection circuit, resistor bias shunt resistance [44], feedback resistance).

- Series white noise (CSA input transistor thermal and flicker noise).

- Series 1/f (flicker) noise (caused by charge carriers that are randomly trapped and released between the interfaces of two materials).

An analytical expression of the noise spectral density at the shaper output and the Equivalent Noise Charge (ENC) can be expressed as

$$ENC^2 = ENC_i^2 + ENC_w^2 + ENC_{1/f}^2, \tag{2.9}$$

where ENC_i is the total current noise, ENC_w is the total white noise and $ENC_{1/f}$ is the total flicker noise.

The noise performance of a module provides an invaluable insight into the state of the sensor and FEE electronics. Knowing the nominal ENC allows the detection and investigation of potential external noise sources. Moreover, it provides means of estimating broken analog connections or hints on how to adjust settings to reduce the noise contribution.

2.4.2 Readout board and Common Readout Interface

The STS readout board (ROB) is a data concentrator board based on the radiation-tolerant GBTx ASIC and Versatile Link devices developed by CERN and others [57], [58]. The board is an interface between many electrical readout links (many FEBs) and the CRIs boards located outside the underground cavern of the CBM experiment [59]. It resides inside the STS enclosure, which means that it will be exposed to high levels of ionizing particles. Therefore, it is built from radiation-hard components. The board is also thermally coupled to the cooling plate, which can reach a temperature down to $-40\,°C$. The ROB needs to reliably work at changing temperature between $-40\,°C$ and $20\,°C$.

The main building elements of the board are three GBTx ASICs and a GBT Slow Control Adapter (SCA) ASIC. Two of the GBTsx ASICs act as slaves and are controlled via the mentioned SCA.

The Common Readout Interface (CRI) is a PCIe card[4] based on Field Programmable Gate Arrays (FPGA). The CRI provides the input to the First-level Event Selector (FLES). It is also a central element of the DAQ chain, as it provides means of data control. Moreover, the CRI has an interface to the TFC system.

[4] PCIe card refers to a kind of network adapter with a PCIe interface.

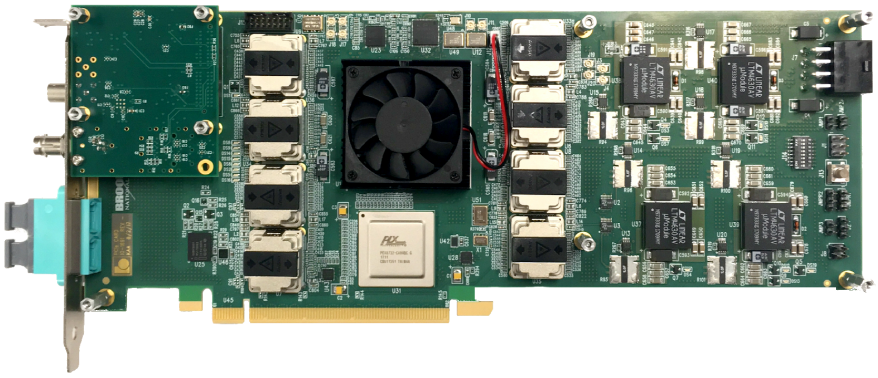

Figure 2.11: The first prototype of the CRI board [60].

2.4.3 Alternative readout chains

There are two alternative readout chains implemented for testing purposes towards the realization of STS. The first readout chain is based on the Data Processing Board (DPB is a FPGA based board), ROBs. The second type of readout chain is GBTxEMU-based. It is an alternative low-cost readout chain that can be used for low-performance setups, e.g., for testing and quality assurance.

Data Processing board based chain

Even though the final solution for the readout is the CRI board, the Data Processing Boards (DPBs) were implemented for developing and testing purposes [61]. To control the communication with the DPB, the IPbus protocol [62] was chosen. It is a communication protocol based on Gigabit Ethernet (GbE) which allows simple and fast communication with FPGAs.

Data acquisition chain based on GBTxEMU board

Another alternative to the two readout chains is the GBTxEMU-based tester. It is based on a commercial Artix-7 board (TE-0712, Trenz Electronics GmbH), and allows emulating GBTX ASIC or the whole ROB. Moreover, it could also be used in an autonomous mode with the addition of an adapter.

The whole examination process towards STS will include testing of about 20000 ASICs, then 2000 FEBs (tested multiple times during the assembly, e.g., after the ASIC wire bonding and after the micro-cable bonding), and eventually the full module. As a hardware platform offering good availability and reasonable production cost, the GBTx65 EMU [63] board was chosen.

The software used for the operation of the emulator board is also based on the IPbus [62] protocol to access registers. The operation begins with the full synchronization of the STS-XYTER links. This process enables communication with the chip, given

no correct time phase between data and clock and incoming data exists. The next step involves the configuration of the chip registers (35496 bits for the AFE control are set). At the same time, the number of enabled up-links, the channel masking, and the timestamp counter are set. From this point on, any custom tests or calibration may proceed. For example, read and write register tests, readout of the VDDM potential values, chip temperature, etc. Moreover, to enable long-term testing, an interface to the control system framework was implemented.

2.5 Highlights from the performance simulations of the STS

The STS performance is mainly determined by its ability to accurately reconstruct tracks of charged particles, which can then be used to determine the momentum of those particles accurately. During the CBM experiment, silicon sensors will be exposed to a total fluence of up to $10^{14}\,n_{eq}cm^{-2}$ which causes a decrease of Charge Collection Efficiency (CCE) (Figure 2.12) and enhanced noise.

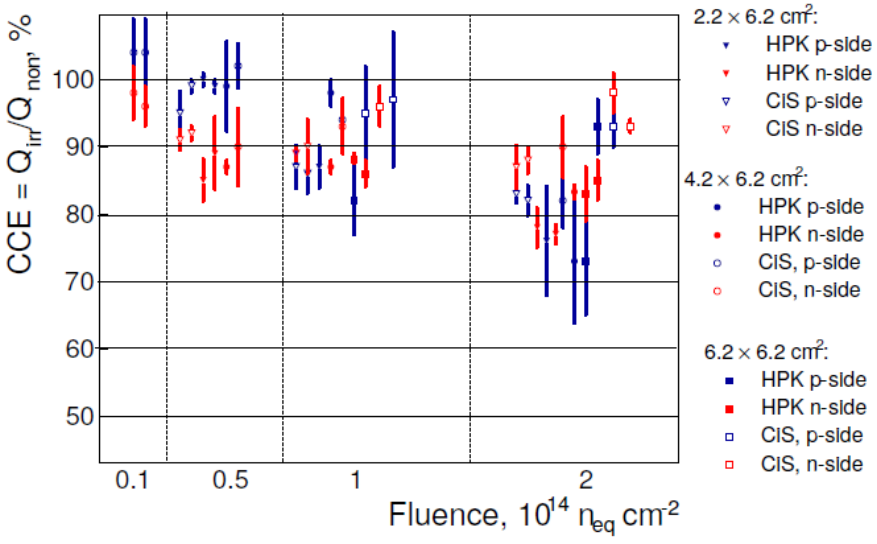

Figure 2.12: CCE as a function of the fluence for sensors studied during the prototyping phase for STS. To ensure the full depletion the sensors were biased to 450 V for fluences up to $1 \times 10^{14}\mathrm{MeVn_{eq}cm^{-2}}$. For the highest fluence the bias voltage was 500 V [46]. Tested sensors were produced by Hamamatsu Photonics (denoted as HPK) and CiS Forschungsinstitut für Mikrosensorik GmbH (denoted as CIS).

This problem can be addressed from a few different perspectives. Firstly, the noise levels of the newly produced modules should be as low as possible. It can be achieved using low-noise electronics and ensuring proper shielding from electromagnetic inter-

ference. The noise levels can also be adjusted by decreasing the temperature or annealing the sensors. Nevertheless, the latter has to be performed in a controlled fashion in order to avoid reverse annealing. Keeping the detectors at temperatures below 0 °C eliminates the reverse term while largely preserving the beneficial one. During maintenance, the ambient temperature has to be raised in a controlled manner to take advantage of short-term annealing and to prevent any reverse effects [42]. Figure 2.13 shows how the silicon sensor would behave after receiving up to $10 \times 10^{13}\,\mathrm{MeVn_{eq}cm^{-2}}$, what is considered to be the maximum dose that the STS sensors will receive. According to this plot, the assumed signal-to-noise ratio of 10 can be achieved even if the sensor CCE drops to 70% if the temperature is kept at −10 °C.

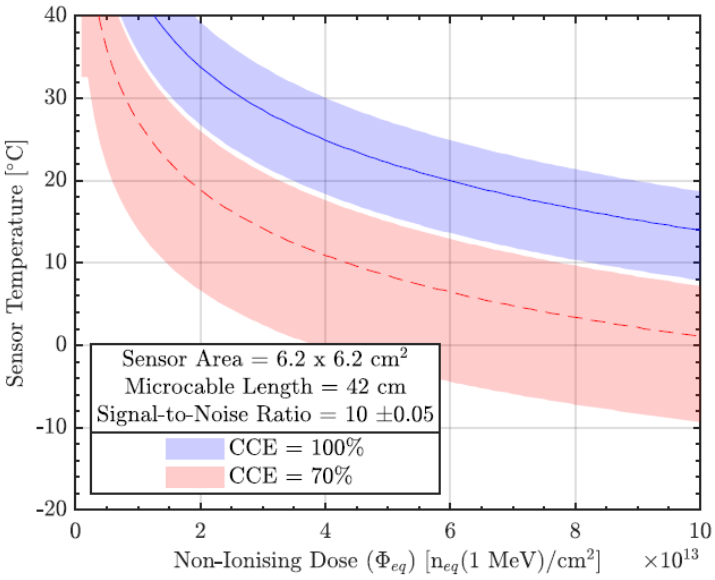

Figure 2.13: Variation of the sensor temperature with accumulated fluence to maintain S/N = 10 for two different CCE levels. The shaded bands indicate 20% modeling error [64].

2.6 Overview of the services for the STS

The STS will feature a number of services and sensors that need to be controlled, monitored, and automatized in order to work efficiently during the operation of the detector. The data from these services provides unique information about the detector state and functioning:

1. Low voltage and high voltage powering modules.
   About 2500 low voltage and 1800 high voltage powering channels will be em-

ployed for the STS. The low-voltage modules will be located in the experiment cave. This location exposes the electronics to elevated radiation levels.

2. Temperature, humidity, pressure sensors.
   A number of different sensors and technologies will be used to monitor the ambient conditions inside the detector. Their performance and values are going to have a direct impact on the detector operation.

3. Cooling plant.
   To avoid reverse annealing of the silicon sensors and thermal runaway scenarios, the detectors will be cooled with temperatures reaching $-40\,°C$ at the end of their lifetime. The cooling plant providing the coolant is a crucial part of the safe operation of the detector.

4. Air-drying system.
   The coldest points inside the STS may reach temperatures down to $-40\,°C$. Therefore, the frost point inside the enclosure has to be fairly below the coolant temperature to avoid possible icing or condensation on the electronics.

2.7 Requirements for the control system

Custom solutions that are applied to STS make the control of this system very challenging. Different services imply different control solutions which need to be implemented. A distributed control system should offer remote control, alarm detection, reporting and logging, data processing (archiving, retrieval, plotting, conversion, analysis), common time management, access security, and automatic sequencing[5]. In addition to that, the DCS for the Silicon Tracking System (STS) is being designed taking into consideration the following aspects:

- Potential control framework should offer the possibility to control a variety of different services, which often have different communication protocols.
- Logging, and monitoring - there should be reliable means of supervision of processes, containers, and Input/Output Controllers[6] (IOCs).
- The control software should be horizontally and vertically scalable when it comes to adding additional computing nodes or applications/Input Output Controllers (IOCs)/instrumentations.
- Supervision - it should be possible to integrate a sub-system oriented with higher-level control structures.

[5] Sequencing, also known as sequential control, it controls the device in a pre-determined order.

[6] An input/output controller is a device that interfaces between an input or output device and the computer or hardware device.

- Flexible - applications should be easy to run on different operating systems and processor architectures.
- Sustainability and support - the experiment is supposed to run for about 10 years, excluding the building and commissioning time. The control system should be sustainable and long-term support provided.
- Reliability - the system should be highly available, minimizing the downtimes,
- network separation - it should be running in a dedicated network (divided into several service-oriented subnets) to have a good overview of the processes and communication between the nodes.
- GUIs - all parameters/process variables[7] should be available in a user-friendly Graphical User Interface (GUI). In case of error or malfunction, it should be stated clearly by the software where the error happened, what could be the potential risk, and what actions need to be taken.

[7] In control theory, a process variable is the currently measured value of a particular part of a process which is being monitored or controlled.

Chapter

3 The Detector Control System, an important part of the online systems

As mentioned in Chapter 2, CBM will face an unprecedented interaction rate in heavy-ion experiments (up to 10^7 events/s). That number also sets a clear requirement for the detector systems and their corresponding data acquisition. Certain design decisions had to be made to reduce the amount of raw data coming from the subsystems due to the huge quantity of incoming data.

Experiments like CMS, use a trigger to [65] reduce the amount of raw data coming from millions of proton-proton collisions. In the case of CBM, to reduce the data amount, the raw data needs to be evaluated in software on Central Processing Unit (CPU) and/or Graphics Processing Unit (GPU) level. The self-triggered readout system implies that the association of data from different detectors to individual physical collision events must be based solely on their timestamp, which is generated in the frond-end electronic (FEE) circuitry. As a result, a central timing system must synchronize the FEE elements to sub-nanosecond precision. On the other hand, the typical event-building action and the high-level trigger are transitioned to the FLES (First-level Event Selector) online computing farm.

The readout hardware is connected to the computing farm via custom-developed optical links that manage clock and time distribution, data transfer, and control communication. The Common Readout Interface (CRI) connects the links to the online farm. The CRI forwards the clock and time information obtained from the Timing and Fast Control (TFC) system to the detector FEE, and also converts the data received from the detector. Figure 3.1 shows the schematic view of the controls and data acquisition chain of the CBM experiment.

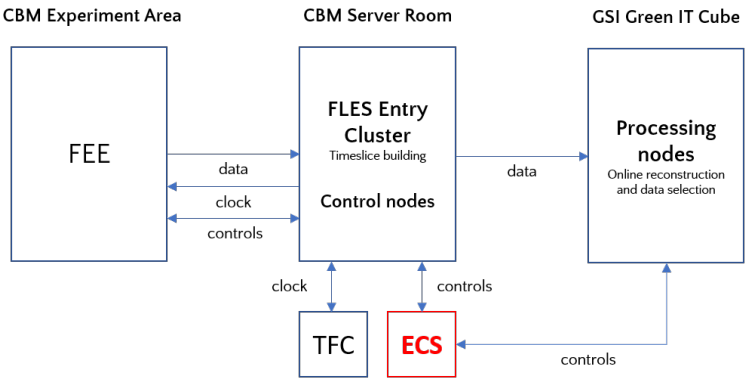

Figure 3.1: General schematics of the CBM readout systems without detector detector-specific systems.

The Experiment Control System (ECS) highlighted in red is also the supervisory structure of the Detector Control System (DCS) which controls and monitors the subsystems. The next sections focus on the software components related to the ECS, and a detailed explanation of the experiment control with its design. The main focus of the recent work is put on the DCS. An introduction to the modern control system frameworks is given, together with a detailed explanation of the functionalities of the specific software components.

3.1 Controlling the CBM experiment

Heavy-ion physics experiments require complex control systems, which are crucial to the successful operation of the detector system. Proper implementation of such systems ensures an understanding of the safety margins and enhanced data production quality. In general, the whole system should be robust, partitioned, modular, distributed, and highly available. Similar topics were also considered while designing the STS control system.

Figure 3.2 depicts the targeted control architecture of the future CBM experiment. It consists of different software agents[1] with clearly defined tasks. During the Phase -0 experiment of the CBM (mCBM) some parts of the future ECS were tested. The respective parts of the controls have been tested in a standalone mode, which means that there has not been any structured communication between DCS, Device Control Agent (DCA), and Experiment Control System (ECS). Nevertheless, for the final experiment, the detector control system should provide the information on the detector state to the agents residing at a higher level in the control hierarchy and also request the state of the DAQ.

[1] A software agent is a persistent, goal-oriented computer program.

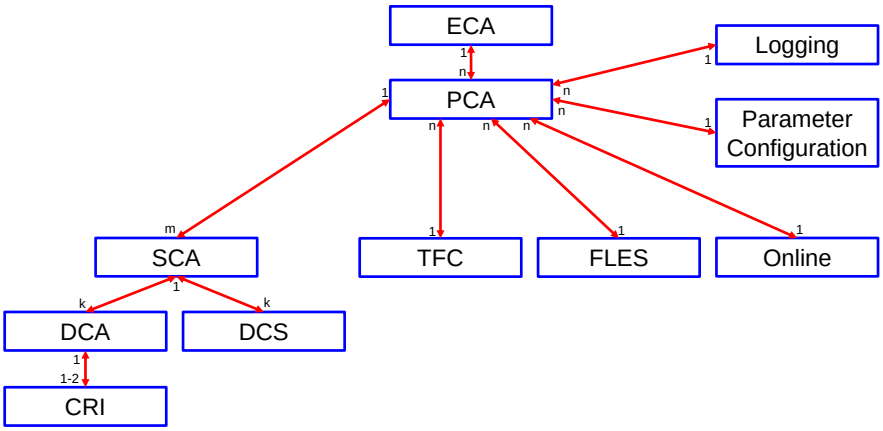

Figure 3.2: ECS core agent relations. The numbers and letters indicate how many instances of agents or systems can run concurrently.

In the next sections, the main features of the control agents are discussed, in particular those that can influence DCS (Partition Control Agent (PCA), System Control Agent (SCA), and DCA). Apart from the mentioned agents, the following components are expected to be part of the experiment control architecture:

- Logging and monitoring system - state or configuration changes should be documented for possible revision.
- First Level Event Selector network (FLESnet) - DAQ software controlling the data readout and timeslice building.
- Online processing - software receiving the data from the FLESnet and processing it.
- Time and Fast Control (TFC) - hardware source of timing information.

3.2 Experiment Control System and its structure

The highest supervisory element of the control strategy is the Experiment Control Agent (ECA). It is the top layer of the whole experiment and it should be constantly running and keeping track of the partitions, the systems in partitions, and the systems out of partitions.

The PCA as shown in Figure 3.2, is the bottom layer of the ECS, which tracks the state and controls a set of detector systems plus all needed central systems. Multiple partitions can run concurrently, potentially allowing for parallel runs with independent detector system sets.

Partition (controlled by PCA) is a component of the ECS describing the combined state of a set of detector systems participating in a common readout. It is used to segment the readout and data flow. It also manages the states of central systems, which do not have partition-level states (e.g. TFC, FLES in case it does not use internal partitions). It provides the address and port required by agents to establish the 0MQ[2] sockets[3] and build the ECS structure upon request.

The PCAs hold internal instances of the necessary System Control Agent (SCA) interfaces, which are responsible for:

- Holding a copy of the current state of the SCA.
- Periodic ping of the SCA to ensure early disconnection detection.
- Sending requests to the SCA and receiving the replies.
- Monitoring the SCA broadcast channel for unexpected state changes.

These should not be confused with the SCA, which are in separate processes (the list will be dynamic and generic at PCA level, and can depend on the systems participating in the readout activities): BMON, MVD, STS, RICH, MUCH, TRD, TOF, PSD.

The SCA is the first detector supervisory layer, which contains the current information about the state of the DAQ and DCS. Its role in division into the underlying systems is discussed in the next subsection.

3.2.1 System Control Agent and its role

The subsystem-specific SCA should manage communication both with the detector-specific agents and with the higher supervisory entities of ECS. Furthermore, SCA should provide higher control levels with the global state whenever it is requested, handle any changes reported by a detector (tracking the state), and provide an interface for the shift crew to monitor the state of the system.

Two main links of the SCA include:

- Detector Control System - Experimental Physics and Industrial Control System EPICS [67] based distributed control system which controls and monitors all the hardware connected to the specific detector (apart from the DAQ specific boards).
- Device Control Agent (DCA) - this agent controls almost all logic on the CRI board (excluding the FLES Interface Module (FLIM) section and direct memory access data path). DCA provides a high-level interface for the higher layers of the control architecture, collectively referred to as EDC.

[2] 0MQ is an asynchronous messaging library [66].

[3] A socket is used by a client to send requests to and receive replies from a service.

3.3 Introduction to controlling a detector

A robust, well-defined control system is a compulsory element for every complex experimental setup, especially in radiation-controlled areas. To ensure the safe operation of a detector subsystem, automation processes are commonly implemented (e.g., in the form of a Finite State Machine[4] (FSM) or hardware interlocks). In the STS case, to ease the use and implementation of a control system, a fairly novel approach was used. It is primarily based on the containerization[5] of different applications used to monitor and control setups.

A control system must provide multiple functionalities to operate effectively. These include communication between hardware and software layers, visualization of data, logging of system events, archiving of historical data, and controlling means. Control can be automated using a FSM or performed manually, depending on the requirements of the system being controlled. The control system can be usually divided into three layers: field layer, control layer, and supervisory layer. The bottom (field) layer contains all the process sensors, actuators, and other devices that are connected to the control system via I/O boards and/or field buses. Communication between the field layer and control layer can be of almost any type compatible with the used components, i.e., Ethernet, Modbus TCP, Profibus. The control logic is introduced in the Programmable Logic Controller (PLCs) and so-called control nodes (single board computers etc.) in the control layer. The supervision layer or supervisory level provides the operators with means of controlling and monitoring the subsystem, for example via command line or a Graphical User Interface (GUI) or Operator Interface (OPI) [68]. Typically, DCS building blocks reside in a dedicated network to avoid unnecessary cross-talk and ensure more efficient debugging.

Figure 3.3 shows a general idea behind the STS DCS from the software point of view. The master node or the central DCS node receives data from the configuration database, which allows the preparation of subsystems for a given action (for example, for a transition into a different state). The master node will be only accessible by the DCS experts, excluding subsystem-related personnel from performing actions on other subsystems DCS. There are also one or more archiving nodes and control nodes, which will contain detector-specific applications. All the mentioned components allow effective control over a detector and deliver crucial operational information (alarms, events, Process Variables (PVs) values, etc.).

[4] A state of the Finite State Machine is clearly defined at any given point in time. It can move to another state by processing an input.

[5] Containerization is the packaging of software code with just the operating system libraries and dependencies required to run the code.

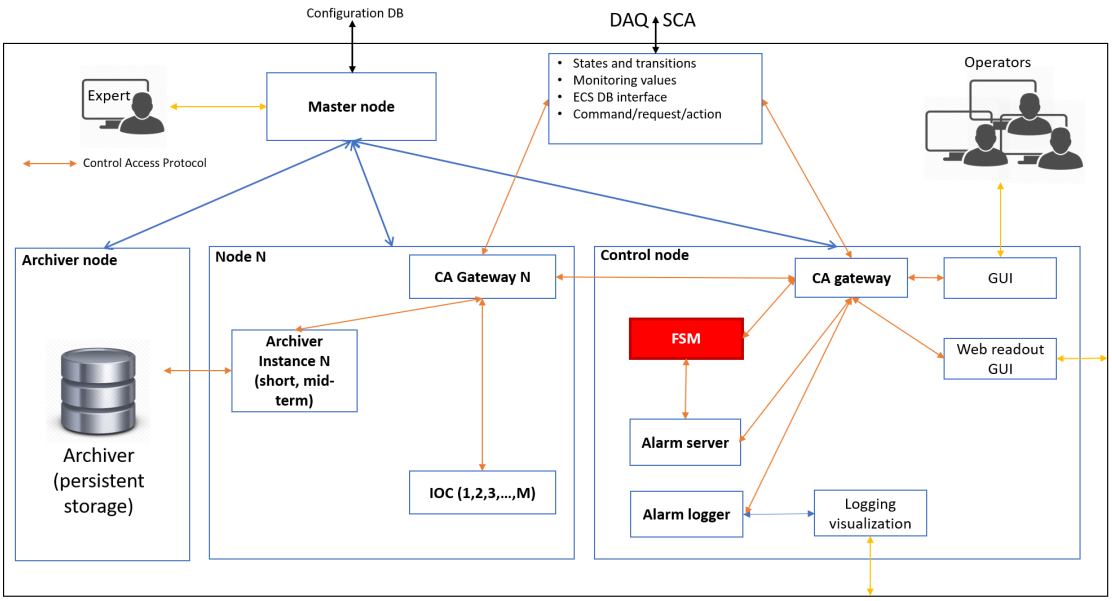

Figure 3.3: Proposed DCS infrastructure for the STS. The scheme describes the most important software components including the archiver, alarm server, alarm logger, GUIs, FSMs, and corresponding interfaces.

3.3.1 Control system for the CBM experiment

EPICS was chosen, as a software platform to implement the CBM DCS. More detailed explanations of how EPICS works are described in the next sections. According to [69], the basic attributes of EPICS are:

- Tool based – minimized need for custom coding
- Distributed – an arbitrary number of IOCs and OPIs, as long as the network does not saturate
- Event driven – it is designed to be event-driven to the maximum extent possible
- High performance, robust
- Scalable
- Under constant development (see latest updates related to the Control System Studio and PVA)

3.3.2 EPICS and its working principle

EPICS is a set of tools and applications which provide a software infrastructure for distributed control systems [70]. This framework could be used for large systems like

particle accelerators, telescopes, etc. as well as for smaller systems featuring only several hundred process variables [71]–[74].

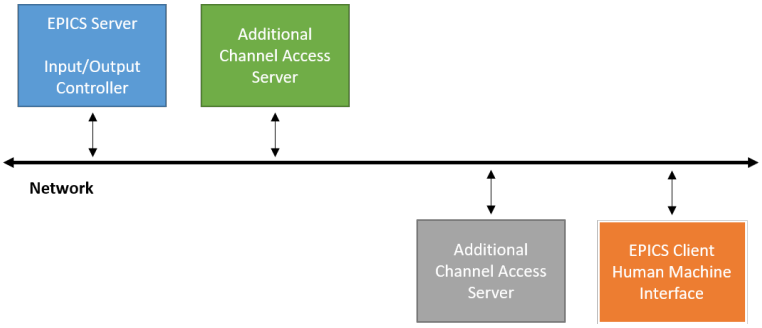

Figure 3.4: EPICS working principle. The servers provide the PVs via the channel access protocol to the other clients in the network.

As described in Figure 3.4, the system uses client/server and publish/subscribe approaches to communicate between different devices/nodes. Most servers, called Input/Output Controllers (IOC) perform I/O[6] and local control tasks and publish this information to clients via dedicated protocols Channel Access and/or pvAccess [67].

3.3.3 Available control tool sets

EPICS and related toolkits offer a complete set of applications to control large experiments. Many sites all over the world have implemented EPICS-based control systems, i.e., HADES [75], J-PARC [76], STAR [77], ITER [78], Australian Synchrotron and many more [79]. Besides, there are also different alternatives to implementing a control system, which include:

- Siemens WinCC [80], [81]
- Tango [82]
- LabVIEW [83]
- Custom software (e.g., python/C++ or stream processing software) [84]

These frameworks were discarded either because of licensing needs (LabVIEW, Siemens WinCC) or lack of extensive experience on-site (Tango). Phoebus [85] was chosen as the collection of tools and applications to monitor and operate STS. All mSTS OPIs were prepared in Phoebus [85]. The detector uses the following Phoebus-related applications:

- Alarms logging

[6] I/O task is anything which the CPU can not perform on its own, and has to rely on other components

- Alarm server
- Save and restore

More details about these applications and their use will be provided in the next sections. Although Phoebus proved to be easy to use and implement new operator screens, there are also alternatives that could provide similar functionalities:

- Bluesky Project (Python-based set of libraries [86])
- React Automation Studio [87]
- Channel Access Tools - MEDM, Alarm Handler (ALH), Archiver (AR) etc.)

3.3.4 EPICS architecture and input/output controller

The core elements of the systems are the input/output controllers (IOCs), which provide control logic for the connected hardware. The IOC uses channel access and/or PVAccess to communicate with clients and contains also the following components [88]:

- IOC database – a memory resident database containing a set of named records of various types [89]
- Record support – a set of support routines defining a record
- Device support and drivers – serve access to external devices
- Monitors and scanners
- Sequencer – an optional extension of the IOC which is a finite state machine

An IOC does not need extensive computing resources, therefore it runs also on low-power single-board computers like Raspberry PI or Odroid. IOCs are also commonly supported by additional modules, device support, libraries, and APIs which altogether provide an efficient way to control various devices.

To communicate with devices, an IOC uses so-called device support. The most commonly used ones include:

- StreamDevice is a generic EPICS device support for devices with a byte stream-based communication interface. That means devices that can be controlled by sending and receiving strings (in the broadest sense, including non-printable characters and even null bytes). Examples of this type of communication interface are serial line (RS-232, RS-485, etc.), IEEE-488 (also known as GPIB or HP-IB), and telnet-like TCP/IP [90].
- devModbus [91] - includes support for three Modbus standards (TCP, RTU, ASCII), used for control of climatic chambers in the STS group.

- asynDriver [92] - asynchronous driver support, which is an interface that implements a device-specific code to low-level communication drivers. Together with the StreamDevice it is the most commonly used one in mSTS.

Control software often needs to be deployed on nodes with different operating systems and/or architectures. Additionally, monitoring the software components may be challenging if the system is built out of several nodes. To address this problem containerization technology was introduced. Besides, this technology has many advantages, as it's:

- Standardized, what makes it portable anywhere
- Independent of the operating system
- Instant replication and easy debugging
- Lightweight - containers share the machine kernel, and they do not require a separate one, which makes them much faster than virtual machines
- Docker daemon monitors the containers instead of the hypervisor in case of virtual machines,
- Processes run as native causing little overhead

Container images[7] for the IOC, as well as other DCS building blocks, were created. More detailed information about containerization and how it was implemented is included in Section 3.4.

3.4 Containerized IOC

Containerization is an increasingly popular method of virtualizing an application without running a full-blown operating system. In current practices, containers are commonly used both in development and production environments, often together with cloud solutions. In the HEP community, containers and their different applications become increasingly popular. According to [93] the first mention of Docker[8] container of the EPICS IOC was related to the Taurus project in 2015 [84]. Since then containerization efforts intensified also within the FAIR based collaborations - CBM/MVD [93] and PANDA DCS [94].

IOC container has been prepared by the DCS group of the PANDA Collaboration and adjusted to the STS needs. The latest IOC's image is built on EPICS R7.0.3.1 image, and

[7] A container image consists of an unchangeable, static file containing executable code that runs independently.

[8] Docker is a set of products that use operating system level virtualization to deliver software in packages called containers.

it contains the most important modules and extensions i.a. asyn, autosave, calc, Modbus, and SNMP (see Figure 3.5). By using so-called volumes (see Figure 3.6) the IOC can be used at any node with the Docker engine. Volumes are one of the mechanisms to manage application data, and it's a proper way to ensure data persistence. When a container is started, Docker loads the read-only image layer, adds a read-write layer on top of the image stack, and mounts volumes onto the container file system. Having prepared database files, st.cmd, and stream protocols if needed, an IOC can be deployed on any node, with any operating system and processor architecture.

Figure 3.5: Schematic view of the EPICS 7.0.3.1 based IOC image and the most commonly used modules.

A general idea of a containerized EPICS IOC is presented in Figure 3.6. Every container is assigned an IP address for every Docker network it connects to. Each network has a default subnet mask and gateway. In order to connect the IOC with other services, the ports used by EPICS (5064, 5065 for channel access protocol and 7064, 7065 for PVAccess) need to be exposed. The deployed containers use the host network to communicate with each other and other nodes.

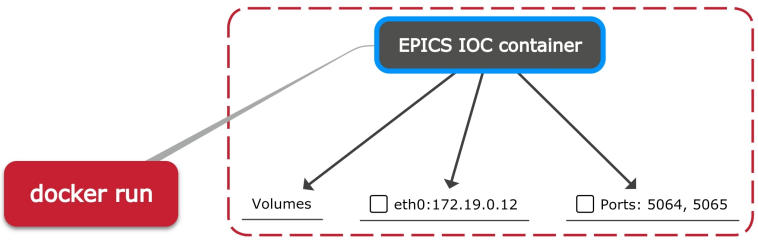

Figure 3.6: A general idea behind the containerization of an IOC.

3.5 Containerization platform – Docker

Docker was chosen as the platform to prepare the images and run the containers. There are also several alternatives to the docker engine, that allow running containers in rootless mode:

- Podman [95]
- Singularity [96]

For the use of containers in the final experiment, the following list of requirements must be taken into consideration:

- Services should be accessible only by experts, crucial services should be hidden from operators (authorization).
- Ssh accesses to the DCS nodes should be limited by authorization plugins to avoid overloading,
- Experiment network should be segmented based on the goals and communication between software entities clearly, defined (DCS, SCA).
- Proper security context should exist for all the services (e.g., root privileges).
- All the changes in the cluster need to be logged.
- Unwanted kernel modules can't be loaded by the containers.
- Cluster and container should be redundant.

One of the features of Docker has been considered risky for the operation of the detector or experiment, especially considering the final system. Docker-based containers run with the root privileges, therefore posing a threat to the operation of the control system. The daemon is a part of the engine that runs the containers that have full privileges not only within the container but also on the node. If a container gets compromised, it may lead to potentially disastrous scenarios, including loss of data or potential threat to the detector – e.g., killing the container. A compromised node can also endanger other nodes in the network. Since late 2020 it is possible to run Docker daemon and containers as a non-root user. Docker daemon and containers themselves can run inside a user namespace [97], therefore mitigating the risk. Thanks to the Open Container Initiative that defines container formats and runtimes, using different engines does not require many changes in the container image.

3.6 Multi-container applications

Over the years EPICS has become a framework that offers users many off-the-shelf applications that ease the implementation and configuration of a control system. Figure 3.7 shows the most commonly used control-related applications.

All the applications in figure 3.7 applications were used as containers based on prepared images and linked using Docker-compose, which is a tool for defining and running multi-container Docker applications [98]. To configure the containers a YAML[9] file has to be populated with the services settings (in this case the services refer to the applications, e.g., IOC. This section summarizes the most important applications used for the DCS and their functionalities.

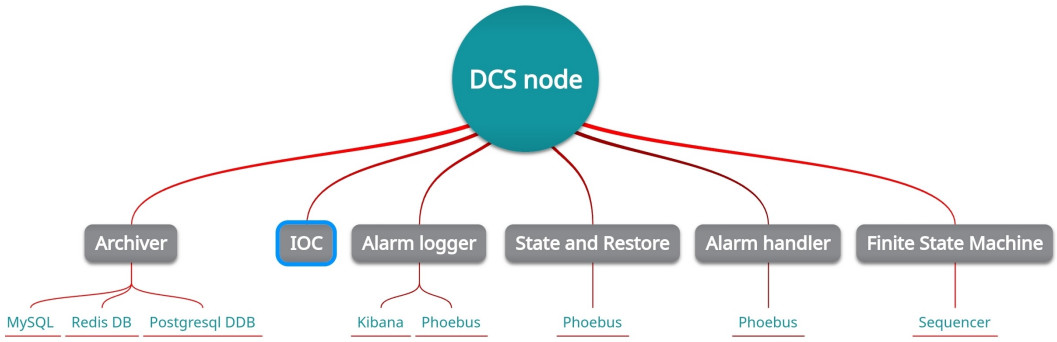

Figure 3.7: Services used in addition to Phoebus functionalities, together forming a full-blown control system.

3.6.1 Control System Studio and Phoebus

Control System Studio (CSS) consists of open-source Java applications and modules which can be used in constructing a control system. Phoebus is an update to the CSS, and significantly improves its performance by removing dependencies on Eclipse RCP. Phoebus uses both channel access protocol and PV access, and it offers graphically based applications to access EPICS PVs, OPIs, PVs history, etc. An example of a chiller GUI is depicted in figure 3.8. One of the main features of Phoebus is its modular nature. Users can develop and add their products, or just include or exclude applications or configurations.

[9] YAML is a human-friendly data serialization language for all programming languages [99].

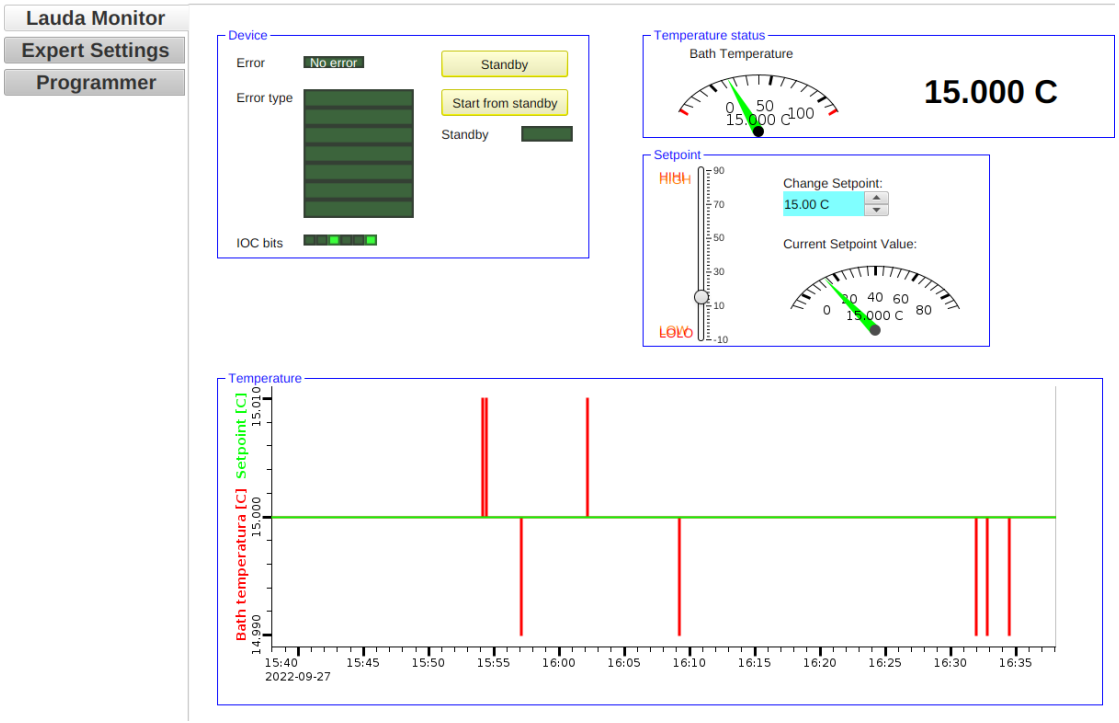

Figure 3.8: An example of a detector system GUI for a cooling unit.

3.6.2 Solutions for archiving the data

Archiver serves as one of the main building blocks of the DCS, as it allows not only to look up the history of a given record but also to download and post-process the data. Archivers make use of the publish/subscribe logic, updating the values on change. In general, the archiver must run smoothly, without significant downtime, and the linked database and other clients should also have a stable connection. A primary choice for STS is the so-called Archiver Appliance [100]. An example of the archiver appliance is divided into short-term storage, medium-term storage, and long-term storage. In principle, a system administrator can adjust these settings to the needs of the specific case. The four Tomcat containers[10] are employed to handle the tasks of the archiver.

The main advantage of the archiver include:

- Data retrieval can be integrated into Phoebus or Matlab.
- It supports a wide range of formats.
- It ensures stable performance, even with a hundred thousand PVs.

[10] An Open source web server by the Apache foundation.

Apart from the Archiver appliance, there are also alternative solutions:

- Cassandra [101]
- RDB Archive engine [102]

3.6.3 Alert communication with alarm server

An alarm server monitors a chosen set of PVs, including their alarm state. EPICS records facilitate fields related to the alarm thresholds and their severity, evaluated each time the record is processed. Every numeric value could have two uppers and two lower boundaries, with assigned severities (NO_ALARM, MINOR, MAJOR). EPICS by itself, does not take any actions on the detector hardware when the alarm threshold is exceeded. On the other hand, a Phoebus-based GUI will change the font color (MINOR - orange, MAJOR - red) of the variable once the alarm appears. If the connection to the alarm server exists, then the server acts upon a change in the alarm status of a record. The user interfaces show alarms, allow acknowledgment, and provide guidance and helpful links. Apache Kafka is a distributed event store and stream-processing platform which serves as a communication bus between the alarm server and Phoebus. An example of the mSTS alarm handling GUI is depicted in Figure 3.9. It provides not only a visual notification of an alarm but also guidance, displays, and commands.

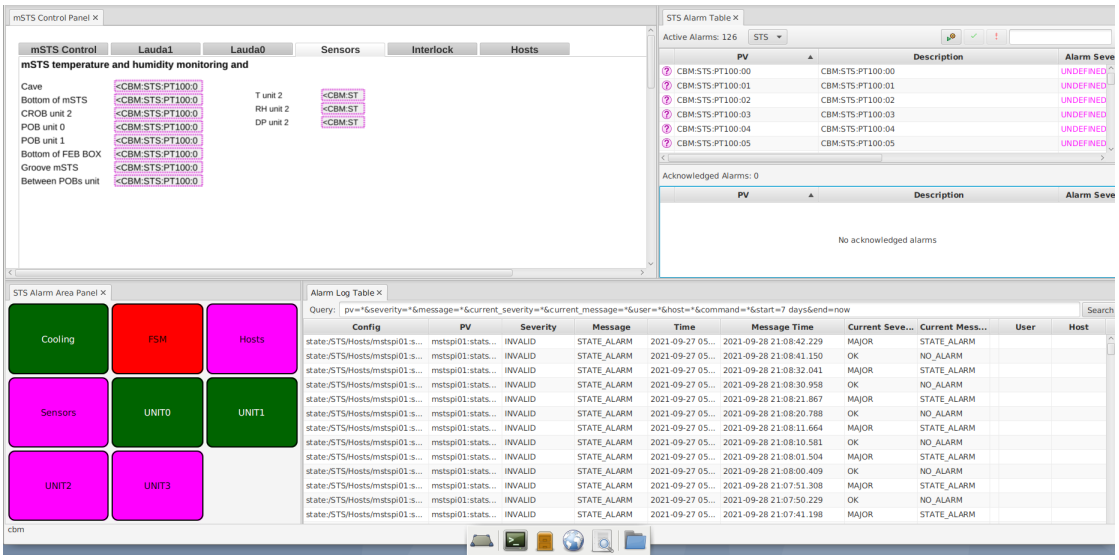

Figure 3.9: Phoebus alarm handler view – top left part some GUIs, the top right part is the alarm table showing the current and acknowledged alarms, bottom left features a color status of respective nodes (e.g., cooling), bottom right shows the latest entries in the log.

3.6.4 State and commands logging

Logging is another important part of the DCS. It allows monitoring and checking of all the changes in the configuration and alarms of all the process variables. Thanks to the logs acquired by the dedicated service, debugging becomes much easier. The alarm logging service enables the logging of configuration changes, state changes logging and commands. Similarly to the alarm server, it uses Apache Kafka for data transfer. Apart from the logs, there is also a GUI available in the Phoebus [103], an operator can also use the Kibana[11] web interface to discover patterns and trends in the data.

3.6.5 Finite state machine as an automation and safety mechanism

A finite state machine (FSM) is a software construct that defines states and transitions between these states of the physical device. In a given moment it has a clearly defined state and a given set of rules and conditions apply to this state. An input issued by an operator or automatically by a sensor(s) could trigger a transition. All transitions are unidirectional, but it is possible to define two opposite transitions, e.g., entering and escaping the error state.

One of the possibilities to implement a FSM is to use Sequencer, which is a State Notation Language based on C/C++.:

- Start-up, shut-down, fault recovery, etc.
- Little C code, many states, many transitions
- Short compilation time, and can call any C++ code, easy connection to channelAccess

One of the alternatives to the Sequencer and State Notation language is the PyEPICS-based library Pysmlib[104]. It features several interesting functions like integrated watchdog logic, multi-threading, or configurable logging systems.

3.7 Containerized EPICS-based framework

The containers-based framework introduced in this chapter is the baseline for all the research and development activities throughout this thesis. In principle, most small and/or larger laboratory-based experimental setups do not require full-blown control systems. Hence, in the next two chapters two smaller applications of the developed framework are introduced. In addition to that, the studies and their implications are discussed in detail. Chapter 6 is dedicated to the application of the full control system to the Phase-0 version of the STS.

[11] Source-available data visualization software.

Chapter

4 Control framework applications for the test setups

The EPICS and related toolkits can be used to control large experiments or even beam lines, but also smaller experimental setups, in which only limited functionalities are needed (e.g., data visualization, archiver, and database). In order to evaluate the hardware that should be used for the final experiment, many relatively (few hundreds of PVs) small R&D setups were built and operated. The two following sections introduce the applications of the developed software package for effective control and data acquisition in two chosen setups. The first section focuses on the powering units irradiation studies and implications for the STS. Subsequently, the results from the thermal cycling measurements for the STS electronics will be presented and discussed. The thermal cycling studies aimed to discover operational limitations of the FEE.

4.1 Irradiation studies of the powering units

Radiation-induced effects in electronics play an important role in accelerator facilities. Depending on many factors, i.a. location of the setup, intensity, or energy of the incident particles, damage caused to a semiconductor device may vary greatly. A particle could cause no observable effect, transient disruption of circuit operation, a change of logic state, or even permanent damage to the device or integrated circuit (IC) [105]. Hence, studies on the radiation hardness of the devices used for the CBM experiment are crucial before choosing the final hardware and its exact position.

One of the detector services that is going to be exposed to the elevated level of radiation is the low voltage powering of electronics. The STS will be powered by about 140 low-voltage modules, 16 channels each providing 2100 power channels. In order to estimate the Single Event Effects (SEE) in the powering electronics in the envisaged radiation environment, two irradiation campaigns took place in GSI, Darmstadt. The first one was conducted at the mini-CBM experiment and the second was realized next to

the electrostatic septum of the SIS18 synchrotron. These irradiation campaigns aimed at detecting radiation-induced soft errors. Soft errors are transient faults in semiconductor devices caused by external radiation, such as energetic particles and cosmic rays [106] in the power units electronics and estimating its rate.

A radiation-induced failure in the low voltage powering of the FEE may lead to a rapid decrease of temperature, as the primary coolant temperature may reach down to $-40\,°C$, consequently making the FEE susceptible to thermal stress. The effects of radiation must be therefore studied to ensure the safe operation of the STS. Estimation of the soft error rate (SER) is critical for the smooth operation of the experiment.

4.1.1 FLUKA results as the motivation for the irradiation

All low-voltage power supplies will be placed in a shielded area within the experimental cave. The estimated dose values were calculated using FLUKA code[1] and are summarized in Figure 4.1) [107].

For Au ions beams with the highest available intensities (10^9 ions/s) and energies (11 AGeV), a total dose[2] of 20 mGy is expected after a month of operation in the area between 0 and 0.5 m above the ground (at the planned location of the power crates x = −600 cm, z = −600 cm) and 40 mGy between 1.5 m and 2 m above the ground (x = −600 cm, z = −600 cm).

[1] FLUKA is a fully integrated particle physics Monte Carlo simulation package.

[2] Gray is a SI unit of ionizing radiation dose, defined as the absorption of one joule of radiation energy per kilogram of matter [109].

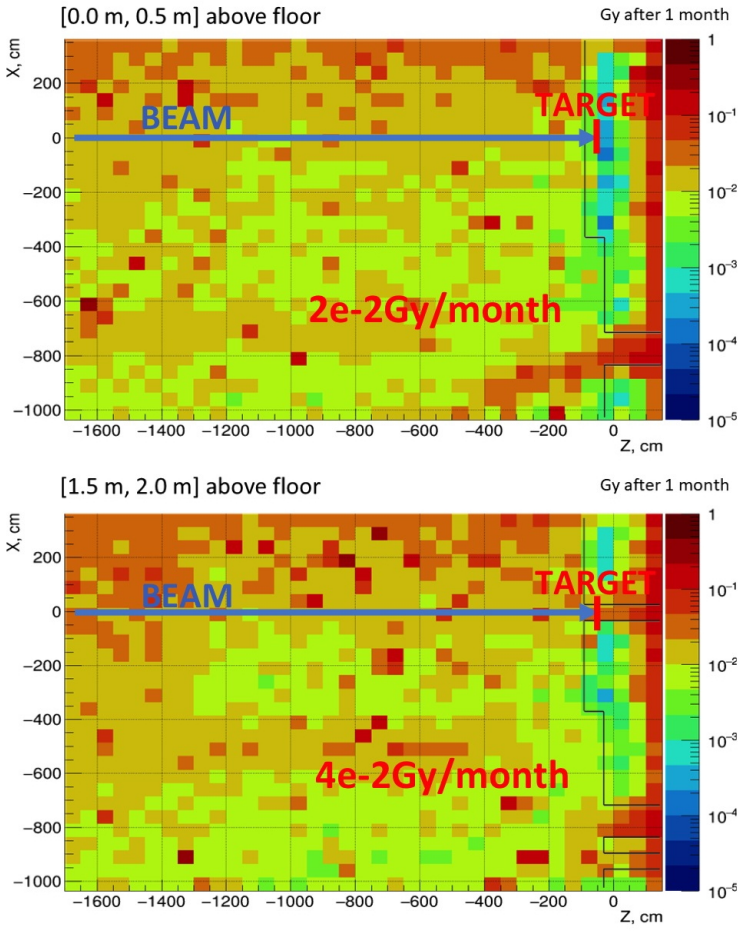

Figure 4.1: Expected dose distribution in the air in the CBM cave under the platform/-below the beam line (11 AGeV Au 10^9 ions/s on 1% Au interaction target). The first simulation depicts the radiation doses at heights between 0 and 0.5 m and the second one from 1.5 m to 2 m [108].

4.1.2 Single Event Effects in electronics

When charged particles interact with the material, they produce electron-hole pairs that deposit charge. This charge is then collected through drift and diffusion to the drain, which can cause soft errors. Although these effects are often limited to a local area, they can sometimes propagate throughout the entire sensitive electronics. Soft errors are most commonly caused by transient effects and static effects, which occur when there is a change in the content of a memory cell.

Different interaction mechanisms may cause both stochastic and deterministic effects in electronics. These effects are directly related to the integrated dose and linear energy

transfer (LET) of the incident particles [110]. LET is defined as the energy absorbed in matter per unit path length traveled by a charged particle

$$L = \frac{dE_{abs}}{dx}. \tag{4.1}$$

A variety of different elements and chemical compounds can be used in electronics, including silicon, silicon dioxide (SiO_2), or boron. The high ambient flux of particles in a particle accelerator environment usually consists of charged particles (mostly protons, and electrons), high-energy photons (gamma and X-rays), and a broad spectrum of neutrons.

Radiation-induced soft errors have become a huge concern in advanced computer chips because uncorrected, they produce a failure rate that is higher than all the other mechanisms compromising reliability combined [111]. These kinds of errors are especially important for high-energy physics and aerospace applications, as they may severely affect the reliability of electronic components. Moreover, cumulative radiation effects occur during the complete lifetime of a transistor as long as it is exposed to radiation [55].

On the other hand, neutrons do not cause direct ionization in silicon or oxygen. These neutral particles interact elastically as well as inelastically, resulting either in the creation of other nuclei and the emission of a light particle or in changes in the kinetic energies of the participants. A few neutron threshold energies for reactions with oxygen and silicon are summarized in Table 4.1. The cross-section for neutron reactions generally decreases with the energy. Moreover, neutrons can indirectly cause SEE by secondary radiation, for example, a reaction with boron which results in the emission of an α particle $^{10}B(n,\alpha)^{7}Li$ [111]–[113].

Table 4.1: Threshold energies of neutron reactions with silicon and oxygen nuclei [114].

Reaction	Neutron Threshold Energy (MeV)
Si elastic	0
Si(n,α)	2.75
Si(n,p)	4
Si(n,d)	10.5
Si(n,$n-\alpha$)	10.35
O elastic	0
O(n,α)	2.35
O(n,$n-\alpha$)	7.61
O(n,p)	10.24
O(n,d)	10.53

4.1.3 Methodology

The subject of the irradiation campaigns was a MPOD mini crate with one low voltage (WIENER [115]) and one high voltage (ISEG [116]) module. The crate CC24 controller (ISEG) offers an embedded EPICS Input Output controller, which was used to detect radiation-induced channel or module failures. All registered failure events were stored in a dedicated database.

In order to correlate the soft failure rate with the absorbed dose, two types of thermoluminescent dosimeters were used. A larger polyethylene sphere ($d = 30\,\text{cm}$) allowed measuring the neutron ambient dose, whilst the cylinder ($d = 5\,\text{cm}$, $h = 6\,\text{cm}$) measured other particles [117]. We assume that the conditions (e.g., neutron spectra) at the CBM experiment will be similar to conditions at SIS18, and at the mCBM experiment. The quality factor sets the relation between equivalent dose and absorbed dose. It converts the measured dose given in Sievert to absorbed energy in Gray. It is assumed that the factor equals 5 for the sphere in both irradiation campaigns. The dose measured with the cylinder is assumed to have a quality factor of 1.

4.1.4 Low statistics data analysis

We assume that failure events (radiation-induced soft errors) are statistically independent and are driven by purely stochastic factors. In addition, we take into account only the total dose measured by the dosimeters, thus rapid dose changes and their effect are not investigated in this contribution. In such a case, the probability of observing n events with the mean value λ is described by the Poisson distribution [118]

$$p(n|\lambda) = \frac{\lambda^n}{n!} e^{-\lambda}, \tag{4.2}$$

where n is the number of occurrences, e is Euler's number. The mean value λ is also considered to be the variance of the distribution and can be calculated as

$$\lambda = n/D_{tot}, \tag{4.3}$$

where D_{tot} reflects the total dose. The standard deviation can be calculated as

$$\sigma = \sqrt{\lambda}. \tag{4.4}$$

Considering $1/\lambda$ has a continuous distribution, and it is an average interval between the events, it can be described by the gamma distribution [118], [119]. The probability density function is

$$f(x, \alpha) = \frac{1}{\Gamma(\alpha)} \cdot x^{\alpha-1} \cdot e^{-x}, \tag{4.5}$$

for $x \geq 0$, where $\alpha > 0$ is the shape parameter, $\Gamma(\alpha)$ is the gamma function defined and $\alpha = 1/\lambda$. The standard deviation for this distribution is given as

$$\sigma = \sqrt{1/\lambda}. \tag{4.6}$$

4.1.5 Irradiation at the mCBM experiment

In order to investigate electronics operation under the realistic conditions, that low voltage modules will face during the CBM experiment, an irradiation campaign took place in the experimental cave of the mCBM experiment. The expected dose rate distribution in the mCBM cave is depicted in Figure 4.2. Different beam intensities and reaction systems (Au+Au, Au+Ni, etc.) were exercised during the experiment.

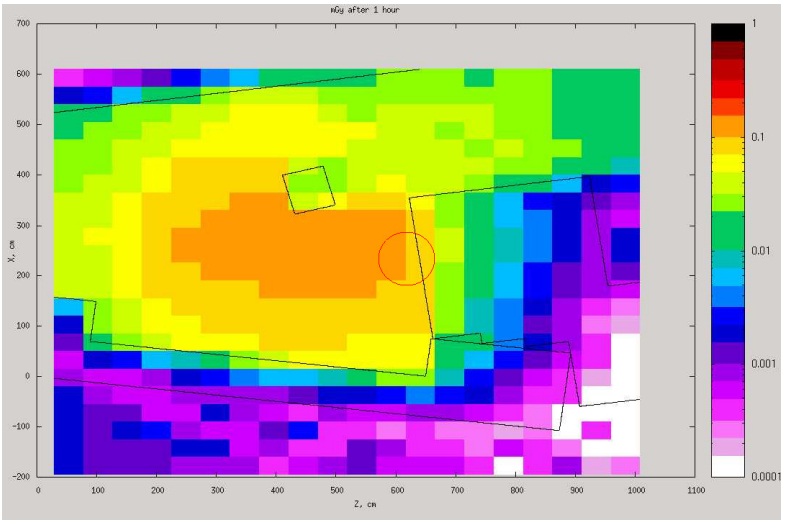

Figure 4.2: Expected dose rate distribution (mGy/hour) in the mCBM cave with 2 AGeV O ions beam of 10^7 ions/s on 4 mm Ni target. In the encircled area the dose reached about 0.1 mGy/hour [108].

To measure the dose that the crate was exposed to, four thermoluminescent dosimeters (TLD) with moderators were used (Figure 4.3). Two of these TLDs were as positioned in the background as can be seen in Figure 4.3, and they served as a reference. Two remaining dosimeters were located next to the irradiated crate. During the irradiation at the mCBM experiment, the dosimeters were read out twice, in order to evaluate the total dose received by the crate. The first value was 19.72 mGy and the second measurement was 72.31 mGy.

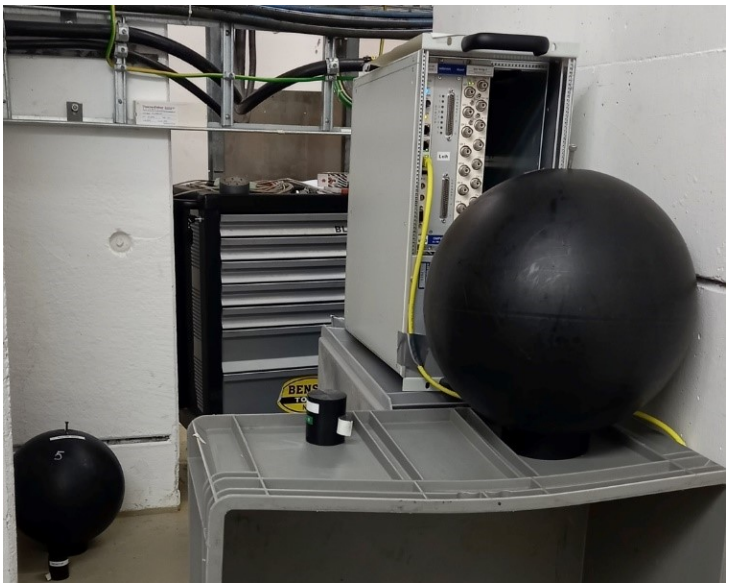

Figure 4.3: Crate irradiation setup at the mCBM experiment. The photo depicts two TLD dosimeters in the background, and two TLD dosimeters and the crate in the foreground.

A SEE in the low voltage module occurred in each part of the irradiation. In both cases, it was possible to recover the functionalities by enabling the channels again. The mean value λ is given as the ratio of failures per unit dose:

$$\lambda = \frac{2}{92\,\mathrm{mGy}} = 0.022\,\mathrm{mGy}^{-1}. \tag{4.7}$$

Considering the reciprocal of lambda, an average dose after a soft error will occur is given

$$1/\lambda = 46 \pm 7\,\mathrm{mGy}. \tag{4.8}$$

Nevertheless, during the first irradiation period, only 2 soft errors were detected, thus the probability of an event per unit dose is almost 0 (see Figure 4.4). In order to increase the statistics a second irradiation campaign took place at SIS18 septum.

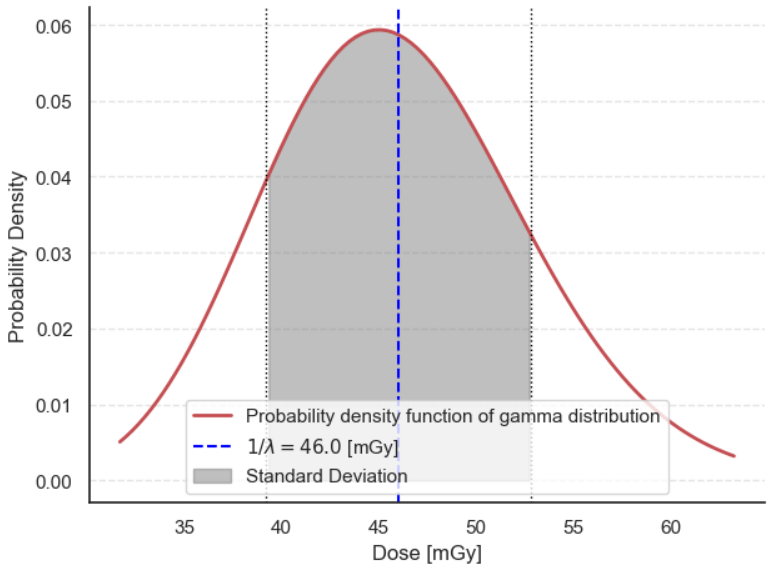

Figure 4.4: The probability density distribution of an event at different dose levels. The reciprocal of lambda denotes the average dose at which an event occurs.

4.1.6 Irradiation at the SIS18 septum

4.1.6.1 Setup description

The setup at the SIS18 septum consisted of two TLD dosimeters (for neutrons and for other particles). Furthermore, the total doses from TLDs were supplemented with readouts from two active dosimeters placed behind the wall (see Figure 4.5). These dosimeters were used to measure the dose rate to assess its influence on the SEE.

Wendi-2 is a precise wide-energy neutron dosimeter [120] that was used to determine the neutron dose rate in the so-called Kickerraum (Figure 4.5). Due to the shielding of the wall, the gamma probe measured mostly background radiation. The TLD dosimeters were placed next to the crate. To calculate the momentary neutron dose next to the crate, a ratio of total doses from both measurement places was used.

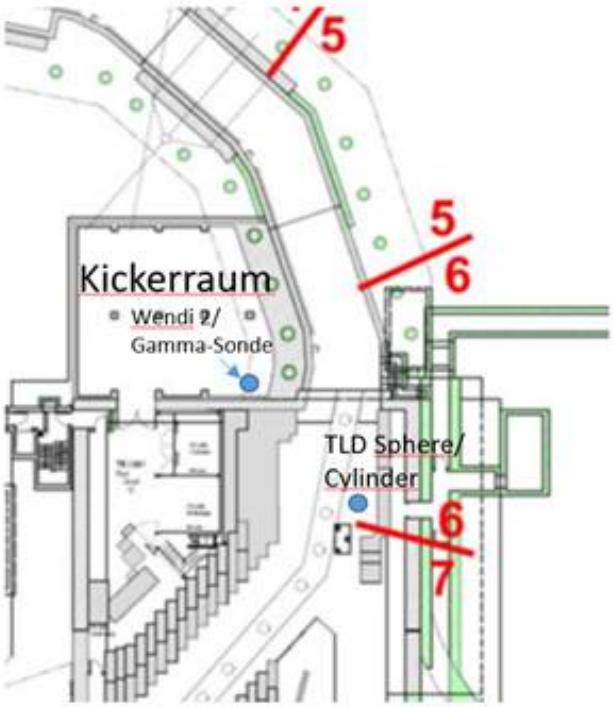

Figure 4.5: Location of the dosimeters and crate at the SIS18. The so-called Kickerraum contained WENDI-2 and Gamma probe, whereas two TLD dosimeters were placed next to the power crate - depicted with a blue dot between segments 6 and 7.

4.1.6.2 Results

During the irradiation period, readings from the dosimeters reached 106.1 mSv and 27.7 mSv for neutrons and other particles respectively. Using assumed quality factors, the ambient dose was converted to the absorbed dose values. Hence, we get in total 49±2 mGy, taking into account 5% standard uncertainty of the TLD dosimeters. During the test, 11 radiation-induced soft failures were identified in the low-voltage module. Therefore, it is possible to estimate an average dose after which a low voltage failure might take place.

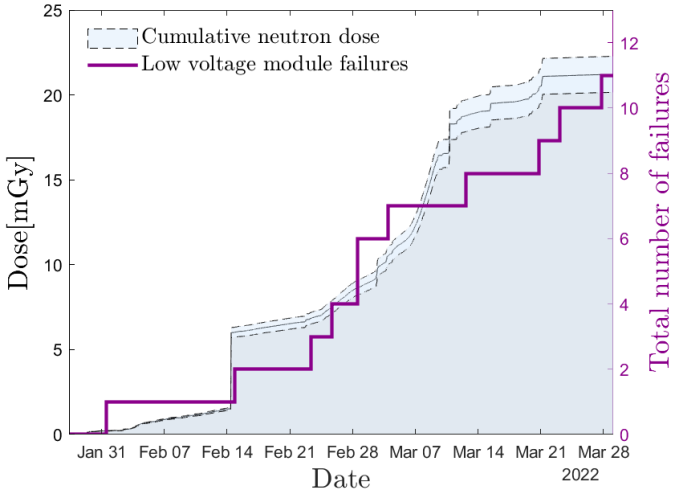

Figure 4.6: Cumulative neutron dose and SEE in the low voltage module.

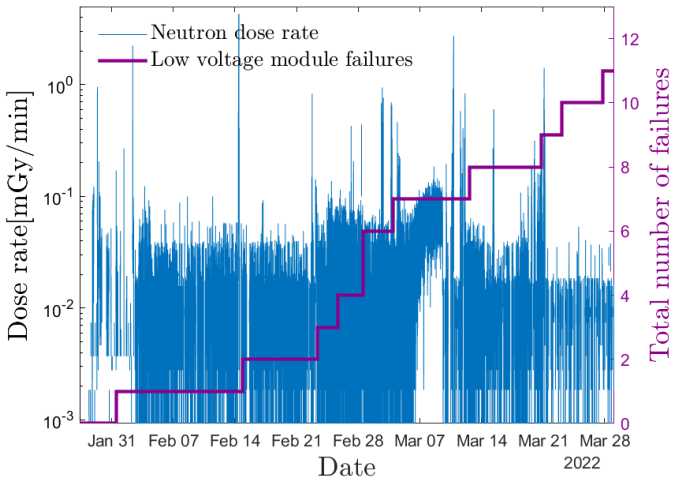

Figure 4.7: Neutron dose rate and failures of the low voltage module.

Figure 4.6 shows how the number of failures cumulates with the total neutron dose, where the longer periods without failure indicate a break in SIS18 operation. Similarly, Figure 4.7 depicts the dose rate and related SEE. For the 11 low voltage module failures, the rate equals to

$$\lambda = \frac{11}{49\,\mathrm{mGy}} = 0.22\,\mathrm{mGy}^{-1}. \tag{4.9}$$

what indicates that the probability of an event after a mGy is low. On average a soft error will occur after (see Figure 4.8)

$$\mathrm{D_{LV}} = 4.45 \pm 2.11\,\mathrm{mGy}. \tag{4.10}$$

After the occurrence of a soft error in the low-voltage module, it was always possible to turn the channels on again.

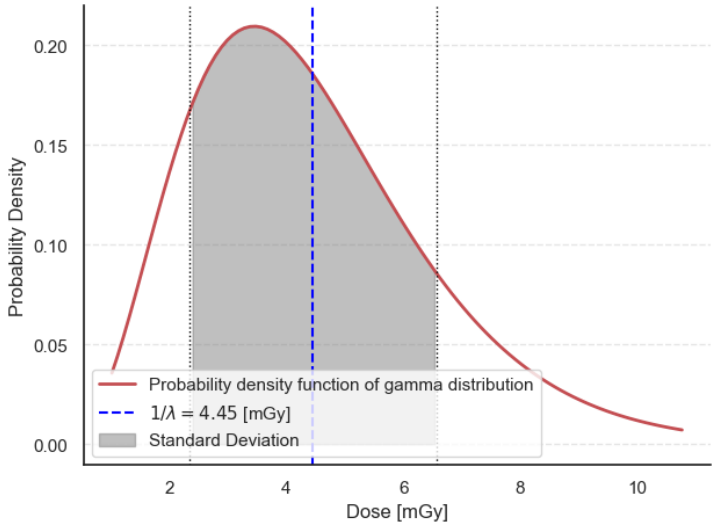

Figure 4.8: The probability density distribution of an event at different dose levels for the Gamma distribution.

In the case of the high voltage module, the SEE do not result in a module switch off, but in disabling channels. In two cases, all channels were switched off, which is counted as if 16 channels were turned off at the same time. Figure 4.9 and 4.10 show the channels failure rate with the increasing cumulative dose.

For the high voltage module, the total number of channels that switched off due to the irradiation is 56. Following a similar procedure as for the previous calculation

$$\lambda = \frac{56}{49} = 1.14 \pm 1.07\,\mathrm{mGy}^{-1}, \tag{4.11}$$

what indicates that more than one soft error can be expected after mGy. If the high voltage module was situated in the same place as the low voltage, a channel switch-off could happen after $0.88\,\mathrm{mGy}$.

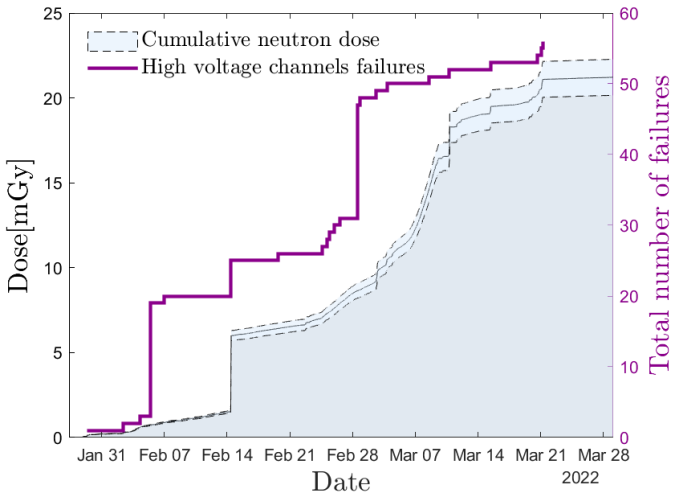

Figure 4.9: Cumulative neutron dose and failures of the high voltage module channels.

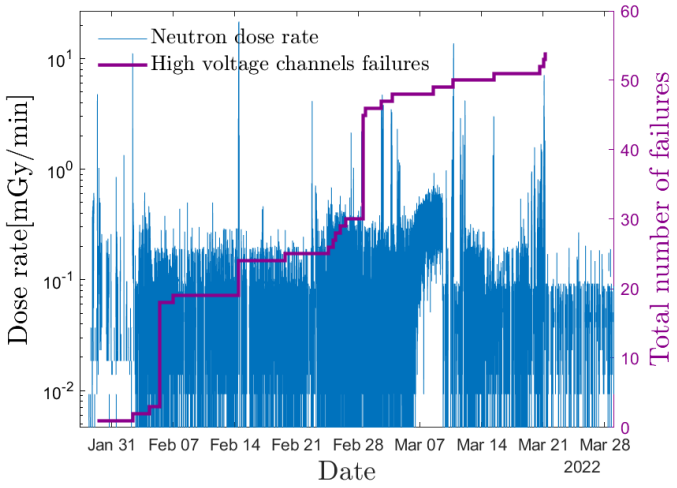

Figure 4.10: Neutron dose rate and failures of the high voltage module channels.

4.1.7 Conclusions

The control framework introduced in the previous chapter served as the data acquisition system for the irradiation of the MPOD crate and two modules. Prepared graphical user interfaces together with archiver, database allowed to track the failure events and compare them later on with the registered dose. Obtained results have a direct influence on the experiment operation.

The FEE of the STS will be powered by about 140 low-voltage modules. Given that in the worst case, some of those modules will be exposed to about 40 mGy/month, the measurement indicates that about 9 SEE per month per module will occur. In practice,

it means that every FEB will need to withstand 9 power cycles at low temperatures per month. Assuming operation of 2 months per year and a total projected operating time of 10 years, electronics must withstand at least 180 power cycles at low temperatures of about −20 °C.

4.1.8 Potential risk to STS operation

If every low voltage module turns off 9 times per month during the operation, the potential consequences need to be carefully assessed. By planning the powering scheme for the STS, the system can be prepared for the foreseen power interruptions. In the worst-case scenario, considering 140 low voltage modules, about 1260 soft errors a month, which corresponds to 1.75 errors per hour. For the 16 ROBs connected to one low voltage module, a temporary shutdown of up to 140 FEBs or 70 modules per hour is expected. The duration of the shutdown is also critical for the operation. A soft error in the low voltage module can most likely be recovered within seconds, preventing extensive thermal stress in the FEE. On the other hand, for the testing scenarios, it is necessary to consider that the electronics experience full thermal stress, in case fast power recovery is not possible. Additionally, power cycles of the FEE in low temperatures may result in thermally induced mechanical stresses on the components of the Printed Circuit Boards (PCBs). Hence, the effects of thermal cycling of the FEE should be carefully studied, in order to evaluate the limits in the performance of the electronics (see section 4.3). Nevertheless, there are also a few methods to decrease the potential risk, both from the radiation-induced damage and potential problems due to thermal shock:

- Additional radiation shielding material around the power supplies
- Powering scheme - for example connecting ROBs and corresponding FEBs to the same low voltage module
- Proper software/hardware mechanisms to switch on the channels in a matter of seconds

4.2 Monitoring of parameters from the STS electronics

FEE monitoring plays a crucial role in the detector operation, but also during the testing phase. Internal parameters of the ASICs in the ROB or FEB deliver information about the stability and onset of failure.

The first application of the introduced control framework was to read out several parameters from different readout chains (see section 2.4 for a detailed explanation of different readout chains). The ROB and DPB based readout chains were used to evaluate the possibility of interfacing values from the DAQ chain to the EPICS-based system. The main purpose was to monitor the stability of the electronics throughout different tests, e.g., during the thermal cycling of FEE. A similar interface was also developed for the GBTxEMU readout chain.

Two FEBs – 16 STS-XYTERs were used to evaluate the performance of the interface and the ASICs. It constituted in total 112 process variables, which makes it a relatively small setup. Those values were then stored in a database and were available from Phoebus for further analysis and visualization.

To get the values from the ASICs a soft IOC with a pyEPICS [121] interface was used. The monitored values included the registers and corresponding values available from GBT SCA ASIC [122] and three GBTX chips:

- GBT SCA – RSSI (Received Single Strength Indicator), input voltage V_{in}, 1.5 V DC/DC converter output voltage V_{out}, 2.5 V DC/DC converter output voltage V_{out} (see figure 4.11), two temperature sensors
- GBTX ASIC - FEC (Forward Error Correction) counts

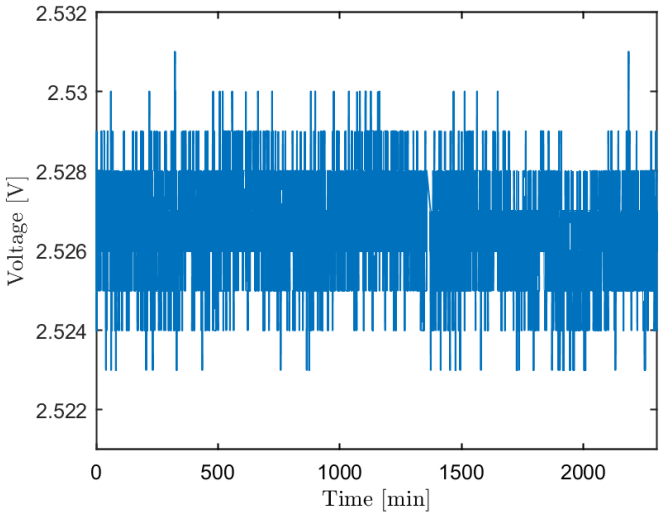

Figure 4.11: V_{out} output voltage from one of the DC/DC converters in the ROB.

The STS-XYTER provides the following information - almost full counter, event missed counter, single event upset counter, the status register, and ADC values: VDDM, CSA bias, temperature.

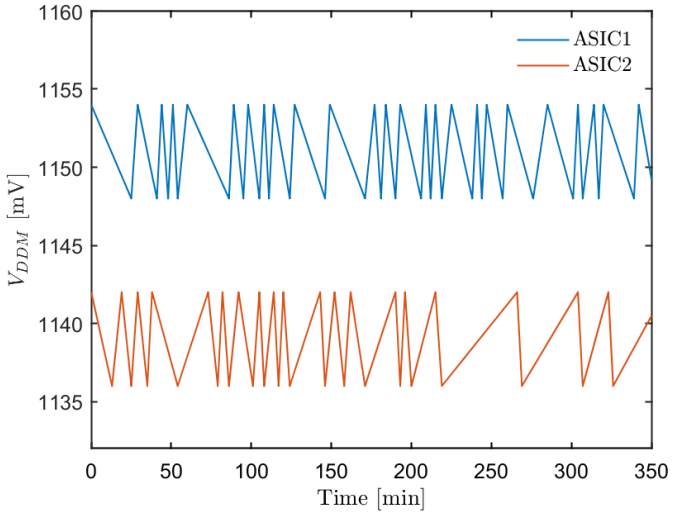

Figure 4.12: V_{ddm} readouts from the diagnostic circuits of two ASICs.

The fluctuations in Figure 4.12 correspond to the Least Significant Bit of the ADC. It's usually defined as

$$LSB = \frac{V_{REF}}{2^N}. \tag{4.12}$$

where the V_{REF} is the reference voltage and N is the number of ADC bits. The interface from the DAQ chain to the EPICS-based system was developed in order to monitor the performance of the FEE during numerous tests including the thermal cycling of the detector electronics and mSTS setup.

4.3 Thermal cycling of detector electronics

Operating temperatures inside the STS enclosure are dictated by the total non-ionizing dose and noise levels. The temperature conditions in the STS could have repercussions on the functioning of detector electronics. Nevertheless, for the first few years of operation, the ambient temperatures will be higher than −10 °C. Operating scenarios of the STS together with other constraints related to, for example, the soft errors rate in the low voltage powering of the FEE, define the testing procedures for all the electronics which will experience thermally induced mechanical stresses.

One of the elements of the detector module which can experience significant mechanical stresses is the FEB. During the commissioning and operation, the FEBs will experience many power cycles. As reported in the [123], the power cycling of the FEBs at room temperature of about 20 °C run flawlessly, not identifying any issues with the boards. Nevertheless, the testing did not reproduce the STS operational conditions.

To evaluate the behavior of the board in realistic conditions, a thermal cycling setup was envisioned. Thermal cycling testing is usually performed in order to determine the ability of different components and solder interconnects to resist extreme temperature changes. Permanent changes to the electrical or physical features may compromise the detector modules performance.

For the control and monitoring of devices, as well as for the processing of data the previously developed control framework was introduced. Implementation of the EPICS-based framework played a crucial role, as it enabled live monitoring of many parameters during the tests.

Firstly, the operation scenarios of the STS will be discussed, as it's necessary to have a profound understanding of the temperatures that the electronics have to withstand. Subsequently, the cycling and the results will be thoroughly discussed.

4.3.1 Nominal operation scenario of the STS

In the nominal operation scenario at the end of the STS lifetime, the FEBs are operated at the nominal power ($\approx 8\ W$), and any excess heat is evacuated by cooling liquid (NOVEC 649) flowing through the FEB cooling plate at −40 °C. Figure 4.13 and 4.14, depict thermal simulations of the cooling plate, FEB box, and the FEB for the nominal operation scenario.

During periods in which the temperature will change due to transitions between detector states, the electronics will experience thermal stresses, which will partially occur with the electronics switched on. The cases discussed relate to the worst-case scenarios, in which the temperature differences are the highest.

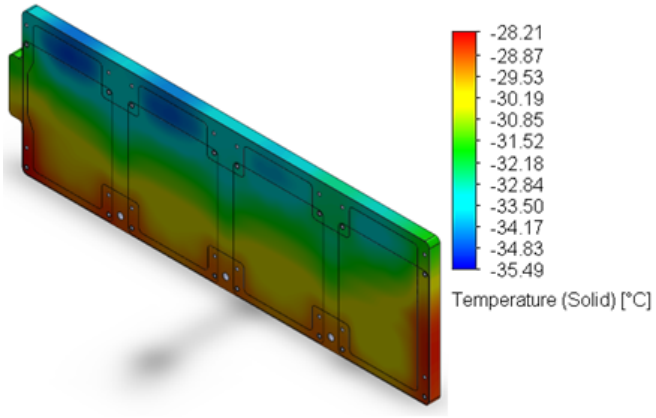

Figure 4.13: Temperature distribution on the cooling plate for the nominal operation scenario [64].

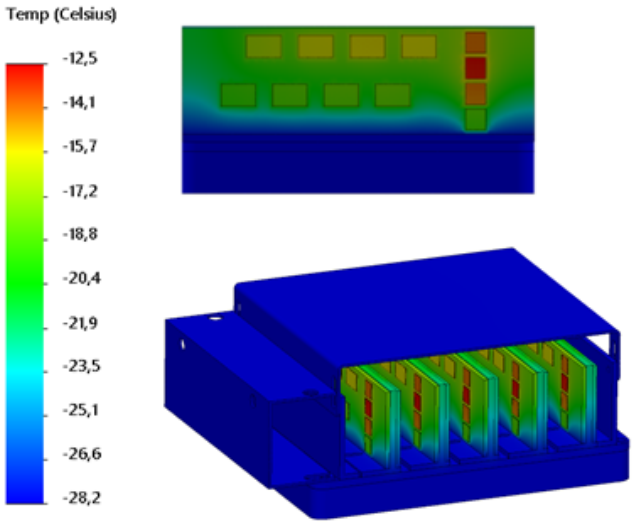

Figure 4.14: Temperature distribution in the FEB box containing 10 FEBs (bottom of the figure) and on the FEB for the nominal operation scenario (top of the figure) [64].

During the active, nominal phase of operation, the temperature change of the electronics could be $\Delta T \approx 20\,°C$ (see Figure 4.15). On the other hand, simulations from Figure 4.14 indicate the minimum temperature the electronics will reach during the operation. This operation mode is summarized in Figure 4.15. The difference is associated with a slow increase of the coolant temperature from $-40\,°C$ to $-20\,°C$. After

switching off the electronics, the temperature reaches the temperature of the cooling plate. The change will be $\Delta T \approx 20\,°C$ (from e.g., $0\,°C$ to $-20\,°C$). These temperatures provide an indication of minimum and maximum thermal cycling set points.

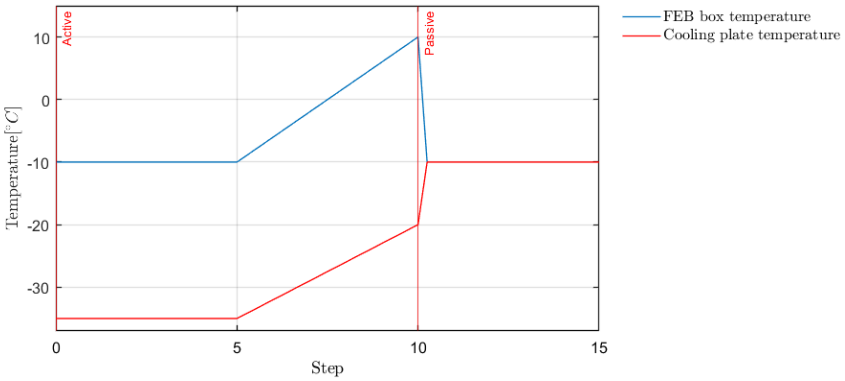

Figure 4.15: An example of STS state transition from operation to safe state - comparison of temperatures of a FEB box and cooling liquid temperature. A step could be defined as a generic time period.

4.3.2 Partial shutdown scenario of the STS

At any given point during operation, the operator may need to power cycle a FEB(s). In this scenario, the temperature of a given FEB may change drastically due to the temporary loss of power. The amount of thermally induced mechanical stress depends on reboot and configuration time. Besides, in case of a radiation-induced soft error in the power supply, the downtime of a FEB may be difficult to predict. If the soft error is instantly recoverable, the FEB will be powered on in seconds after switching off, limiting a deteriorating effect of large temperature changes ΔT.

Figure 4.16 depicts the scenario in which only 5 out of 10 FEBs are on, which results in effectively lower temperatures in comparison to the nominal scenario. Nevertheless, the ΔT remains the same as in the nominal operation scenario. During the operation, this scenario will probably last for a short time (range of seconds), and the temperature of the rebooted FEB will not reach as low temperatures as depicted in the previous simulations.

4.3.3 Loss of power scenario of the STS

The last considered scenario is the so-called loss of power scenario. Out of the three introduced scenarios, it is the least probable one, but it also leads to significant data loss, as 10 FEBs would stop sending data. Such a scenario could happen if all the connected low-voltage channels switch off, e.g., due to radiation. In this case, the FEBs

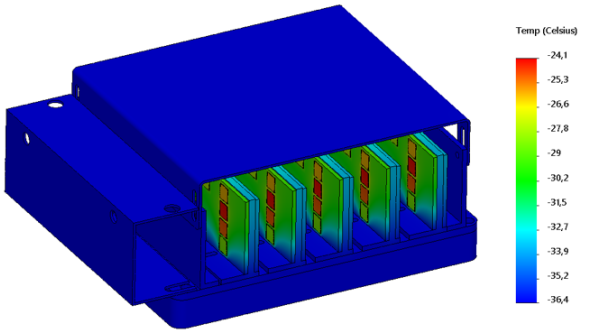

Figure 4.16: Temperature distribution for the partially unpowered FEB [64]. Each cooling shelf inside the FEB box has two glued boards, and one of them is powered.

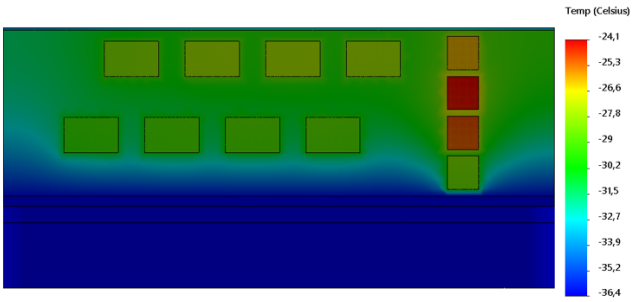

Figure 4.17: Temperature distribution of a FEB for the partial shutdown scenario [64].

would reach the temperature of the cooling block ($T \approx -40\,°\mathrm{C}$) if the powering was not turned on within seconds.

4.3.4 Influence of the coefficient of thermal expansion on the PCB performance

The coefficient of thermal expansion (CTE) is an important property of materials that affects relative movement between PCB components. CTE should be a concern when it comes to PCBs, as out-of-plane CTE could cause cracking and delamination, while in-plane CTE may cause for example shear failures in solder joints [124]. The STS FEB is equipped with many components which could be the reason for malfunctions at low temperatures, making analysis of potential causes a complex task. These components can be seen in Figure 4.19.

Both the LDO regulators and STS-XYTERs are covered with high viscosity glues

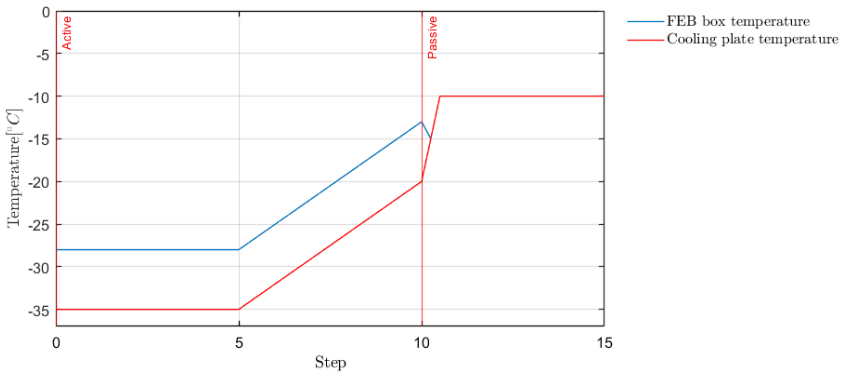

Figure 4.18: An example of STS state transition from operation to safe state - comparison of temperatures of a FEB box and cooling liquid temperature. Step represents a generic time period, indicating the rate of changes in the detector.

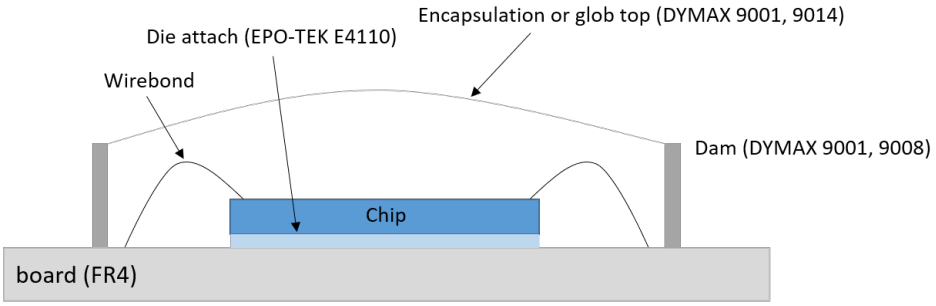

Figure 4.19: Schematics of the glob-topped device with the materials used for the thermal cycling.

known as glob top[3]. Apart from CTE, the performance of the glob top material depends on many other factors:

- Adhesion to the substrates
- Part geometry (including the mass of the components in contact)
- Temperature extremes
- Number of cycles, and transition times

The most common phenomena which cause damage to the glob-topped device are:

- Wire-bond failure

[3] A protective epoxy-based material for microelectronics.

- Failure of the chip to board or substrate joint
- Damage to protective chip passivization layer
- Chip cracking
- Metallization pattern shift
- Development of voids or notches in metallization tracks

According to the data on electronics failures analyzed by the U.S. Air Force over about 20 years, it was shown that 50% of these failures are related to connectors, 30% to interconnects, and 20% to component parts. Hardware failures may occur due to handling, vibrations, or stress of different origins (including thermal stress). About 55% of the electronics failures are due to high temperatures and temperature cycling, 20% of the failures are related to vibration and shock, and 20% are due to humidity [125].

To protect the STS microelectronics, DYMAX 9001 was the glob top choice for the FEBs, and it was then replaced by its successor DYMAX 9014. The LDO regulators and ASICs are made of silicon. The linear CTE of glob top materials (DYMAX 9001, DYMAX 9014, DYMAX 9008) and conductive glue (EPO-TEK E4110) is by an order of magnitude higher than the coefficient for the PCBs and silicon. Additionally, a volume expansion influences the relative position of different components during thermal cycling.

Table 4.2: Coefficient of thermal expansion of different materials below the glass transition temperature.

Material	CTE α_2 [µm/m/°C]]
DYMAX 9001-E-V3.5 [126]	180
DYMAX 9014 [127]	192
DYMAX 9008 [128]	230
EPO-TEK E4110 [129]	150
FR4 (PCB material) [130]	15
Silicon [131]	2.6

Three main components which need to be analyzed during the testing are the glues (glob top and conductive glue), bonds, and microelectronics (LDO regulator and STS-XYTER). From the thermal cycling point of view, power dissipation is one of the key differences between the DC linear voltage regulator and the front-end chip. Figure 4.20 depicts the temperature distribution of a powered board. The board was screwed to the cooling plate, which was at 20 °C.

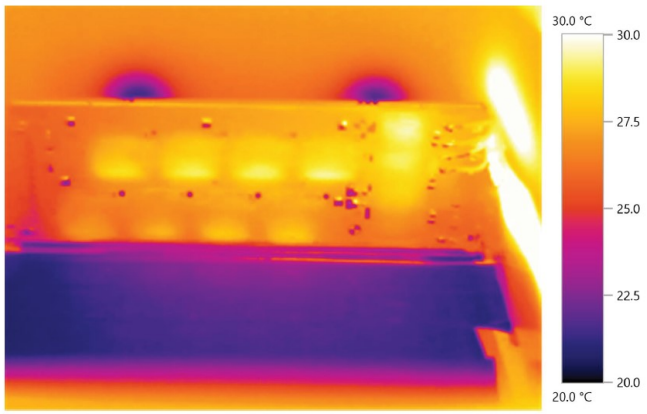

Figure 4.20: Temperature of the FEB components measured with a thermal camera for the low power consumption scenario, [132]. The LDO (on the right side of the picture) appear to be hotter than STS-XYTER chips.

4.3.5 Experimental setup for thermal cycling of STS electronics

In order to investigate the effect of thermal cycles of the FEBs, a setup consisting of FEBs, a readout board, Lauda chiller, a climatic chamber, temperature sensors, and humidity sensors was introduced. A detailed overview of the setup is depicted in Figure 4.21. The software part features the Control System Studio (Phoebus) for monitoring, accessing the database (Redis DB), and monitoring the PVs. Moreover, all values are saved with archiver appliance. The second node features a LabView-based interface for reading out additional humidity sensors. This node was later depreciated, and relative humidity readouts were taken from the built-in Relative Humidity (RH) sensor inside the climatic chamber.

The main objective was thermal cycling of the FEBs, which consists of 4 LDO regulators (two 1.2 V LDO and two 1.8 V LDO regulators) and 8 ASICs. The diagnostic circuit of the STS-XYTER helped to identify PCB related malfunctions. In order to read the temperatures, VDDM, and CSA bias values from the chip, a dedicated soft IOC[4] was deployed. To acquire the previously mentioned values, the pyEPICS library [121] was used, and the GBTxEMU-based readout chain (see subsection 2.4.3) was adjusted to publish the values via channel access protocol.

[4]Purely software-based IOC, not connected to any hardware.

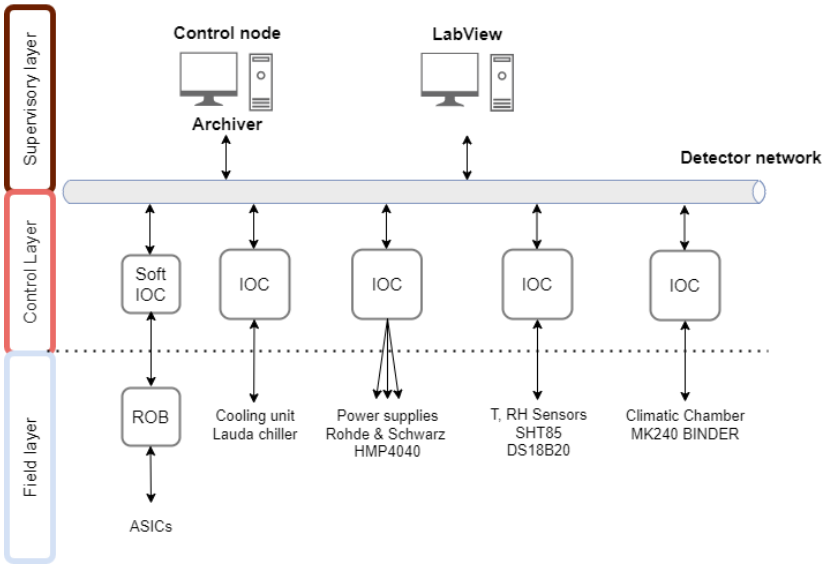

Figure 4.21: Schematics of the thermal cycling setup. The readout of relative humidity and temperature sensor is realized through Single Board Microcontrollers (SBM) and Raspberry PI. Python interface was developed for both readout chains (ROB and GBTxEMU based).

Apart from the ASIC-specific values, are other parameters taken into consideration which are as follows:

- Currents and voltages supplied to the 1.2 V and 1.8 V LDO regulators on the FEB.
- Temperature changes on the T-shelf (as seen in Figure 4.23), which are read-out by a Single Board Microcontroller (SBM).
- Humidity and temperature in the climatic chamber (Sensiron SHT85 sensors plus built-in sensors).
- Set point temperature of the Kryo 51 coolant (used as an alternative for NOVEC) [133].

There are different glob-top materials that match the STS requirements. To get a better understanding of their performance, FEBs with different glob tops were assembled as shown in Figures 7 and 8. Moreover, to understand the impact of the glob top material, a board without glob top on LDOs regulators was assembled. In total, four different FEB flavors can be distinguished:

- With DYMAX 9001 as the glob top (see Figure 4.22)
- With DYMAX 9014 as the glob top

- With DYMAX 9001 as the fill and DYMAX 9008 as the dam [5] (see Figure 4.23)
- Without glob top and ASICs (see Figure 4.22)

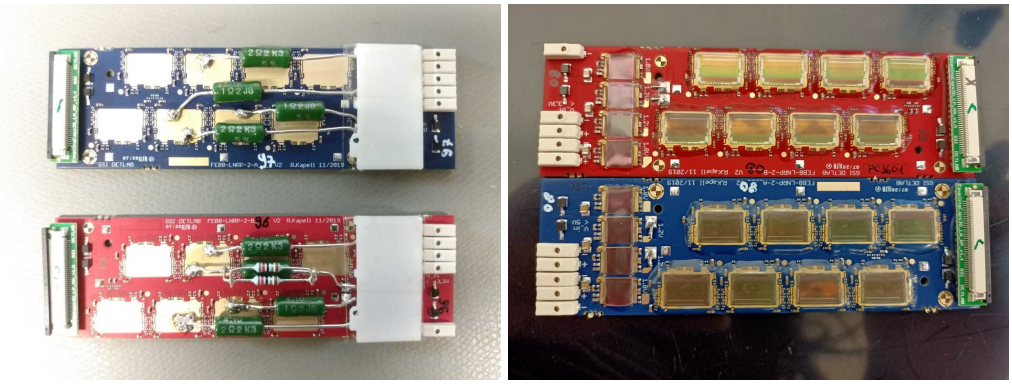

Figure 4.22: The left picture depicts two FEBs (version A and B) with the LDO regulators covered with 3D-printed protection cap and without glob top. These two boards feature resistors simulating the power consumption of the STS-XYTERs. The right picture depicts two fully assembled FEBs with STS-XYTER version 2.1 and DYMAX 9001 as the glob top.

To prepare for the thermal cycling, the assembled boards (type A and B) were mounted on a cooling shelf (initially with thermal pads, later by gluing it to the T-shelf's surface) and then eventually placed on a cooling plate in the climatic chamber (see Figure 4.23). In order to reproduce similar conditions as in the STS (coolant temperature at −40 °C) KRYO 51 coolant was used instead of the NOVEC 649 liquid. Additionally, the chamber temperature was always kept below the temperature of the cooling plate to avoid icing. During the cycling, the voltage drop at the LDO regulators was the same 0.6 V for all the boards.

Figure 4.23: A FEB glued to the T-shelf, with 3 DS18B20 temperature sensors installed on the T-shelf (left) and two FEBs mounted on a T-shelf with thermal pads inside a climatic chamber (right).

[5] Dam and fill is a technique for properly covering wire bonded die. It is a two-step method in which a dam is dispensed around the top of the component first, followed by filling the center.

4.3.6 Testing procedure

The FEBs, Readout Boards (ROBs), and Power Boards (POBs) are going to be cooled, and they will experience thermal stress on the components. According to the previously introduced operation scenarios, these boards need to withstand:

- Without the powering $\Delta T \approx 20\,°\mathrm{C}$
- With powering $\Delta T \approx 20\,°\mathrm{C}$
- More than 180 cold startups, as indicated in section 4.1.7

To find the operational limits of the boards and reproduce the operation scenarios the testing was divided into three stages: passive cycling, active cycling, and power cycles down to $-40\,°\mathrm{C}$ (so-called cold startup). The transition time between the extreme temperatures (for passive and active cycling) is not manually regulated and is solely determined by the power of the Lauda chiller and the climatic chamber.

The main object of the tests was the FEBs and its sensitivity to the thermally induced mechanical stresses. In the two main sets of measurements so far, in total 12 FEBs in different configurations were tested. After each round of thermal cycling (usually 50 cycles), the boards were inspected optically under the microscope for any signs of deterioration or visible changes. On the other hand, during the cycling with powering and low-temperature power cycling, the STS-XYTERs were extensively tested. The ASICs test included configuration of the chip, changing CSA values to trigger different current consumption, but also ID consistency check, write/read registers test, and internal pulses. By performing the tests, it is possible to evaluate the performance of the board and estimate the influence of thermal cycling.

4.3.6.1 Passive cycling

Passive cycling refers to a process of changing the temperature of a tested object in a defined range (e.g., from $-20\,°\mathrm{C}$ to $-10\,°\mathrm{C}$) without powering. This way the stress on the board and its components is lower. Passive cycling was performed in a series of 50 repetitions between optical and electrical inspections. During this part, the following temperature differences were tested:

- Set A - 8 FEBs (3 FEBs type A, 3 FEBs type B and 2 FEBs without glob top and ASICs) were tested in the realistic operating scenarios of the STS [$-20\,°\mathrm{C}$, $-10\,°\mathrm{C}$], [$-30\,°\mathrm{C}$, $-10\,°\mathrm{C}$], [$-40\,°\mathrm{C}$, $-10\,°\mathrm{C}$].
- Set B 2 out of 4 FEBs (1 out of 2 FEBs A and 1 out of 2 FEBs B) were tested more extensively by increasing ΔT - [$-20\,°\mathrm{C}$, $20\,°\mathrm{C}$].

The FEBs, regardless of the type (A or B), are treated equally from the mechanical point of view. The components and the way the boards are assembled are the same.

The characteristic of passive cycling was as follows:

- Set B was tested without current trip conditions and for set A trip current was set to 3.1 A.
- To prevent the occurrence of condensation or icing on the electronics, the Lauda chiller was deliberately set to maintain a temperature that was a few degrees higher than the ambient chamber temperature. This precautionary measure was taken to mitigate the risk of moisture condensing on the electronics and causing potential damage.
- The periods at the maximum and minimum temperature were always the same and equaled 20 minutes.

No performance deterioration was observed during the passive cycling, which is most likely related to the fact that the boards were previously unused.

4.3.6.2 Active cycling

Active cycling refers to cycling with the electronics switched on at all times. It was performed in a series of 50 repetitions, but due to the fact that the FEBs were powered, all the boards and STS-XYTERs were continuously tested, and the current consumed varied by around 1 A at most. The boards underwent the followings cycles:

- Set A - 8 FEBs - [−10 °C, 20 °C] and [−40 °C, −10 °C]
- Set B - 4 FEBs (2 FEBs A and 2 FEBs B) ΔT - [−20 °C, 20 °C], [−30 °C, 20 °C], [−40 °C, 20 °C]

A detailed view of a few cycles is presented in Figure 4.24. Figure depicts active cycling from −30 °C to 20 °C. Similarly to passive cycling, the temperature of the cooling block is kept a few degrees (2 – 3 °C) above the ambient temperature, although the effective temperature of the active components (STS-XYTERs and LDO regulators) is much higher. The two bottom graphs show how cycling affects the STS-XYTERs diagnostic circuit. The VDDM value varies from about 1200 mV up to 1240 mV, but it does not have any effect on the performance of the chip, as the operating range could vary as much as 100 mV. The measured values of the VDDM may also vary across the FEB, which can be seen in Figure 4.25. These differences emphasize the need to properly calibrate the ADC of the diagnostic circuit, as the measured values should not be too far from the nominal 1.2 V[6] supplied by the 1.2 V LDO regulator.

Moreover, during the active cycling, 3 DS18B20 sensors were glued on the T-shelf (see section 4.3.5. The sensors were glued to the T-shelf, in order to determine how the temperature changes when the final thermal interfaces are used (glue between the FEB and T-shelf and carbon composite between the T-shelf and cooling block). Figure 4.26 depicts the difference between the temperatures measured by different sensors during cycling.

[6] Considering that the voltage drop across the 1.2 V line connecting the subsequent chips is negligible.

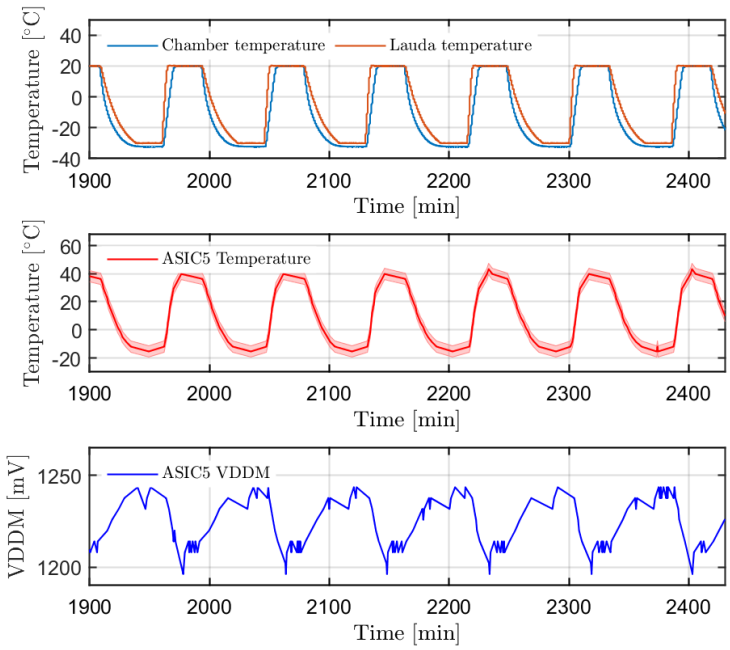

Figure 4.24: A detailed view on the performed active cycling. The top figure depicts the temperature of the chamber temperature and the set point of the Lauda chiller. Two lower figures show how the readout of temperature and VDDM from a chosen STS-XYTER depends on the cycling temperature.

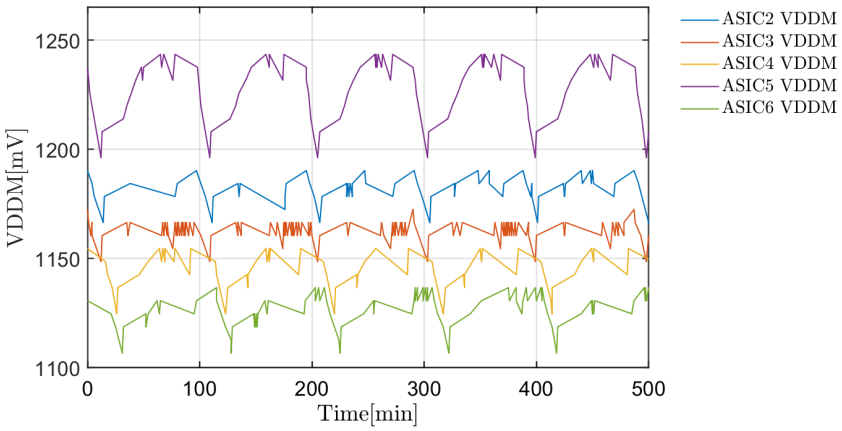

Figure 4.25: VDDM values comparison for different chips in the board. The tests in the chips were performed sequentially, therefore time shift between maxima can be seen.

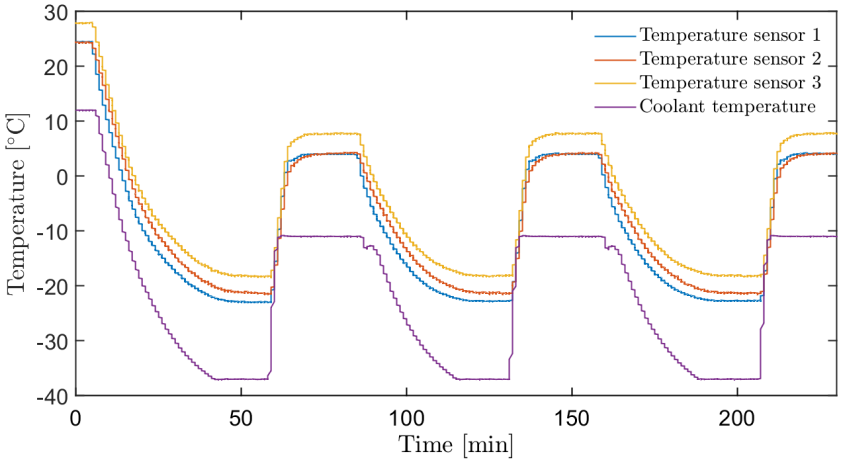

Figure 4.26: Temperature evolution of the T-shelf during the active cycling. The DS18B20 [134] sensor has an uncertainty of 0.5 °C.

Temperature sensor 1 was placed above the LDO regulators, therefore the measured values are always higher than for the two other sensors. Temperature sensor 2 was placed on top of the T-shelf but on the other side of the board. Sensor 3 was placed on the side of the T-shelf next to the powering services, its temperature is significantly lower, which is clearly visible at −38 °C, as it is placed closer to the heat exchanger (the cooling plate). This behavior was also confirmed by the simulations - see Figure 4.14 and Figure 4.17.

4.3.6.3 Low-temperature power cycling

Contrary to the two introduced thermal cycling methods, power cycling is performed at a stable temperature. After switching the power on at low temperature, the FEBs functionalities are tested and the power supply output is switched off. This process is then repeated a few hundred times.

Power cycling at low temperatures is considered one of the riskiest events that may cause a board to fail. As identified during the irradiation of the power supplies, we should expect at least 180 radiation-induced soft errors in the low-voltage modules. Radiation-induced phenomena (latch-up in the chips, and soft errors in the powering units) limit the lifetime of the electronics and could cause the boards to fail over time. FEBs will also be power cycled during testing, commissioning, and operation of the detector, increasing the total number of power cycles up to two/three times. The previously introduced FEBs underwent the following power cycling in low temperatures:

- Set A - 4 FEBs - 200 cycles at $T = -30\,°C$, 4 other FEBs (including the one without chips) 300 cycles at $T = -30\,°C$
- Set B - 2 FEBs - 50 cycles at $T = -20\,°C$, 2 other FEBs 50 cycles at $T = -30\,°C$

Figure 4.27 shows how the current drawn by the 1.2 V LDO regulators and 1.8 V LDO regulators changes in the course of different tests performed in the STS-XYTERs. The highest current values (for the 1.2 V LDO regulator) are reached during write/read tests of the registers. The changes of the 1.2 V LDO regulator current are related to the changes of the CSA values during testing. During one run of the testing script, the CSA changes from 5 to 31 (the most probable range for the chip during STS operation).

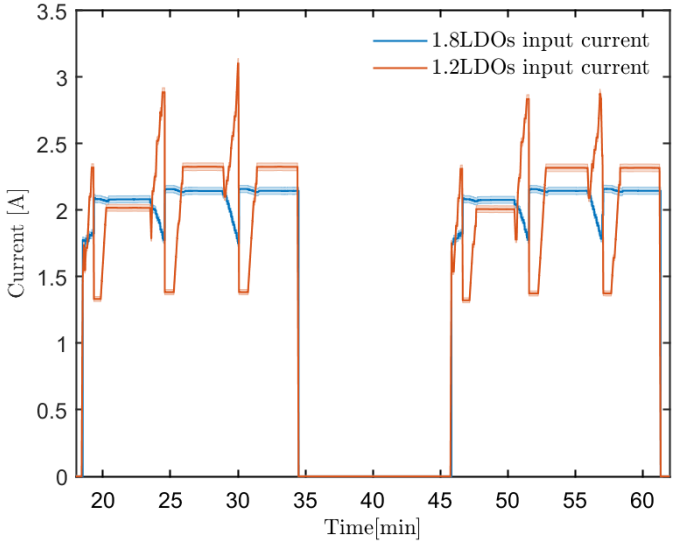

Figure 4.27: Cold startup of one of the FEB: current consumed by the 1.8 V and 1.2 V LDO regulators during the test procedure. During the period, in which the power is on, each chip undergoes 3 testing cycles.

4.3.7 Results and onset of failure analysis

Already during preliminary thermal cycling activities (not discussed in this thesis), it was determined that the LDOs are more prone to fail than the STS-XYTERs. Therefore, the main effort was put to gain statistics by testing multiple boards and to identify the onset of a potential LDO regulator-related failure. To get a better understanding of the conditions leading to failures, the two sets (A and B) of measurements were compared.

In the case of set A, which featured 8 FEBs: 4 FEBs with DYMAX 9001, 2 FEBs with DYMAX 9008 as the DAM and 9001 as the fill, and 2 FEBs without STS-XYTERs and globtop over the LDO regulators, during the passive cycling and active cycling no failure was observed. No deterioration was observed under the microscope. First failures were detected during the power cycling at $T = -30\,°C$, as summarized in Table 4.3.

The onset of the LDO failure can be seen in Figure 4.28. At about 500 min the 1.2 V LDO regulator input current started dropping, indicating increasing resistance in the circuit. As depicted in Figure 4.28 once the temperature reached 20 °C the current consumption was again nominal. After about 3000 min, this effect turned out to be

Table 4.3: Detailed description of the LDO failure with regard to the type and number of cycles.

Globtop	Failure Appearance	Remarks
DYMAX Dam 9008, fill 9001	≈ 100 power cycles	1.8 V LDO failure (AVVD18)
DYMAX 9001	≈ 200 power cycles	1.2 V LDO failure after cycling
DYMAX 9001	≈ 200/300 power cycles	1.2 V LDO failure during cycling

irreversible, and we observed the complete failure of the 1.2 V LDO regulator. After about 100 cycles, the current consumption measured at the level of the power supply dropped to almost 0 A.

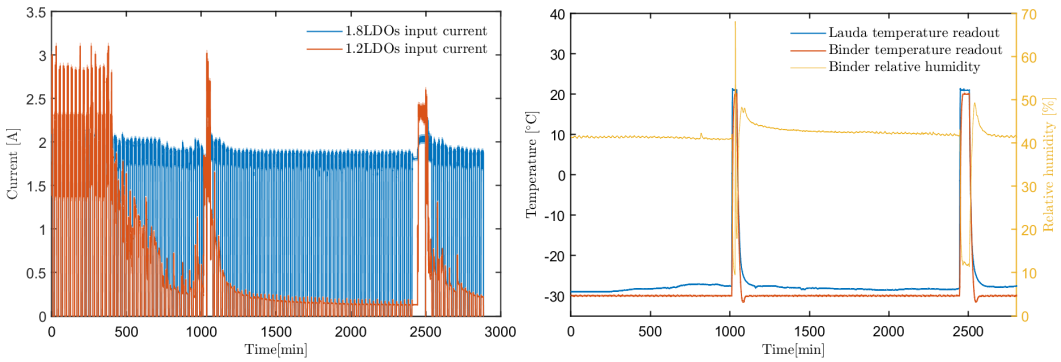

Figure 4.28: Current consumed by the 1.8 V and 1.2 V LDO regulators during the cold startup testing at $T = -30\,°C$ (left) Comparison of the lauda chiller set-point, readouts from the internal temperature and relative humidity sensors of the climatic chamber (right).

Similarly, the onset of the FEB malfunction can be seen in the diagnostic circuit of the STS-XYTER (see figure 4.29). VDDM drops significantly, at the point at which the LDO stops providing the nominal current. The temperature measured by the chip drops by 15 °C, and the VDDM reaches 0 mV, indicating a problem with 1.2 V LDO regulator It was later identified that one of the bond connections of the LDOs pad got detached from the board due to thermal stress. Therefore, the output current of the LDO was reduced to a few mA and the voltage was not delivered to the Analog Frond End of the ASICs.

One of the potential failure mechanisms can be seen in Figure 4.30. An air bubble seen on the right photo caused the regulator to lift from the PCBs surface, resulting in bond breaks. Hence, the LDO was not providing the nominal voltage and current to the chips.

Table 4.4: Detailed description of the LDO failure with regard to the type and number of cycles

Globtop	Cycles	Failure	Remarks
DYMAX 9001	50 passive cycles [−20 °C, 20 °C] 50 active cycles [−20 °C, 20 °C] 50 cold startups at $T = -20$ °C	43th active cycle [−30 °C, −20 °C]	1.2 V LDO failure
DYMAX 9001	50 passive cycles [−20 °C, 20 °C] 50 active cycles [−20 °C, 20 °C] 50 cold startups at $T = -20$ °C, 50 active cycles [−30 °C, 20 °C]	40th cold startup at $T = -30$ °C	failure of both 1.2 V LDOs 1.8 V LDO failure
DYMAX 9001	50 passive cycles [−30 °C, 20 °C] 50 active cycles [−30 °C, 20 °C]	29th cold startup −40 °C	1.2 V LDO failure

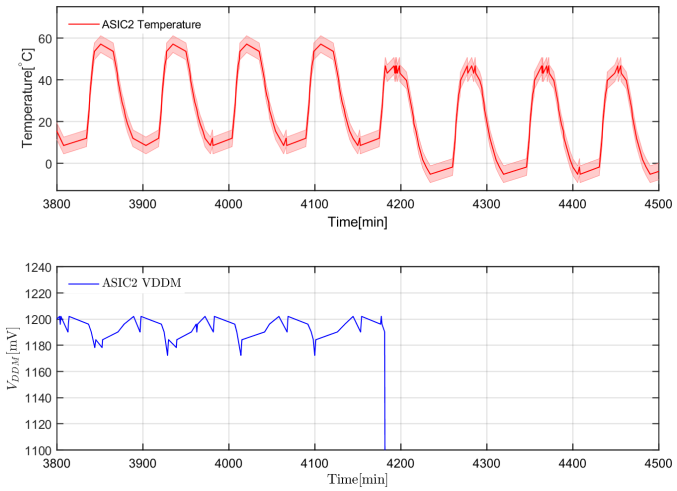

Figure 4.29: Temperature and VDDM of a chosen STS-XYTER, and the onset of LDO regulator failure.

4.3.8 Conclusions

The deployed part of the developed EPICS-based framework for the thermal cycling of the STS electronics enabled automation of the cycling process, storing the necessary data and analyzing it in order to evaluate the capabilities of the FEBs.

In total 12 FEBs were investigated in order to find the safe temperature operation range. Performed thermal investigations led to discovering the limitations of the FEBs, namely failures related to the LDO regulators. The realized measurements led to 6 out of 24 1.2 V LDO failures and 2 out of 20 1.8 V LDO regulator-related failures. The more frequent 1.2 V LDO regulator failure can be associated with larger current changes, leading to larger temperature differences. Furthermore, the boards initially tested in harsher conditions (larger difference between the extreme temperatures) tend to fail sooner. Moreover, the FEBs without ASICs and globtop on the LDO regulator didn't

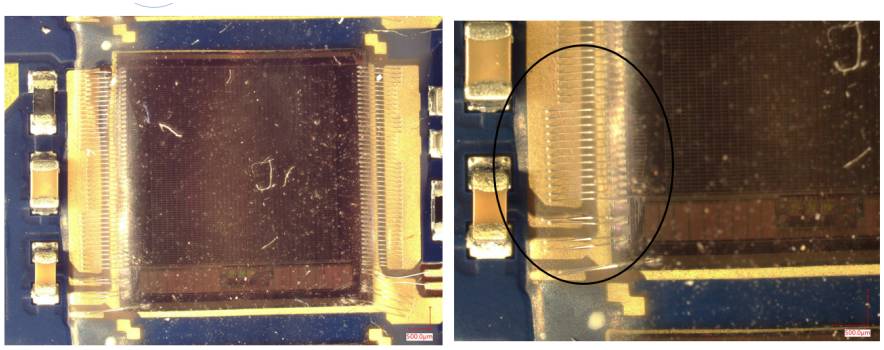

Figure 4.30: Microscopic view of the air bubble between glob top and bonds of the LDO.

show any sign of malfunction. Nevertheless, due to the lack of ASICs, it was impossible to change the analog line current.

As described in the introduction to thermal cycling, one of the most probable mechanisms leading to the LDO regulator-related failure is the mismatch of the CTE. It may potentially result in failure of the LDO regulator due to e.g., the lift of bonds.

Findings in this section obtained through the deployed control system architecture provide crucial information on how to improve the module and their performance before the mass production of the modules for the final STS.

Chapter

5 Solutions for humidity monitoring in STS

The research conducted for the STS focused on designing and testing different relative humidity and temperature sensors. This chapter provides an overview of the various solutions for ambient sensing, as we as an assessment of whether the tested technology meets the requirements. Particular attention was given to characterizing fiber optic sensors in order to develop safety requirements and systems that would mitigate potential risks posed by an environment with excessive moisture.

5.1 Sensors requirements

The design of the STS [34] defines the requirements for potential ambient sensors. As described in Section 2.3, the ambient temperature will reach −10 °C and the cooling liquid (3M NOVEC 649) will be circulating at temperatures close to −40 °C. Therefore, the first boundary condition arises: the frost point and the dew point inside the STS have to be below −40 °C to avoid ice formation or condensation on the FEE. During the detector commissioning, the temperatures will be higher, and relative humidity (RH) can be measured more accurately[1].

During the detector lifetime (10 years), there will be few opportunities to perform any upgrades. Therefore, the sensors have to withstand the radiation accumulated during that period (about 10kGy). As few sensors will be placed in the vicinity of the beam pipe, the total dose could reach more than 10 kGy [34]. The humidity measurements will be distributed, implying that different sensors may face different doses. The sensors have to be insensitive to the magnetic field of 1 T m since the whole detector resides in a dipole magnet. An ideal humidity sensor should also meet the following requirements:

- Small dimensions and mass (especially when placed close to the active area of the system).

[1] Performance of the commercial RH sensors usually decreases below 0°.

- Accurate (up to 2%) relative humidity readouts at temperatures down to −20 °C.
- Respond to a wide range of RH values from 0% to 80%,
- high repeatability and low hysteresis.
- Reliable operation across long distances (the readout device will be at least 20 m away from the detector).

On the other hand, due to overpressure conditions inside the STS enclosure, a low response time (seconds) is not necessarily needed, which is discussed in the next sections of this chapter. In terms of detector safety and implementation of the sensors readouts in the hardware and software interlocking, the time response up to minutes is considered to be acceptable.

5.2 Vapor pressure and its significance

The RH, or the dew/frost point, are commonly used parameters to describe the number of water molecules in the air. The dew point is the temperature at which water vapor in any gas medium (at constant pressure) begins to condense into liquid water at the same rate at which it evaporates.

Water vapor condenses as liquid water at gas temperatures above 0 °C. The dew point is defined as a liquid condensation layer. Water vapor deposits as solid ice at gas temperatures far below 0 °C. On the other hand, the frost point is defined as a solid condensation layer. However, for gas temperatures ranging from 0 °C to approximately −20 °C, the state of the condensed layer is unknown; it could be either water, ice, or a combination of both [135].

The first documented formula for vapor pressure (over water and over ice) was introduced by Goff and Gratch in 1945 [136]. The original correlation (over water) is as follows

$$\begin{aligned}\log(e_s^*) &= a(T_{st}/T - 1) + b(\log(T_{st}/T) - c(10^{11.344(1-T/T_{st})} - 1) \\ &+ d(10^{-3.49149(T_{st}/T-1} - 1) + \log(e_{st}^*),\end{aligned} \tag{5.1}$$

where log refers to the logarithm base 10, e_s is the saturation water vapor pressure (hPa), a to d are constants; $a = -7.9$, $b = 5.03$, $c = 1.38 \times 10^{-7}$, $d = 1.38 \times 10^{-7}$, e_s^* is the stream-point pressure (1013.246 hPa), and T_{st} is the boiling point (at 1 atm) temperature (373.15 K). A similar equation can also be formulated for the vapor pressure over ice.

These equations marked the first attempts to formulate a highly accurate description of water dynamics in the air. The Magnus formula is easier to implement than Equation 5.1 and allows converting between the saturation vapor pressure and temperature with a minimal error [137]

$$e_s^* = c \cdot e^{(aT/(b+T))}, \tag{5.2}$$

where RH is usually defined as the ratio of the water vapor pressure (e) to the equilibrium vapor pressure over the water plane (e_s^*)

$$RH = 100\frac{e}{e_s^*}. \tag{5.3}$$

Based on the parameters approximations by Sonntag ($c = 6.11\,\text{hPa}$, $a = 17.62$, $b = 243.12\,°\text{C}$) [137], the formula converges to

$$e_s^* = 6.112 \cdot e^{(17.62\,T/243.12)}. \tag{5.4}$$

The dew formation corresponds to the equation

$$e_s^*(T_d) = e_{st}(T). \tag{5.5}$$

Sonntag approximation results in a maximum error of $0.35\,°\text{C}$ between $-45\,°\text{C}$ and $60\,°\text{C}$ in comparison to the more complex formula described in [138]. Inserting the equation 5.3 and 5.4 to the 5.5 leads to the formula below, which provides the dew point in °C

$$T_d(T, RH) = \frac{\lambda(\ln(\frac{RH}{100}) + \frac{\beta T}{\lambda + T})}{\beta - (\ln(\frac{RH}{100}) + \frac{\beta T}{\lambda + T})}. \tag{5.6}$$

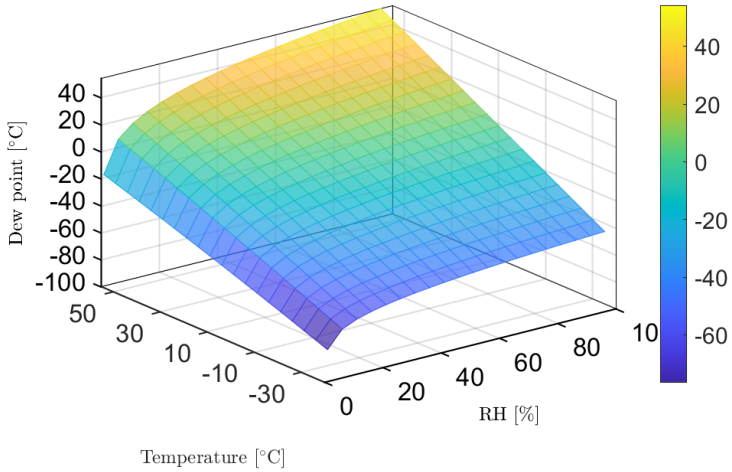

Figure 5.1: Dew points calculated with Magnus formula with parameters approximations by Sonntag [137].

The dew points calculations based on relative humidity and temperature can be seen in Figure 5.1. In order to compare the results of different relative humidity sensors and dew points sensors, uncertainties of the dry-bulb[2] temperature and RH are required.

[2] "Dry Bulb Temperature" refers essentially to the ambient air temperature. It is called "Dry Bulb" because the air temperature is indicated by a thermometer, not affected by the moisture of the air.

The individual standard uncertainty μ is defined as the uncertainty of the result of a measurement expressed as its standard deviation [139]. Hence, assuming the rectangular[3] distribution of uncertainty for the sensors that measure the temperature and relative humidity

$$\mu(x_i) = \frac{a}{\sqrt{3}}, \tag{5.7}$$

where a is the uncertainty available in the datasheets, and x_i represents the measured i value. The combined uncertainty μ_c can be derived from Equation 5.5 based on the law of propagation of uncertainty [140]

$$u_{Td} = \left[\left(\frac{\partial T_d}{\partial T_a} \right)^2 \mu^2(T) + \left(\frac{\partial T_d}{\partial RH} \right)^2 \mu^2(RH) \right]^{1/2}. \tag{5.8}$$

In each system, we assume that measuring dew point temperature or relative humidity is statistically independent of measuring air temperature and the confidence level for the uncertainty interval is 68%.

5.3 Overview of different technologies

Nowadays, electronic humidity sensors are commonly used in industry, scientific research facilities, and civil infrastructure. In general, we can classify the sensors based on their operating principle - changes in current, voltage, weight, or conductivity can be subsequently associated with humidity changes if the underlying detection principles relate to interaction with water. Resistive and capacitive sensors represent over 75% of all the sensors used today. As the names indicate, their working principles are based on resistance and capacitance changes, respectively.

The efforts to employ miniaturized sensors in HEP experiments have been ongoing for many years. A general review of the dew point and relative humidity sensing techniques was presented in [141]. On the other hand, a more recent overview with a case-specific study related to HEP is summarized in [142].

The two most challenging requirements in the case of STS are radiation hardness and insensitivity to the magnetic field. Radiation can affect sensor materials in different ways depending on their type, rate of interaction, and material composition. Sensor structures are affected by radiation due to modifications to their lattice structures. For example, capacitive sensors like HIH3610 [143] and HIH4030 [144] tested in CERN turned out to be critically damaged after irradiation [145]. It was also recently reported that capacitive sensors from IST AG [146] have a linear response to the radiation (what can be corrected [147]). Employing such sensors in a HEP experiment, especially in a tracker surrounded by a magnet, raises questions about the sensitivity to the magnetic field [145].

[3] Rectangular distribution has a probability that all outcomes in a given range are equally likely.

One of the possible solutions is using fiber optic-based sensors, which are by design insensitive to the magnetic field. Another possibility is to use a sampling system, which sucks the air from the detector and using e.g., a vacuum pump transports it to the area with lower radiation and without a magnetic field.

For the STS a distributed sensing system featuring a few different technologies is considered. The following sensors are discussed in the next sections: capacitive, fiber optic, and dew point transmitters.

5.3.1 Industrial capacitive sensors and their performance at negative temperatures

The capacitive sensors, in the simplest form, can be made out of two parallel plates, where the capacitance between the two electrodes is given by

$$C = \epsilon_r \epsilon_0 \frac{A}{d}, \tag{5.9}$$

where the ϵ_r and ϵ_0 are the relative and vacuum permittivity constants, A is the plate surface area and d is the plate distance. If the humidity changes can be associated with the changes of one of the parameters, the RH can be therefore calculated. The capacitive RH sensors can measure below $0\,°C$, they are fairly miniaturized and insensitive to pressure changes. The main drawbacks of these sensors are listed below:

- Limited long-term stability
- Sensitive to water condensation
- Limited distance to the readout device
- Most of the sensors are not radiation-hard

Two different RH capacitive sensors have been tested in low-temperature regimes - IST HYT221 [148] and Sensiron SHT85 [149]. Figure 5.2 depicts the RH and temperature accuracy of the first sensor. Measuring humidity at low temperatures below $-20\,°C$ and 5% RH leads to large dew point errors ($7\,°C$ and more). The estimated dew point errors calculated with the Magnus formula are presented in figure 5.3.

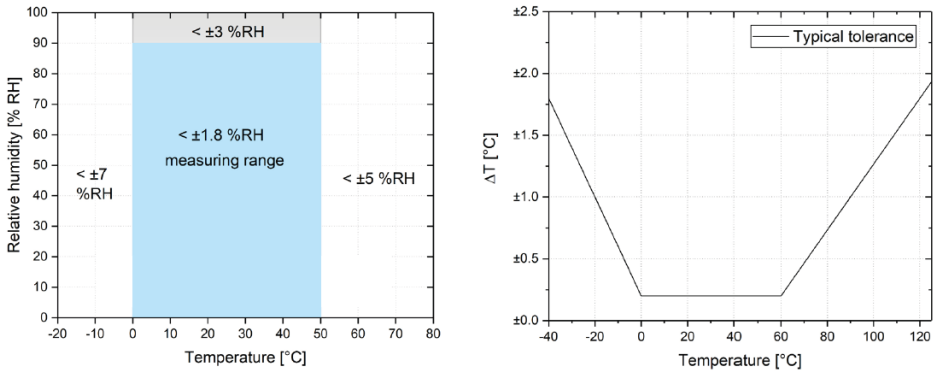

Figure 5.2: Relative humidity and temperature uncertainties of the IST AG HYT221 sensor in different environmental conditions [148].

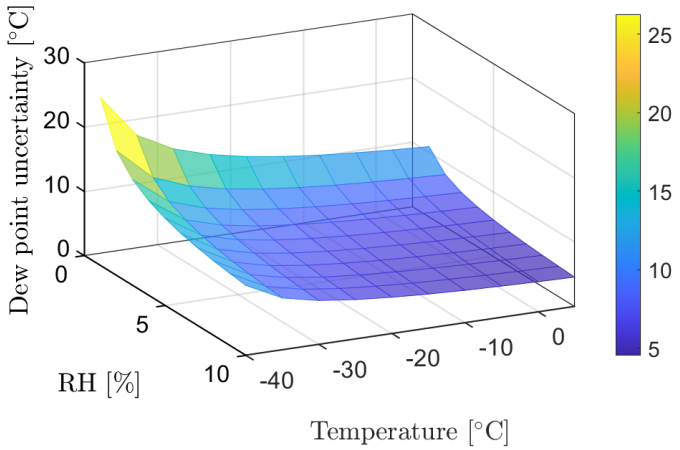

Figure 5.3: Dew point error based on values from Figure 5.2 for IST AG HYT221.

Figure 5.4 shows the uncertainties for the measurements with the SHT85 sensor above 0 °C. The data below 0 °C is not provided, therefore an extrapolation was made in order to have a comparison with the HYT221 sensor. The results are presented in Figure 5.5. In this case, the errors reach up to 5 °C at the lowest temperatures and RH levels.

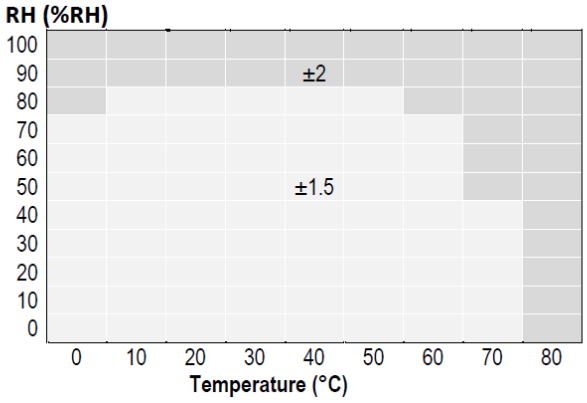

Figure 5.4: Relative humidity uncertainties for the SHT85 hygrometer, the temperature uncertainty is 0.2 °C [149].

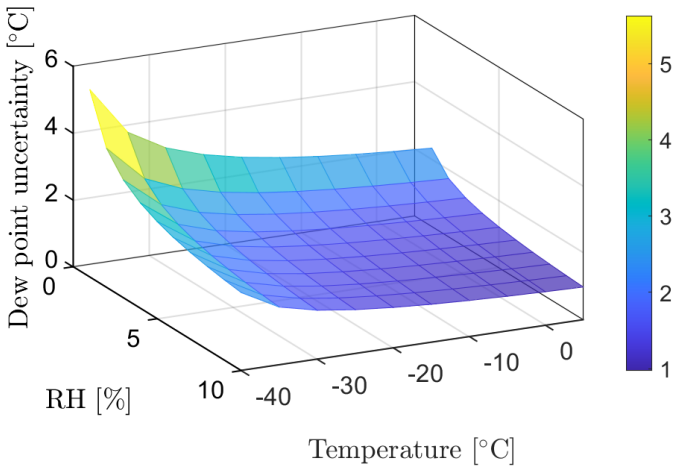

Figure 5.5: Dew point error based on Figure 5.4.

The above-presented results do not take into account additional effects that alter the calculations, like hysteresis or drift, which could together contribute by 1% or more to the RH measurement. The performance of the SHT85 also decreases in the low-temperature regime, but the extent is not determined in this work. The comparison of the industrial capacitive sensors shows a large performance disproportion.

The studied sensors are much cheaper than custom trace humidity measurement systems (sampling systems) or fiber optic sensors. The readout of such sensors may be affected by the radiation and magnetic field, so they can be considered a reliable solution for a long-term operation in the STS. The next type of sensor that yields promising results is based on fiber optic sensing technology.

5.3.2 Description of the Fiber Optic Sensing technology

Fiber optic sensors-based (FOS) system usually consists of three main components an optical source, transducer, and detector. In general, the sensing principle relies on modifying one or more properties of light (most commonly a laser, diode, or LEDs are employed as the optical sources) passing through a transducer which is located inside the fiber. A schematic view of a sensing setup is presented in Figure 5.6. Distributed sensing or even continuous sensing offers a unique opportunity for many sensing points in one fiber [150].

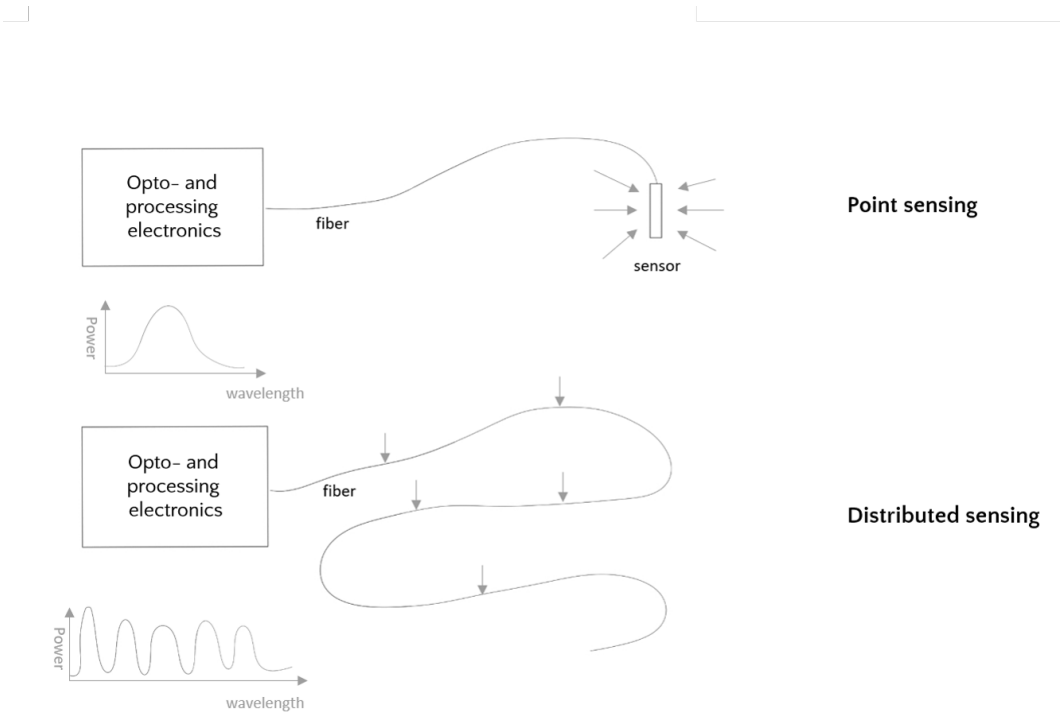

Figure 5.6: Comparison of different sensing possibilities with the FOS. Opto- and processing electronics are commonly called optical interrogator.

In general, humidity sensing can be classified according to the underlying operating principles [151]. Furthermore, we can distinguish intrinsic and extrinsic sensors that indicate whether sensing occurs inside or outside the fiber. The main effort has focused on in-fiber grating sensors, which belong to a class of intrinsic FOS that has gained popularity in recent years.

The main efforts were concentrated on a technology called Fiber Bragg Grating (FBG). The driving factor for this decision was the successful implementation of the sensors of this type in the Compact Muon Solenoid (CMS) at CERN, which was extensively reported in a number of papers and summarized in [145]. Moreover, a few

similar implementations were summarized in [152] and [153].

Fiber optic sensors have notable advantages in comparison to conventional sensors:

- Fibers can be insensitive to radiation or have predictable behavior
- Magnetic field insensitive
- Good signal transmission over long distances
- Multiplexing capabilities (see figure 5.6)
- Immunity to electrostatic and electromagnetic interference
- Resistant to harsh conditions - the sensors are completely passive elements, hence they offer long durability

On the other hand, FOS are difficult to integrate with hardware interlocks. Handling and installation of the sensors might be more challenging due to the risk of damaging the fiber or the sensor.

5.3.2.1 Fiber Bragg Grating based sensor for humidity monitoring

A FBG is a selective filter inside the optical fiber that reflects light signals at a specific wavelength known as the Bragg wavelength (λ_B). Such a filter is created by inscribing a systematic variation of the fiber refractive index [154]. This characteristic wavelength (λ_B) is dependent on the fiber effective refractive index (η_{eff}) and the grating pitch (Λ) of the FBG [155]

$$\lambda_B = 2\eta_{eff}\Lambda. \tag{5.10}$$

Both factors can be affected by strain, temperature, magnetic field, and/or pressure changes, thus various sensing possibilities are available with the FBG [156]. In general, wavelength shift λ_B can be formulated as

$$\frac{\Delta\lambda_B}{\lambda_B} = (1 - P_e)\epsilon + [(1 - P_e)\alpha + \xi]\Delta T, \tag{5.11}$$

where P_e is a photo-elastic constant (optical properties change under mechanical deformation), ϵ is a strain induced on the fiber, α is the thermal expansion coefficient of the coated FBG, and the ξ is the thermo-optic coefficient (change of the refractive index with the temperature) of the fiber. Using a FBG sensor for strain measurements requires decoupling the strain from the temperature. This solution is commonly called temperature compensation [156].

The most commonly used solution involves using two sensors next to each other, either inscribed in the same fiber or in another one placed in the vicinity of the main sensor. The first sensor is responsible for measuring the strain, and the second one

measures the temperature in strain-free conditions. The wavelength shift $\Delta\lambda$ induced by the ΔT can be described as

$$\frac{\Delta\lambda_B}{\lambda_B} = [(1 - P_e)\alpha + \xi]\Delta T. \tag{5.12}$$

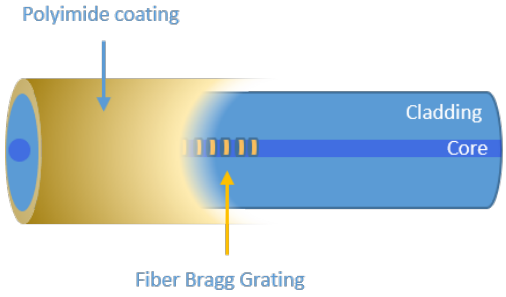

Figure 5.7: FBG-based sensors for the RH measurements.

It is possible to measure RH instead of the strain by applying a hygroscopic material (for example, polyimide or di-ureasil) to the fiber cladding[4] (see figure 5.7). The Bragg wavelength shift becomes the superposition of temperature and humidity effects (see equation 5.13) [152], [153].

$$\frac{\Delta\lambda_B}{\lambda_B} = \Delta T S_T + \Delta RH S_{RH}, \tag{5.13}$$

where λ_B is the Bragg wavelength, and $S_{RH/T}$ are the sensitivity coefficients for RH and temperature, respectively.

Similarly to the strain measurement, it's crucial to have precise temperature readouts in the vicinity of the coated FBG. Otherwise, the actual RH readout may be dominated by uncertainty or just an inaccurate temperature measurement. FBG sensors should also be packaged appropriately and kept strain-free to prevent additional stress, which is not related to the RH changes. Detailed discussion about the experimental setup, chosen design of the FBG sensors, and their features will be presented in Section 5.6.

5.3.3 Trace humidity sensing

Due to expected very low dew point levels inside the STS (below −45 °C) and the requirement to keep the device safe, it was proposed to use trace humidity sensors in so-called sniffing (sampling) system [145]. The most common sensing techniques include:

[4] Cladding is a layer of material with a lower refractive index that covers the core of a fiber optic cable. The core of the fiber optic cable is of a higher refractive index than the surrounding cladding.

- tunable diode laser (dew points from −100 °C to 20 °C),
- oscillating quartz crystal sensor (dew points from −100 °C to 0 °C),
- aluminum oxide sensor (dew points from −100 °C to 20 °C),
- chilled mirror dew point hygrometer (dew points from −100 °C to 100 °C).

Aluminum oxide interacts with water, and it is considered the sensor sensing layer. In its design, the sensors resemble the capacitive ones. Aluminum oxide-based sensors are characterized by very low uncertainties. In addition to that, the implementation in a hardware-based interlock is much easier than in the case of the FOS (the readout system is based on analog signals). An example of a sampling system is presented in Figure 5.8. The readout can be placed in distant areas without extensive ionizing radiation or magnetic field. The air is sucked from the detector by a vacuum pump, transported to the sampling cabinet, and then the dew point is measured by the aluminum oxide sensor.

Another precise and commonly used method, especially for the calibration of other humidity sensors, is the chilled mirror hygrometer. The mirror is cooled slowly and in a controlled manner until condensate can be detected on it. Using a vapor pressure curve, it is possible to determine the partial pressure of water vapor at the dew point of flowing gas. A careful measurement presupposes that equilibrium conditions are reached. This can only be achieved by approaching the dew point approximately with the temperature regime and repeating it several times. The measurement range of the Michell S8000 chilled mirror is presented in Figure 5.9. The chilled mirror together with the HYT221 and SHT85 were used to calibrate and characterize FBG-based FOS.

Figure 5.8: Left: Michell ES20 ceramic metal-oxide sampling system [157] Right: Michell S8000 Remote High Precision Chilled Mirror Hygrometer [158].

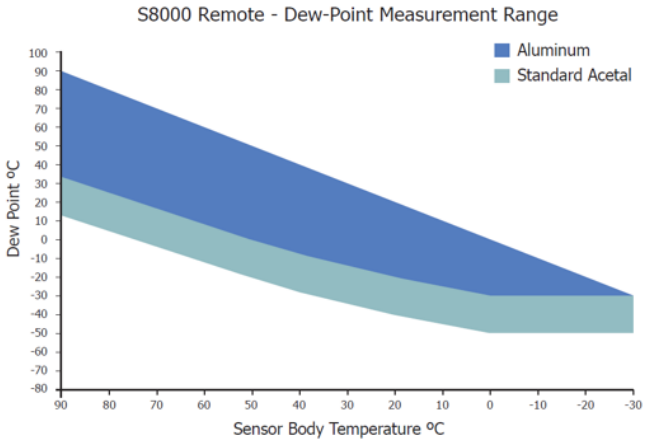

Figure 5.9: Dew point measuring ranges of S8000 device for two different mirrors [158].

5.3.4 Sensors performance in high radiation environments

Implementing a cost-effective distributed sensing system in highly irradiated environments is a challenging task. Sampling systems with multiple sensing lines are considered to be the most reliable way, but their cost per sensing point is relatively high.

Over the years, capacitive sensors have been widely used in many industrial applications, but their susceptibility to radiation does not qualify them as appropriate and reliable sensors for long-term STS operation [142], [145], [159]. The sensor internal electronic circuit is its most vulnerable part [160].

In recent decades, researchers have studied the effects of different types of radiation on optical fibers. When radiation interacts with materials, it changes their characteristics and often affects the performance and reliability of the devices, with pronounced consequences. For all these reasons, careful investigations concerning how radiation affects the operation of components intended for use in these harsh environments were conducted. The radiation may cause point defects inside the fiber, causing the attenuation of the signal [161]. Nowadays, it is possible to fabricate radiation hard fibers [162], for example, as reported by Berruti [145] commonly used Corning SMF-28 optical fibers are considered radiation tolerant. However, a careful choice of fiber material is needed, as its sensitivity depends on many factors such as dose, dose rate, and wavelength.

A second element that might be sensitive to radiation is the Fiber Bragg Grating, as the radiation may affect the wavelength shift [163]. The grating itself can survive high doses, but it is not completely insensitive to radiation. Similarly, as with the fibers materials, many factors can influence the response to the radiation of the grating. Some of them like the doping concentration (fiber is often doped with e.g., germanium), or

hydrogen loading[5] [163]. The next section will clarify the process of choosing the humidity sensor in more detail.

5.4 Characterization of the FBG-based FOS

The main efforts were concentrated to optimize the design of the polyimide-coated FBG sensors in order to be able to measure in low temperatures. According to [152] the RH sensitivity increases linearly with coating thickness, but the time response increases as well (see figure 5.10). The RH sensitivity increases linearly with the coating thickness, so in principle, a better humidity sensitivity would result in a more precise sensor.

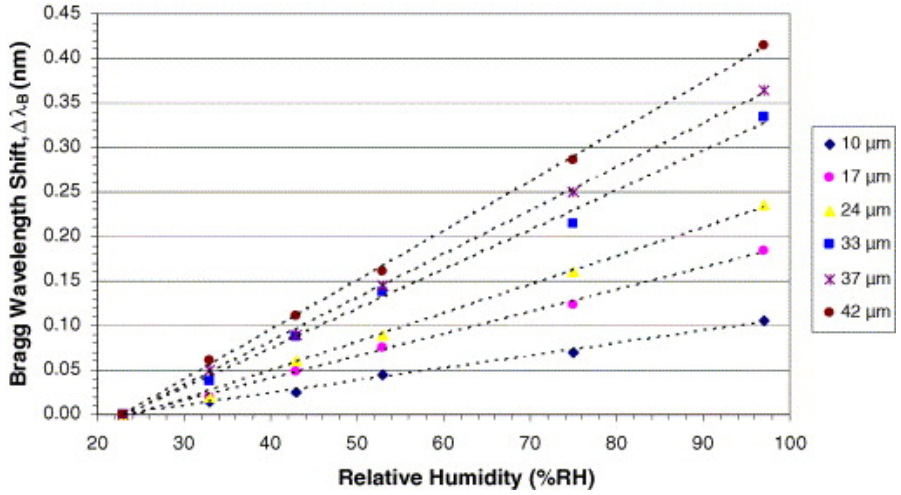

Figure 5.10: RH response of the sensors with different coating thicknesses, from 23 to 97%RH at constant room temperature [152].

The higher thickness increases time response, as seen in Figure 5.11. The most dangerous scenarios in STS include an uncontrolled change of humidity, which should be detected within minutes to conduct necessary actions in the control system. Therefore, the chosen coating thickness is between 15 µm and 20 µm, slightly higher than the first reported distributed sensing system implemented for the CMS at CERN, where 10 µm were used.

[5] hydrogen is used to increase the sensitivity of the optical fiber to the UV-light laser

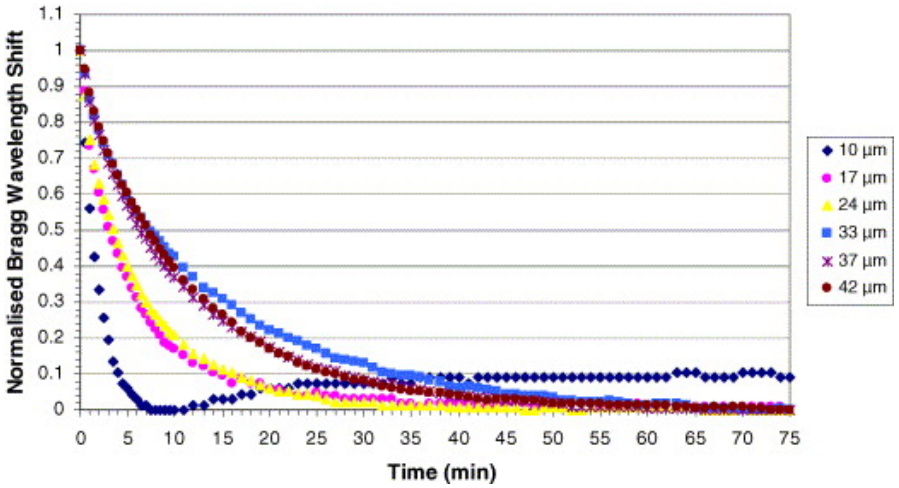

Figure 5.11: Recovery time of the sensors from 75% to 33% RH [152].

Two different FOS designs were compared:

- Multiplexed version with 5 FBGs inscribed in a germanium-doped fiber (see figure 5.13). The polyimide layer was applied in four steps, 5 µm each with 1.25 µm uncertainty for each layer. In total, the coating thickness was about 20 µm±5 µm. The temperature compensation was ensured by a second FBG array which measures only temperature.
- The second design is a hygrometer with temperature and humidity sensors inscribed into one fiber. The coating thickness was chosen to be 15 µm. The tested sensors are depicted in Figure 5.12.

To characterize a RH FBG-based sensor, the humidity, and temperature sensitivity coefficient have to be determined. In addition to that, parameters like time response, hysteresis, or repeatability contribute to the total uncertainty of the sensor.

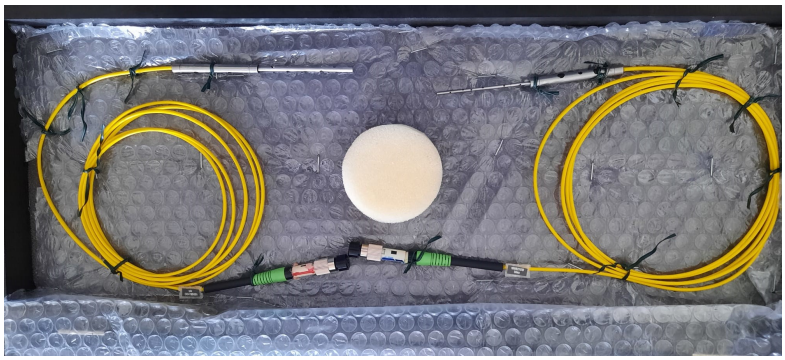

Figure 5.12: Hygrometer (temperature and humidity sensitive FBGs inscribed into the same fiber). The only difference between the two hygrometers in the photo is the diameter of the holder/packaging of the RH sensitive FBG (manufactured by AOS GmbH [164]).

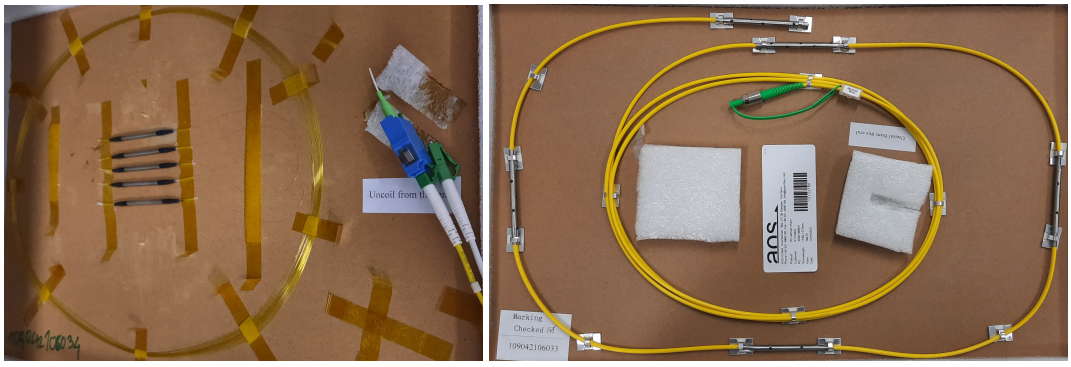

Figure 5.13: The left photo shows the temperature sensing array and the right one shows the RH sensing array after packaging the FBG in strain-free conditions. The fibers do not have the jacket applied on the polyimide coating. The arrays were manufactured by Technica [165] and packaged by AOS Electronics [164].

5.5 Experimental setup

The sensors were calibrated using a S8000 chilled mirror hygrometer [158]. Additionally, to compare the results, two industrial RH sensors were used: HYT221 and SHT85 (see section 5.3.1). The temperature during the testing was controlled by a Binder MKF chamber [166] which offers also relative humidity control down to 0 °C. The experimental setup scheme is shown in Figure 5.14.

Two calibration methods were used to characterize the FBG-based relative humidity sensors. The first method involved the use of different saturated salt solutions:

- Lithium chloride - RH at 25 °C 11%

- Magnesium(II) chloride - RH at 25 °C 33%
- Sodium chloride - RH at 25 °C 75%

Saturated salt solutions have well-defined relative humidity values at a given temperature [167]. This method offers a cost-effective way to calibrate a RH. The second method relied on the humidity control (10% to 80% with a 10% increment) of the climatic chamber.

The sensing instrument (light source) was the Micron Optics Hyperion SI255 [168]. The SI255 is supplied with high power, low noise, ultra-wide swept wavelength laser. It is guaranteed to provide absolute accuracy of 1 pm at every scan within the operating range of 1500 – 1600 nm [168].

The setup was controlled by the developed EPICS based framework. The custom-written IOCs were used to obtain data from the temperature and humidity sensors, as well as from the climatic chamber. The data related to the fiber optic sensors were collected through ENLIGHT[6] software, and a custom IOC connected to it. Subsequently, all the data was stored using an archiver appliance to a Redis database.

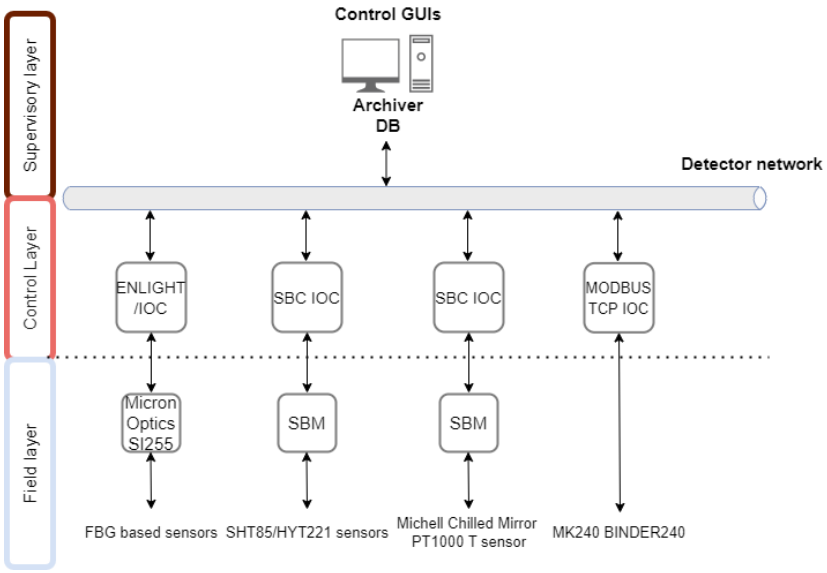

Figure 5.14: Controls architecture for the temperature and humidity sensor measurement.

[6]ENLIGHT Sensing Analysis Software is a powerful utility that is included with Micron Optics sensing interrogators.

5.5.1 Sensors characterization

Initially, the basic parameters of the sensors were checked. The Bragg wavelength and the corresponding spectral response of the sensors. Figure 5.15 shows an example of the readout of the SI255 device from the hygrometer. In order to perform an accurate calibration of the sensors, the RH and temperature sensitivity factors have to be determined.

The climatic chamber offers the temperature control between −40 °C and 180 °C. As both methods to control humidity offer only limited capabilities, below 0 °C for calibration of series production a new custom humidity control system will need to be considered [145], [169].

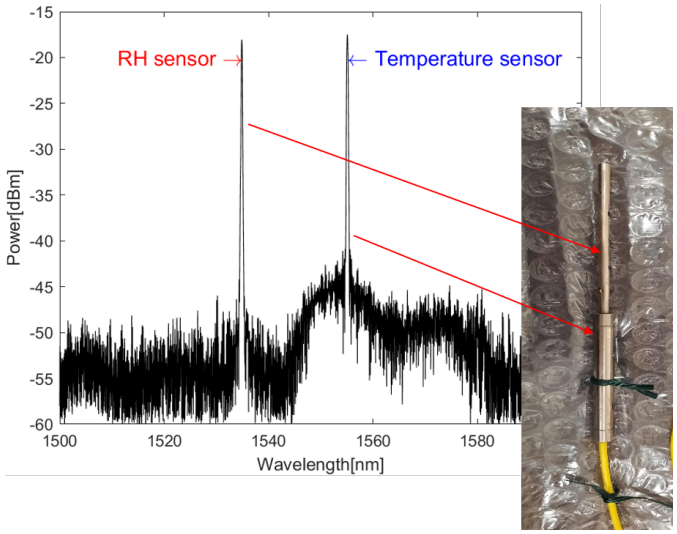

Figure 5.15: The spectral response of the FBG reflected wavelength. Each of the peaks is correlated with one of the gratings in the fiber.

One of the most important sensor characteristics is accuracy, which holds information about the deviation of the measured value from the ideal value. Overall, the uncertainty comprises several factors [170]:

- Calibration error – a constant error over the whole range of measurements, its source is related to the accuracy of the reference device and the calibration method applied.
- Hysteresis - a deviation of the sensor output to a certain point of the input single when approached from opposite directions (see Figure 5.16).
- Non-linearity – in the characterization of the FBGs it is assumed that the response of the sensors to the stimulus (increasing humidity or temperature) is linear. Therefore, any deviation from the linearity is considered a contribution to the uncertainty,

- Repeatability – the error caused by the inability of a sensor to represent the same value at the same conditions.

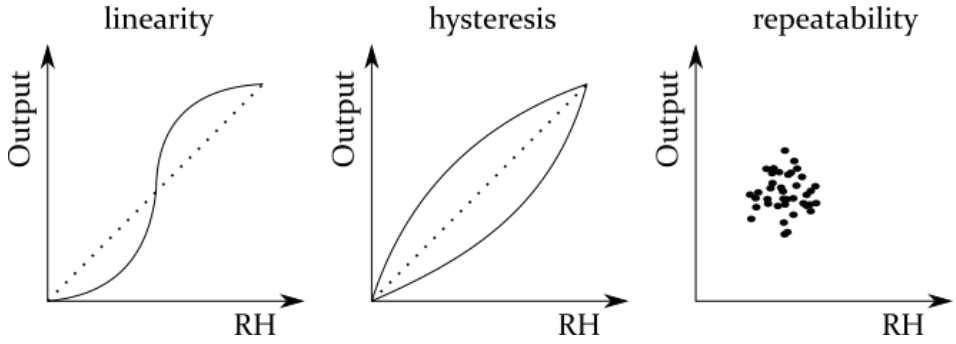

Figure 5.16: Different contributions to the sensors accuracy.

By combining all the errors, the total uncertainty of a sensor is as follows

$$\mu_c = \sqrt{\mu_1^2 + \mu_2^2 + ... + \mu_i^2 + ... + \mu_n^2}. \tag{5.14}$$

The total uncertainty of a FBG sensor may consist of many other factors (including the uncertainty of the peak wavelength measurement). Nevertheless, the factors listed above were considered to have the largest contribution.

5.6 Results

In this section, the efforts to calibrate and characterize the humidity array and hygrometers are described in detail. The calibration relied on the Bragg wavelength shift measurements while increasing the RH levels at the constant temperature value. This measurement was then repeated for different temperature values.

For the calibration with the saturated salt solutions, the sensors were exposed to the given salt for a prolonged time of about 6 hours. The calibration step in the climatic chamber lasted about 2 hours. Keeping the sensors for this time at constant conditions, ensured that the equilibrium was reached.

5.6.1 Characterization of RH FOS

The test subjects were two hygrometers (15 µm polyimide coating) and 5 RH sensors (20 µm) polyimide coating in an array with 15 cm distance between the subsequent sensors. The spectral response of the array can be in Figure 5.17. The spectral responses are usually the first sign that the sensors perform correctly.

The second test involved evaluating the humidity response of the sensor in the range (10% to 80%), see Figures 5.18 and 5.17. In both cases, increasing the relative humidity

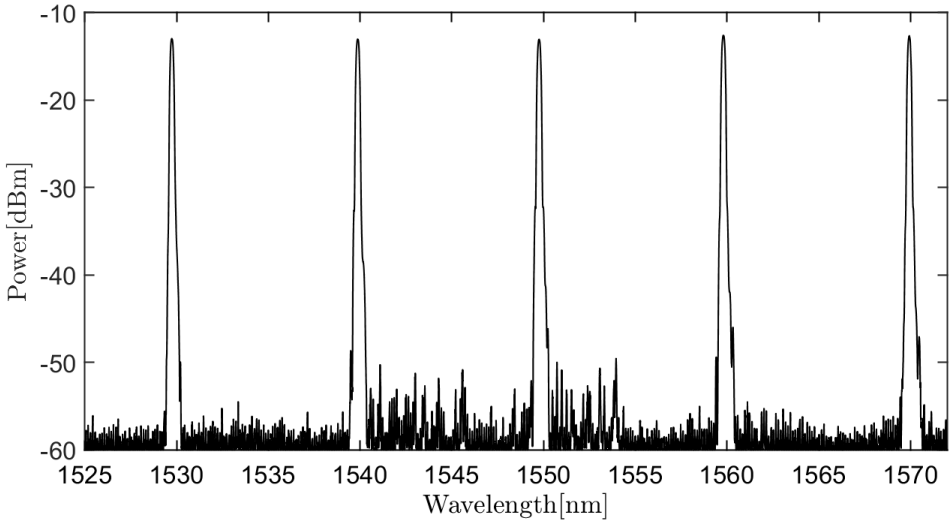

Figure 5.17: Spectral response of the RH sensors in the array.

inside the test chamber results in the shift of the Bragg wavelength toward higher values. It is related to the increasing strain on the grating resulting from the deposition of water molecules in the polyimide. These measurements were taken at a stable temperature of 20 °C. Figures 5.19 and 5.20 depict the calibration curves of the hygrometer

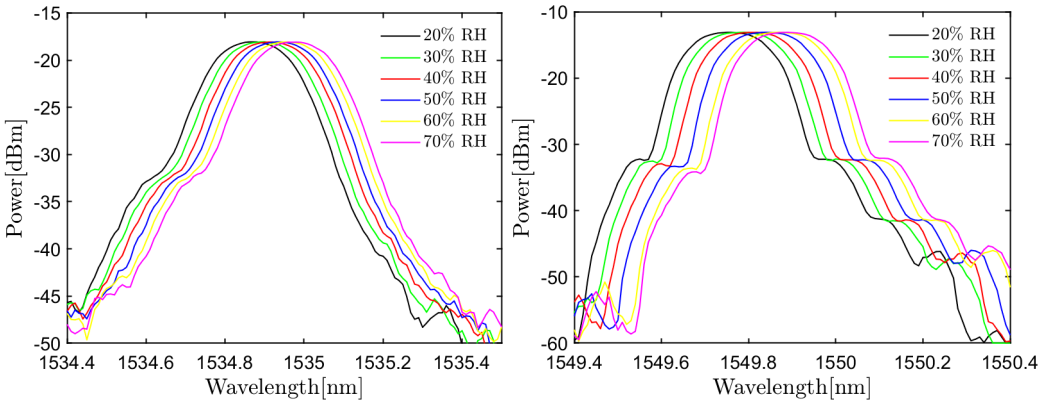

Figure 5.18: Humidity induced Bragg wavelength shift of the hygrometer (left) and first sensor in the array (right). The spectral response is depicted as the power of the reflected wavelength.

and one of the array sensors. The calibration curves were obtained by changing the humidity values from 10% up to 80% at a constant temperature. The temperature range was from −20 °C to 30 °C with an increment of 5 °C. Figures 5.19 and 5.20 depict a linear response to the humidity increase at every temperature.

The measurements below 0 °C have relatively large uncertainty, due to the limited humidity control and fewer stable measurement points (due to humidity fluctuations). Furthermore, the change of temperature also results in the shift of the Bragg wavelength toward smaller values, which is also in agreement with results in [153] and [145]. In the array calibration, two curves for −5 °C and −10 °C are missing. This is related to the unrealistically high uncertainties, most likely caused by an additional strain applied to the sensors after handling.

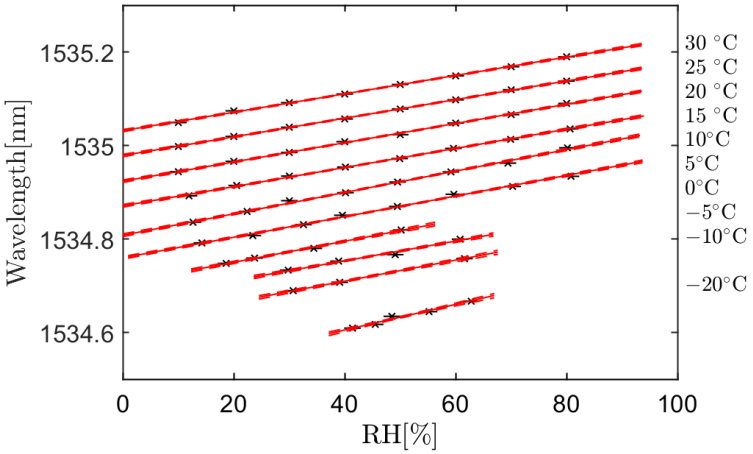

Figure 5.19: Calibration curves for the hygrometer.

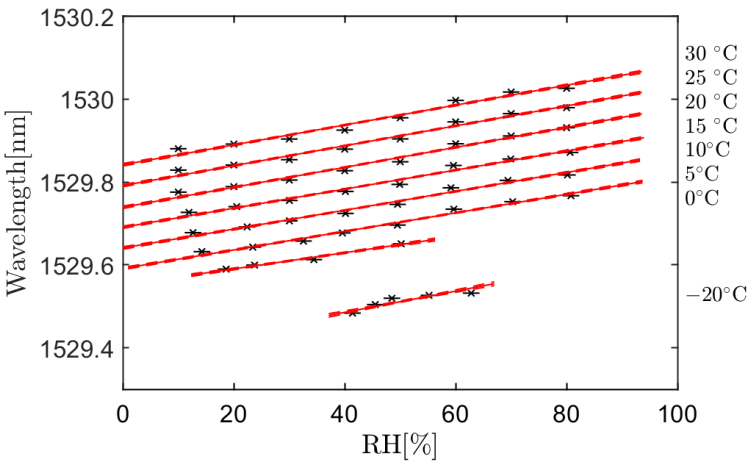

Figure 5.20: Calibration curves for the first RH sensor in the array.

The uncertainties of the reference devices (the Michell chilled mirror ±1%RH and the PT1000 temperature sensor - 0.001 °C) are taken into account, together with linear fit error. The uncertainties are assumed to be following the Gaussian distribution and the confidence level of 68%. The slopes of the obtained fits are the humidity sensitivities of the sensors. These values at different temperatures and their corresponding uncertainties are depicted in Figure 5.21.

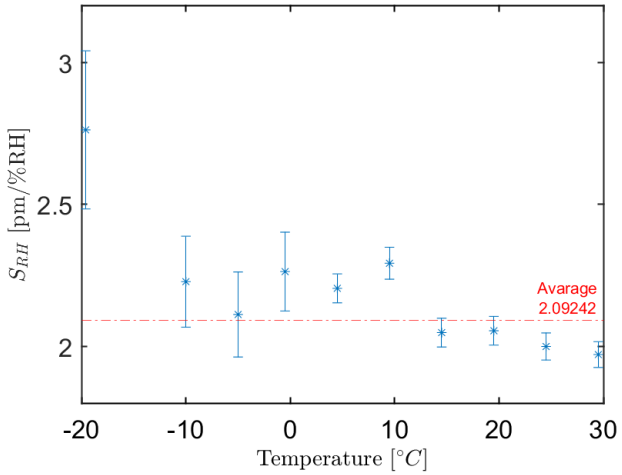

Figure 5.21: Humidity sensitivity (S_{RH} at different temperatures with the corresponding uncertainty for the FBG-based hygrometer.

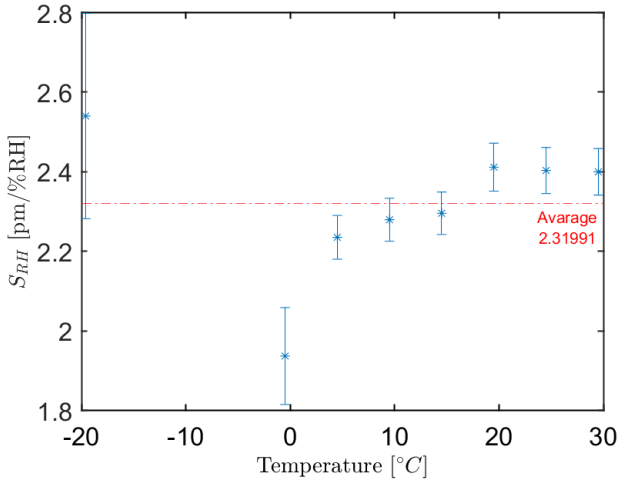

Figure 5.22: Humidity sensitivity S_{RH} at different temperatures with the corresponding uncertainty for the first RH sensor in the array.

Similar plots were also obtained for all the other RH sensors of the array (see Figure 5.23). The second hygrometer did not show a linear response to the changing conditions, which is further discussed in the next section.

The average S_{RH} for the array sensors is $2.77 \pm 0.03 \frac{\text{pm}}{\%\text{RH}}$ and $2.09 \pm 0.02 \frac{\text{pm}}{\%\text{RH}}$ for the hygrometer. Given the uncertainty of the coating thickness, these results are in line with the findings in [152] and [153] for coating thicknesses between 15 µm and 20 µm. The uncertainty obtained from the calibration is much smaller than the error introduced by the interrogator itself, which is 1 pm. The hygrometer measures with an accuracy of 0.5%RH and for the array sensors on average 0.36%RH.

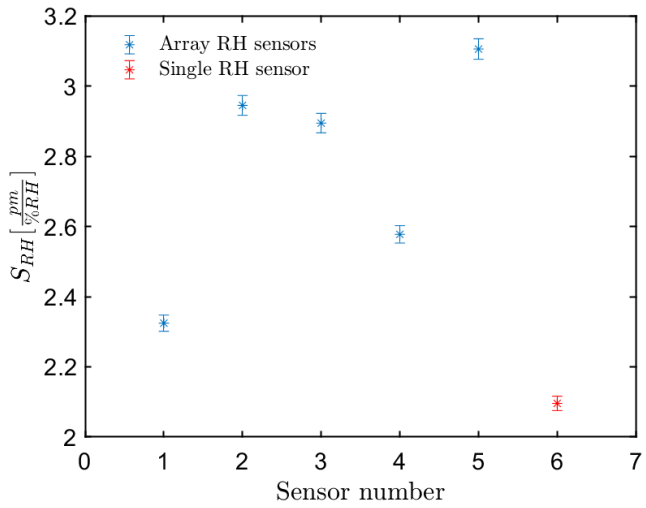

Figure 5.23: Humidity sensitivity S_{RH} of the sensors with the corresponding uncertainty.

The second coefficient called temperature sensitivity (S_T) conveys information on how the wavelength shifts depend on the changing temperature. In this case, for the stable RH values, the temperature was changed between −20 °C and 30 °C. The average temperature sensitivity S_T value for the array is $10.25 \pm 0.02 \frac{\text{pm}}{°\text{C}}$ and for the hygrometer $10.87 \pm 0.02 \frac{\text{pm}}{°\text{C}}$ (see Figure 5.24). The S_T is about an order of magnitude larger than the humidity sensitivity (S_{RH}). That implies that the temperature sensor located next to the RH one should measure with good accuracy, in order to avoid a huge uncertainty of the humidity measurement. A 0.1 °C temperature uncertainty leads to almost 0.5%RH uncertainty in the case of the hygrometer and 0.36%RH in the RH array.

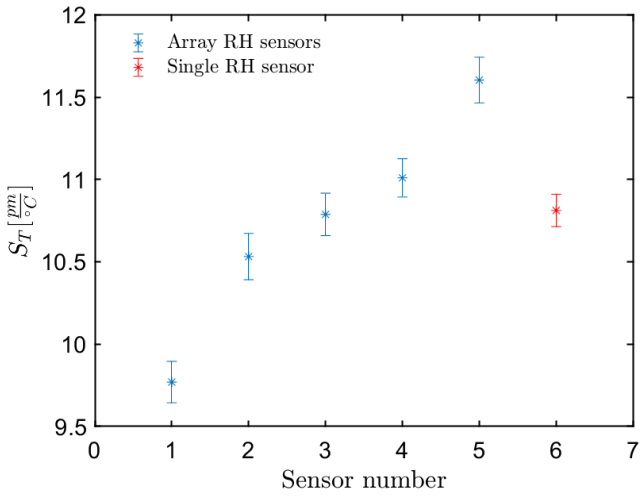

Figure 5.24: Temperature sensitivity S_T of the sensors with the corresponding uncertainty.

5.6.2 Calibration with saturated salt solutions

The two mentioned hygrometers were also at first tested with the use of the saturated salt solutions method. The details of this approach are given in section 5.5. The results of these measurements are depicted in Figure 5.25. The Sensor depicted as FBG RH FOS 1 does not have a linear response to the changing humidity and temperature, therefore it was excluded from further tests.

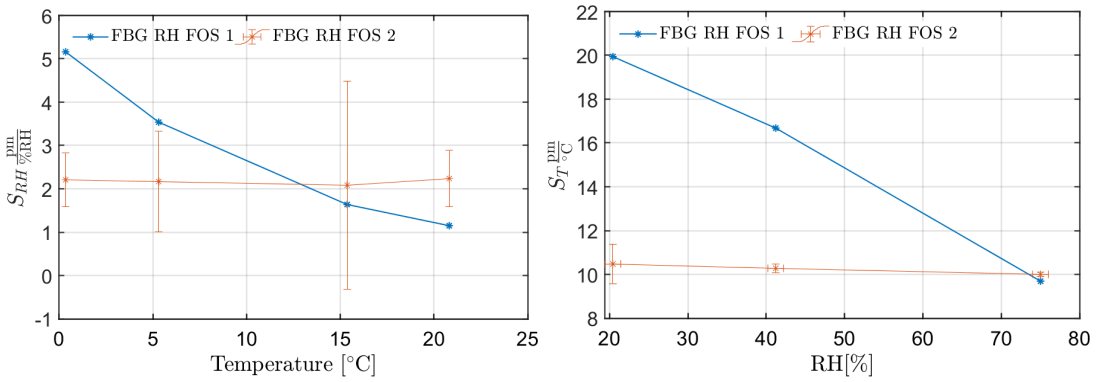

Figure 5.25: Relative humidity S_{RH} and temperature sensitivity S_T as per the results from the calibration with the saturated salt solutions. Average error for the $S_{RH} = \pm 1.21$ pm and for the $S_T = \pm\ 0.4$ pm.

The comparison of the results from two different calibration methods for the hygrometers is depicted in Table 5.1. The calibration method based on the saturated salt solutions has larger uncertainties due to the small number of calibration points. Nev-

ertheless, the method involving saturated salt solutions is a very cost-effective method allowing the characterization of the sensors, but it can not be used in a wide temperature range, especially below 0 °C as the relative humidity provided by the solution is not constant.

Table 5.1: Comparison of the temperature and humidity sensitivity obtained through calibration based on different approaches.

Means of controlling humidity	$S_{RH}[\frac{\text{pm}}{\%\text{RH}}]$	S_{RH} uncertainty [pm]	$S_T[\frac{\text{pm}}{°\text{C}}]$	S_T uncertainty [pm]
Saturated salt	2.17	1.21	10.25	0.4
Climatic chamber	2.09	0.06	10.87	0.02

5.6.3 Time response

The time response of the hygrometer and the array sensors was investigated as well. The sensors were compared during the increasing humidity from about 20% to 80%. The FBG based FOS has a much longer time response than the capacitive sensors (seconds). The time response of different sensors is often compared using for example the time to reach 63% of set value τ_{63}.

Figures 5.26 and 5.27 depict the comparison of the time response of the hygrometer and one of the array sensors with commercial capacitive sensors (two SHT85 and HYT221 sensors). The response of the FOS is shown as wavelength change. It is also noteworthy that the response is about twice slower at 0 °C. The average response time at 0 °C for the array sensors is 10.7 min, and 4.8 min for the hygrometer. On the other hand, at 20 °C those values equal 2.3 min and 2 min. Small differences among the array sensors were also seen, but they most likely correspond to slight differences in the coating thickness and the position inside the climatic chamber.

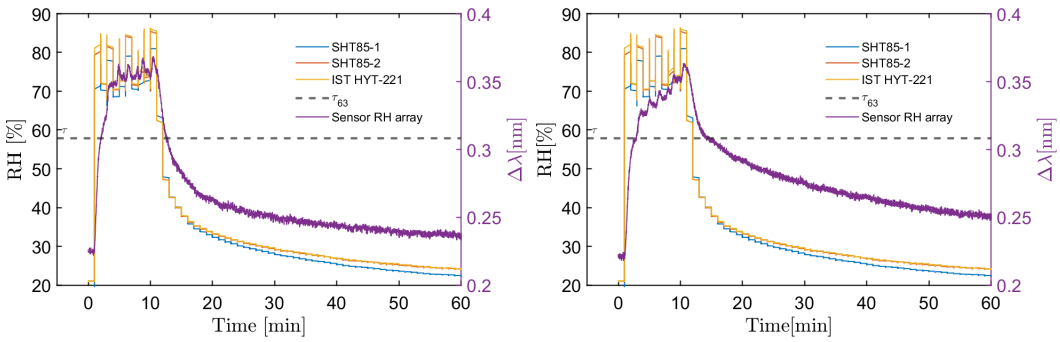

Figure 5.26: Time response of the hygrometer and array sensors, and comparison to the capacitive sensors. The dashed line represents the 63% of the final RH value at 0 °C.

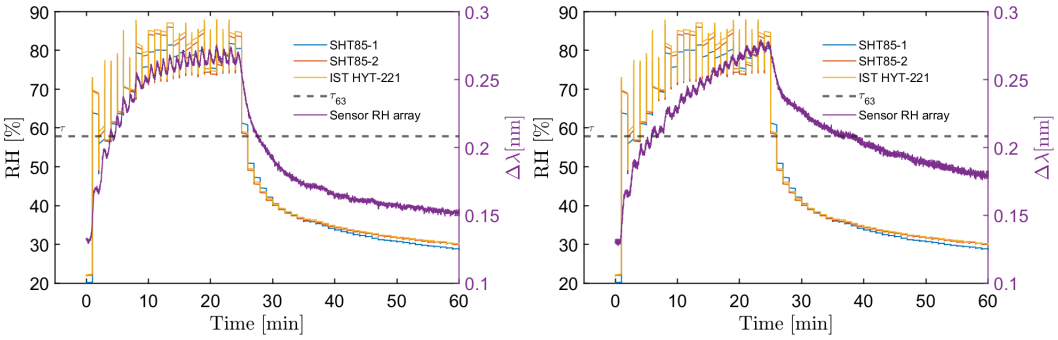

Figure 5.27: Time response of the hygrometer and array sensors, and comparison to the capacitive sensors. The dashed line represents the 63% of the final RH value at 20 °C.

Longer response times for the array sensors are related to the thicker polyimide coating. The second contribution might be related to the slightly different packaging of the sensors.

5.6.4 Hysteresis

Figures 5.28 and 5.29 show the hysteresis of the hygrometer and two array sensors. The first figure shows the wavelength change during the stepwise increase of relative humidity from 10% to 70% (with 10% step), and also while decreasing the RH. The temperature fluctuations during the hysteresis measurement are depicted in Figure 5.29. The resolution of the optical interrogator is 1 pm. Hence, any temperature uncertainty of 0.1 °C and relative humidity uncertainty of 0.5% are related to the device resolution. Based on Bragg wavelength measurement differences at each point, the hysteresis of the hygrometer is 0.72 ± 0.48% RH, and for the array sensors 2.67 ± 0.33% RH.

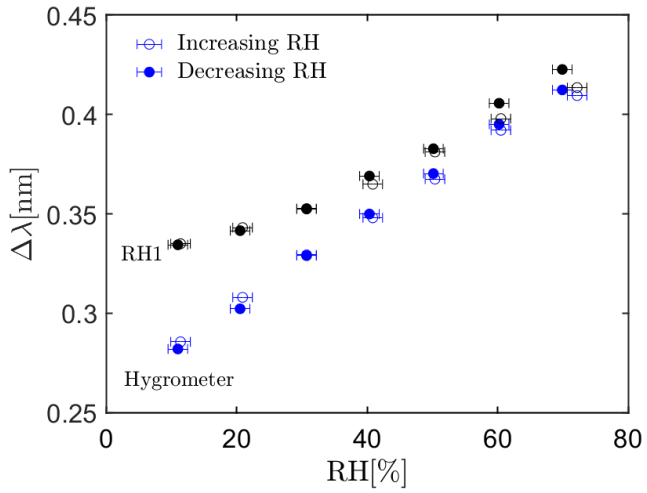

Figure 5.28: Hysteresis of the hygrometer and the first array sensor at a constant temperature of 25 °C.

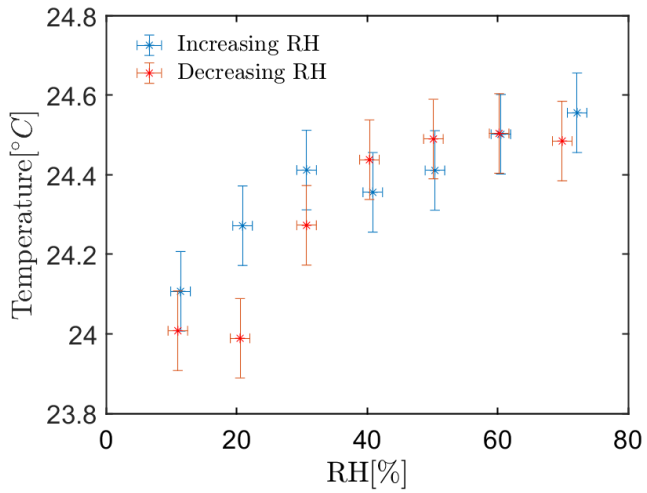

Figure 5.29: Temperature stability during the hysteresis measurement.

5.6.5 Repeatability

The repeatability of the hygrometer was also determined by performing three measurements that involved increasing humidity from about 10% to 80% and then decreasing it again in steps of 10% to the baseline value. The sensor shows acceptable stability and repeatability after 7 days since the first measurement. The sensors in the array showed a large offset which is most likely related to the holder/packaging of the sensor and the difficulty to keep the sensors in strain-free conditions, as they are located very close to each other (less than 15 cm).

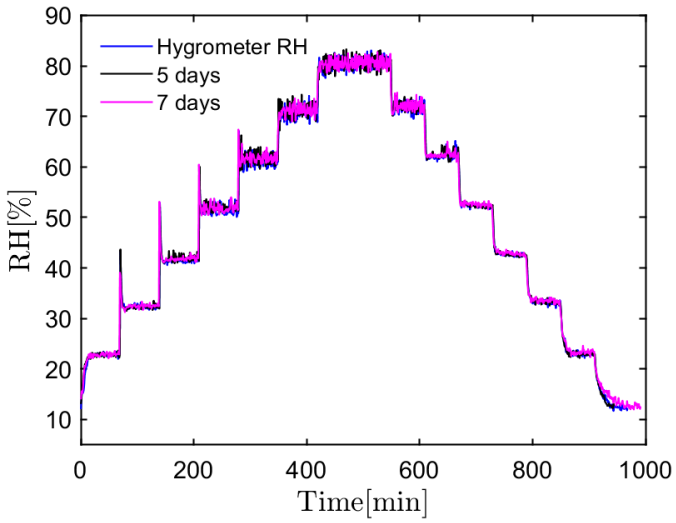

Figure 5.30: Repeatability of the hygrometer. Three subsequent measurements were compared after 5 and 7 days after the first test.

5.6.6 Conclusions

The total uncertainty of the hygrometer measurement obtained after including the calibration error, repeatability, and hysteresis is 1.7% RH. For the array sensors, the uncertainty is about 4%.

As the hygrometer design turned out to be more consistent and robust, its performance was also compared with the E20 sampling system [157] and its ceramic sensor. The array did not provide the expected repeatability, and it will be further tested inside the thermal demonstrator (see section 7.1). Moreover, below −20 °C the attenuation of the signals was observed, which may be related to the design of the packaging of the array sensors.

The performance of the hygrometer was confirmed during the low-temperature tests with the industrial capacitive sensors and the trace humidity sensor, which is summarized in Figure 5.31. The uncertainties of the sensors are not shown, in order to highlight the trends of the respective sensors. The largest uncertainty is associated with the SHT85 capacitive sensor. The ceramic sensor dew-point values are characterized by low uncertainty of up to 1 °C.

The response of the hygrometer was also compared with the sampling system and different lengths of the guidelines leading to the ceramic sensor. In the final detector, the sampling system electronic circuitry will be placed at least 20 m away from the detector. The tubing is going to increase the response time of the sampling system.

Figure 5.32 shows the comparison of the results obtained with two different lengths of leading tubes. The tube length was 2 m and 12 m, for the left and right figures, respectively. The obtained time response was 1.5 min and 3 min. Assuming that the

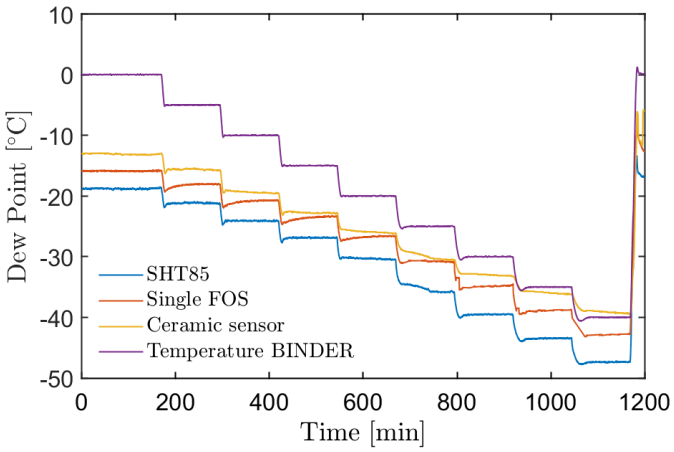

Figure 5.31: Comparison of the dew points calculated using the Magnus formula for the industrial sensor SHT85, metal oxide trace humidity sensor (ceramic sensor), and the hygrometer. For the comparison, the temperature inside the Binder climatic chamber was also plotted.

flow does not depend on the distance from the sampling point if the tube was 30 m the response would be 5.7 min. Figure 5.33 shows the behavior of the FBG-based hy-

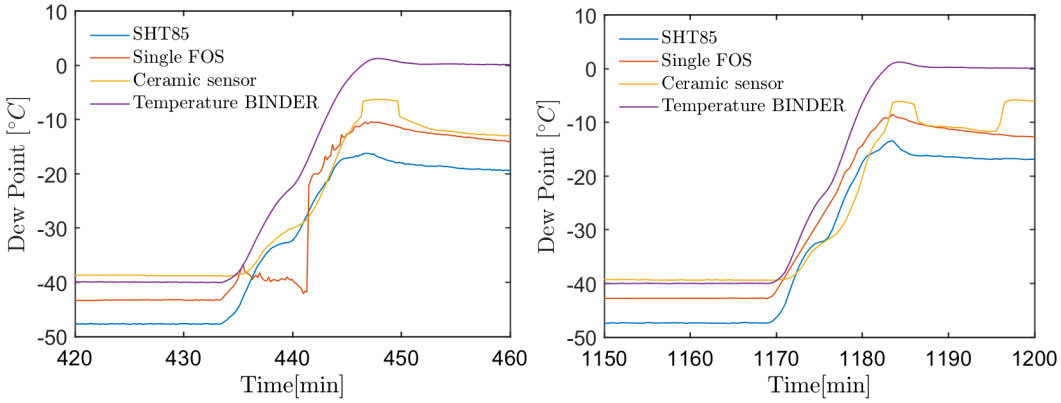

Figure 5.32: Time response comparison of different sensors. Left - 2 m tube to the ceramic sensor, right - 12 m tube to the ceramic sensor.

grometer at low dew points. The sensing limits are clearly represented in Figure 5.33. The hygrometer performance is limited to the dew point of −70 °C (see the area highlighted with the red rectangle). Nevertheless, at such low dew points, the uncertainties become much higher. It is also noteworthy that that limit refers to the ambient temperature of 10 °C. On the other hand, for the measurements at 20 °C the dew point reaches −50 °C/−40 °C. Based on the obtained values, the sensor can accurately measure down to about 1%.

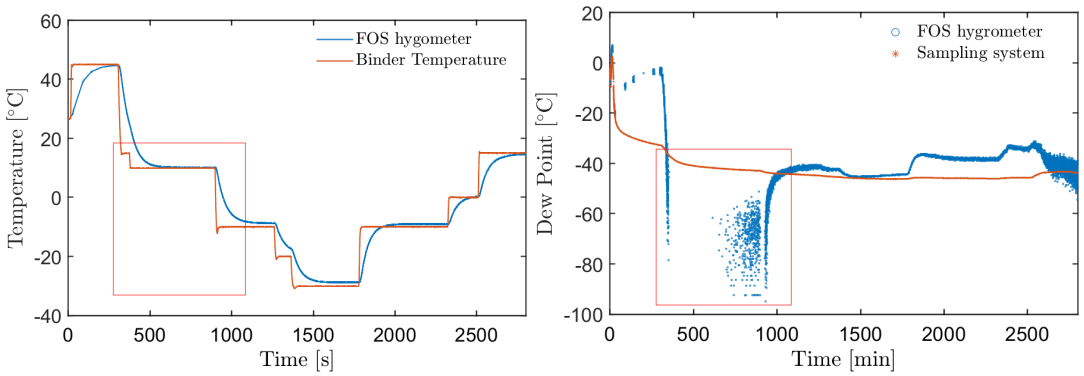

Figure 5.33: A comparison of the readouts from the temperature sensors inside the Binder chamber with the FBG-based hygrometer (left). Dew point during the changing ambient conditions per the hygrometer and the ceramic sensor.

5.7 Final considerations

The characterization of the FOS brought information on the advantages and limits of this particular technology with the use of polyimide as the sensitive material. In principle, the tested hygrometer meets the requirements set for the STS. The distributed system will feature the sampling system, FOS, and capacitive sensors.

An array of sensors could still be considered, but the distance between the gratings should be much larger than 15 cm to ensure that the sensors can be packaged in strain-free conditions. As stated in Section 5.3.4, the FBG based FOS can be considered radiation hard. According to [145], the sensors can be used in radiation environments by pre-irradiating them before installation, to reduce radiation-induced cross-sensitivity.

Moreover, the capacitive industrial sensors will be used next to the FOS. The main purpose will be to use them during the commissioning and in order to recalibrate the FOS if the installation will cause any additional stress on the grating.

The last technology foreseen for the distributed sensing system is the metal oxide (ceramic) moisture sensors. It is the most reliable solution that will be used also for the interlocking system. Several sampling points inside the detector enclosure will measure trace humidity and serve as a reference for the two other measurement technologies. The system should also be redundant and accurate during 10 years of operation. Therefore, a viable solution is to install a chilled mirror hygrometer in the vicinity of the sampling system readout in order to cross-check the readouts and ensure safety.

Chapter

6 mSTS as pathfinder for the DCS

The mCBM [171] experiment is considered a FAIR Phase 0 experiment and the precursor of the CBM experiment. The first mCBM campaign took place in 2019 after two years of preparations in the detector test area HTD [172]. The first mSTS prototype was operated together with mTRD, mTOF, mRICH, and mPSD, and it consisted of one tracking station, built of 4 detector modules (8 FEBs) mounted onto two carbon ladders, and then subsequently in two C-frames. The next iteration of the mSTS detector features 11 detector modules, and it was assembled in order to have a better understanding of the components and the operation of a more complex structure. Completing 11 modules (together with the QA procedures, testing of the STS-XYTER and FEBs), readout, and control software, set an important milestone on the way to the STS. The first section of this chapter gives an overview of the mCBM experiment, focuses on the DCS architecture, and gives an introduction to the detector operation. The next sections summarize the assembly of mSTS and its hardware. At last, the results obtained through the DCS consisting of power dissipation considerations, ambient conditions monitoring, and leakage current evaluation and calculations are discussed.

6.1 mCBM – the phase 0 experiment

The mCBM experiment aims to test and optimize the performance of the detectors, including crucial software and hardware components. The experiment uses beams from SIS18 synchrotron at energies up to 2 AGeV and intensities up to 10^9 ions/s. The test setup is positioned downstream of a solid target centered around a polar angle of 25° (see Figure 6.1).

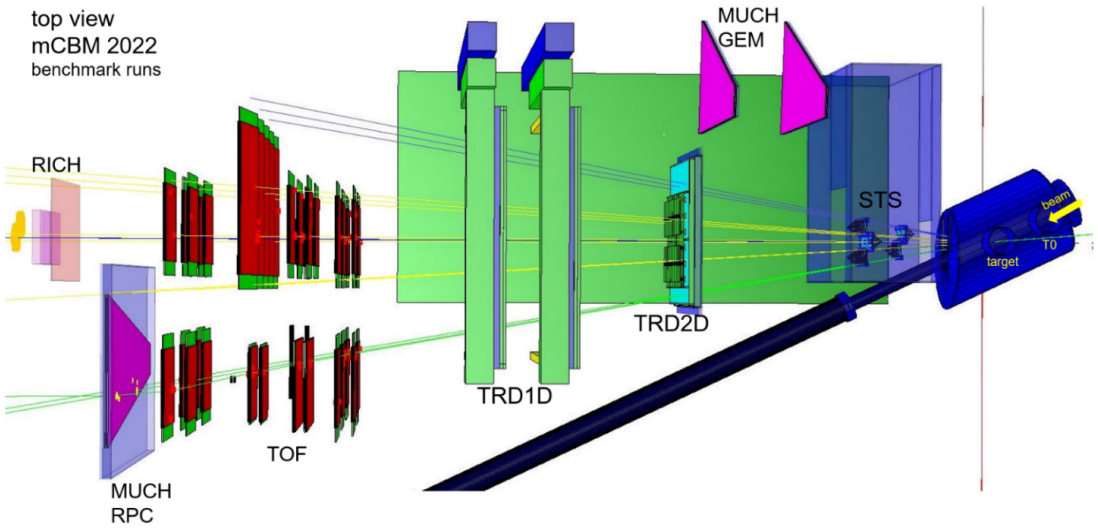

Figure 6.1: Schematic view of the mCBM experiment in 2022.

Timely development of the DAQ, First Level Event Selector (FLES), and DCS will significantly reduce the commissioning time required for the CBM experiment at the SIS100 synchrotron. The mCBM DAQ is based on the Common Readout Interface (CRI) (see Section 2.4). Each subsystem uses at least one CRI board.

Apart from exercising the readout chain and DCS, the mCBM aims to operate the subsystems in the high-rate nucleus-nucleus collision environment. Testing and improving the free streaming data acquisition and transport to the computer farm is also a huge advantage ahead of the main experiment. Furthermore, offline data analysis, online tracking, event reconstruction, and event selection algorithms have been intensively investigated.

Figure 6.2 depicts the latest mSTS detector, which features 4 units forming 2 tracking stations of 5 ladders, 11 modules, 24 FEBs (22 readout FEBs + 2 pulser FEBs), and 176 readout ASICs. The above-mentioned pulser FEBs are additional boards that are triggered by the common external pulser and were added to the system as a time reference and to check the time correlations between mCBM subsystems. Most of the components used for the assembly of the detector are close to the final ones, therefore the operation of the mSTS gives us a unique opportunity to study the performance of the module in detail.

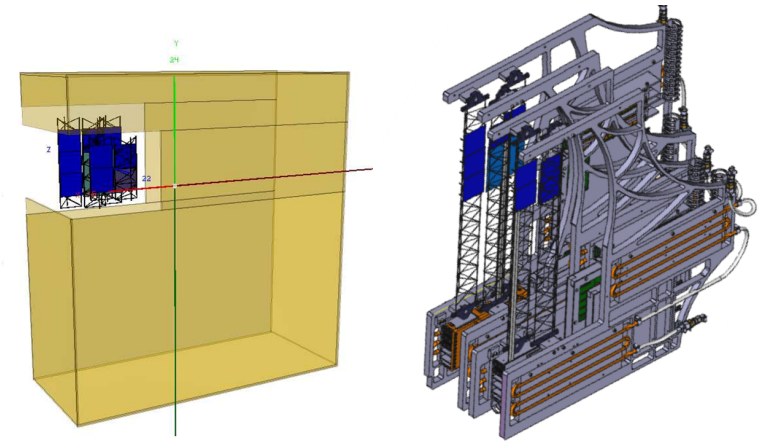

Figure 6.2: Mechanical design (right) and simplified geometry of mSTS together with its enclosure (left).

6.1.1 Data-taking campaigns

After the commissioning of the mCBM experiment in June 2021 with CRI based readout and with both mSTS tracking stations in June 2021, the first data-taking took place in July, featuring collisions of O ions on a Ni target at 2 AGeV with intensities up to 10^{10} ions/spill. The spill duration was set to 10 sec, and the effective intensity reached 10^{9} ions/s. This campaign allowed performing last checks of the DCS and other systems before the announced Λ benchmark runs in 2022 [173].

During that beam campaign, very good spatial and time resolutions were confirmed [174]. Moreover, a clear distinction between noise and minimum ionizing particles (MIPs) signal was seen. The vertex reconstruction was completed using the correlations of mSTS hits within the two stations or with other detectors. Hit reconstruction efficiency of 97.5% was achieved, which is consistent with the expectation from simulations, using the mTOF as an additional external reference [174].

The preceding runs with U ions beams and Au target (T = 1 AGeV and average collision rate of 400 kHz) took place in March 2022. The benchmark runs with Ni + Ni (T = 1.93 AGeV and average collision rate of 200-300 kHz) were realized in June 2022. During the data taking with the heaviest systems, the silicon sensors were exposed to significant particle flux, which will be discussed in the next sections.

6.2 Introduction to the detector control

The next sections give an overview of the control system and its applications. The mSTS detector uses most of the container-related developments including Phoebus, Alarm-system, Alarm-logger, Elasticsearch, Kibana, Archiver, Redis DB, and the underlying stream-processing platform. The mCBM subdetectors require control sys-

tems, but some services and related hardware used for the Phase-0 experiment are in most cases different from those, to be used for the final experiment. It implies that the efforts toward the DCS will have to be intensified as the services will be close to completion. The prototyping of the DCS refers mostly to the software components that could be maintained and used during the commissioning and operation of the future experiment.

As described in the Chapter 3.3.2, the network serves as a medium allowing a server and a client to publish and subscribe to process variables. Those variables are distinguished by its name and follow the convention described in the next subsection.

6.2.1 Distinguishing the services and their names

The naming convention should clearly define the detector place and its functions. A record comprises a record name and aliases that help to identify the variable. In a general case, the naming convention uses the following specifiers with a colon as a delimiter:

1. Experiment: CBM
2. Subsystem: STS
3. Service: Air Drying/Powering (Optional)
4. Location: Unit/Ladder/FEB or controller number/module number/channel number
5. FEB service: high voltage/low voltage
6. Value abbreviation: e.g., IMon/VMon

For example, to measure leakage current for a given side of the silicon sensors (the first line represents the name and the second one the alias):

```
CBM:STS:1:0:2:HV:MeasureCurrent
CBM:STS:11111:5:1:MeasureCurrent
```

The first line of the example above points to a defined place and functionality in the detector - the current of the High Voltage (HV) channel of the given FEB. The second line indicates the channel in the power supply module which is being used. This naming convention is then followed by the other services - low voltage power, cooling, etc.

6.2.2 Network structure

There are three main networks in the mCBM experiment. The first one so-called detector network allows monitoring and control of hardware connected to the respective subsystem. All DCS infrastructure, including the main node, is located in that network. The second network FLES network is focused only on the data coming from the

detectors. The third network is dedicated to the operators and data-taking operations. All these networks are interconnected via gateways.

6.2.3 Detector control system for mSTS

A breakdown of the mSTS DCS architecture is presented in Figure 6.3. The supervisory layer features several nodes: 2 single board computers (SBCs) and two nodes - the control and archiver node.

The first one of the main nodes takes care of the control and monitoring of the whole system (all the containers and applications), and the second node serves as a backup and archiving node. The control layer comprises all the necessary IOCs and underlying nodes. The last layer (field layer) features all readout boards, sensors, power supplies, cooling units, etc. The system sums up to about 5000 process variables and about 10% of them have to be archived. The control system software (containers, IOCs) needs to be also monitored, in order to detect any kind of malfunction.

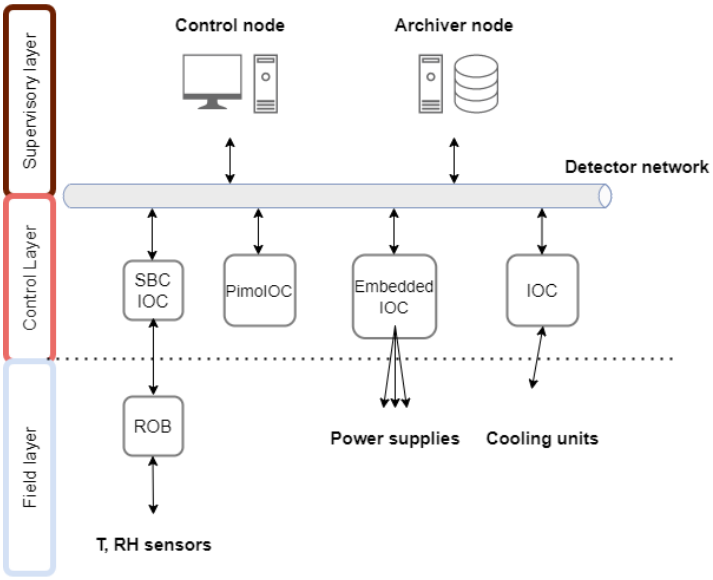

Figure 6.3: A general structure of the mSTS DCS architecture. The IOC-based ping monitor is denoted as PimoIOC (see Chapter 3).

6.2.4 Finite state machine and its role

mSTS, as opposed to the final STS, does not require sophisticated hardware and software interlocking mechanisms. The biggest risk to the safe operation are:

- Too high ambient temperature (exceeding 60 °C)

- Ambient temperature reaching dew point
- Sudden loss of cooling unit (e.g., due to radiation-induced damage)
- High leakage current (usually too high currents are managed by the trip conditions of the power supply)

A proposed FSM for mSTS DCS can be seen in Figure 6.4. Each state of the FSM represents a well-defined detector state. After initialization of all the services, the detector enters into the standby state, in which the cooling stabilizes and the detector is prepared for the next steps. Next transitions and stages prepare mSTS for the operation and data taking, low voltage and subsequently high voltage channels are turned on. In case any of the issues listed above happens, the detector is brought into a safe state (error state), which in most cases requires operator intervention. The global states mentioned to the right of the block diagram are the states propagated to the higher levels of control instances (SCA/ECS).

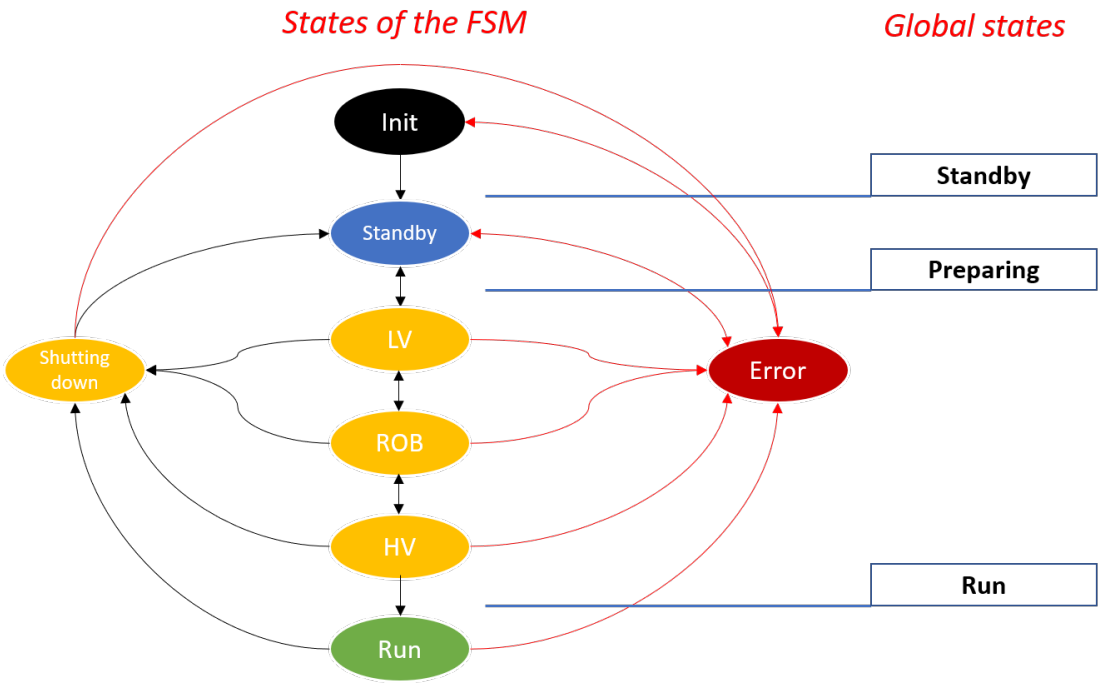

Figure 6.4: Proposed finite state machine for mSTS.

6.2.5 Containers monitoring - Weave Scope

Weave Scope [175] is a visualization and monitoring tool for containerization platforms (e.g., Docker). It offers a detailed view of the entire infrastructure and allows for diag-

nosing any problems with the distributed containerized control system. Weave Scope has proved to be a useful tool for running commands and configuring the containers after their initialization. Figure 6.5 depicts the deployed mSTS services. For example, the IOC container publishes the values from the chillers, hence the container is connected to Phoebus, archiver, alarm-server, and sequencer.

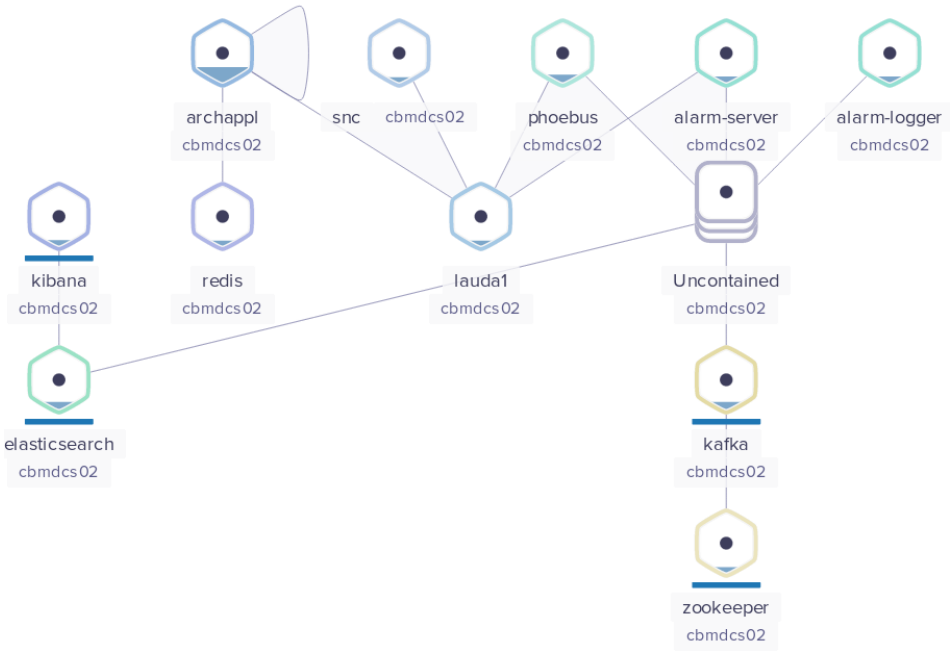

Figure 6.5: mSTS - Weave Scope view of the deployed services.

6.2.6 IOC monitoring - heartbeat and ping monitor

Apart from container monitoring, the IOCs database also contains a heartbeat record, which indicates whether the IOC is working properly. An additional tool called PIMO IOC was also deployed. It is a ping monitor, which checks if a given IOC is reachable in the network. Losing an IOC would indicate an error. When it comes to machine safety, mSTS DCS FSM should also react to the disconnection of PVs which are being monitored.

6.2.7 Process variables monitoring and control

As described in Figure 6.3, the three monitoring blocks are relative humidity and temperature sensors, cooling, and powering. To monitor ambient conditions, seven PT100 temperature sensors and one relative humidity sensor (Sensiron SHT85) were placed

inside mSTS [149]. Additionally, one sensor was placed outside the detector enclosure to monitor the temperature in the experimental cave. The temperature sensors were read out using a dedicated readout board connected to a Raspberry Pi [176] board which runs an IOC process. Similarly, the humidity sensors were read out by a microcontroller board connected to the same SBC and IOC.

The control of the mSTS modules powering is organized twofold. All low voltage and high voltage modules are controlled via CC24 controller [177] inside MPOD crates [178]. Each CC24 controller has an embedded IOC which was customized for the system requirements. An operator can either use the SNMP based communication, ca-tools, or a dedicated GUI. In the case of SNMP scripts, the user has access to single channels, and specific channel-hardware connection knowledge is required to properly handle the detector. On the other hand, thanks to the aliases assigned to the process variables, specific channels could be switched on (via channel access protocol, PV access, or Graphical User Interface) by knowing the position of the FEB in the detector.

6.3 mSTS assembly and its services

The silicon detector comprises 11 modules (22 FEBs) and 2 pulser boards. Each module consists of a silicon sensor, shielded microcables, and 2 FEBs. Two different silicon sensor sizes were used to assemble mSTS modules - 62×62 mm and 62×124 mm. Each side of the sensor has 1024 strips which are connected via microcables to the readout electronics - 8 STS-XYTERs on the FEB. The low-mass microcables transport the analog signals, and they can be affected by any electromagnetic interference (EMI). The analog signals received by the STS-XYTER chips are then amplified and converted into digital hit data words. Subsequently, the digital signals are transported via the data cables to CROBs (in total 5 readout boards - one for each mSTS ladder) to the CRI, and then from there to the FLES, where they are processed and stored for analysis. In total, mSTS has 22528 readout channels, which constitute only 1.25% of the final detector. In order to avoid overheating and reduce noise, the FEE needs to be properly cooled and powered.

6.3.1 Powering of the detector modules

The powering of the mSTS is organized similarly as it will be implemented for the final STS (see section 2.3.2 and figure 6.6) [179]. Each power board (in total 5 POBs - one for each ladder) is populated with DC/DC converters (1.8 V and 2.4 V, 2.5 V and 3 V [50]). These boards are connected to the low voltage power supply (WIENER [115]). The double-sided silicon sensors are symmetrically reverse-biased (±75 V) and operated in a constant voltage mode. Each side of the sensor is connected to a high-voltage module located in the same crate as the low-voltage ones. The details of the powering scheme and the modules mounted on the carbon ladders can be seen in Figure 6.6.

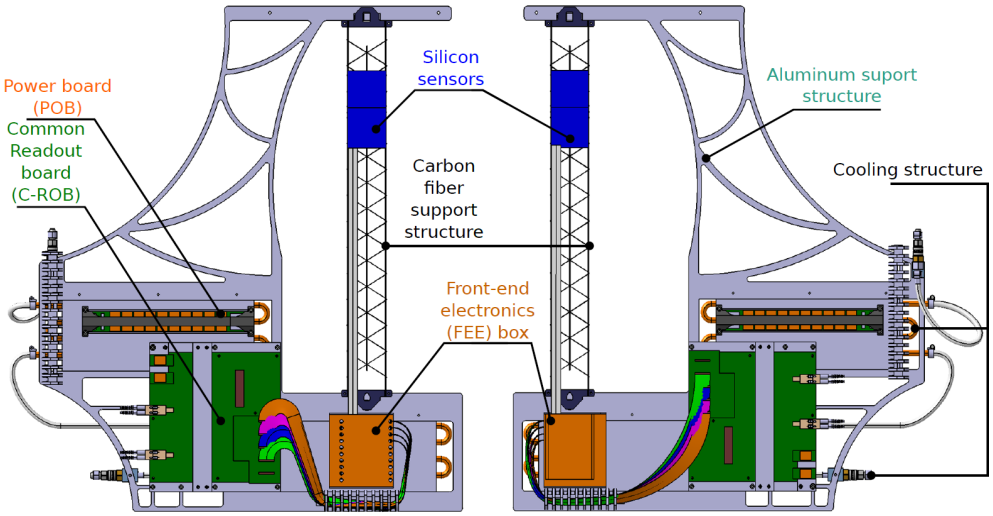

Figure 6.6: Schematic view of the first station of the mSTS. It depicts the main structures of the C-Frame.

6.3.1.1 Noise considerations

Noise[1] problems are the most common and critical issues while building a particle detector. In an environment with many devices, noise sources may be difficult to detect, and it could be sometimes even more difficult to minimize the interference. The total noise contribution can be divided into four components [180]:

- Thermal noise $n_{TH}(t)$
- Electromagnetic interference (EMI) between the detector and FEE connection, $n_{D-E}(t)$
- EMI between FEE and external connections, $n_{E-F}(t)$
- Additional sources, related to the intrinsic noise of the FEE elements, $n_{add}(t)$

From the practical point of view, designing and implementing a proper powering and grounding scheme play a critical role in the data quality from the detector [181]. The silicon sensors are characterized by very low signal levels, which makes them particularly sensitive to noise pickup. In the case of the mSTS, the FEE is located between 45 cm and 49 cm from the silicon sensor. The microcables connecting the two mentioned elements (sensor and FEB) are shielded, but the EMI of the analog signal could be clearly observed when the cables are not completely flat (due to e.g., external stresses). The other contribution which is related to the noise picked up between

[1] Unwanted high-frequency disturbance or interference with outside electrical signals.

the FEE and external connections is suppressed by an additional filter box (first order RC-filter) for the silicon sensor biasing lines. The total noise in the system serves as a reference for the minimum signal level that could be processed. More detailed considerations about the intrinsic noise influence on the system are described in the section 6.3.1. During the laboratory tests, satisfactory performance of the detector modules was achieved (1000 e ENC). Nevertheless, the performance in the experiment area can differ greatly, due to the influence of devices belonging to other subsystems or the accelerator services. The problem with the noise performance of the modules was also identified in this case, and substantial efforts were taken in order to find the noise sources and limit their influence (increasing the analog-digital converters (ADC) threshold values of the STS-XYTERs).

The appropriate grounding of the FEE reduces capacitive coupling between the structure and the sensitive areas of the FEE. Furthermore, it generates low impedance at the power connector input to reduce external current interference going through FEE electronics. The mSTS enclosure is connected to a dedicated ground of the mCBM experiment, preventing any EMI in the lines that may affect the performance. The mSTS enclosure is decoupled from the experiment table (no direct connection of any conducting elements). In reality, there are no perfect grounds, even in the same line there might be potential differences.

Figure 6.7 depicts the power distribution of the mSTS. The floating ground scheme for the sensors biasing circuity and the front-end electronics come with important boundary conditions for the powering - each module side requires a separate powering line [55]. In order to further reduce possible noise pickup, a return path capacitor was implemented at the FEB connectors and the HV common return (depicted as C-RTN) was connected to the enclosure.

6.3.2 Detector modules

The detector modules used to build mSTS differ not only in microcable lengths, and sensor size but also in the version of LDO regulators and DC/DC converters output voltage, which may affect parameters like power dissipation or the general performance (ENC levels). The module assembly is more broadly discussed in section 6.3.1. The respective components of each mSTS unit can be found in Table 6.1. Before assembling mSTS, extensive measurements of all the building blocks were performed. Figure 6.8 and 6.9 show noise measurements of two modules from different units. Unit 1 is the only unit used before for the previous mCBM campaign [183]. It is one of the oldest units, and it is also slightly irradiated, thus sensors leakage currents are higher than the new modules. The module of unit 1 (Figure 6.9) has larger noise and a more pronounced odd-even effect than unit 0 module. In both modules, the Z-strips (p-side channel numbers 0 to 134) are clearly recognizable.

Figure 6.9 also shows the estimated ENC values for different components of the module (sensor, microcables, and ASICs). The ENC estimation is based on a simple parameterization of the ENC versus capacitance for the STS-XYTER. The targeted ENC value

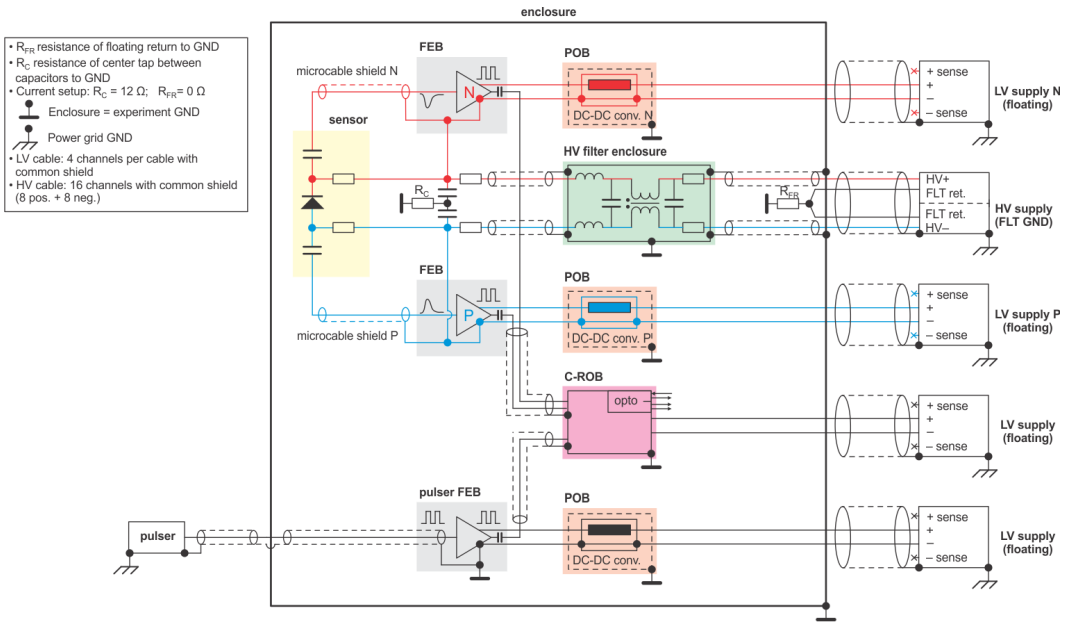

Figure 6.7: Power distribution scheme of the mSTS [182].

for mSTS modules is 1000 e, but the measurement outcome depends also on the sensor size, microcables length, and nuances of the assembly process. In the case of mSTS modules the targeted ENC value was achieved during the laboratory testing. Nevertheless, based on the obtained data and the ADC thresholds settings used during the data-taking campaign it was concluded that the ENC levels were higher than 1000 e.

Table 6.1: Description of the main components of mSTS units. During the module assembly, different versions of the components were used. An important difference was the use of SCL 1.8 V LDO regulators in combination with a diode to achieve the necessary 1.2 V operation potential in the ASICs.

Unit	Ladder	Silicon sensors	Microcables	DC/DC converters	STS-XYTER version	LDO regulators
0	0	62x62 mm^2 62x62 mm^2	490 mm 450 mm	2.5 V, 3 V	2.2	1.8 V and 1.2 V
1	0	62x62 mm^2 62x62 mm^2	490 mm 450 mm	2.5 V, 3 V	2.1	1.8 V and 1.8 V with diode
2	0	62x62 mm^2 62x124 mm^2	490 mm 420 mm	2.5 V, 3 V	2.2	2.4 V and 1.2 V
3	0	62x62 mm^2 62x62 mm^2 62x62 mm^2	490 mm 450 mm 420 mm	2.4 V, 2.4 V	2.1	1.8 V and 1.8 V with diode
3	1	62x62 mm^2 62x124 mm^2	490 mm 420 mm	2.4 V, 2.4 V	2.1	1.8 V and 1.8 V with diode

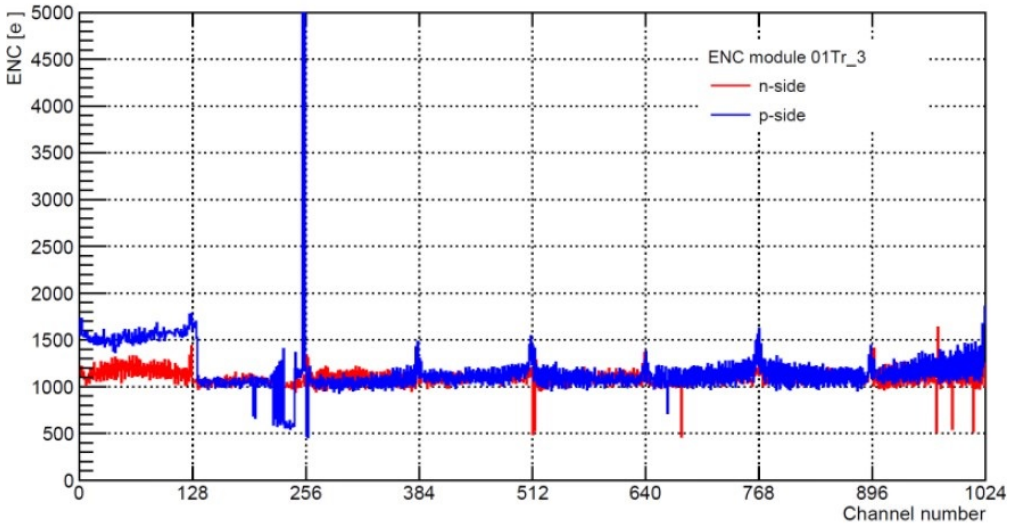

Figure 6.8: Equivalent Noise Charge for module 0 of unit 0 measured at the mCBM experimental site [184]. Values from all the analog channels (128 per chip) of the ASICs are depicted.

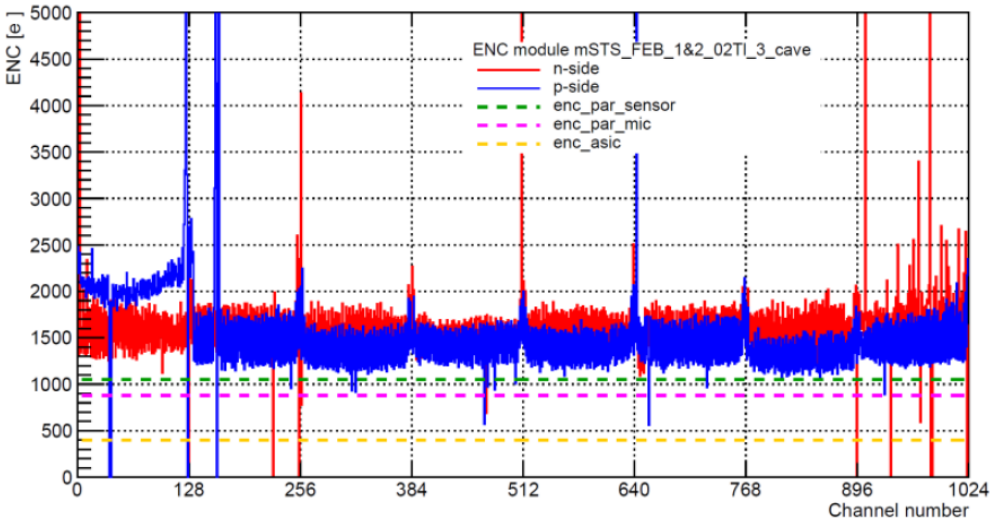

Figure 6.9: Equivalent Noise Charge plot for module 0 of unit 1 measured at the mCBM experimental site [184]. Three additional lines describing the noise contribution from ASIC, ASIC+microcables and ASIC+microcables+sensor are depicted.

6.3.3 Considerations about the detector cooling

In order to avoid overheating of the FEE and POBs, the electronics need to be cooled. The cooling system for mSTS is a water-based system, where the main heat exchange elements inside the detector are cooling plates. Three Lauda chillers [185] were used to pump chilled water through the cooling plate and efficiently evacuate excess heat. These chillers were also integrated into the control system via RS232-to-Ethernet converter.

Figure 6.10 depicts the bath temperature[2] during the 430 days of operation. Initially, mSTS was cooled with two Lauda chillers. During the data taking in June 2022, one of the chillers failed due to radiation-induced damage (depicted in Figure 6.10). Since a similar chiller was unavailable, two others, less powerful units were employed. Hence, the values from the third cooling unit can be seen only during the last months of operation.

Figure 6.10 also shows the dew point inside the mSTS, which should always be below the coolant temperature, in order to avoid condensation on the FEE. The coolant temperature that enters the detector is slightly higher (depending on the actual temperature in the experiment location). This difference ensures that there is no risk related to the condensation inside the detector. The dew point changes are summarized in Figure 6.10. It is calculated based on the measured RH and temperature, which change depending on the conditions (FEE on/off, seasons of the year). In addition to that, the mSTS enclosure is not tight, allowing air circulation.

6.3.4 Installation of the mSTS detector

Figure 6.11 depicts the assembly process of mSTS. Before transferring the detector to the mCBM experiment, modules of every unit were tested several times (to access the noise related performance by measuring ENC):

- Before ladder assembly
- After installation on the unit
- After assembling the C-frame in the mSTS enclosure

The detector services (LV, HV, cooling), as well as the optical fiber panel were installed on the mSTS enclosure front wall [186]. At that point, the detector was ready to be transferred to the experimental area and the commissioning began.

The first photo on the left side depicts the first c-frame after installing it inside the detector enclosure. The second photo shows one of the last stages of the detector assembly, where all detector modules are mounted. The last photo shows the detector after its transfer to the experimental area and the last checks related to detector services.

[2]The temperature of the water inside the chiller is considered a bath temperature.

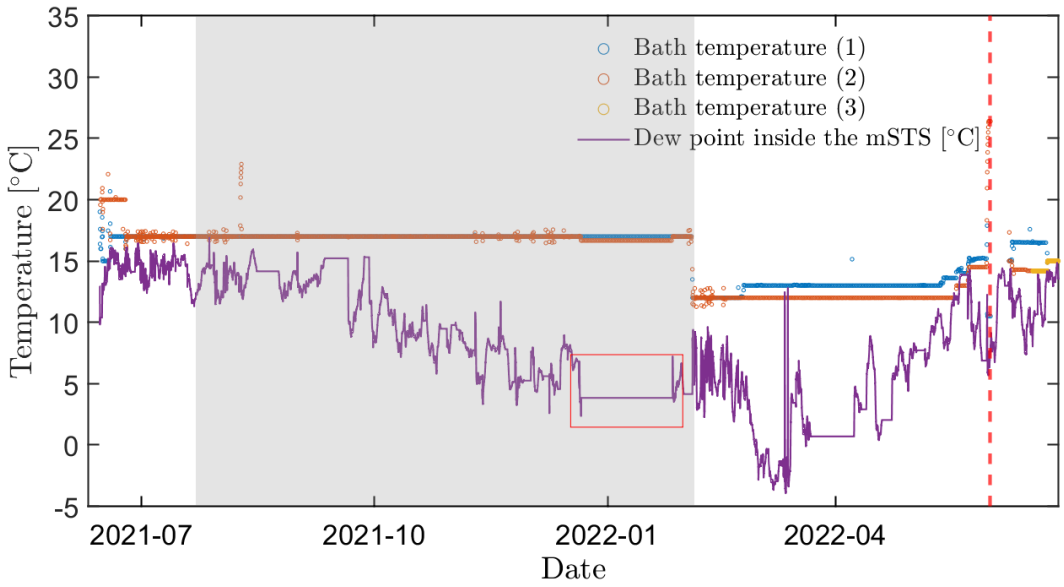

Figure 6.10: Temperature readouts of the three Lauda chillers used for the mSTS and the dew point inside the enclosure. The period without beam time is shown as a grey area. The red rectangle represents an example of the period when the system was completely off.

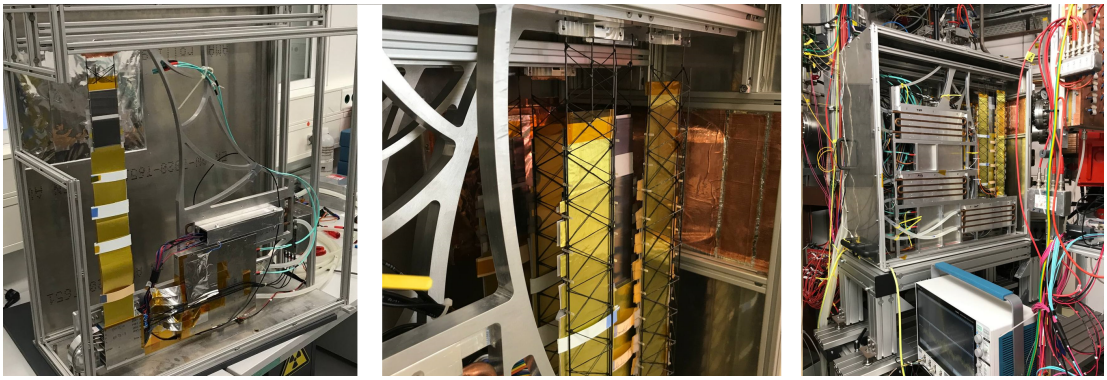

Figure 6.11: Assembly process of the mSTS (from left to right).

6.4 Operation of mSTS

The mSTS DCS is a fairly automatized system, in which monitoring and control are realized by the Finite State Machine. Critical parameters that are monitored with the DCS include leakage currents, temperatures, dew point, availability of the nodes as well as the overall system state (based on the FSM). All the logs are available either in Phoebus or Kibana, and the alarm server together with Phoebus takes care of notifying

the operator about alarms (exceeding limits, communication errors, etc.). The next section contains the summary of the most important findings which were obtained through the DCS.

6.4.1 Power dissipation estimations

Power consumption of the 11 modules (22 FEBs) of mSTS was studied in detail to better understand the differences between the modules and estimate how predictions meet the experimental results. The results obtained through the FEE were compared with the measurements of two separate front-end boards and average values from modules calibration. In order to compare the results, the CSA control registers (front and back register) of all STS-XYTERs were scanned from 7 to 42 with a step of 5. The power dissipation was calculated with Ohm's law 6.1 based on the voltage drops. For the mSTS the power was calculated at the power supply level

$$P = V \cdot I, \tag{6.1}$$

where V and I are the voltage change and current. Figure 6.12 depicts the powering scheme of a FEB. Table 6.2 contains the power dissipation values for different elements of the powering scheme in the function of the CSA registers values for measurements conducted with a separate pair of FEBs. The two mentioned FEBs were powered directly using a LV power supply (R&S HMP4040 [187]). The power dissipation estimations for the distribution lines and the DC/DC converters were performed based on the assumed efficiency of 80%. This efficiency drops to 65% at 10 °C with currents approaching the device output limit (3 A). Another assumption was also made for the voltage drop in the LDO regulators of 0.6 V.

In this case, due to the settings of the ASICs the currents for the digital line were slightly higher than expected values for the operation - around 2.3 A instead of 1.9 A. The current of analog lines (two 1.2 V LDO regulators) is mostly defined by the CSA register values, and in this case, varied from 1.4 A to 4.1 A. The voltage drop of every element in the distribution lines could not be accurately determined. Hence, the calculations were made for the distribution lines based on the currents measured for the FEBs and they can not be considered as a reference. A detailed description of the powering scheme can be found in section 6.3.1.

Table 6.2: Power dissipation of the powering system in the function of the CSA registers values. Once the ASICs are configured, the digital line current remains constant. The SMX ASIC is denoted as Integrated Circuit (IC).

CSA register	Power dissipation [W]				
	ASICs	1.8 V LDO regulator	1.2 V LDO regulator	DC/DC converter 3 V distribution lines	DC/DC converter 2.5 V distribution lines
15	5.28	1.38	0.84	2.97	1.29
63	10.26	1.38	2.46	2.97	6.36

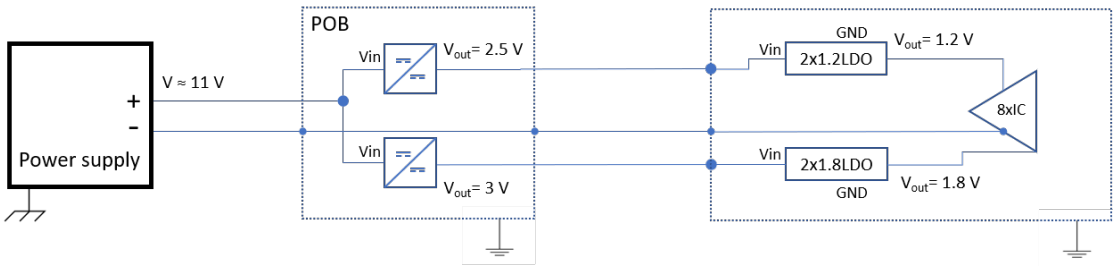

Figure 6.12: Schematics of the powering scheme of the FEB. The focus was put on the elements that contribute the most to the overall power dissipation.

Figure 6.13 illustrates the distribution of the power dissipation among the different elements of the powering system for different values of the CSA current. While increasing the power consumption of the ASICs, there is also a significant rise in the power dissipated by the DC/DC converters and distribution lines.

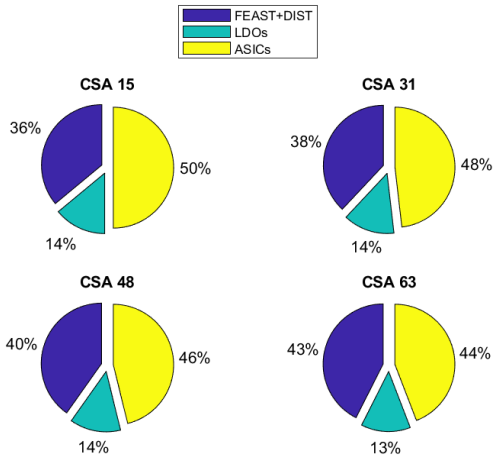

Figure 6.13: Power dissipation share of different elements of the power supply circuit as a function of the CSA value.

Figure 6.14 and 6.15 show the current drawn by 4 FEBs of unit 1 depending on the settings of the CSA. It was determined that the CSA value of 31 should be the nominal value for the STS modules. This value also ensures proper signal amplification, (CSA value of 31 corresponds to approximately 2 mA per analog channel). The CSA value may vary from ASIC to ASIC to address the different requirements of the modules (depending for example on their noise levels). In principle, the ASIC Analog Front End AFE is powered by two power domains (1.2 V - VDDM and 1.8 V - AVDD). By adjusting the CSA registers settings, the VDDM domain is influenced.

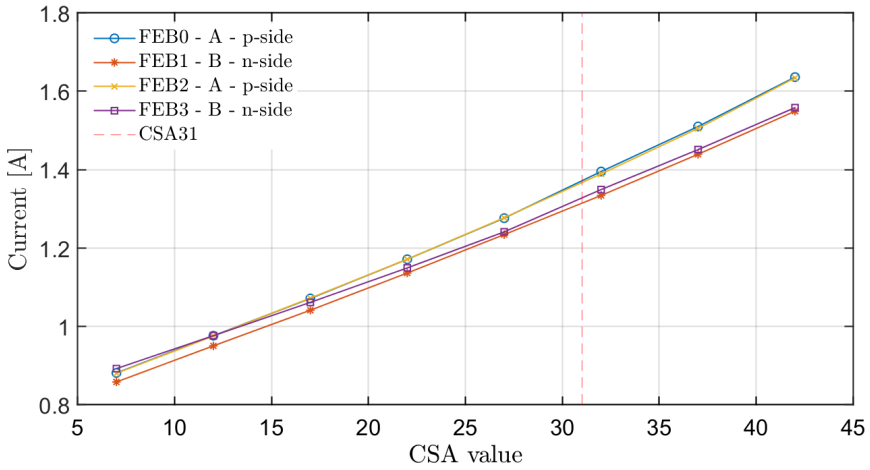

Figure 6.14: Low voltage FEB current measured at the power supply in the function of CSA settings of unit 2.

Similar measurements were also conducted for all the other detector modules (see Appendix B). The average values of the current for every unit are depicted in Figure 6.16. For the older modules, especially those powered by 2.4 V and 2.4 V DC/DC converters (unit 3), the currents are significantly higher, reaching 1.6 A - 1.8 A at the CSA 31. The AFE of the modules of unit 1 are powered by the 1.8 V LDO regulators with a diode, which causes a voltage drop of approximately 0.6 V. Nevertheless, this sub-optimal solution can be also seen via increased current and power dissipation of the unit 1 modules. The modules current of units 0 and 2 are similar, as they use the same components, which are also considered the final ones for STS.

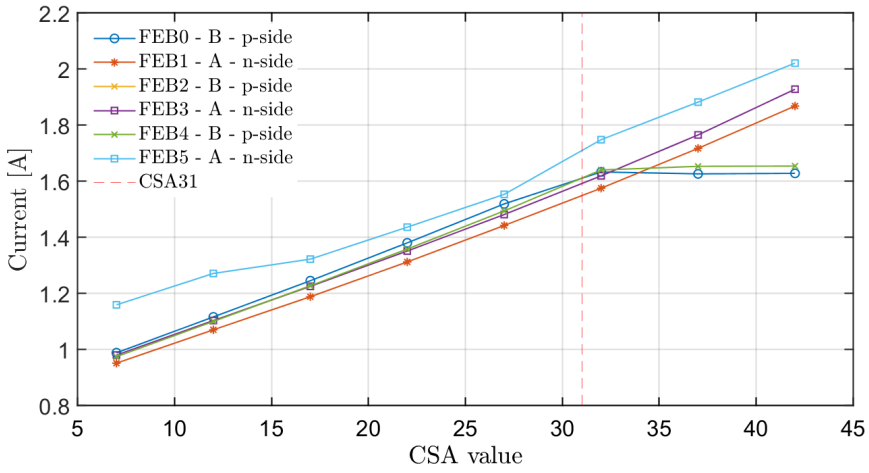

Figure 6.15: Low voltage FEB current measured at the power supply in the function of CSA settings of the unit 3 ladder 0. FEB2 did not respond during the testing.

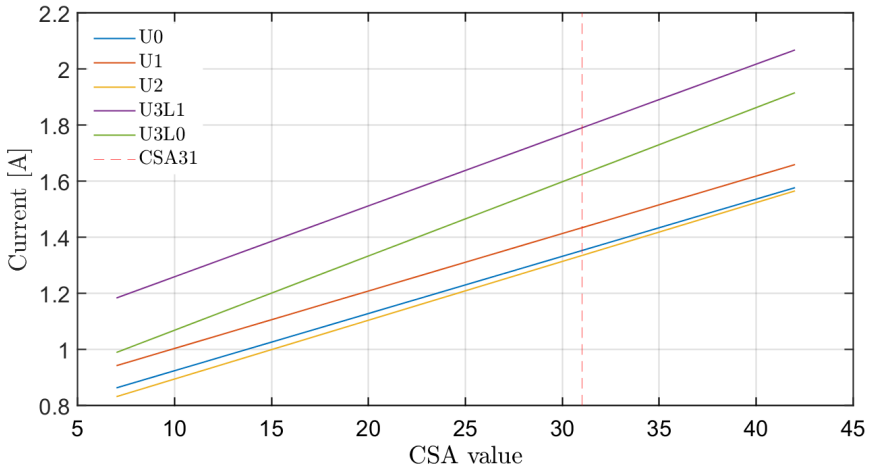

Figure 6.16: Average current of each mSTS unit.

The mSTS modules are powered in the constant voltage mode, which means that the output voltage is always 10.5 V. Knowing the currents at the power supply level, cable lengths, and voltage drops on subsequent components, it is possible to calculate the power dissipation. To estimate the power consumption based on the values from the module testing prior to the detector assembly. Average values of the currents are presented in Table 6.3. By adding estimates related to the distribution lines and DC/DC converters from figure 6.12 it is possible to compare these values with mSTS results.

Table 6.3: Currents drawn by the analog front end and to the digital part depending on the set CSA value.

CSA	Current digital [A]	Current AFE [A]
15	1.9	1.02
31	1.9	2.05
48	1.9	3.07
63	1.9	4.10

Figure 6.17 shows the comparison of the power consumption of mSTS units with the calculations based on the average current from the modules testing (depicted as FLA v2) and FEB currents measurement (denoted as FLA).

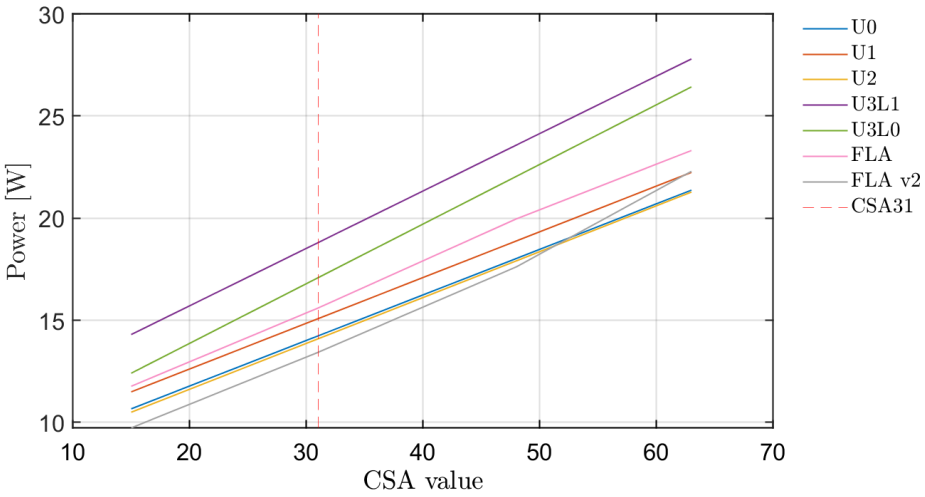

Figure 6.17: Average power dissipation of the units compared with predictions based on theoretical power dissipation in the components (depicted as FLA and FLA v2).

The estimation based on the average current from the modules testing has the lowest power consumption values up to CSA of 48. The values obtained from that estimation are close to those from units 0 and 2. These units are considered to be built from almost final components. Hence, the power consumption of these modules should serve as a reference for further calculations. Some parameters related to the voltage drop may change in STS, mostly due to different powering lines lengths and diameters of the wires, as well as different connectors. The values stated in Table 6.4 can not be considered as a reference. The results provide an estimation of the power consumption and also show how the module assembly evolved.

Table 6.4: Total power consumption of the 876 modules of STS based on the calculations from Figure 6.17.

	CSA 31	CSA 48
FLA estimation	23.5 kW	30.9 kW
Unit 3	30.2 kW	35.7 kW
Unit 2	26.7 kW	30.8 kW

6.4.2 Parameters monitoring and obtained data

All the software and hardware components mentioned in the previous sections deliver essential information about the detector safety and operational state. Thanks to the ongoing ambient monitoring, many issues of the subsystem were discovered and addressed, e.g., not sufficient cooling. Figure 6.18 shows the temperature trends obtained through DCS during the 430 days of operation. The first temperature sensor (depicted in blue) was placed at the top of the mSTS enclosure and the second one (depicted in orange) is located on the upper part of unit 2. Temperatures registered in mSTS vary not only depending on the FEE powering (peaks observed throughout the operation) but also on the temperature in the cave. The broader peak at the end of the studied period (red dashed line) is associated with the cooling unit failure. There are also a few periods, with the longest in December and January when the detector was not operated.

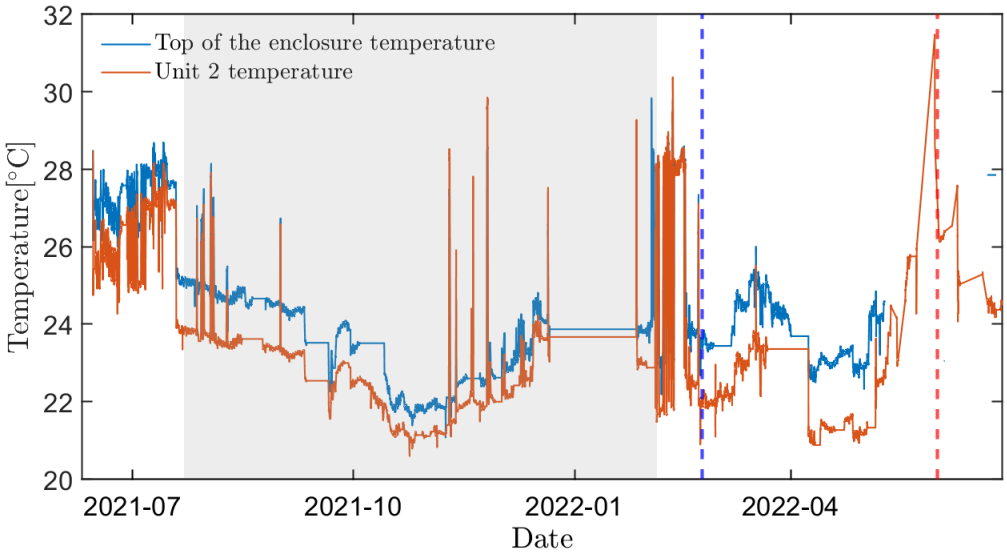

Figure 6.18: Temperature monitoring in the mSTS detector using PT100 sensors. The gray area refers to the period without any major data-taking activities.

To ensure the safe operation of the system, it was also necessary to have information about the dew point. Water condensation on the parts of the FEE could cause the electronics to fail. Figure 6.19 depicts the trends in the dew point and temperature over the mentioned period. The coolant setpoint was always carefully adjusted depending on the situation in the experimental cave, and it varied between 12 °C and 17 °C.

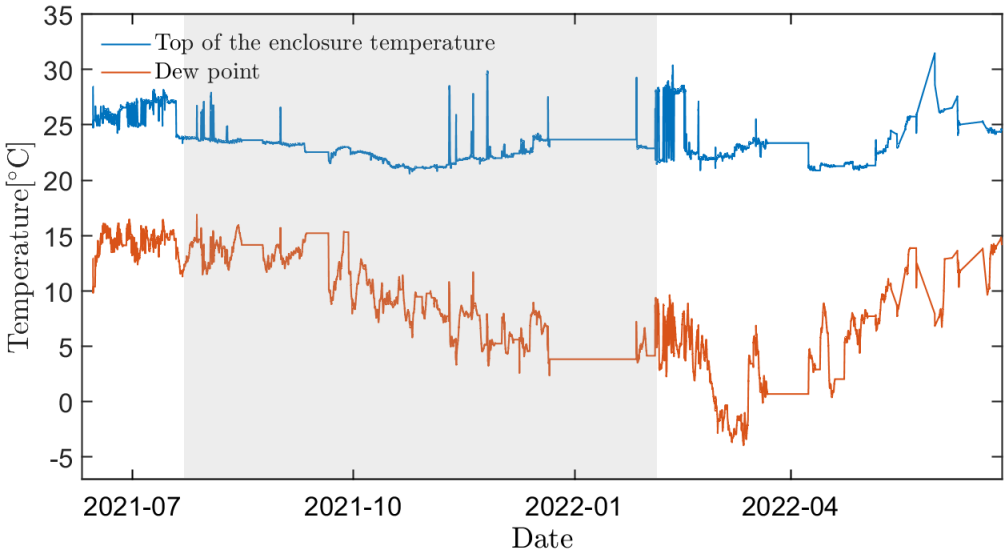

Figure 6.19: Temperature and dew point monitoring. Dew point calculations are based on the RH and temperature measurement of the SHT85 sensor.

Temperature sensors (PT100) are also used to monitor the temperature on the powering boards. A comparison of the temperatures on the POB of units 1, 2, and between two POBs of unit 3 are presented in Figure 6.20. The temperature measured in unit 3, especially at the beginning of the operation (depicted with the red rectangle), was much higher than those measured in units 0 and 1. This effect is associated with insufficient cooling which was resolved at the beginning of 2022. At the right end of the plot, cooling unit failure is also visible.

Additionally, the temperature on the ROB and FEB was monitored, as depicted in Figure 6.21. Interestingly, the temperature on the ROB is higher than the temperature on the FEB box on unit 2. Unit 2 features 2 modules, 4 FEBs (+ pulser board) in the FEB box (each drawing about 1.6 A at constant 10.5 V), in comparison to the ROB which is powered with 7 V and consumes about 0.8 A. This is, most likely, related to the better contact of the FEB box to the cooling plate.

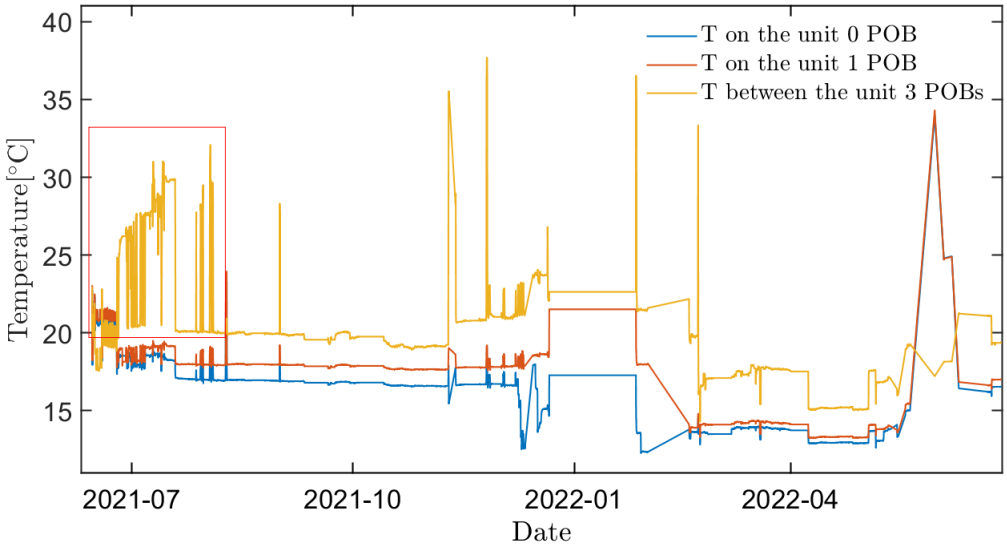

Figure 6.20: Temperature monitoring on the POBs enclosure using the PT100 sensors.

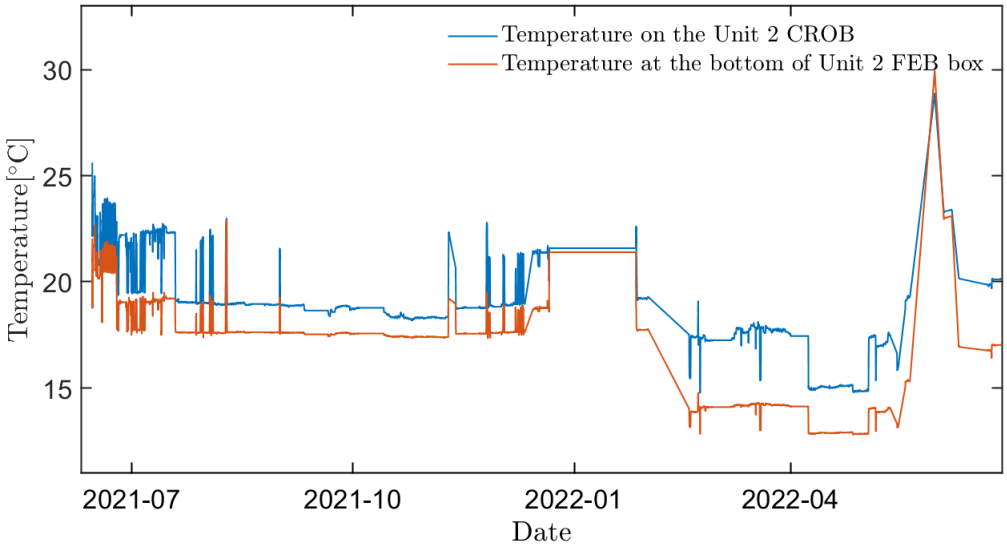

Figure 6.21: Temperature on the ROB, and underneath theFEB box using the PT100 sensors

6.4.3 Monitoring of the leakage current

Information about the temperatures serves not only to ensure detector safety but also to properly understand the behavior of the silicon sensors. Knowing the temperature trends over the irradiation period, it is possible to normalize the leakage current from different points to a certain reference value, e.g., 20 °C. Firstly, if the exact temperature

characteristic of the sensors is now known, it is necessary to rely on a temperature sensor placed close to the semiconductor. In the mSTS several temperature sensors are measuring ambient conditions, an overview can be seen in figure 6.22. The temperature inside the box is significantly lower, which indicates properly working cooling. Higher temperatures are also seen on the top of the detector, where the excess heat is not evacuated.

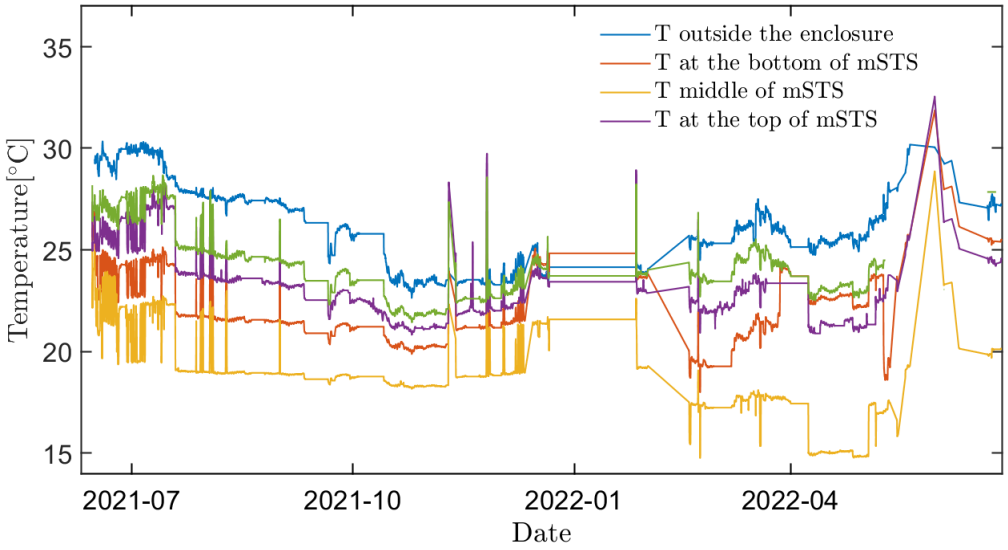

Figure 6.22: Comparison of the temperatures inside mSTS with the temperature in the experimental cave.

As the silicon sensors are symmetrically biased, the nominal operating voltage was chosen to be ±75 V (to assure full depletion of the non-irradiated silicon sensors). The reverse polarity also implies negative current values. In most of the plots, the leakage current of only one side of the silicon sensors will be shown. The other side of the sensor is characterized by the same trends but with opposite sign.

The leakage current changes of the STS silicon sensors during data-taking can be seen in figure 6.23. Due to radiation-induced surface and bulk damage, the leakage current increased with the increasing total fluence (as foreseen in the Hamburg Model). In order to properly compare the leakage current before and after the irradiation, it is necessary to have the same ambient conditions or to measure the temperature and then normalize the current to 20 °C. Apart from the constant rise of the leakage current during the data-taking, two particular parts of the plot can be distinguished. The first one just after 600 min, when increased beam intensity (about 10^8 ions/spill) caused the spill structure to appear. A similar trend can also be observed from around 1600 min. The sensors of different units behave slightly differently, depending on their position relative to the beam, sensor size, or possible differences in the assembly procedure.

An example of the normalization of the unit 0 sensors is depicted in Figure 6.24. A

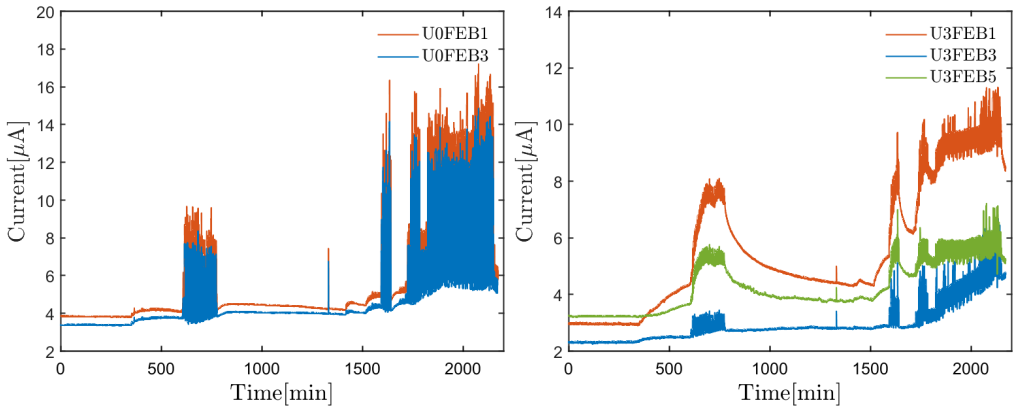

Figure 6.23: Leakage current of the silicon sensors in modules of units 0 and 3 during collisions of U ions with the Au target of different thicknesses.

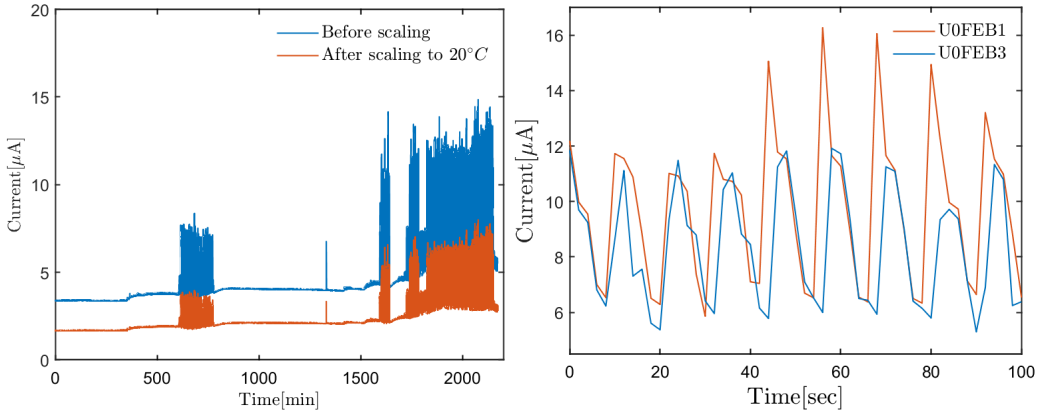

Figure 6.24: Unit 0 FEB 3- normalization of the current (left) and zoomed-in view of the spill structure seen by the silicon sensors (spill of 10 s length).

more detailed view of the spill structure is shown on the right plot. It can be clearly seen, that the reaction products traversing the silicons cause a significant leakage current increase of about 10 µA (for the highest beam intensities - 10^9 ions/s). Comparison of the average leakage current from two units after normalization to 20 °C is shown in Figure 6.25. Throughout the year 2021, only a few beam time campaigns took place. The increase in the leakage current due to radiation-induced damage is negligible. On the other hand, during the beam campaigns of 2022, the effect of radiation can be clearly seen. The leakage current value obtained for module 0 of unit 3 differs from the performance of other modules, indicating an electrical problem.

The quantitative current changes over the mCBM campaign are shown in Table 6.5. To better understand the overall results, it is important to take a look at the position of the silicon sensors with respect to the beam (see figure 6.26). The sensors located

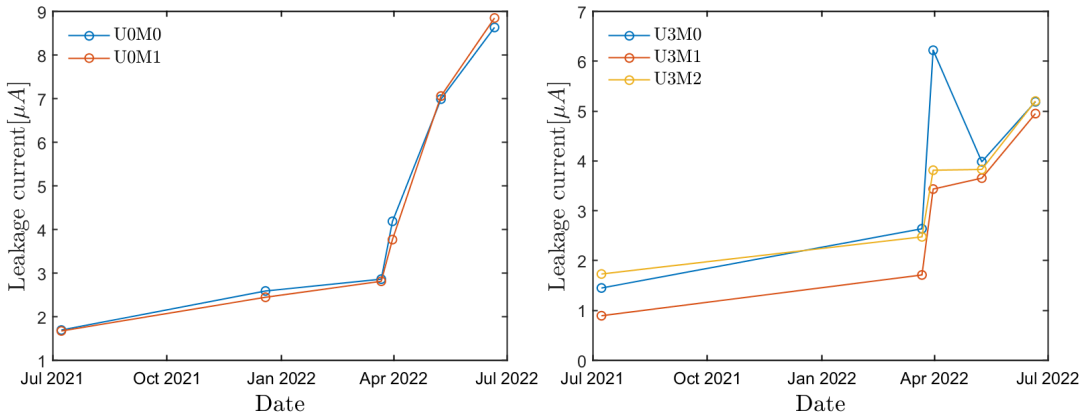

Figure 6.25: Average leakage current evolution of the mSTS sensors over the 430 days of operation.

closer to the collision point (from unit 0) are more irradiated than sensors from units 2 and 3. Furthermore, the results obtained from unit 3 are inconsistent throughout the experiment, which means that those modules seem to experience electrical problems (e.g., short circuits). By applying the formulas introduced in Chapter 2.2, it is possible to estimate the fluence accumulated by the sensors based on the leakage currents differences (Table 6.5). The major uncertainty is connected to the damage coefficient (α). The α of $5,53 \times 10^{-17}$ A/cm was chosen based on the analysis prepared by [188].

Table 6.5: Leakage current differences and corresponding fluence estimations based on the Hamburg model for all the mSTS modules.

Module	Current difference [uA]	Fluence [n/cm$_2$]
U3L1M0	16.2	2.5×10^{11}
U3L1M1	7.6	5.8×10^{10}
U3L0M0	3.7	5.7×10^{10}
U3L0M1	4.1	6.2×10^{10}
U3L0M2	3.5	5.3×10^{10}
U2M0	3.6	5.5×10^{10}
U2M1	6.3	4.8×10^{10}
U1M0	6.4	9.8×10^{10}
U1M1	6	9.1×10^{10}
U0M0	6.9	1.1×10^{11}
U0M1	7.2	1.1×10^{11}

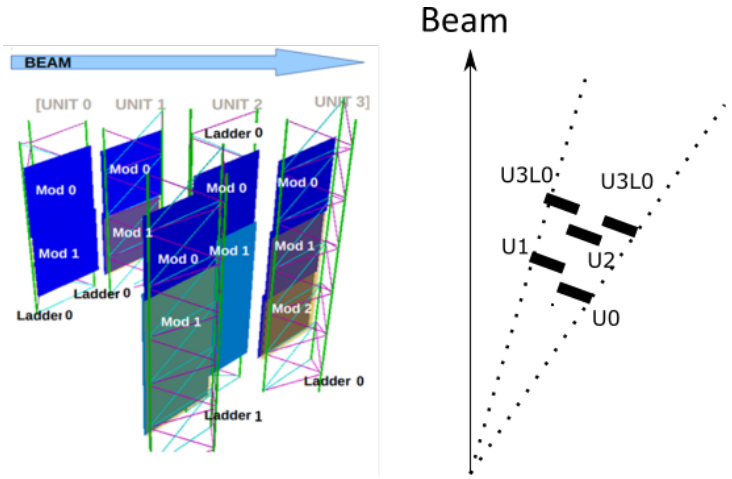

Figure 6.26: Schematic view of the mSTS sensor position with respect to the beam.

6.4.4 Current-voltage characteristic of chosen modules

The dependence of current on the biasing voltage provides (IV) crucial information about the detector performance (see section 2.3.1):

- Shot noise, closely related to the leakage current, which increases with the fluence
- Type inversion
- Annealing, and reverse annealing processes

Figure 6.27 shows IV curves of two selected modules from two different units (1 and 3) measured before assembly and at different moments of the module operation in the mSTS. Leakage current measurements are scaled down to 20 °C but the relative humidity was different for each measurement. The IV measured during the QA procedure before the assembly of the module is depicted in yellow and shows a typical behavior of a reverse-biased silicon diode with a full depletion reached around 60-70 V. The two other IV measurements for each module took place after assembly in mSTS, the beam campaign with the U ions beam, and at the end of data-taking for 2022. The linear behavior of the sensors can be seen after the module assembly, measuring with an external high-voltage filter in a floating scheme and low-voltage powering lines. Even though it is difficult to distinguish the point of full depletion, the current was still in the expected range. The unit 3 sensor shows a breakdown at a similar biasing voltage for all three measurements.

Figure 6.28 shows the IV measurement of a module assembled similarly to the ones used in the mSTS detector. This module was tested without additional HV filter, LV connection, and the Keithley [189] power supply instead of ISEG HV module. The HV filter was integrated into the new version of the FEB (FEB8-3).

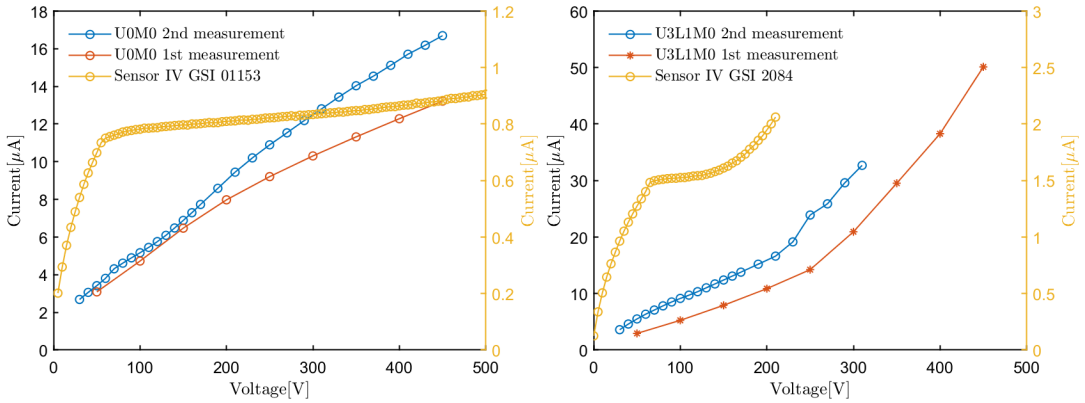

Figure 6.27: IV curves for two modules from different mSTS units (Left: module 0 of unit 0, right: module 0 of ladder 1 of unit 3). Silicon sensors were tested in the clean laboratory (yellow curve), then subsequently after the first beam time (with U ion beam) and at the end of the test period in June 2022 (second measurement).

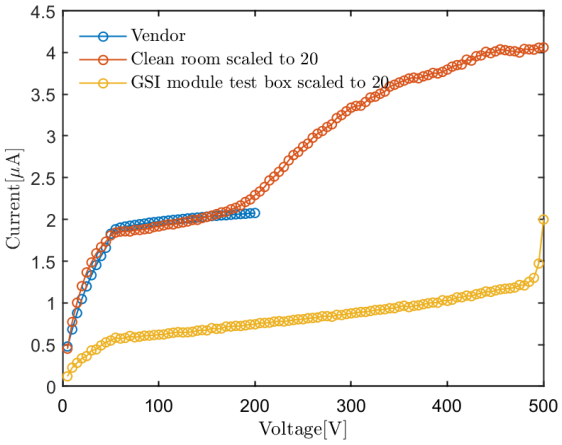

Figure 6.28: IV curves of another silicon sensor measured by the vendor before shipping, before the assembly, and then after it.

Linear behavior of the current-voltage characteristics from Figure 6.27 indicates a resistive element added to the circuitry, which is related to the LV power supply. The system is operated in the floating ground scheme. The LV power supplies in reality are not completely floating, but they have a floating regulator which starts conducing current above a certain threshold voltage. Since the system is highly integrated and compact, it's not always possible to remove the LV connection to the module, hence the unwanted resistive part persists. Therefore, when measuring the IV we do not only observe the typical IV curve for the silicon sensor in reverse mode but also the resistive behavior coming from the LV power supply.

6.4.5 Data rates and leakage current

Data rates from subsystems contain essential information about the detector performance. Figure 6.29 shows an example of the mCBM Au+Au system (T = 1 AGeV) and later with Ni+Ni system, due to reaching the maximum data transfer (without the mSTS detector). Data rates are clearly correlated with the beam intensity. Regardless of the beam intensities, mSTS (with the chosen settings) is responsible for more than half of the total data. During the beam intensities of 10^8 ions/s, mSTS data rate was around 500 MB/s, and with the maximum beam intensities, it scaled up 2000 MB/s, reaching the limits of the data transmission for a FEB 8 with 2 uplinks per ASIC.

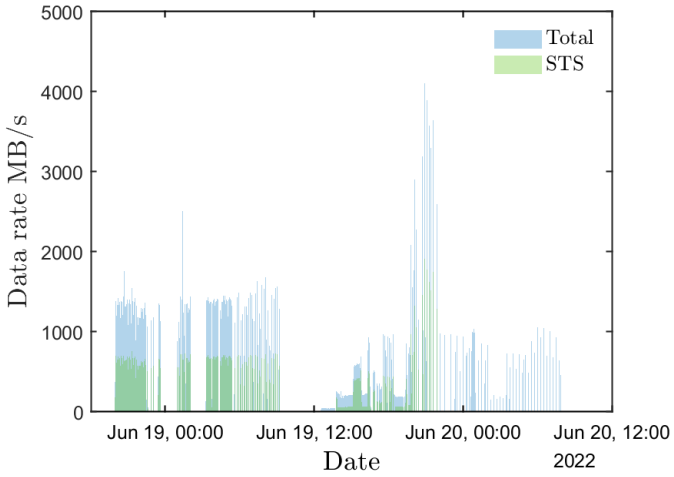

Figure 6.29: Data rates of all the mSTS units in comparison to the overall data rate of all subsystems during data-taking.

There is a direct correlation of the leakage current increment with the beam intensity, which also determines the mSTS data rate (see Figure 6.30). This correlation gives more insight into the operation and state of the silicon sensors.

6.5 Conclusions

The successful operation of the mSTS, including the DCS and DAQ chain, set an important milestone toward the completion of the STS project. The first extensive and successful data-taking activities with two tracking stations concluded the commissioning of the mSTS detector. The prototyping of the DCS supervisory layer of mSTS took place, and it was successfully implemented, proving that the concept was extremely flexible and useful, not only for large detectors, and accelerator setups but also for smaller experiments. After almost two years of operation, container based system was found to be a reliable, easily maintainable solution. Yet, for the final system, several additional applications are needed. The STS detector will be much more complex and

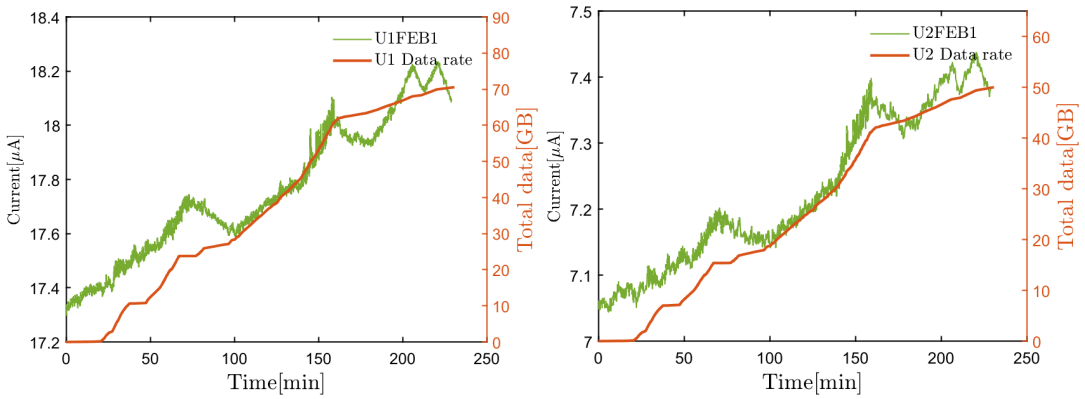

Figure 6.30: Leakage current evolution of the mSTS silicon sensors and respective integrated data rate.

challenging when it comes to configuration and operation. For the final setup, it will be extremely important to have both hardware and software interlocking to ensure the machine safety.

mSTS did not publish its overall status to any external software agent. Due to that reason, some information like ASIC internal temperature or VDDM were only accessible via the data acquisition chain (DCA-CRI). In the future, each subsystem will have an assigned Subsystem Control Agent (SCA) to tackle control of the readout chain and the DCS.

Temperature sensors located inside the mSTS and information about the current drawn by the sensors indicate the silicon sensors state. The sensors may degrade over time due to radiation-induced damage, which leads i.a. to the leakage current increase, type inversion, etc. Those effects can be partially studied through the DCS and the control strategy adopted respectively to the results.

Figure 6.31 shows how the DCS performed during about 2 years of operation. Due to the radiation-induced soft errors in the controllers of the cooling units, there were several occasions that the operation of the STS had to be halted. Usually, such an interruption in the operation was automatically triggered by the FSM. Listed errors might also include the intervention in the system. In that case, the error related to the cooling system was logged, but the FSM might have been off.

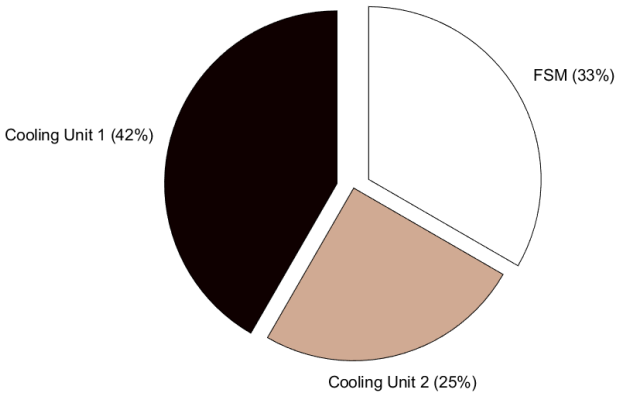

Figure 6.31: Results from the operation.

Chapter

7 Summary and overview on DCS toward the full STS system

The first section of this chapter covers the next major STS milestone, which is the thermal demonstrator. The next section gives an outlook for the STS and the foreseen developments of the DCS. Finally, the major achievements of the thesis will be highlighted and shortly described.

7.1 Thermal Demonstrator

Another important milestone toward the assembly of STS is the thermal demonstrator. Its aim is to test dummy silicon sensors and electronics parts under realistic mechanical boundary conditions and to experimentally demonstrate the feasibility of STS's cooling concepts.

Figure 7.1 depicts the thermal demonstrator with the respective dummy detector modules. These objects are placed on carbon fiber ladders and mounted in the C-shaped aluminum frames. The power dissipation of the whole dummy structure mirrors the actual power dissipation of a detector module.

The excess heat has to be evacuated in order to prevent the silicon sensors from thermal runaway and to avoid reverse annealing. This scenario is going to be exercised in the thermal demonstrator. It is going to be achieved with a 3M 649 NOVEC-based cooling system. The lowest temperatures that the demonstrator will experience, reach down to $-40\,°C$.

Due to the low temperatures inside the system, the frost point needs to be kept at values below $-45\,°C$. To achieve this, a dedicated air drying system was developed and will be tested together with a sampling system and fiber optic sensors for the dew point and humidity measurements, respectively.

The ambient conditions inside the demonstrator will reach similar ones as during the STS operation. The thermal demonstrator serves not only to demonstrate and evaluate

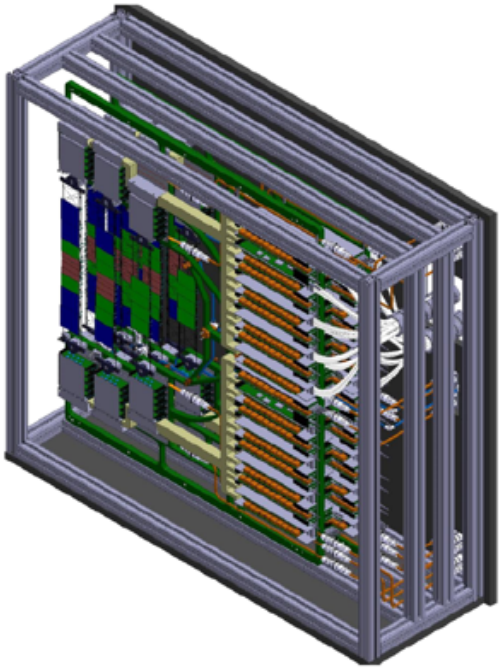

Figure 7.1: Computer aided design of the thermal demonstrator [190]. The dummy modules are mounted onto carbon ladders and placed in the C-frames, as the silicon detectors will be.

the cooling of the STS but also to perform long-term humidity and dew point measurements with the FOS and sniffing system described in Chapter 5. Therefore, is a unique opportunity to test the temperature, RH, and dew point sensors.

Apart from the humidity sensors, the thermal demonstrator features also temperature sensors:

- to evaluate the performance of the cooling plate and the thermal interfaces, each dummy FEB is populated with 3 temperature sensors,

- to assess how much heat should be dissipated by the dummy silicon sensors. Each dummy sensor has two temperature sensors.

A few services including the cooling plant that delivers the cooling liquid to the test objects, humidity sensors but also interlocks, and control strategies can be developed and then adjusted for the STS. Hence, the thermal demonstrator is also a perfect opportunity to develop control system applications that will reduce the commissioning time of the STS. In this case, further improvements of the containerized framework

should be considered, e.g., orchestration[1] of the containers. The next sections focus on the further improvements of the DCS in order to have a reliable and easy-to-maintain solution for the final systems.

7.1.1 Outlook for the DCS software services

Software applications introduced in the thesis proved to be extremely useful for small and medium size setups (up to a few thousand PVs. Nevertheless, for the final experiment, a more sophisticated software infrastructure is needed.

The final system will feature an orchestrator which should be scalable, highly available, provide logging, and monitoring capabilities, and be redundant. Orchestration leads to automation of the container deployment, as well as to balance the workload. Orchestrators can:

- Automatically deploy containers based on policies, application load, and environmental metrics.
- Identify failed containers or clusters and heal them.
- Manage application configuration.
- Connect containers to storage and manage networking.
- Improve security by restricting access between containers, and between containers and external systems.

Examples of orchestrators include DockerSwarm [191], and Kubernetes [192]. One of the recent applications of Kubernetes was reported in [193], where the whole test beam line is operated with containers. Similarly, the whole CBM DCS could be operated with containers and orchestration tools.

Apart from the orchestration, the DCS should be supplemented with:

- Gateway(s) - considering the low voltage powering of the STS FEE, which consists of about 2100 low voltage channels, 140 modules, and 14 crates. Each crate has a controller with an embedded IOC, publishing all the process variables. By putting the power supplies into a different subnet or network, it is possible toe easily debug potential problems and limit the network traffic. That is why it has been endorsed to use CA Gateway [194] or PV gateway, which will take care of regulating access between the subnets in the DCS network. It also provides additional access security, assuring that the IOCs running the key services like powering run smoothly.
- Time synchronization - as mentioned in Section 3.6.2, the archiver could be split into a few nodes serving as temporary data storage (short-term, mid-term).

[1] Orchestration is the coordination and management of computer systems, applications, and/or services.

Proper daily backup to GSI managed database would be recommended, but it depends mostly on the database services provided by the GSI IT. So far, the Redis DB has been used, but also other options should be considered.

- Logbook - one of the missing elements in the mSTS architecture is a logbook. So far, for all the mCBM-related activities, elog [195] was used. For the final experiment, a dedicated elog branch will be implemented and the elog client will be used [196],

- Save and restore service - it is organized twofold. A tool, called autosave, which is a part of the synApps module [197] preserves PVs values through the IOC reboot. The second set of tools that permits taking snapshots and saving configurations is MASAR [198]. It is a more complex tool than autosave, offering also a Phoebus-based GUI.

- Data persistence - to properly archive and analyze the data, it is necessary that all nodes, IOCs, and other software applications are synchronized. As it is impossible to adjust the clock in the containers, it should be synchronized on each node separately. The central DCS node will provide a Network Time Protocol (NTP) daemon that will be synchronized with one of the public, official sources. By doing so, the clocks of all the containers running control applications will be automatically synchronized even if the external network connection is not available.

- Communication protocol - it was reported during the EPICS Collaboration meeting 2022 [199] that the transition to the newer protocol (PV access) is ongoing. Nevertheless, CA and PVA are both included in the EPICS 7, which should be the base image of the CBM IOC image, and also for the next versions of the IOC. PVA is under constant development and will offer even more features in the coming years, thus for the future CBM experiment (timeline of more than 10 years), it is an optimal choice.

7.1.2 Failover considerations

The high availability of services plays a key role in the safe operation of a detector. Once all the services are deployed, only short breaks are foreseen during 10 years of operation. The STS has to be constantly cooled, in order to avoid performance degradation of the silicon sensors and FEE.

Crucial elements of the STS, like the air drying plant or the cooling plant, will be monitored and controlled by a PLC-based system. This hardware layer will provide essential safety measures in case of failure. The PLC will also be linked to an IOC publishing the values to the software layer.

Even before triggering the hardware interlock, any potentially hazardous system behavior will be discovered by the software of the control system. In order to ensure

maximum safety, failover mechanisms will be exercised to mitigate potential IOC failures. There are two considered methods to address failover:

1. Considering a scenario in which the hardware is controlled, e.g., via a network. In that case, it is possible to deploy a backup IOC, which has the same configuration as the main IOC, therefore providing a replacement if it fails. Under some standards, like example RS232, it is not considered good practice to have two IOCs connected to the same node. Furthermore, in the case of RS232 a multiplexer would be needed to implement a redundant solution.

2. A second possibility is to use failover mechanisms based on an orchestrator, in this case, the deployment and life cycle of a container is governed by an additional tool, i.e., Kubernetes. In case one of the containers (IOCs) hangs up, it will be automatically stopped, and a new container will take over the tasks. Nevertheless, the newly deployed container could have a different configuration, therefore changing the state of the whole system.

7.2 Final remarks

The scope of the thesis focused on developing a modular control system framework that can be implemented for small, medium, and large experimental setups. This framework was used for setups that required a remote operation, like the irradiation of the powering modules for the FEE, but also in laboratory-based setups where the automation and archiving were needed (thermal cycling of the STS electronics).

With the help of the EPICS related applications, it was found that the low voltage powering module will experience soft errors of up to 9 per month during the CBM operation. Such behavior poses a risk to the experiment operation as it could cause deterioration of the physics performance, but also a possible danger to the FEE. On the other hand, the HV channels would be switched off even more often, but in the case of the CBM they are located far away from the experimental site.

It was further assessed what are the limitations of the FEBs with respect to the thermal cycling and the mechanical stress that is therefore induced. The results served as an indication of possible failure modes of the FEB at the end of STS lifetime. Failure modes after repeated cycles, and potential reasons were determined (e.g., CTE difference between the materials).

Another application of the developed framework was related to the testing and characterization of the humidity sensors. A general strategy for ambient parameters monitoring inside the STS was developed, and potential sensor candidates were chosen. A sampling system with a ceramic sensor and FOS were identified as reliable solutions for the distributed sensing system. Additionally, the industrial capacitive sensors will be used as a reference during the commissioning.

The FOS hygrometer turned out to be a more reliable solution in comparison to a sensor array. One of the possible reasons of worse performance is a relatively low dis-

tance between the subsequent sensors and a thicker coating. The results obtained from the time response study pointed out that the thinner coating of about 15 μm should be a good compromise between the humidity sensitivity and the time response.

Chapter 6 focused on the main implementation of the containerized-based control system framework for the mSTS. The deployed system proved to be a reliable solution and ensured the safety of the detector for almost 1.5 years. Moreover, the data related to the performance of the detector modules were analyzed and significant progress in the quality of modules is observed. Obtained data was also used to estimate the total fluence, which was based on the leakage current changes.

Zusammenfassung

Die Facility of Antiproton and Ion Research in Europe (FAIR) [21] ist eine internationale Initiative zur Schaffung einer Forschungseinrichtung für beschleunigerbasierte Forschung. Sie wird einzigartige Forschungsmöglichkeiten in den Bereichen Hadronen- und Kernphysik, Atomphysik, nukleare Astrophysik, Materialforschung, Plasmaphysik und biologische Strahlungsphysik bieten, einschließlich der Entwicklung neuartiger medizinischer Behandlungen und Anwendungen für die Weltraumforschung [22].

Das Compressed Baryonic Matter (CBM) ist eines der Kernexperimente in FAIR. Das Ziel des CBM-Forschungsprogramms ist die Erforschung des QCD-Phasendiagramms im Bereich hoher Baryonendichten mit Hilfe von hochenergetischen Kern-Kern-Kollisionen. Das STS ist ein zentrales Detektorsystem des CBM, das in einem 1 Tm untergebracht ist und bei einer Betriebstemperatur von etwa −10 °C arbeitet, um den strahlungsinduzierten Volumenstrom in den 300 µm doppelseitigen Silizium-Mikrostreifensensoren niedrig zu halten. Neben dem STS verfügt das CBM-Experiment über einen Mikro-Vertex-Detektor (MVD), einen Ring-Imaging-Tscherenkov-Detektor (RICH), Übergangsstrahlungsdetektoren (TRD), einen Flugzeitdetektor (TOF) und einen Projektil-Spektraldetektor (PSD).

Silicon Tracking System

Die physikalischen Beobachtungsgrößen bestimmen zusammen mit der vorgesehenen Beschleunigerenergie und Strahlintensität die Anforderungen an das Detektorsystem. Das STS ist für die Spurrekonstruktion sowie für die Impulsbestimmung der geladenen Teilchen ausgelegt. Diese Teilchen entstehen bei Kollisionen eines Ionenstrahls mit Energien zwischen 3 AGeV und 14 AGeV (Protonen 29 GeV) mit einem Target. Bei einer zentralen Au+Au-Kollision entstehen zum Beispiel bis zu 700 Spuren. Das STS erstreckt sich über mehr als 1 m stromabwärts des Targets und wird in einem Volumen von 3 m^3 installiert.

Das STS umfasst acht Tracking-Stationen mit 876 Modulen. Jedes Modul wird kalibriert und getestet, um seine Leistung zu ermitteln. In den nächsten Schritten wird das Modul auf einer Kohlenstoffleiter montiert, und anschließend werden diese Objekte vertikal auf sogenannten C-Frames angeordnet.

Der Schwerpunkt dieser Arbeit lag auf der Entwicklung eines universellen Kontrollsystems, das auf das Silicon Tracking System (STS) ausgerichtet ist. Das entwickelte

Framework wurde in einer Reihe von Test-Setups verwendet, von kleinen bis hin zu kompletten Implementierungen der Detektor-hardware. Das Ziel dieser Arbeit ist es, das Kontrollsystem zu entwickeln und die mit ihm erzielten Ergebnisse aufzuzeigen.

Online-Systeme und ihre Aufgaben

Für das Hochgeschwindigkeits-CBM-Experiment spielt das triggerlose Datenauslese- und Erfassungssystem eine entscheidende Rolle. Die mit Zeitstempeln versehenen Signale werden ohne Ereigniskorrelation ausgelesen und an eine Hochleistungs-Rechenfarm, den GSI Green IT Cube, übertragen. In einem ersten Schritt werden die Spuren der geladenen Teilchen aus den Raum- und Zeitinformationen der verschiedenen Detektorsignale rekonstruiert. Anschließend werden die Teilchen identifiziert, wobei sekundäre Zerfallspunkte und Informationen aus RICH oder MUCH, TRD und TOF berücksichtigt werden. Schließlich werden die Teilchen zu Ereignissen gruppiert, die zur Speicherung ausgewählt werden, wenn sie wichtige Observablen enthalten. Parallel dazu werden das Ereignis und seine Ebene anhand von Informationen aus dem PSD charakterisiert. Ein weiteres wichtiges Online-System wird Experiment Control System (ECS) genannt und besteht aus einer Softwarestruktur, die die Automatisierung, Überwachung und Steuerung der Hardware und der Detektor-Subsysteme ermöglichen soll. Das Detektor-Kontrollsystem (DCS) ist eines der wichtigsten Online-Systeme.

Detektor-Kontrollsystem

Experimente der Hochenergiephysik erfordern komplexe Kontrollsysteme, die für den erfolgreichen Betrieb der Anlage entscheidend sind. Die ordnungsgemäße Implementierung solcher Systeme gewährleistet höhere Sicherheitsmargen und eine bessere Qualität der Datenproduktion. Im Allgemeinen sollte das gesamte System robust, partitioniert, modular, verteilt, mobil und hochverfügbar sein. Ähnliche Themen wurden auch bei der Entwicklung des STS-Steuerungssystems berücksichtigt.

Experimental Physics and Industrial Control System (EPICS) und die zugehörigen Toolkits können zur Steuerung großer Experimente oder sogar Strahllinien verwendet werden, aber auch für kleinere Experimente, bei denen nur begrenzte Funktionalitäten benötigt werden (z. B. Datenvisualisierung, Archivierung und Datenbank). Um die Hardware zu testen, die für das endgültige Experiment verwendet werden sollte, wurden viele relativ kleine Forschungs- und Entwicklungsprojekte (einige Hundert Prozessvariablen) gebaut und betrieben. In den beiden folgenden Abschnitten werden die Anwendungen des entwickelten Softwarepakets zur effektiven Steuerung und Datenerfassung in zwei ausgewählten Versuchsaufbauten vorgestellt. Der erste Abschnitt befasst sich mit den Studien zur Bestrahlung der Stromversorgungseinheiten und den Auswirkungen auf die STS. Anschließend werden die Ergebnisse der zyklischen thermischen Tests der STS-Elektronik vorgestellt und diskutiert. Ziel der thermischen Zyklusstudien war es, die Ggrenzen des Frontend-boards (FEB) zu ermitteln.

Bestrahlung von Stromversorgungsmodulen für Niederspannungselektronik

Die Niederspannungsversorgung der Frontend-Elektronik wird in der Experimentierhalle installiert sein. Die Frontend-Elektronik der STS wird von etwa 140 Niederspannungsmodulen gespeist. Angesichts der Tatsache, dass einige dieser Module im schlimmsten Fall etwa 40 mGy/Monat ausgesetzt sein werden, ergibt die Messung, dass etwa 9 SEE pro Monat und Modul auftreten werden. In der Praxis bedeutet dies, dass jedes FEB bis zu 9 Leistungszyklen bei niedrigen Temperaturen pro Monat aushalten muss. Geht man von einem Betrieb von 2 Monaten pro Jahr und einer voraussichtlichen Gesamtbetriebsdauer von 10 Jahren aus, muss die Elektronik mindestens 180 Stromzyklen bei niedrigen Temperaturen von etwa -20 °C standhalten. Andererseits würden die Hochspannung-Kanäle noch häufiger abgeschaltet, aber im Fall der CBM befinden sie sich weit entfernt vom Versuchsbereich.

Thermisches Zyklieren von STS-Elektronik

Insgesamt wurden 12 FEBs untersucht, um die Randbedingungen für den Temperaturbetriebsbereich zu finden. Die durchgeführten thermischen Zyklen führten zur Bestimmung der Grenzen der FEBs, nämlich Ausfälle im Zusammenhang mit den Niederspannungsregler (LDO Reglern). Die Ergebnisse dienten als Hinweis auf mögliche Versagensarten des FEB am Ende der STS Lebensdauer. Die Versagensarten nach wiederholten Zyklen und die möglichen Gründe wurden ermittelt (z. B. Wärmeausdehnungskoeffizient Unterschiede zwischen den Materialien).

Lösungen für die Feuchteüberwachung in STS

Die dritte Testaktivität, die eine wichtige Forschungsarbeit für das STS darstellt, bezieht sich auf die Entwicklung und Prüfung verschiedener Sensoren für relative Luftfeuchtigkeit und Temperatur. Aufgrund der rauen Bedingungen im Detektor ist die Auswahl der Feuchtigkeitssensoren eine wichtige Aufgabe, die eine wichtige Aufgabe, die die Betriebssicherheit des Detektors gewährleisten soll. Ein Überblick wurde geschafft über die verschiedenen Lösungen für die Erfassung der Umgebungsparameter und beantwortet die Frage, ob die getestete Technologie den Anforderungen entspricht. Die meisten Anstrengungen wurden unternommen, um faseroptische Sensoren zu charakterisieren und anschließend Sicherheitsanforderungen und Systeme zu entwickeln, die potenziellen Risiken, die z. B. durch eine zu feuchte Umgebung entstehen, entgegenzuwirken.

Die Charakterisierung der Faseroptische Sensoren brachte Informationen über die Vorteile und Grenzen dieser besonderen Technologie mit der Verwendung von Polyimid als empfindlichem Material. Im Prinzip erfüllt das getestete Hygrometer die für die STS gestellten Anforderungen. Das verteilte System wird das Probenahmesystem, Faseroptische Sensoren (FOS) und kapazitive Sensoren umfassen. Ein Array von Sensoren könnte noch in Betracht gezogen werden, aber der Abstand zwischen den Gittern

sollte viel größer als 15 cm sein, um sicherzustellen, dass die Sensoren spannungsfrei verpackt werden können.

Die Faser-Bragg-Gitter-basierten können FOS als Strahlungsfest angesehen werden. Nach [133] können die Sensoren in Strahlungsumgebungen eingesetzt werden, nachdem sie vor der Installation vorbestrahlt werden, um die strahleninduzierte Querempfindlichkeit zu verringern.

Außerdem werden die kapazitiven Industriesensoren neben dem FOS eingesetzt. Der Hauptaufgabe besteht darin, sie während der Inbetriebnahme zu verwenden und das FOS neu zu kalibrieren, falls die Installation eine zusätzliche Belastung des Gitters verursacht.

Die letzte Technologie, die für das verteilte Messsystem vorgesehen ist, sind die Metalloxid-(Keramik-)Feuchtigkeitssensoren. Dies ist höchstwahrscheinlich die zuverlässigste Lösung, die auch für das Verriegelungssystem verwendet wird. Mehrere Probenahmestellen innerhalb des Detektorgehäuses werden die Spurenfeuchte messen und als Referenz für die beiden anderen Technologien dienen.

mSTS als Wegbereiter für das DCS

Das mCBM-Experiment [159] gilt als FAIR-Experiment der Phase 0 und als Vorläufer des CBM. Die erste mCBM-Kampagne fand 2019 nach zwei Jahren Vorbereitungszeit im Detektortestgebiet HTD [160] statt. Der erste mSTS-Prototyp wurde zusammen mit mTRD, mTOF, mRICH und mPSD betrieben und bestand aus einer Tracking-Station, die aus vier Detektormodulen (8 FEBs) bestand, die auf zwei Kohlenstoffleitern und anschließend in zwei C-Frames montiert wurden. Die nächste Iteration des mSTS-Detektors besteht aus 11 Detektormodulen und wurde zusammengebaut, um ein besseres Verständnis der Komponenten und des Betriebs einer komplexeren Struktur zu erlangen. Die Fertigstellung von 11 Modulen (zusammen mit den Qualitätssicherungsverfahren, STS des STS-XYTERs und der FEBs), der Auslese- und der Steuerungssoftware, stellt einen wichtigen Meilenstein auf dem Weg zum STS dar. Das mCBM Experiment, konzentriert sich auf die DCS-Architektur und erschafft einen Einblick in den Betrieb des Detektors. Schließlich werden die mit dem DCS erzielten Ergebnisse erörtert, die Überlegungen zur Verlustleistung, zur Überwachung der Umgebungsbedingungen und zur Bewertung und Berechnung des Leckstroms erortet.

Der erfolgreiche Betrieb des mSTS, einschließlich der DCS- und DAQ-Kette, stellt einen wichtigen Meilenstein auf dem Weg zum Abschluss des STS-Projekts dar. Die ersten umfangreichen und erfolgreichen Datenerfassungsaktivitäten mit zwei Tracking-Stationen schlossen die Inbetriebnahme des mSTS-Detektors ab. Der Prototyp der DCS-Überwachungsschicht von mSTS wurde erfolgreich implementiert und bewies, dass das Konzept nicht nur für große Detektoren und Beschleunigeraufbauten, sondern auch für kleinere Experimente äußerst flexibel und nützlich ist. Nach fast zwei Jahren Betrieb hat sich das auf Containern basierende System als zuverlässige, leicht zu wartende Lösung erwiesen. Für das endgültige System werden jedoch noch einige zusätzliche Anwendungen benötigt. Da der STS-Detektor wird sehr viel kom-

plexer und anspruchsvoller sein wird, wenn es um die Konfiguration und den Betrieb geht. Bei der endgültigen Einrichtung wird es äußerst wichtig sein, dass sowohl die Hardware als auch die Software verriegelbar sind, um die Sicherheit der Maschine zu gewährleisten.

Fazit

Erfolgreiche Implementierungen des EPICS-basierten containerisierten Software-Frameworks wurden in dieser Arbeit vorgestellt. Die Vielseitigkeit und Modularität des Frameworks ermöglichte die Gewinnung von Daten aus kleineren Versuchsanordnungen, z. B. zyklische thermische Belastung der Front-End-Elektronik des Detektors, bis hin zu wesentlich größeren Versuchsanordnungen (z.B. mSTS). Die erzielten Ergebnisse lieferten einzigartige Daten, die für die erfolgreiche Integration und den Betrieb des künftigen STS verwendet werden sollen. Das entwickelte Frameworkhat alle Anforderungen für die relativ kleinen Setups erfüllt. Trotzdem wird das STS ein komplizierteres Steuerungssystem erfordern, das sowohl Hardware- als auch Software-Sicherheitskomponenten bieten sollte.

List of Figures

List of Tables

Appendix

A Example of deploying an IOC with YAML file

An example YAML file used to deploy IOC. In this particular case, the IOC operated a BINDER MK240 climatic chamber [166] using Modbus protocol [91]. The volumes are used to acquire database files and synchronize the time with the node. The container is deployed in the host network and the so-called pseudo-terminal is activated (tty). The time of the container is synchronized with the local time of the node.

```
version: "3.7"
services:
  binder:
    container_name: binderioc
    volumes:
      - "/home/cbm/dcs-sts/config/:/config"
      - "/etc/localtime:/etc/localtime:ro"
      - "/etc/timezone:/etc/timezone:ro"
    network_mode: "host"
    image: "paluma.rub.de/panda-ioc"
    tty: true
    command: /config/iocBoot/iocBinder/st.cmd
```

B CSA scans for modules of the mSTS

The figures depict the low voltage modules current trends of the STS modules in the function of the CSA value settings. The nominal operational value of 31 value is also marked. The respective components that cause higher average current for unit 1 and 3 are listed in Chapter 6. Modules of unit 2 were also assembled with the latest components, therefore their performance is similar to modules of unit 0.

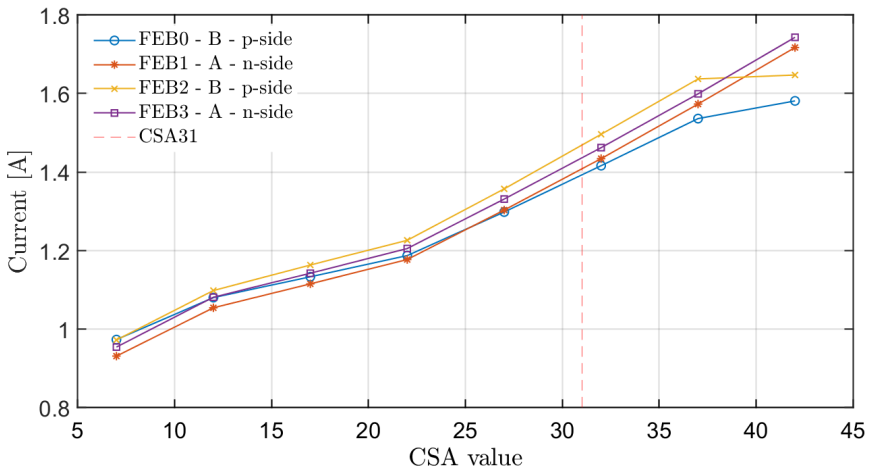

Figure B.1: Currents of four FEBs of Unit 1 in function of CSA value setting.

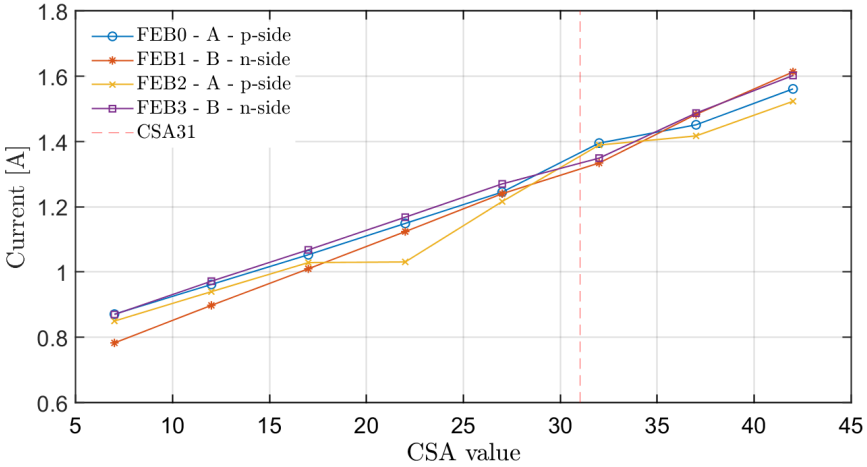

Figure B.2: Currents of four FEBs of Unit 2 in function of CSA value setting.

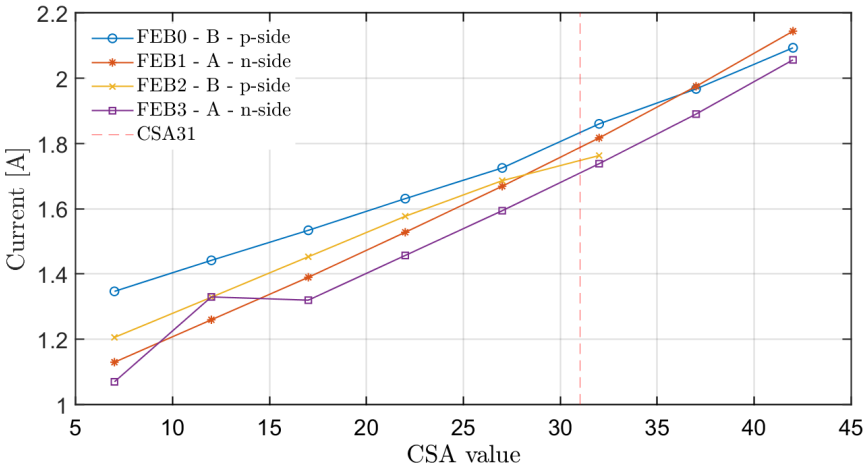

Figure B.3: Currents of four FEBs of Unit 3 Ladder 0 in the function of CSA value settings.

Appendix

C Leakage current evolution

Figure C.1 depicts the leakage current evolution of the remaining mSTS modules. Leakage current trends of Unit 1, 2, and module 1 of Unit 3 Ladder 3 are in agreement. Module 0 of Unit 3 has increased current values most likely due to an electrical issue that reveals itself in an unusually high leakage current increase.

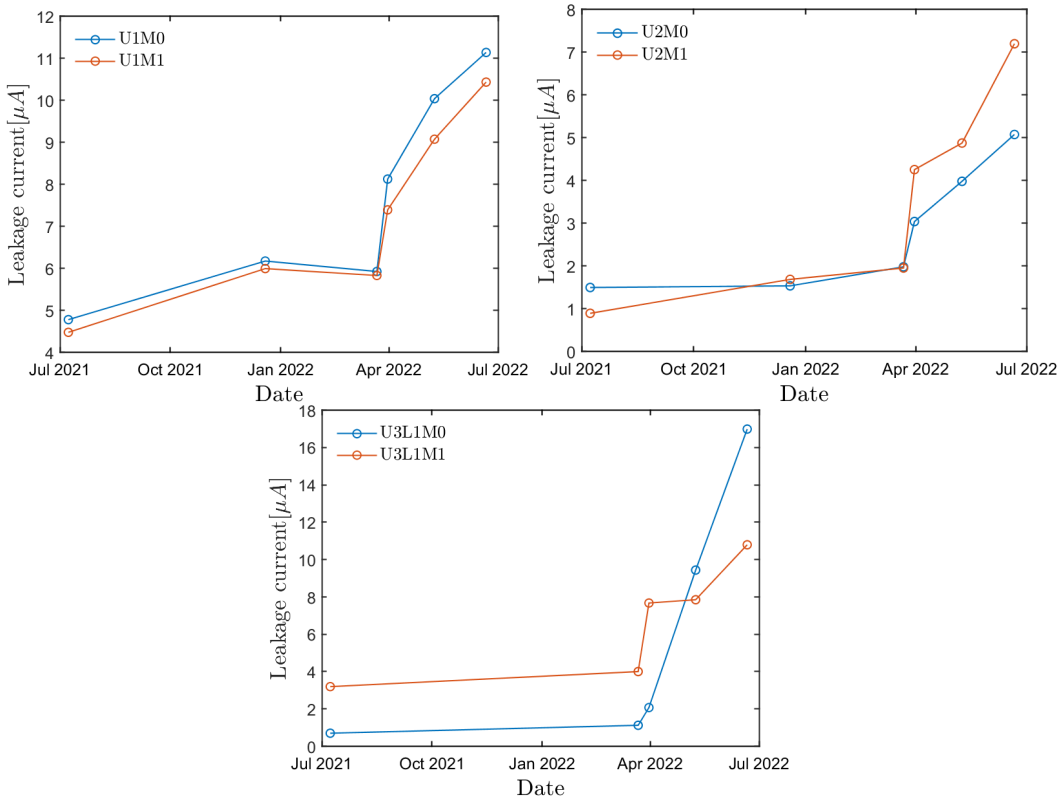

Figure C.1: Leakage current evolution during the mSTS operation - unit 1, unit 2 and unit 3 ladder 1.

Bibliography

[1] S. Berryman, "Ancient atomism", E. N. Zalta and U. Nodelman, Eds., 2022 (cit. on p. 1).

[2] R. Mann, *An Introduction to Particle Physics and the Standard Model*. CRC Press, 2010. DOI: 10.1201/9781420083002 (cit. on p. 1).

[3] O. of science. "Doe explains...the standard model of particle physics". (), [Online]. Available: https://www.energy.gov/science/doe-explainsthe-standard-model-particle-physic (cit. on p. 2).

[4] K. Fukushima and C. Sasaki, *The phase diagram of nuclear and quark matter at high baryon density*, 2013. DOI: 10.48550/ARXIV.1301.6377. [Online]. Available: https://arxiv.org/abs/1301.6377 (cit. on p. 3).

[5] R. Gupta, *Introduction to lattice qcd*, 1998. DOI: 10.48550/ARXIV.HEP-LAT/9807028. [Online]. Available: https://arxiv.org/abs/hep-lat/9807028 (cit. on p. 3).

[6] T. Matsui and H. Satz, "J/ψ Suppression by quark-gluon plasma formation", *Physics Letters B*, vol. 178, no. 4, pp. 416–422, 1986, ISSN: 0370-2693. DOI: https://doi.org/10.1016/0370-2693(86)91404-8. [Online]. Available: https://www.sciencedirect.com/science/article/pii/0370269386914048 (cit. on p. 3).

[7] J. Rafelski and B. Müller, "Strangeness production in the quark-gluon plasma", *Phys. Rev. Lett.*, vol. 48, pp. 1066–1069, 16 Apr. 1982. DOI: 10.1103/PhysRevLett.48.1066. [Online]. Available: https://link.aps.org/doi/10.1103/PhysRevLett.48.1066 (cit. on p. 3).

[8] M. Stefaniak, "The soup that is not too hot", Sep. 2022. arXiv: 2209.08126 [nucl-ex] (cit. on pp. 3, 6).

[9] J. Rafelski, "Melting hadrons, boiling quarks", *The European Physical Journal A*, vol. 51, no. 9, Sep. 2015. DOI: 10.1140/epja/i2015-15114-0. [Online]. Available: https://doi.org/10.1140%2Fepja%2Fi2015-15114-0 (cit. on p. 3).

[10] Y. Aoki, G. Endrődi, Z. Fodor, S. D. Katz, and K. K. Szabó, "The order of the quantum chromodynamics transition predicted by the standard model of particle physics", *Nature*, vol. 443, no. 7112, pp. 675–678, Oct. 2006. DOI: 10.1038/nature05120. [Online]. Available: https://doi.org/10.1038%5C%2Fnature05120 (cit. on p. 4).

[11] A. Bazavov, T. Bhattacharya, M. Cheng, *et al.*, "Chiral and deconfinement aspects of the QCD transition", *Physical Review D*, vol. 85, no. 05, Mar. 2012. DOI: 10.1103/physrevd.85.054503. [Online]. Available: https://doi.org/10.1103%5C%2Fphysrevd.85.054503 (cit. on p. 4).

[12] J. Stachel, A. Andronic, P. Braun-Munzinger, and K. Redlich, "Confronting LHC data with the statistical hadronization model", *Journal of Physics: Conference Series*, vol. 509, p. 012019, May 2014. DOI: 10.1088/1742-6596/509/1/012019. [Online]. Available: https://doi.org/10.1088%2F1742-6596%2F509%2F1%2F012019 (cit. on p. 4).

[13] *2012 Asia-Europe-Pacific School of High-Energy Physics: Fukuoka, Japan 14 - 27 Oct 2012. 1st Asia-Europe-Pacific School of High-Energy Physics*, Comments: 8 lectures, 285 pages, published as CERN Yellow Report https://cds.cern.ch/record/1443909, CERN, Geneva: CERN, 2014. DOI: 10.5170/CERN-2014-001. [Online]. Available: http://cds.cern.ch/record/1443909 (cit. on p. 4).

[14] Y. Sakai, K. Kashiwa, H. Kouno, and M. Yahiro, "Phase diagram in the imaginary chemical potential region and extended $\mathbb{Z}_3$ symmetry", *Phys. Rev. D*, vol. 78, p. 036001, 3 Aug. 2008. DOI: 10.1103/PhysRevD.78.036001. [Online]. Available: https://link.aps.org/doi/10.1103/PhysRevD.78.036001 (cit. on p. 4).

[15] C. S. Fischer, J. Luecker, and C. A. Welzbacher, "Phase structure of three and four flavor qcd", *Phys. Rev. D*, vol. 90, p. 034022, 3 Aug. 2014. DOI: 10.1103/PhysRevD.90.034022. [Online]. Available: https://link.aps.org/doi/10.1103/PhysRevD.90.034022 (cit. on p. 4).

[16] A. N. Tawfik and A. M. Diab, "Polyakov su(3) extended linear-σ model: Sixteen mesonic states in chiral phase structure", *Phys. Rev. C*, vol. 91, p. 015204, 1 Jan. 2015. DOI: 10.1103/PhysRevC.91.015204. [Online]. Available: https://link.aps.org/doi/10.1103/PhysRevC.91.015204 (cit. on p. 4).

[17] B. Friman, C. Hohne, J. Knoll, *et al.*, Eds., *The CBM physics book: Compressed baryonic matter in laboratory experiments*. 2011, vol. 814. DOI: 10.1007/978-3-642-13293-3 (cit. on pp. 4–8).

[18] R. Sahoo, "Possible Formation of QGP-droplets in Proton-Proton Collisions at the CERN Large Hadron Collider", *AAPPS Bull.*, vol. 29, no. 4, pp. 16–21, 2019, 6-pages, Featured invited article for beginners in the field, appeared in AAPPS

Bulletin. DOI: 10.22661/AAPPSBL.2019.29.4.16. arXiv: 1908.10566. [Online]. Available: https://cds.cern.ch/record/2745520 (cit. on p. 5).

[19] T. C. Collaboration, "Challenges in QCD matter physics –the scientific programme of the compressed baryonic matter experiment at FAIR", *The European Physical Journal A*, vol. 53, no. 3, Mar. 2017. DOI: 10.1140/epja/i2017-12248-y. [Online]. Available: https://doi.org/10.1140%2Fepja%2Fi2017-12248-y (cit. on pp. 6–8).

[20] L. Turko, "Looking for the phase transition - recent NA61/SHINE results. Looking for the phase transition - recent NA61/SHINE results", *Universe*, vol. 4, no. 3, p. 52, 2018. DOI: 10.3390/universe4030052. arXiv: 1801.06919. [Online]. Available: https://cds.cern.ch/record/2301677 (cit. on p. 6).

[21] ——, "NA61/SHINE experiment - programme beyond 2020", *Particles*, vol. 1, no. 1, pp. 296–304, 2018, 7 pages, 6 figures, 27 references, Lecture given at the Colloqium on Nonequilibrium Phenomena in Strongly Correlated Systems, Dubna, 18 - 19 April, 2018. DOI: 10.3390/particles1010024. arXiv: 1811.05522. [Online]. Available: https://cds.cern.ch/record/2649393 (cit. on p. 6).

[22] L. Kumar, "Star results from the rhic beam energy scan-i", *Nuclear Physics A*, vol. 904-905, pp. 256c–263c, 2013, The Quark Matter 2012, ISSN: 0375-9474. DOI: https://doi.org/10.1016/j.nuclphysa.2013.01.070. [Online]. Available: https://www.sciencedirect.com/science/article/pii/S0375947413000894 (cit. on p. 7).

[23] Y. Yang, "The star detector upgrades for the bes ii and beyond physics program", *Nuclear Physics A*, vol. 1005, p. 121 758, 2021, The 28th International Conference on Ultra-relativistic Nucleus-Nucleus Collisions: Quark Matter 2019, ISSN: 0375-9474. DOI: https://doi.org/10.1016/j.nuclphysa.2020.121758. [Online]. Available: https://www.sciencedirect.com/science/article/pii/S0375947420300683 (cit. on p. 7).

[24] D. Almaalol, M. Hippert, J. Noronha-Hostler, *et al.*, *Qcd phase structure and interactions at high baryon density: Continuation of bes physics program with cbm at fair*, 2022. DOI: 10.48550/ARXIV.2209.05009. [Online]. Available: https://arxiv.org/abs/2209.05009 (cit. on p. 7).

[25] P. Senger, "Astrophysics in the laboratory—the CBM experiment at FAIR", *Particles*, vol. 3, no. 2, pp. 320–335, Apr. 2020. DOI: 10.3390/particles3020024. [Online]. Available: https://doi.org/10.3390%2Fparticles3020024 (cit. on p. 7).

[26] W. Reisdorf, M. Stockmeier, A. Andronic, *et al.*, "Systematics of pion emission in heavy ion collisions in the regime", *Nuclear Physics A*, vol. 781, no. 3-4, pp. 459–508, Jan. 2007. DOI: 10.1016/j.nuclphysa.2006.10.085. [Online]. Available: https://doi.org/10.1016%%5C2Fj.nuclphysa.2006.10.085 (cit. on p. 7).

[27] "The Accelerator Facility ". (Nov. 2022), [Online]. Available: https://www.gsi.de/en/researchaccelerators/fair/the_machine (visited on 11/19/2022) (cit. on pp. 8, 9).

[28] W. Henning, "Fair — an international accelerator facility for research with ions and antiprotons", *AIP Conference Proceedings*, vol. 773, no. 1, pp. 3–5, 2005. DOI: 10.1063/1.1949487. eprint: https://aip.scitation.org/doi/pdf/10.1063/1.1949487. [Online]. Available: https://aip.scitation.org/doi/abs/10.1063/1.1949487 (cit. on p. 8).

[29] P. Spiller, R. Balss, P. Bartolome, *et al.*, "The fair heavy ion synchrotron sis100", *Journal of Instrumentation*, vol. 15, no. 12, T12013, Dec. 2020. DOI: 10.1088/1748-0221/15/12/T12013. [Online]. Available: https://dx.doi.org/10.1088/1748-0221/15/12/T12013 (cit. on p. 8).

[30] P. Sievers, K. Knie, M. Steck, B. Franzke, and V. Gostishchev, "Concept for the Antiproton Production Target at FAIR", *Conf. Proc. C*, vol. 1205201, V. Suller, Ed., pp. 2570–2572, 2012 (cit. on p. 9).

[31] A. Rost. "BMON/T0 for CBM: towards technical note". (Dec. 2022), [Online]. Available: https://indico.gsi.de/event/15512/contributions/66325/attachments/41383/57386/BMON_status_Rost.pdf (cit. on p. 11).

[32] M. Deveaux, M. K. P. Klaus, C. M. J. Michel, and J. Stroth, "The micro-vertex detector of the cbm experiment at fair", Tech. Rep., 2021 (cit. on p. 11).

[33] A. Malakhov and A. Shabunov, Eds., *Technical Design Report for the CBM Superconducting Dipole Magnet*. Darmstadt: GSI, 2013, 80 S. [Online]. Available: https://repository.gsi.de/record/109025 (cit. on p. 11).

[34] J. Heuser, W. Müller, V. Pugatch, *et al.*, Eds., *[GSI Report 2013-4] Technical Design Report for the CBM Silicon Tracking System (STS)*. Darmstadt: GSI, 2013, 167 p. [Online]. Available: https://repository.gsi.de/record/54798 (cit. on pp. 11, 20–23, 25, 27, 83).

[35] S. Chattopadhyay, Y. P. Viyogi, P. Senger, W. F. J. Müller, and C. J. Schmidt, Eds., *Technical Design Report for the CBM : Muon Chambers (MuCh)*. Darmstadt: GSI, 2015, 190 S. [Online]. Available: https://repository.gsi.de/record/161297 (cit. on p. 11).

[36] "Technical Design Report for the CBM Ring Imaging Cherenkov Detector", Tech. Rep., 2013, 215 p. [Online]. Available: https://repository.gsi.de/record/65526 (cit. on p. 11).

[37] "The Transition Radiation Detector of the CBM Experiment at FAIR : Technical Design Report for the CBM Transition Radiation Detector (TRD)", Darmstadt, Tech. Rep. FAIR Technical Design Report, 2018, 165 p. DOI: 10.15120/GSI-2018-01091. [Online]. Available: https://repository.gsi.de/record/217478 (cit. on p. 12).

[38] N. Herrmann, Ed., *Technical Design Report for the CBM Time-of-Flight System (TOF)*. Darmstadt: GSI, 2014, 182 S. [Online]. Available: https://repository.gsi.de/record/109024 (cit. on p. 12).

[39] F. Guber and I. Selyuzhenkov, Eds., *Technical Design Report for the CBM Projectile Spectator Detector (PSD)*. Darmstadt: GSI, 2015, 75 S. [Online]. Available: https://repository.gsi.de/record/109059 (cit. on p. 12).

[40] I. Kisel, "Event reconstruction in the cbm experiment", *Nuclear Instruments and Methods in Physics Research Section A: Accelerators, Spectrometers, Detectors and Associated Equipment*, vol. 566, no. 1, pp. 85–88, 2006, TIME 2005, ISSN: 0168-9002. DOI: https://doi.org/10.1016/j.nima.2006.05.040. [Online]. Available: https://www.sciencedirect.com/science/article/pii/S0168900206008151 (cit. on p. 12).

[41] G. Lutz, *Semiconductor Radiation Detectors: Device Physics*. New York: Springer, 1999, ISBN: 978-3-540-64859-8 (cit. on p. 15).

[42] F. Hartmann, *Evolution of Silicon Sensor Technology in Particle Physics*, ser. Springer Tracts in Modern Physics. Springer, 2017, vol. 275, ISBN: 978-3-319-64434-9, 978-3-319-64436-3. DOI: 10.1007/978-3-319-64436-3 (cit. on pp. 15, 17, 20, 31).

[43] O. Sokolov, "Prototyping of silicon strip detectors for the inner tracker of the ALICE experiment", Ph.D. dissertation, Utrecht U., 2006 (cit. on p. 16).

[44] H. Spieler, *Semiconductor Detector Systems*. Jan. 2007, pp. 1–512, ISBN: 9780198527848. DOI: 10.1093/acprof:oso/9780198527848.001.0001 (cit. on pp. 16, 18, 22, 27).

[45] M. Moll, "Radiation damage in silicon particle detectors: Microscopic defects and macroscopic properties", Ph.D. dissertation, Hamburg U., 1999 (cit. on pp. 17, 19).

[46] I. Momot, "Characterization and radiation hardness studies of the silicon microstrip sensors for the CBM experiment", Ph.D. dissertation, Goethe U., Frankfurt (main), 2019 (cit. on pp. 20, 30).

[47] I. Selyuzhenkov and A. Toia, Eds., *CBM Progress Report 2016*. Darmstadt: GSI, 2017, 223 Seiten : Illustrationen, grafische Darstellungen, Literaturangaben, ISBN: 978-3-9815227-4-7. [Online]. Available: https://repository.gsi.de/record/201318 (cit. on p. 21).

[48] *Private information from m. teklishyn* (cit. on p. 22).

[49] C. Simons, K. Schuenemann, R. Visinka, *et al.*, "Status of sts module assembly at gsi", Darmstadt, Tech. Rep. 2021-00421, 2021, 235 p. DOI: 10.15120/GSI-2021-00421. [Online]. Available: https://repository.gsi.de/record/237432 (cit. on p. 23).

[50] CERN. "Radiation tolerant 10W Synchronous Step-Down Buck DC/DC converter ". (Oct. 2022), [Online]. Available: https://espace.cern.ch/project-DCDC-new/Shared%5C%20Documents/FEAST2Mod_Datasheet_gb2016.pdf (visited on 10/27/2022) (cit. on pp. 23, 120).

[51] K. Kasinski, R. Szczygiel, W. Zabolotny, J. Lehnert, C. Schmidt, and W. Müller, "A protocol for hit and control synchronous transfer for the front-end electronics at the cbm experiment", *Nuclear Instruments and Methods in Physics Research Section A: Accelerators, Spectrometers, Detectors and Associated Equipment*, vol. 835, pp. 66–73, 2016, ISSN: 0168-9002. DOI: https://doi.org/10.1016/j.nima.2016.08.005. [Online]. Available: https://www.sciencedirect.com/science/article/pii/S016890021630818X (cit. on p. 24).

[52] K. Kasinski, R. Kleczek, and R. Szczygiel, "Front-end readout electronics considerations for silicon tracking system and muon chamber", *Journal of Instrumentation*, vol. 11, no. 02, p. C02024, Feb. 2016. DOI: 10.1088/1748-0221/11/02/C02024. [Online]. Available: https://dx.doi.org/10.1088/1748-0221/11/02/C02024 (cit. on p. 24).

[53] K. Kasinski, A. Rodriguez-Rodriguez, J. Lehnert, *et al.*, "Characterization of the sts/much-xyter2, a 128-channel time and amplitude measurement ic for gas and silicon microstrip sensors", *Nuclear Instruments and Methods in Physics Research Section A: Accelerators, Spectrometers, Detectors and Associated Equipment*, vol. 908, pp. 225–235, 2018, ISSN: 0168-9002. DOI: https://doi.org/10.1016/j.nima.2018.08.076. [Online]. Available: https://www.sciencedirect.com/science/article/pii/S0168900218310349 (cit. on p. 27).

[54] K. Kasinski, R. Szczygiel, and W. Zabolotny, "Back-end and interface implementation of the sts-xyter2 prototype asic for the cbm experiment", *Journal of Instrumentation*, vol. 11, no. 11, p. C11018, Nov. 2016. DOI: 10.1088/1748-0221/11/11/C11018. [Online]. Available: https://dx.doi.org/10.1088/1748-0221/11/11/C11018 (cit. on p. 26).

[55] A. R. Rodriguez, "The cbm silicon tracking system front-end electronics : From bare asic to detector characterization, commissioning and performance", Ph.D. dissertation, Universitätsbibliothek Johann Christian Senckenberg, 2020, p. 175 (cit. on pp. 26, 27, 54, 122).

[56] "CBM Progress Report 2017", Darmstadt, Tech. Rep. CBM Progress Report 2017, 2018, V, 214 Seiten : Illustrationen, grafische Darstellungen. DOI: 10.15120/GSI-2018-00485. [Online]. Available: https://repository.gsi.de/record/209729 (cit. on p. 27).

[57] S. Bonacini, K. Kloukinas, and P. Moreira, "E-link: A Radiation-Hard Low-Power Electrical Link for Chip-to-Chip Communication", 2009. DOI: 10.5170/CERN-2009-006.422. [Online]. Available: http://cds.cern.ch/record/1235849 (cit. on p. 28).

[58] C. Soós, M. B. Marin, S. Détraz, *et al.*, "The versatile transceiver: Towards production readiness", *Journal of Instrumentation*, vol. 8, no. 03, p. C03004, Mar. 2013. DOI: 10.1088/1748-0221/8/03/C03004. [Online]. Available: https://dx.doi.org/10.1088/1748-0221/8/03/C03004 (cit. on p. 28).

[59] J. Lehnert, A. Byszuk, D. Emschermann, *et al.*, "Gbt based readout in the cbm experiment", *Journal of Instrumentation*, vol. 12, no. 02, p. C02061, Feb. 2017. DOI: 10.1088/1748-0221/12/02/C02061. [Online]. Available: https://dx.doi.org/10.1088/1748-0221/12/02/C02061 (cit. on p. 28).

[60] W. M. Zabołotny, G. H. Kasprowicz, A. P. Byszuk, *et al.*, "Selection of hardware platform for CBM Common Readout Interface", in *Photonics Applications in Astronomy, Communications, Industry, and High Energy Physics Experiments 2017*, R. S. Romaniuk and M. Linczuk, Eds., International Society for Optics and Photonics, vol. 10445, SPIE, 2017, p. 1 044 549. DOI: 10.1117/12.2280938. [Online]. Available: https://doi.org/10.1117/12.2280938 (cit. on p. 29).

[61] P.-A. Loizeau, D. Emscherman, J. Lehnert, W. F. J. Müller, and J. Yang, "The prototype readout chain for CBM using the AFCK board and its software components", in *Photonics Applications in Astronomy, Communications, Industry, and High-Energy Physics Experiments 2015*, R. S. Romaniuk, Ed., ser. Society of Photo-Optical Instrumentation Engineers (SPIE) Conference Series, vol. 9662, Sep. 2015, 96622X, p. 96622X. DOI: 10.1117/12.2205820 (cit. on p. 29).

[62] "IPbus software ". (Jan. 2023), [Online]. Available: https://github.com/ipbus/ipbus-software (cit. on p. 29).

[63] W. Z. et. al., "Fpga-related development for cbm daq", Darmstadt, Tech. Rep. 2021-00421, 2021, 235 p. DOI: 10.15120/GSI-2021-00421. [Online]. Available: https://repository.gsi.de/record/237432 (cit. on p. 29).

[64] *Private information from K. Agarwal* (cit. on pp. 31, 67, 69).

[65] "Trigger and data acquisition ". (Mar. 2023), [Online]. Available: https://cms.cern/detector/triggering-and-data-acquisition (cit. on p. 35).

[66] "0MQ Library". (Nov. 2022), [Online]. Available: https://zeromq.org/ (visited on 11/17/2022) (cit. on p. 38).

[67] "Experimental physics and industrial control system". (Jul. 2022), [Online]. Available: https://epics-controls.org/ (cit. on pp. 38, 41).

[68] P. Gayet and R. Barillère, "Unicos a framework to build industry like control systems: Principles and methodology", Jul. 2022 (cit. on p. 39).

[69] "Experimental physics and industrial control system documentation". (Jul. 2022), [Online]. Available: https://docs.epics-controls.org/en/latest/guides/EPICS_Intro.html (cit. on p. 40).

[70] "EPICS License". (Jul. 2022), [Online]. Available: https://epics.anl.gov/license/open.php (cit. on p. 40).

[71] A. J. K. L. R. Dalesio and M. R. Kraimer, "EPICS architecture", (cit. on p. 41).

[72] J. Hill, "Channel access: A software bus for the laacs", *Nuclear Instruments and Methods in Physics Research Section A: Accelerators, Spectrometers, Detectors and Associated Equipment 293.1-2*, vol. 293, pp. 1–2, Aug. 1990. DOI: 10.1016/0168-9002(90)91459-o (cit. on p. 41).

[73] L. R. D. et al., "The experimental physics and industrial control system architecture: Past, present, and future", *Nuclear Instruments and Methods in Physics Research Section A: Accelerators, Spectrometers, Detectors and Associated Equipment 352.1-2*, pp. 179–184, Dec. 1994. DOI: 10.1016/0168-9002(94)91493-1 (cit. on p. 41).

[74] B. K. C. M. R. Kraimer and M. Anderson. "Alarm handler for the advanced photon source control system". (Jan. 1991) (cit. on p. 41).

[75] "Experiments at GSI ". (May 2023), [Online]. Available: https://epics-controls.org/projects-archive/experiments-at-gsi/n (cit. on p. 41).

[76] M. O. et al., "Upgrade of j-parc/mlf general control system with epics/css", *Proceedings of ICALEPCS2013*, pp. 179–184, Dec. 1994. DOI: 10.1016/0168-9002(94)91493-1 (cit. on p. 41).

[77] J. Adam, M. G. Cherney, J. D'Alesio, *et al.*, "Upgrade of hardware controls for the STAR experiment at RHIC", *Nuclear Instruments and Methods in Physics Research Section A: Accelerators, Spectrometers, Detectors and Associated Equipment*, vol. 1013, p. 165 644, Oct. 2021. DOI: 10.1016/j.nima.2021.165644. [Online]. Available: https://doi.org/10.1016%5C%2Fj.nima.2021.165644 (cit. on p. 41).

[78] D. Leone, V. Carrubba, S. Mazzaro, M. Nobili, D. Cucè, and D. Hamilton, "Epics application for iter rh supervisory control system", *Fusion Engineering and Design*, vol. 169, p. 112 429, 2021, ISSN: 0920-3796. DOI: https://doi.org/10.1016/j.fusengdes.2021.112429. [Online]. Available: https://www.sciencedirect.com/science/article/pii/S0920379621002052 (cit. on p. 41).

[79] "EPICS sites". (Jul. 2022), [Online]. Available: http://epics-controls.org/epics-users/projects/ (cit. on p. 41).

[80] J. M. M. Camacho, J. C. Cabanillas Noris, and I. León-Monzón, "Detector control system for forward diffractive detector", *Rev. Mex. Fis. Suppl.*, vol. 3, no. 2, p. 020 716, 2022. DOI: 10.31349/SuplRevMexFis.3.020716 (cit. on p. 41).

[81] L. Goralczyk, A. F. Kostopoulos, B. Schofield, and J.-C. Tournier, "CERN SCADA Systems 2020 Large Upgrade Campaign Retrospective", *JACoW*, vol. ICALEPCS2021, pp. 156–160, 2022. DOI: 10.18429/JACoW-ICALEPCS2021-MOPV017 (cit. on p. 41).

[82] J. Santander-Vela, M. Bartolini, M. Miccolis, and N. Rees, "From SKA to SKAO: Early Progress in the SKAO Construction", *JACoW*, vol. ICALEPCS2021, MOAL03, 2022. DOI: 10.18429/JACoW-ICALEPCS2021-MOAL03. arXiv: 2110.13329 [astro-ph.IM] (cit. on p. 41).

[83] A. N. State *et al.*, "The slow control system of the FRS Ion Catcher", *Nucl. Instrum. Meth. A*, vol. 1034, p. 166 772, 2022. DOI: 10.1016/j.nima.2022.166772 (cit. on p. 41).

[84] "Taurus". (Jul. 2022), [Online]. Available: https://www.taurus-scada.org/ (cit. on pp. 41, 43).

[85] "CS-Studio/Phoebus". (Jul. 2022), [Online]. Available: https://control-system-studio.readthedocs.io/en/latest/index.html (cit. on p. 41).

[86] "Bluesky". (Jul. 2022), [Online]. Available: https://blueskyproject.io/ (cit. on p. 42).

[87] "React Automation Studio". (Jul. 2022), [Online]. Available: https://github.com/React-Automation-Studio/React-Automation-Studio1 (cit. on p. 42).

[88] M. R. Kraimer, *EPICS Input / Output Controller (IOC) Application Developer's Guide*, EPICS Realease 3.13.0beta12. Argonne, Jun. 1998 (cit. on p. 42).

[89] "EPICS Documentation". (Nov. 2022), [Online]. Available: https://docs.epics-controls.org/en/latest/guides/EPICS_Intro.html#ioc-software-components (cit. on p. 42).

[90] "Stream Device". (Aug. 2022), [Online]. Available: https://paulscherrerinstitute.github.io/StreamDevice/ (cit. on p. 42).

[91] "Modbus". (Aug. 2022), [Online]. Available: https://epics-modbus.readthedocs.io/en/latest/ (cit. on pp. 42, 163).

[92] "AsynDriver". (Aug. 2022), [Online]. Available: https://epics-modules.github.io/master/asyn/ (cit. on p. 43).

[93] P. L. Klaus, "Development of the control system for the vacuum operation and validation of the mvd prototype for the cbm experiment", Ph.D. dissertation, 2021, p. 172. DOI: 10.21248/gups.63325 (cit. on p. 43).

[94] F. Feldbauer. "Container virtualization for EPICS". (Aug. 2022), [Online]. Available: https://indico.gsi.de/event/9524/contributions/41177/attachments/29562/36756/epics-tut.pdf (visited on 08/01/2022) (cit. on p. 43).

[95] "Podman ". (Aug. 2022), [Online]. Available: https://podman.io/ (cit. on p. 45).

[96] "EPICS Collaboration Meeting 2022 ". (Aug. 2022), [Online]. Available: https://docs.sylabs.io/guides/3.5/user-guide/introduction.html# (visited on 08/31/2022) (cit. on p. 45).

[97] "Docker - Rootless mode ". (Aug. 2022), [Online]. Available: https://docs.docker.com/engine/security/rootless/ (cit. on p. 45).

[98] "Docker compose ". (Aug. 2022), [Online]. Available: https://docs.docker.com/compose/ (visited on 08/31/2022) (cit. on p. 46).

[99] "YAML Ain't Markup Language ". (Nov. 2022), [Online]. Available: https://yaml.org/ (cit. on p. 46).

[100] "The EPICS Archiver Appliance ". (Aug. 2022), [Online]. Available: https://slacmshankar.github.io/epicsarchiver_docs/index.html (cit. on p. 47).

[101] "RDB Archive Engine ". (Aug. 2022), [Online]. Available: https://oss.aquenos.com/epics/cassandra-archiver/ (visited on 08/31/2022) (cit. on p. 48).

[102] "RDB Archive Engine ". (Aug. 2022), [Online]. Available: https://control-system-studio.readthedocs.io/en/latest/services/archive-engine/doc/index.html (visited on 08/31/2022) (cit. on p. 48).

[103] "Alarm Logging Service ". (Aug. 2022), [Online]. Available: https://control-system-studio.readthedocs.io/en/latest/services/alarm-logger/doc/index.html (visited on 08/31/2022) (cit. on p. 49).

[104] "Raspberry Pi ". (Feb. 2023,), [Online]. Available: https://github.com/darcato/pysmlib (cit. on p. 49).

[105] P. Dodd and L. Massengill, "Basic mechanisms and modeling of single-event upset in digital microelectronics", *IEEE Transactions on Nuclear Science*, vol. 50, no. 3, pp. 583–602, 2003. DOI: 10.1109/TNS.2003.813129 (cit. on p. 51).

[106] N. Seifert, B. Gill, S. Jahinuzzaman, *et al.*, "Soft error susceptibilities of 22 nm tri-gate devices", *IEEE Transactions on Nuclear Science*, vol. 59, no. 6, pp. 2666–2673, 2012. DOI: 10.1109/TNS.2012.2218128 (cit. on p. 52).

[107] A. Ferrari, P. Sala, A. Fasso, and J. Ranft, "Fluka: A multi-particle transport code", 2005. DOI: CERN-2005-10(2005),INFN/TC_05/11,SLAC-R-773 (cit. on p. 52).

[108] A. Senger. "FLUKA results for CBM". (Dec. 2022), [Online]. Available: http://web-docs.gsi.de/~kisselan/CBM_FLUKA.htm (cit. on pp. 53, 56).

[109] B. N. Taylor. "The International System of Units (SI)". (Nov. 2022), [Online]. Available: https://physics.nist.gov/cuu/pdf/sp330.pdf (visited on 11/13/2022) (cit. on p. 52).

[110] D. Lo Presti, N. H. Medina, M. A. Guazzelli, *et al.*, "Neutron radiation effects on an electronic system on module", *Review of Scientific Instruments*, vol. 91, no. 8, p. 083 301, 2020. DOI: 10.1063/5.0010968. eprint: https://doi.org/10.1063/5.0010968. [Online]. Available: https://doi.org/10.1063/5.0010968 (cit. on p. 54).

[111] R. Baumann, "Radiation-induced soft errors in advanced semiconductor technologies", *IEEE Transactions on Device and Materials Reliability*, vol. 5, no. 3, pp. 305–316, 2005. DOI: 10.1109/TDMR.2005.853449 (cit. on p. 54).

[112] R. Baumann, "Soft errors in advanced semiconductor devices-part i: The three radiation sources", *IEEE Transactions on Device and Materials Reliability*, vol. 1, pp. 17–22, Jan. 2001 (cit. on p. 54).

[113] H. Tang and K. Rodbell, "Single-event upsets in microelectronics: Fundamental physics and issues", vol. 28, pp. 111–116, Feb. 2003 (cit. on p. 54).

[114] D. Brown, M. Chadwick, R. Capote, *et al.*, "Endf/b-viii.0: The 8th major release of the nuclear reaction data library with cielo-project cross sections, new standards and thermal scattering data", *Nucl. Data Sheets*, vol. 148, 2018. DOI: 10.1097/00004032-200008000-00010 (cit. on p. 54).

[115] "WIENER". (Dec. 2022), [Online]. Available: https://www.wiener-d.com/about-us/ (cit. on pp. 55, 120).

[116] "ISEG". (Dec. 2022), [Online]. Available: https://iseg-hv.com/en (cit. on p. 55).

[117] A. Sokolov, E. Kozlova, and T. Radon, "Bonner cylinder set for neutron spectroscopy at high energy accelerators", *Radiation protection dosimetry*, vol. 187, Jun. 2019. DOI: 10.1093/rpd/ncz140 (cit. on p. 55).

[118] "NIST/SEMATECH e-Handbook of Statistical Methods ". (Jun. 2023), [Online]. Available: https://www.itl.nist.gov/div898/handbook/eda/section3/eda366b.htm (cit. on p. 55).

[119] M. DeGroot and M. Schervish, *Probability and Statistics*, ser. Pearson custom library. Pearson Education, 2013, ISBN: 9781292025049. [Online]. Available: https://books.google.gr/books?id=hIPkngEACAAJ (cit. on p. 55).

[120] R. Olsher, H. Hsu, A. Beverding, *et al.*, "Wendi: An improved neutron rem meter", *Health physics*, vol. 79, pp. 170–81, Sep. 2000. DOI: 10.1097/00004032-200008000-00010 (cit. on p. 58).

[121] "PyEpics: Epics Channel Access for Python ". (Aug. 2022), [Online]. Available: https://cars9.uchicago.edu/software/python/pyepics3/ (visited on 08/31/2022) (cit. on pp. 64, 72).

[122] A. Caratelli, S. Bonacini, K. Kloukinas, *et al.*, "The GBT-SCA, a radiation tolerant ASIC for detector control and monitoring applications in HEP experiments", *JINST*, vol. 10, p. C03034, 2015. DOI: 10.1088/1748-0221/10/03/C03034. [Online]. Available: https://cds.cern.ch/record/2158969 (cit. on p. 64).

[123] P. Senger and V. Friese, "CBM Progress Report 2021", Darmstadt, Tech. Rep. 2022, 2022, 239 p. DOI: 10.15120/GSI-2022-00599. [Online]. Available: https://repository.gsi.de/record/246663 (cit. on p. 66).

[124] E. T. Haugan and P. Dalsjør, "Characterization of the material properties of two fr4 printed circuit board laminates", Tech. Rep. 2014. [Online]. Available: https://publications.ffi.no/nb/item/asset/dspace:2376/13-01956.pdf (cit. on p. 69).

[125] D. S. Steinberg, *Vibration Analysis for Electronic Equipment*, 3rd ed. John Wiley, and Sons, 2000, ISBN: 9780471376859; 047137685X (cit. on p. 71).

[126] "9001-E-V3.5 Product Data Sheet ". (), [Online]. Available: https://prostech.vn/wp-content/uploads/2018/07/9001-e-v35.pdf (visited on 10/13/2022) (cit. on p. 71).

[127] "Dual-Cure 9014 ". (Oct. 2022), [Online]. Available: https://dymax.com/content/download/3660/file/9014%5C%20PDS.pdf (visited on 10/13/2022) (cit. on p. 71).

[128] "Ultra Light-Weld® 9008 Flexible, UV-Curable Encapsulant ". (Feb. 2022), [Online]. Available: https://dymax.com/content/download/3767/file/9008%20PDS.pdf (visited on 02/18/2023) (cit. on p. 71).

[129] "EPO-TEK E4110 Data sheet ". (Oct. 2022), [Online]. Available: https://www.epotek.com/docs/en/Datasheet/E4110.pdf (visited on 10/13/2022) (cit. on p. 71).

[130] N. Paydar, Y. Tong, H. Akay, and W. Boehmer, "Finite element mesh generation and analysis of solder joints for fatigue life predictions", p. 179, Aug. 1993 (cit. on p. 71).

[131] H. Watanabe, N. Yamada, and M. Okaji, "Linear thermal expansion coefficient of silicon from 293 to 1000 k", *International Journal of Thermophysics*, vol. 25, pp. 221–236, Jan. 2004. DOI: 10.1023/B:IJOT.0000022336.83719.43 (cit. on p. 71).

[132] L. Flehinghaus. "FEB8-2 diagnostic circuit studies after thermal cycling (summer student project) ". (Oct. 2022), [Online]. Available: https://indico.gsi.de/event/15765/ (visited on 10/20/2022) (cit. on p. 72).

[133] "KRYO51 datasheet ". (Oct. 2022), [Online]. Available: https://www.lauda.de/fileadmin/assets/downloads/pdf/Kryo_51_en-GB_2020.pdf (visited on 10/13/2022) (cit. on p. 73).

[134] "DS18B20 datasheet ". (Oct. 2022), [Online]. Available: https://datasheets.maximintegrated.com/en/ds/DS18B20.pdf (visited on 10/13/2022) (cit. on p. 78).

[135] N. W, X. Z, K. R, *et al.*, "Development of a dew/frost point temperature sensor based on tunable diode laser absorption spectroscopy and its application in a cryogenic wind tunnel", *Sensors (Basel)*, vol. 18(8), no. 2704, Aug. 2018. DOI: 10.3390/s18082704 (cit. on p. 84).

[136] J. Goff and S. Gratch, "Low-pressure properties of water from −160 to 212°f", *Transactions of the American Society of Heating and Ventilating Engineers*, pp. 347–354, 1946 (cit. on p. 84).

[137] O. A. Alduchov and R. E. Eskridge, "Improved magnus' form approximation of saturation vapor pressure", Nov. 1997. DOI: 10.2172/548871. [Online]. Available: https://www.osti.gov/biblio/548871 (cit. on pp. 84, 85).

[138] B. Hardy, "Its-90 formulations for vapor pressure, frostpoint temperature, dewpoint temperature, and enhancement factors in the range −100 °C to 100 °C", *The Proceedings of the Third International Symposium on Humidity & Moisture*, 1998 (cit. on p. 85).

[139] B. N. Taylor and C. E. Kuyatt, "Guidelines for evaluating and expressing the uncertainty of nist measurement results", Gaithersburg, Tech. Rep., 1994. DOI: 10.15120/GSI-2022-00599. [Online]. Available: https://emtoolbox.nist.gov/Publications/NISTTechnicalNote1297s.pdf (cit. on p. 86).

[140] X. Lin and K. Hubbard, "Uncertainties of derived dewpoint temperature and relative humidity", *Journal of Applied Meteorology*, vol. 43, pp. 821–825, May 2004. DOI: 10.1175/2100.1 (cit. on p. 86).

[141] Z. Rittersma, "Recent achievements in miniaturised humidity sensors—a review of transduction techniques", *Sensors and Actuators A: Physical*, vol. 96, no. 2, pp. 196–210, 2002, ISSN: 0924-4247. DOI: https://doi.org/10.1016/S0924-4247(01)00788-9. [Online]. Available: https://www.sciencedirect.com/science/article/pii/S0924424701007889 (cit. on p. 86).

[142] A. Kapic, A. Tsirou, P. G. Verdini, and S. Carrara, "Humidity Sensors for High Energy Physics Applications: A Review", *IEEE Sensors J.*, vol. 20, no. 18, pp. 10 335–10 344, 2020. DOI: 10.1109/JSEN.2020.2994315. [Online]. Available: https://cds.cern.ch/record/2729065 (cit. on pp. 86, 94).

[143] "Honeywell HIH3610". (Dec. 2022), [Online]. Available: https://mou.sr/3VTUwY8 (cit. on p. 86).

[144] "Honeywell HIH4030". (), [Online]. Available: https://mou.sr/3FtqLYM (cit. on p. 86).

[145] G. M. Berruti, "Radiation tolerant fiber optic humidity sensors for High Energy Physics applications", Presented 15 Dec 2015, 2015. [Online]. Available: https://cds.cern.ch/record/2143228 (cit. on pp. 86, 90, 92, 94, 99, 102, 111).

[146] "MK33". (Dec. 2022), [Online]. Available: https://www.ist-ag.com/sites/default/files/downloads/mk33%5C_aucu.pdf (cit. on p. 86).

[147] A. Kapic, A. Tsirou, P. Verdini, and S. Carrara, "Radiation tolerance of capacitive humidity sensor for high energy physics applications", *IEEE Sensors Letters*, vol. PP, pp. 1–1, Nov. 2019. DOI: 10.1109/LSENS.2019.2953136 (cit. on p. 86).

[148] "HYT 271/939P/221 Digital Humidity and Temperature Module". (Nov. 2022), [Online]. Available: https://www.ist-ag.com/sites/default/files/downloads/DHHYT-Modules_E_1.pdf (visited on 11/12/2022) (cit. on pp. 87, 88).

[149] "Datasheet SHT85 Humidity and Temperature Sensor ". (Aug. 2022), [Online]. Available: https://www.mouser.com/catalog/specsheets/Sensirion_10022018_HT_DS_SHT85_V0.9_D1.pdf (cit. on pp. 87, 89, 120).

[150] K. Grattan and T. Sun, "Fiber optic sensor technology: An overview", *Sensors and Actuators A: Physical*, vol. 82, no. 1, pp. 40–61, 2000, ISSN: 0924-4247. DOI: https://doi.org/10.1016/S0924-4247(99)00368-4. [Online]. Available: https://www.sciencedirect.com/science/article/pii/S0924424799003684 (cit. on p. 90).

[151] S. A. Kolpakov, N. T. Gordon, C. Mou, and K. Zhou, "Toward a new generation of photonic humidity sensors", *Sensors*, vol. 14, no. 3, pp. 3986–4013, 2014, ISSN: 1424-8220. DOI: 10.3390/s140303986. [Online]. Available: https://www.mdpi.com/1424-8220/14/3/3986 (cit. on p. 90).

[152] T. Yeo, T. Sun, K. Grattan, D. Parry, R. Lade, and B. Powell, "Characterisation of a polymer-coated fibre bragg grating sensor for relative humidity sensing", *Sensors and Actuators B: Chemical*, vol. 110, no. 1, pp. 148–156, 2005, ISSN: 0925-4005. DOI: https://doi.org/10.1016/j.snb.2005.01.033. [Online]. Available: https://www.sciencedirect.com/science/article/pii/S092540050500122X (cit. on pp. 91, 92, 95, 96, 104).

[153] P. Kronenberg, P. K. Rastogi, P. Giaccari, and H. G. Limberger, "Relative humidity sensor with optical fiber bragg gratings", *Opt. Lett.*, vol. 27, no. 16, pp. 1385–1387, Aug. 2002. DOI: 10.1364/OL.27.001385. [Online]. Available: http://opg.optica.org/ol/abstract.cfm?URI=ol-27-16-1385 (cit. on pp. 91, 92, 102, 104).

[154] K. Hill and G. Meltz, "Fiber bragg grating technology fundamentals and overview", *Journal of Lightwave Technology*, vol. 15, no. 8, pp. 1263–1276, 1997. DOI: 10.1109/50.618320 (cit. on p. 91).

[155] A. Othonos, K. Kalli, and G. E. Kohnke, "Fiber bragg gratings: Fundamentals and applications in telecommunications and sensing", *Physics Today*, vol. 53, pp. 61–62, 2000 (cit. on p. 91).

[156] Y.-J. Rao, "In-fibre bragg grating sensors", *Measurement Science and Technology*, vol. 8, no. 4, p. 355, Apr. 1997. DOI: 10.1088/0957-0233/8/4/002. [Online]. Available: https://dx.doi.org/10.1088/0957-0233/8/4/002 (cit. on p. 91).

[157] "ES20 Compact Sampling System User's Manual". (Nov. 2022), [Online]. Available: https://www.processsensing.com/docs/manual/ES20-97447-Users-Manual-V2.pdf (visited on 11/17/2022) (cit. on pp. 93, 109).

[158] "S8000 Remote High Precision Chilled Mirror Hygrometer". (Nov. 2022), [Online]. Available: http://www.michell.com/uk/documents/S8K421_97307_UK_Datasheet-V4.pdf (visited on 11/18/2022) (cit. on pp. 93, 94, 97).

[159] M. Pärg, "Measuring relative humidity in the radioactive environment of the irrad proton facility", [Online]. Available: https://cds.cern.ch/record/2286011/files/Relative_humidity_IRRAD_Marten_P%5C%C3%5C%A4rg.pdf (cit. on p. 94).

[160] I. Shchemerov, S. Legotin, P. Lagov, *et al.*, "Radiation effect on the polymer-based capacitive relative humidity sensors", *Nuclear Engineering and Technology*, vol. 54, no. 8, pp. 2871–2876, 2022, ISSN: 1738-5733. DOI: https://doi.org/10.1016/j.net.2022.02.027. [Online]. Available: https://www.sciencedirect.com/science/article/pii/S1738573322001000 (cit. on p. 94).

[161] B. Risch, B. Overton, J. Rosko, *et al.*, "Optical fiber and cable reliability for high radiation environments", Nov. 2022 (cit. on p. 94).

[162] J. Troska, J. Batten, K. A. Gill, and F. Vasey, "Radiation effects in commercial off-the-shelf single-mode optical fibers", in *Photonics for Space Environments VI*, E. W. Taylor, Ed., International Society for Optics and Photonics, vol. 3440, SPIE, 1998, pp. 112–119. DOI: 10.1117/12.326687. [Online]. Available: https://doi.org/10.1117/12.326687 (cit. on p. 94).

[163] A. Gusarov and S. Hoeffgen, "Radiation effects on fiber gratings", *Nuclear Science, IEEE Transactions on*, vol. 60, pp. 2037–2053, Jun. 2013. DOI: 10.1109/TNS.2013.2252366 (cit. on pp. 94, 95).

[164] "AOS GmbH". (Dec. 2022), [Online]. Available: https://www.aos-fiber.com/ (cit. on p. 97).

[165] "Technica". (Dec. 2022), [Online]. Available: https://technicasa.com/ (cit. on p. 97).

[166] "Binder MKF-240 ". (Nov. 2022), [Online]. Available: https://www.binder-world.com/int-en/product/mkf-240 (visited on 11/19/2022) (cit. on pp. 97, 163).

[167] M. Fossa and P. Petagna, "Use and Calibration of Capacitive RH Sensors for the Hygrometric Control of the CMS Tracker", CERN, Geneva, Tech. Rep., 2003. [Online]. Available: http://cds.cern.ch/record/687857 (cit. on p. 98).

[168] "Si255 Optical sensing instrument ". (Nov. 2022), [Online]. Available: https://lunainc.com/product/si255-optical-sensing-instrument (visited on 11/19/2022) (cit. on p. 98).

[169] L. B. Veldscholte and S. de Beer, "OpenHumidistat: Humidity-controlled experiments for everyone", Dec. 2021. DOI: 10.1016/j.ohx.2022.e00288. arXiv: 2112.08500 [physics.ins-det] (cit. on p. 99).

[170] J. Fraden, *Handbook of Modern Sensors: Physics, Designs, and Applications (Handbook of Modern Sensors)*. SpringerVerlag, 2016, ISBN: 978-3-319-19303-8 (cit. on p. 99).

[171] "mCBM ". (Aug. 2022), [Online]. Available: https://www.gsi.de/work/forschung/cbmnqm/cbm/activities/mcbm (cit. on p. 113).

[172] "Mcbm@sis18 is on its way", Darmstadt, Tech. Rep. CBM Progress Report 2017, 2018, V, 214 Seiten : Illustrationen, grafische Darstellungen. DOI: 10.15120/GSI-2018-00485. [Online]. Available: https://repository.gsi.de/record/209729 (cit. on p. 113).

[173] C.Sturm, "Achievements of the mcbm beam campaign 2021", Darmstadt, Tech. Rep. 2022, 2022, 239 p. DOI: 10.15120/GSI-2022-00599. [Online]. Available: https://repository.gsi.de/record/246663 (cit. on p. 115).

[174] D. Ramirez and A. Toia, "Performance of the msts detector during the mcbm beam campaign 2021", Darmstadt, Tech. Rep. 2022, 2022, 239 p. DOI: 10.15120/GSI-2022-00599. [Online]. Available: https://repository.gsi.de/record/246663 (cit. on p. 115).

[175] "Weave Scope ". (), [Online]. Available: https://www.weave.works/oss/scope// (visited on 02/08/2023) (cit. on p. 118).

[176] "Raspberry Pi ". (Feb. 2023), [Online]. Available: https://www.raspberrypi.com/products/raspberry-pi-4-model-b/ (cit. on p. 120).

[177] "CONTROLLER MODULE FOR USE WITH MMS COMPATIBLE ECH CRATE SERIES AND MODULES ". (Aug. 2022), [Online]. Available: https://iseg-hv.com/en/products/detail/MMS-Controller (cit. on p. 120).

[178] "MPOD - Universal Multichannel Low- and High- Voltage System ". (Aug. 2022), [Online]. Available: https://www.wiener-d.com/product/mpod-full-size-crate/ (cit. on p. 120).

[179] P. Koczon, C. J. Schmidt, U. Frankenfeld, *et al.*, "The powering concept of the Silicon Tracking System for CBM@FAIR", *PoS*, vol. TWEPP2019, p. 063, 2020. DOI: 10.22323/1.370.0063 (cit. on p. 120).

[180] F. Arteche, C. Esteban, M. Iglesias, C. Rivetta, and F. Arcega, "Detector noise susceptibility issues for the future generation of high energy physics experiments", *Proceedings of the Topical Workshop on Electronics for Particle Physics, TWEPP 2008*, Jan. 2011 (cit. on p. 121).

[181] V. Bobillier, J. Christiansen, G. Corti, *et al.*, "Grounding, Shielding and Cooling Issues on LHCb Electronics at the LHC pit 8", 2008. DOI: 10.5170/CERN-2008-008.497. [Online]. Available: https://cds.cern.ch/record/1159563 (cit. on p. 121).

[182] *Private information from A. Lymanets* (cit. on p. 123).

[183] J. M. Heuser, "Assembly and commissioning of the msts detector for mcbm startup", Darmstadt, Tech. Rep. CBM Progress Report 2018, 2019, 220 p. DOI: 10.15120/GSI-2019-01018. [Online]. Available: https://repository.gsi.de/record/220128 (cit. on p. 122).

[184] *Private information from A. Rodriguez* (cit. on p. 124).

[185] "Lauda cooling thermostats". (Nov. 2022), [Online]. Available: https://www.lauda.de/en/constant-temperature-equipment/thermostats/cooling-thermostats/eco (cit. on p. 125).

[186] M. Teklishyn and A. Lymanets, "Assembly, testing and comissioning of the msts detector", Darmstadt, Tech. Rep. 2022, 2022, 239 p. DOI: 10.15120/GSI-2022-00599. [Online]. Available: https://repository.gsi.de/record/246663 (cit. on p. 125).

[187] "R&S HMP4000 Power supply series ". (Nov. 2022), [Online]. Available: https://www.rohde-schwarz.com/us/products/test-and-measurement/dc-power-supplies/rs-hmp4000-power-supply-series_63493-47360.html (cit. on p. 127).

[188] P. Larionov, "Systematic irradiation studies and Quality Assurance of silicon strip sensors for the CBM Silicon Tracking System", Ph.D. dissertation, Frankfurt U., 2016 (cit. on p. 137).

[189] "DC Power supply ". (Nov. 2022), [Online]. Available: https://www.tek.com/en/products/keithley/dc-power-supplies (cit. on p. 138).

[190] K. Agarwal. "DEVELOPMENT OF COOLING DEMONSTRATOR FOR THE CBM SILICON TRACKING SYSTEM (STS)". (Nov. 2022), [Online]. Available: https://indico.gsi.de/event/8809/contributions/38305/attachments/27598/34477/20190320_Agarwal_DPG_v02.pdf (cit. on p. 144).

[191] "Swarm mode overview ". (Aug. 2022), [Online]. Available: https://docs.docker.com/engine/swarm/ (cit. on p. 145).

[192] "Production-Grade Container Orchestration ". (Aug. 2022), [Online]. Available: https://kubernetes.io/ (cit. on p. 145).

[193] G. Knap, T. Cobb, Y. Moazzam, U. Pedersen, and C. Reynolds, "Kubernetes for epics iocs", in *Proceedings of the 18th International Conference on Accelerator and Large Experimental Physics Control Systems*, (Shanghai, China), K. F. (KEK), Y. Y. (SARI), Y. L. (SARI), Z. C. (SARI), and V. R. S. (GSI), Eds., Oct. 2021, ISBN: 978-3-95450-221-9 (cit. on p. 145).

[194] "Gateway: The Process Variable Gateway ". (Aug. 2022), [Online]. Available: https://epics.anl.gov/extensions/gateway/index.php (cit. on p. 145).

[195] S. Ritt. "Electronic Logbook ". (Aug. 2022), [Online]. Available: https://elog.psi.ch/elog/index.html#links (cit. on p. 146).

[196] F. Feldbauer. "Elog Client for Phoebus ". (Aug. 2022), [Online]. Available: https://indico.fhi-berlin.mpg.de/event/52/contributions/564/attachments/222/683/phoebus-elog-client.pdf (cit. on p. 146).

[197] "synApps - autosave ". (Aug. 2022), [Online]. Available: https://epics.anl.gov/bcda/synApps/autosave/autosave.html (visited on 08/31/2022) (cit. on p. 146).

[198] "MAchine SAve and Restore ". (Aug. 2022), [Online]. Available: https://control-system-studio.readthedocs.io/en/latest/services/save-and-restore/doc/index.html (visited on 08/31/2022) (cit. on p. 146).

[199] "EPICS Collaboration Meeting 2022 ". (Aug. 2022), [Online]. Available: https://controlssoftware.sns.ornl.gov/training/2022_EPICS/ (visited on 08/31/2022) (cit. on p. 146).

Glossary

A | B | C | D | E | F | G | H | I | J | L | M | N | O | P | Q | R | S | T

A

ADC

Analog Digital Converter. 24, 26, 65, 122, 123

AFE

Analog Front End. 24, 129, 131

ALH

Alarm Handler. 42

ALICE

A Large Ion Collider Experiment. 7, 22

API

Application Programming Interface. 42

AR

Archiver. 42

ASIC

Application-specific Integrated Circuit. 21, 23–29, 64, 71–75, 80–82, 114, 122–124, 127–129, 140, 141, 159, 162

B

BES

Beam Energy Scan. 6

BMON

Beam Monitor. 11, 38

C

CA

Cellular Automaton. 12

CBM

Compressed Baryonic Matter. 7–12, 24, 27, 28, 30, 35, 36, 40, 43, 51, 53, 55, 113, 114, 116, 145–147, 151, 154, 156

CCE

Charge Collection Efficiency. 17, 31

CERN

Conseil Européen pour la Recherche Nucléaire. 22, 90, 95

CMS

Compact Muon Solenoid. 22, 35, 90, 95

CPU

Central Processing Unit. 35

CRI

Common Readout Interface. 24, 28, 29, 35, 38, 114, 115, 120, 141, 155

CROB

Common Readout Board. 120

CSA

Charge Sensitive Amplifier. 26, 27, 65, 72, 75, 79, 127–129, 131, 132, 160, 162

CSS

Control System Studio. 46

CTE

Coefficient of Thermal Expansion. 69, 70, 82, 147

D

DAQ

Data Acquisition. 10, 24, 27, 28, 36–38, 64, 65, 114, 140, 152

DB

Database. 115

DCA

Device Control Agent. 36–38, 141

DCS

Detector Control System. 12, 13, 32, 36–40, 43, 45–47, 49, 113–119, 126, 127, 132, 140, 141, 143, 145, 146, 152, 155, 159

DPB

Data Processing Board. 25, 29, 64

E

ECA

Experiment Control Agent. 37

ECS

Experiment Control System. 12, 36–38, 118, 155

EDC

Experiment and Detector Control. 38

EMI

Electromagnetic Interference. 120–122

ENC

Equivalent noise charge. 28, 122, 123

EPICS

Experimental Physics and Industrial Control System. 38, 40, 41, 43, 44, 46, 48, 51, 55, 64, 65, 98, 147

F

FAIR

Facility for Antiproton and Ion Research. 8, 9, 43, 113

FBG

Fibre Bragg Grating. 90–92, 96, 97, 99, 100, 106, 110, 111, 158, 159

FEB

Front End Board. 13, 21–26, 28, 29, 63, 64, 66–76, 78–81, 113, 114, 116, 120–122, 127–130, 133, 134, 136, 138, 140, 144, 147, 151, 155–157, 160, 161, 165, 166

FEE

Front end electronics. 13, 21, 23, 24, 28, 35, 51, 62–66, 83, 120–122, 125, 127, 132, 133, 145–147

FLES

First Level Event Selector. 24, 28, 35, 38, 114, 120, 155

FLIM

FLES Interface Module. 38

FOS

Fibre Optic Sensor. 90, 91, 93, 96, 106, 111, 144, 147, 151, 152, 158

FPGA

Field Programmable Gate Arrays. 28, 29

FSM

Finite State Machine. 39, 40, 49, 118, 119, 126, 141, 155

G

GBT

Giga-Bit Transceiver. 28, 64

GEM

Gas Electron Multiplication. 11

GPU

Graphics Processing Unit. 35

GSI

GSI Helmholtz Centre for Heavy Ion Research. 9, 51, 154

GUI

Graphical User Interface. 33, 39, 46–49, 120, 146, 156

H

HADES

High Acceptance Di-Electron Spectrometer. 7, 9, 41

HEP

High Energy Physics. 43, 86

HV

High Voltage. 116, 122, 125, 138, 147

I

IOC

Input/Output Controller. 32, 40–44, 46, 64, 72, 98, 117, 119, 120, 145–147, 155, 163

ITER

International Thermonuclear Experimental Reactor. 41

J

J-PARC

Japan Proton Accelerator Research Complex. 41

L

LDO

Low-dropout regulator. 25, 69, 71–74, 76, 78–82, 122, 123, 127, 129, 157, 162

LET

Linear Energy Transfer. 54

LHC

Large Hadron Collider. 3, 4, 7, 154

LV

Low voltage. 13, 125, 127, 138, 139

M

MAPS

Monolithic Active Pixel Sensor. 11

mCBM

mini Compressed Baryonic Matter. 13, 36, 55–57, 113–115, 122, 124, 125, 136, 140, 152, 156, 159, 160

MIP

Minimum Ionizing Particle. 115

MRPC

Multi-Gap Resistive Plate Chambers. 12

mSTS

mini Silicon Tracking System. 41, 43, 48, 65, 113–115, 117–123, 125–127, 130–132, 135, 137–141, 146, 148, 152, 153, 159–162, 167

MUCH

Muon Chambers. 11, 12, 26, 38

MVD

Micro Vertex Detector. 11, 38, 43

N

NTP

Network Time Protocol. 146

O

OPI

Operator Interface. 39–41, 46

P

PANDA

antiProton ANihilation at DArmstadt. 43

PCA

Partition Control Agent. 37, 38

PCB

Printed Circuit Board. 63, 69, 71, 72, 80

PLC

Programmable Logic Controller. 39, 146

POB

Powering Board. 23, 75, 120, 125, 133, 134, 160

PSC

Polarity Selection Circuit. 26

PSD

Projectile Spectators Detector. 12, 38

PV

Process Variable. 39, 41, 46–48, 51, 72, 119, 145, 146, 155

Q

QCD

Quantum Chromodynamics. 3, 4, 7

QGP

Quark Gluon Plasma. 3, 7

R

RH

Relative Humidity. 72, 83–85, 87–89, 95, 97–100, 102–104, 106, 107, 125, 133, 158–160

RHIC

Relativistic Heavy Ion Collider. 3, 4, 6, 154

RICH

Ring Imaging Cherenkov. 11, 12, 38

ROB

Readout Board. 24, 25, 28, 29, 63, 64, 75, 133, 134, 155, 156, 160

RPC

Resistive Plate Chambers. 11

S

SBC

Single Board Computer. 117, 120

SBM

Single Board Microcontroller. 73, 157

SCA

System Control Agent. 37, 38, 45, 118, 141

1) Slow Control Adapter. 28, 64

SEE

Single Event Effects. 51, 54, 57, 58, 60–62, 156

SER

Soft Error Rate. 52

SNMP

Simple Network Management Protocol . 120

SPS

The Super Proton Synchrotron. 3

STAR

Solenoidal Tracker at RHIC. 7, 22, 41

STS

Silicon Tracking System. 11, 13, 15, 20–32, 36, 38–43, 47, 49, 51, 52, 62, 63, 66, 68–70, 73–75, 81–84, 86, 87, 89, 92, 94, 95, 111, 113, 116, 117, 120, 129, 131, 132, 135, 140, 141, 143–145, 147, 149–153, 155–157, 162, 165

T

TCP

Transmission Control Protocol. 39

TFC

Timing and Fast Control. 24, 28, 35, 37, 38, 155

TLD

Thermoluminescent Dosimeters. 56, 58

TOF

Time of Flight. 10, 12, 38

TRD

Transition Radiation Detector. 11, 12, 38